UNIVERSITY OF PRETORIA
DEPARTMENT OF MINING ENGINEERING
PRETORIA

SLOPE STABILITY ANALYSES IN COMPLEX GEOTECHNICAL CONDITIONS – THRUST FAILURE MECHANISM

by

Krassimir Nikolov Karparov, PrEng

Submitted in partial fulfilment of the requirements for the degree Philosophiae Doctor (Mining Engineering) in the Faculty of Engineering, Built Environment and Information Technology, University of Pretoria, Pretoria

January, 2007

As far as the laws of mathematics refer to reality, they are not certain, and as far as they are certain, they do not refer to reality.

Albert Einstein (1879–1955), German-born scientist, *The Tao of Physics,* Chapter 2 (1975).

DEDICATION

To my son Nickola, born when I was busy working on this Thesis

To my wife Zdravka Karparov, for taking the functions of mother and father in the family when I was busy

To my brother Roumen Karparov, PrEng; MSc, mother Stoyna Karparova and father Nickola Karparov for their support and encouragement during the work

ACKNOWLEDGEMENTS

First of all, I would like to express my immeasurable gratitude to my supervisor, Prof. Matthew Handley for his support and guidance in all my years at The University of Pretoria. His patience and encouragement are something I deeply appreciate and admire.

I also own many thanks to Prof. Andre Fourie, Prof. Nielen van der Merwe and Coaltek 2020 Management team for their support and opportunity to make this Dissertation.

I would like to extend my thanks to:

1. Prof. Peter Lilly from Western Australian School of Mines, Curtin University of Technology for his helpfulness and encouragement
2. Prof. Hennie Theart from the Geology Department, University of Pretoria, for his comments about the grains in the microscopic pictures
3. Prof. Roland Merkle, from the Geology Department, University of Pretoria, for his assistance in the microscopic measurements
4. Dr. Boatang Chen from CSIRO for his help in the study cases collection and comments
5. Dr. Roumen Angelov from the Department of Mathematics, University of Pretoria, for his advises and comments in the equations development
6. Ivan Canadi from Anglo Coal, Rock Mechanics Department, for his assistance, discussions and comments
7. Anglo Coal Rock Mechanics Department for their help and support

DECLARATION

I declare that this Dissertation contains only my own original work, except where reference is made with acknowledgement to contribution from others. I also declare that this material has not been submitted for any other purpose or examination to any other Department or University.

Signed this ---------- day of ----------

Krassimir N. Karparov, PrEng; FSAIMM

SUMMARY

SLOPE STABILITY ANALYSES IN COMPLEX GEOTECHNICAL CONDITIONS – THRUST FAILURE MECHANISM

by

Krassimir Nikolov Karparov

Supervisor: Prof. Matthew Handley

Department: Mining Engineering

Degree: Philosophiae Doctor (Mining Engineering)

Key terms: slope stability, undulated formation, embedded weaker layer, co-linear flakes, cohesive zone, frictional zone, relaxation stress, active block, passive block, and safety factor.

In this thesis a previously unknown mechanism of failure in multilayered slope profiles is identified. In some conditions this mechanism does not confirm to the known failure models (relating to circular failure) used in slope stability analysis. For this reason, major failures have occurred in the artificial cuts despite the fact that the limit equilibrium methods suggest that these cuts would be stable. The limit equilibrium methods were originally created to apply to earth dam walls. In the open pit mining environment, where we face inhomogeneous and inclined multilayered structures, the assumptions of these limit equilibrium methods appear to be inapplicable (e.g. assumption for the equal shear strength along the failure surface).

Analysis starts with a general picture of the stress state in the highwall slope, given extant geological conditions and rock properties. The study then focuses on a comparison of the crack-tip stress changes in the rockmass with and without inclusions at the microscopic

level. Basing some assumptions on binocular microscope observations of grain structures, it is possible to measure the size of the different inclusions and show that the microscopic carbon flakes present in the rock fabric make a major contribution to the failure process in a mudstone layer in the slope.

The approach adopts the fracture-process zone ahead of a crack tip as the controlling parameter of flaw propagation in rock. Flaw coalescence, which is poorly accounted for in current fracture models, is attributable to two phenomena: the flaw propagation due to high level of applied stress; and the linking of fracture-process zones due to the small distance between neighbouring flaws. A condition of flaw coalescence is given based on these two mechanisms.

This development allows defining of two zones along the failure surface (frictional and cohesive). In the slope-stability field the shear strength of the rock along the failure plane is a composite function of cohesive and frictional strength.

For instance, the relaxation stress normal to bedding, induced by overburden removal, provides an investigation method for the determination of the weakest minerals, which may act as flaws for fracture propagation in low-porosity rock. A method has been developed to determine the critical stress for tensile fracture propagation due to the rock structure and the stress reduction normal to bedding.

A proposed failure mechanism is based on the polygonal failure surfaces theory developed by Kovari and Fritz

(1978), Boyd's field observations (1983), Stead and Scoble's (1983) analyses, Riedel (1929) Shear Fracture Model, Tchalenko and Ambraseys (1970), Gammond's (1983) and Ortlepp (1997) observations for natural shear failures, computer modelling by McKinnon and de la Barra (1998), the results of many laboratory experiments reported by Bartlett et al. (1981) and the author's experience. The proposed failure mechanism evaluates stability of the artificial slope profile due to the embedded weak layer structure, layer thickness, layer inclination and depth of the cut. On the basis of the observations and the above-mentioned modified fracture model, the slope profile is divided into two blocks; passive and active blocks. With this new model, it is possible to calculate slope safety factors for the slope failure cases studied in the industry. It has been found that, whereas the conventional slope stability models predict stable conditions, the new model suggests that the slope is only marginally stable (i.e. that failure can be expected).

TABLE OF CONTENTS

LIST OF FIGURES

LIST OF PICTURES

LIST OF TABLES

LIST OF NOTATIONS

A	Area
A_c	Actual contact area
dA	Area of an element
a	Half of the crack length
a_c	Critical half crack length
b	Half of the distance between the outer ends of two neighbor co-linear flakes with developed FPZ
c	Rock cohesion
c_j	Cohesion along the plane of weakness
c_u	Undrained shear strength
c_{av}	Average cohesion of the profile
$\bar{c}_I$	Cohesion of the Active block inner side
$\bar{c}_O$	Cohesion of the Active block outer side
CTOD	Crack tip opening displacement
D-B	Dugdale-Barenblatt
DDM	Displacement discontinuity method
d	Grain diameter
e	Half of the distance between the inner ends of two neighbor co-linear flakes
f	Half of the distance between the outer ends of two neighbor co-linear flakes
F_n	Normal load
FD	Final difference method
F_0	Initial load
FOS	Factor of safety
G	Shear modulus (Rigidity)
g	Earth acceleration
h	Depth (Chapter 2)
H	Slope height
k	K-ratio (Chapter 2); argument (Chapter 4)
k^*_H	Stress concentration coefficient for horizontal

	stress component
k^*_V	Stress concentration coefficient for vertical stress component
K_{IC}	Mode-I fracture toughness coefficient
K_q	Fracture toughness calculated using linear elasticity
ΔK_{tip}	Difference between the near the tip SIF and the field SIF
K_{tip}	Near the tip SIF
K_0	Field SIF
K^N_I	Stress intensity factor under the load $\Delta\sigma_N$
K^D_I	Stress intensity factor in the fracture process zone
K^N_{IA}	Stress intensity factor under the load $\Delta\sigma_N$ in point A
K^N_{IB}	Stress intensity factor under the load $\Delta\sigma_N$ in point B
K^N_{IC}	Stress intensity factor under the load $\Delta\sigma_N$ in point C
K^N_{ID}	Stress intensity factor under the load $\Delta\sigma_N$ in point D
l	Inclusion’s length (in Chapter 5); Length of the fracture process zone (in Chapter 6)
l_c	Critical length of the fracture process zone
l_B	Length of the Passive block failure surface
l_c	Cohesive zone length along the Passive block failure surface
l_f	Frictional zone length along the Passive block failure surface
l_I	Shear failure length along the inner side of the Active block
l_O	Shear failure length along the outer side of the Active block

m	Axes along the plane of weakness (Chapter 2) Layer thickness (Chapter 8)
n	Axes normal to the plane of weakness
OCR	Overconsolidation ratio
p	Plasticity factor
P_A	Active block load
P_F	Frictional zone load
P_c	Cohesive zone load
R_P	Passive block reaction applied to the active block
$\overline{R}$	Combined action of the active block load and the passive block reaction to the active block outer shear failure surface
SCC	Stress concentration coefficient
TAT	Tributary area theory
W	Inclusion's thickness or width

Greek symbols

α	Inclination angle (Chapters 2 and 3)
$\Delta\delta_p$	Displacement difference between two cycles during the loading process before failure
$\Delta\delta_i$	Displacement difference between two cycles during the unloading process before failure
β	Angle formed by the principal stress direction and the joint (Chapter 2) Slope angle (Chapter 3) Angle between the axes and the center point of an element (Chapter 4)
β_I	Inclination of the inner side of the active block shear failure plane
β_O	Inclination of outer side of the Active block

	shear failure plane
γ	Total unit weight of the soil
λ	Directional *cosine* matrix
ϕ	Angle of internal friction
ϕ_j	Joint plane friction angle
φ	Failure plane angle
φ_j	Dilation angle along the weak bedding plane
χ	Stress coefficient
ρ	Rock density
π	The number pi
ν	Poisson's ratio
σ_0	Stress on element
$\Delta\sigma_N$	Normal to sedimentation stress difference
$\Delta\sigma_{ij}$	Stress difference
$\Delta\sigma_{XX}$	Stress difference of the horizontal stress components
$\Delta\sigma_{YY}$	Stress difference of the vertical stress components
$\Delta\sigma_{XY}$	Stress difference of the shear stress components
σ_H	Horizontal stress component
σ_N	Normal to the fracture stress component
σ_V	Vertical stress component
σ_H^F	Horizontal stress component calculated by FLAC
σ_V^F	Vertical stress component calculated by FLAC
σ^V_{xx}	Horizontal stress component in virgin condition
σ^V_{yy}	Vertical stress component in virgin condition
σ^V_{xy}	Shear stress component in virgin condition
σ^R_{xx}	Resultant horizontal stress component
σ^R_{yy}	Resultant vertical stress component
σ^R_{xy}	Resultant shear stress component
σ^V_N	Normal to sedimentation stress component in virgin condition

σ^{R}_{N}	Normal to sedimentation stress component calculated from resultant stress components
$\tilde{\sigma}(x)$	Tensile stress in the fracture process zone
$\sigma(x)$	Closing cohesive stress
σ_1	Local maximum principal stress at the crack tip
σ_3	Minor principal stress
σ_t	Tensile strength
σ_{tj}	Tensile strength along the sedimentation
σ_{tt}	Tensile stress
σ_c	Maximum pressure for a uniaxial compressive test (Chapter 2)
	Critical fracture stress (Chapter 4)
σ_{CD}	Crack damage stress
σ_N^c	Critical stress corresponding to the crack propagation
σ_N^L	Critical stress corresponding to the linking of the fracture process zone
σ_N^P	Stress of the co-linear flaws propagation and coalescence
$\Delta\sigma_N^c$	Critical value of the normal to sedimentation stress difference
$\Delta\sigma_N^P$	Normal to bedding stress difference of the co-linear flaws propagation and coalescence
σ^{V}_{ij}	Virgin stress component
σ^{R}_{ij}	Resultant stress component
σ^{I}_{ij}	Induced stress component
σ_y	Yield strength
τ	Shear stress
τ_f	Shear stress of failure
ξ	Local distance
ε	Strain
ϖ	Layers inclination angle

ϖ_A Layers inclination angle in the active block wedge

ϖ_F Layers average inclination angle along the passive block frictional zone

ϖ_C Layers average inclination angle along the passive block cohesive zone

CHAPTER 1
INTRODUCTION

Any rock type in opencast extraction is always susceptible to slope-stability problems. The slope profile is usually an inhomogeneous structure comprising anisotropic layers characterised by different strength parameters. These composite structures often present problems, raising questions about stresses and deformations specifically related to weaker layers or regions in the rock mass. The widely used slope-stability modelling with equilibrium methods has proved ineffective for studying the effects of horizontal stress and complex geotechnical conditions because they generally assume homogeneity, isotropy, and simple structure.

One of the most recognised books (in the field of rock slope design), namely "Rock Slope Engineering" (Hoek and Bray, 1981) was first published 26 years ago, and there have been few new developments in slope stability analysis since. The means for predicting the number and tonnage of multibench structurally controlled failures (wedge, plane shear and step-wedge) are also well developed in the CANMET(1997) “Pit Slope Manual”, but this manual brings few new developments to slope stability analysis. Anderson and Richards, (1992) stated that rockmass strength models, developed stress field models, and rockmass displacement models for overall slope instability had not yet been developed, and this remains true today.

1.1 BACKGROUND TO THE PROBLEM

Most textbooks on soil mechanics or geotechnical engineering include references to several alternative limit equilibrium methods of slope-stability analysis. In a survey of these methods, undertaken by Wright et al. (1973), the characteristics of all accepted methods were summarised, including the ordinary method of slices (Fellenius, 1936), Bishop's Modified Method (Bishop, 1955), force equilibrium methods (e.g. Lowe and Karafiath, 1960), Janbu's procedure for slices (Janbu, 1957), Morgenstern and Price, (1965) and Spencer's method (Spencer, 1967). There seems to be some consensus that the Morgenstern-Price method is one of the most reliable.

All limit equilibrium methods are based on an assumption that the failing soil mass could be divided into slices. This slicing requires further assumptions regarding the magnitude and direction of the side forces influencing equilibrium. The assumption made about side forces is one of the main characteristics that distinguishes one limit equilibrium method from another, and yet is itself an entirely artificial distinction (Bromhead, 1992).

By using these analytical techniques, some broad assumptions are made for each of the failure modes, particularly where the failure mode is other than classic:

a) Constant shear strength along the failure surface;
b) Distribution of normal stress round the slip surface;

c) Distribution of interslice forces along the profile;

d) The position of the line of thrust; and

e) The *k* - ratio ($k=\sigma_H/\sigma_V$) influence on the slope-stability and failure surface.

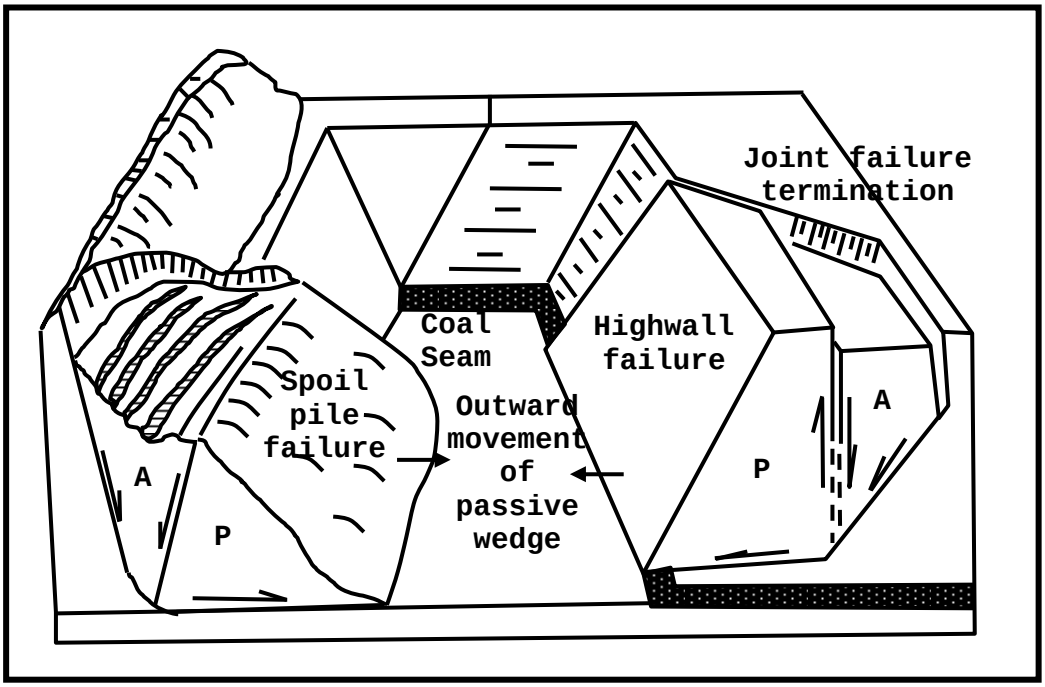

Figure 1.1

Slope and spoil failures reported by Boyd (1983)

Sturman (1984), Singh and Singh (1992), Malgot et al. (1986) and Boyd (1983 – Figure 1.1) reported different cases of slope instabilities. The failure events in their analyses dealt with divergences from the standard failure modes. In the considered cases, all of these authors recognise two block types (the so called "passive" and "active" block), which constitute the failure.

Stead and Scoble (1983) analysed 226 slope instabilities that took place in British coal mines. Their study (Figure 1.2) shows that in about 66% of the failures (the planar, biplanar and multi planar modes) the failure mode is different from the classic model as

geological features trigger almost half of them. The remaining planar failures appear to be stress related. At present there is no reliable technique for application to such cases.

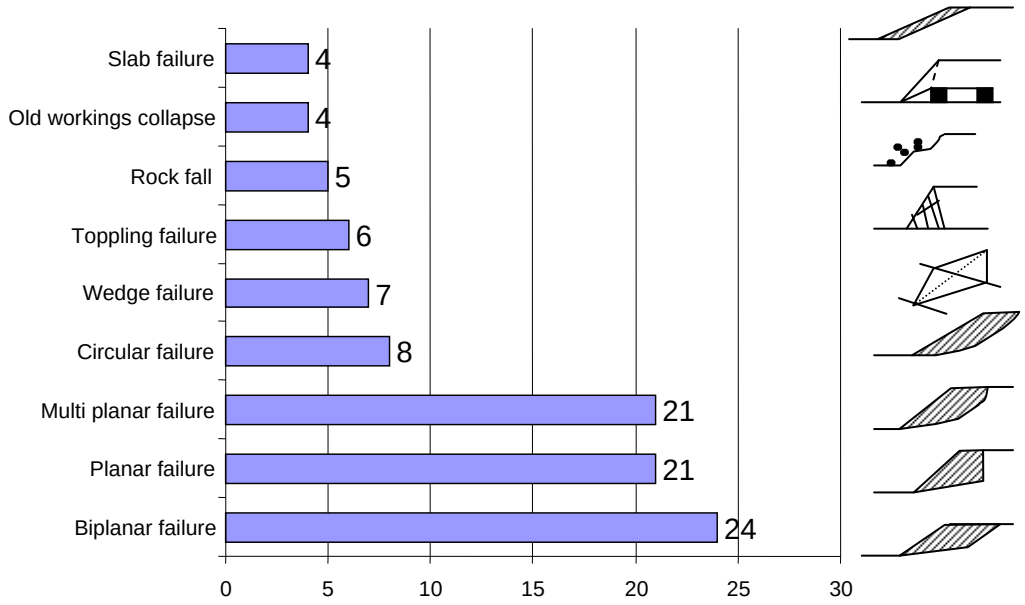

Figure 1.2

Typical failure modes (given in percentages) based on 226 study cases (after Stead and Scoble, 1983)

The author has experience with slope failures that have taken place in South African coalfields. Some coal mines exploit uneven seams in undulated strata, where slope failures exhibit the passive wedge mode as shown on Figure 1.1. The author's observations were that the most common effect of faulting in such a situation was the provision of a rear release plane, frequently with associated adversely dipping strata. In almost all of the cases, a relatively weaker layer was embedded in the profile and exposed at the toe of the slope. In almost all of the cases the weaker layer was shale. In the areas with almost flat strata it is usual to have swelling in such a shale layer, as can be seen on Picture 1.1.

The failure situation becomes more complicated if opencast mining activities are in progress in the vicinity of existing undulated strata formations. The potential for slope failure increases when these strata formations form inclined beds, dipping toward the pit.

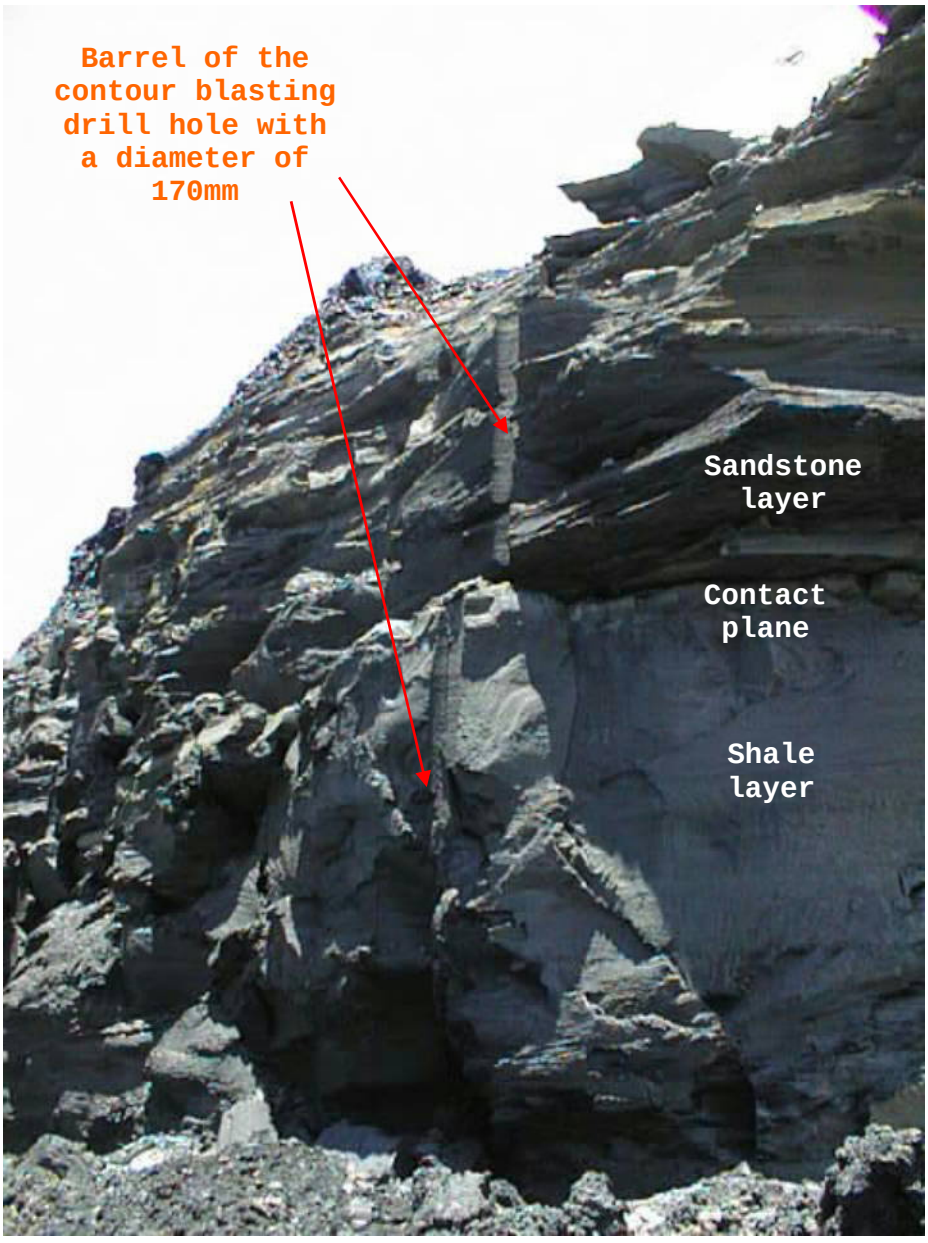

Picture 1.1

Shale swelling exposed at the toe of slope in gently inclined strata (strata inclined at 5^0)

Further complications could be created by the remains of old mining activities in the form of pillars left underground, and now exposed at the toe of the slope.

1.1.1 Geological history and its effect on geotechnical complexity

A representative stratigraphic column can be seen in Figure 1.3. The principal palaeo-feature of the deposits is the uneven dolomite base, which has led to sediments deposited on it being uneven. The strata are not uniformly thick or level, but undulate following the dolomite base. The coal seams, as well as the other strata, are thinner above palaeo-highs and thicker above palaeo-lows. This feature has resulted in strata dipping up to 15^0 between crests and troughs in the dolomite palaeo-surface. The dolomite highs themselves are dome shaped and 200-300m in diameter. Refer to Figure 1.10 for typical features of the geological formations.

Note that the undulated strata formations described above are definitely not tectonic formations, but are the result of weathering and chemical erosion, which has sculpted a karstic topography on this dolomitic basement. This process was followed by glaciation, which smoothed the rugged karstic topography and formed tillite deposits in the sinkholes. Cairncross (1989) states that the coal sequence accumulated in the fringes of fluid-glacial currents at the end of the Paleozoic when the southern tip of Africa was located near the South Pole.

The above-described processes generated a rugged topography of ridges and sinkholes prior to the accumulation of the coal-bearing sequence above it. The undulated strata reflect the underlying dolomitic palaeo-surface by having a similar topography, in that they are approximately circular in form in plan (with a diameter of a few hundred metres) and have a hill-like form. The dolomite palaeo-surface was formed in white dolomite belonging to the Transvaal Supergroup. Further widening and joining of the karstic features in the dolomite after the deposition of the overlying sediments also contributed to the degree of undulation in formations in the overlying coal bearing strata.

Cairncross (1989) asserts that the development of coal on top of glacial deposits represents the corresponding rise in temperatures as Africa drifted away from the extreme latitudes. A more temperate climate allowed the growth of mostly deciduous vegetation in a swampy near-shore environment where rivers transported re-worked glacial tillite materials into a subsiding intracratonic basin. The coal-bearing strata probably represent the gradual formation and final drowning of retrogressive deltaic lobes, where fluid-glacial features of the Dwyka formation are overlain by retrograde deltaic sediments, which are in turn overlain by beach and marine deposits of the now-recognised Hard Overburden, and Hard Interburden (see Figure 1.3) as the sea level gradually rises (Cairncross, 1989). Grit, sand and mudstone partings within the coal seams may represent clastic inundation of peat swamps by mud from anastomosing currents, and occasional marine incursions (Cairncross, 1989).

Diagenesis and coalification of lignite deposits occurred after the onset of regional extension related to the break-up of Gondwana during the late Paleozoic to early Triassic, and corresponding intrusion of doleritic dykes (Snyman and Barclay, 1989).

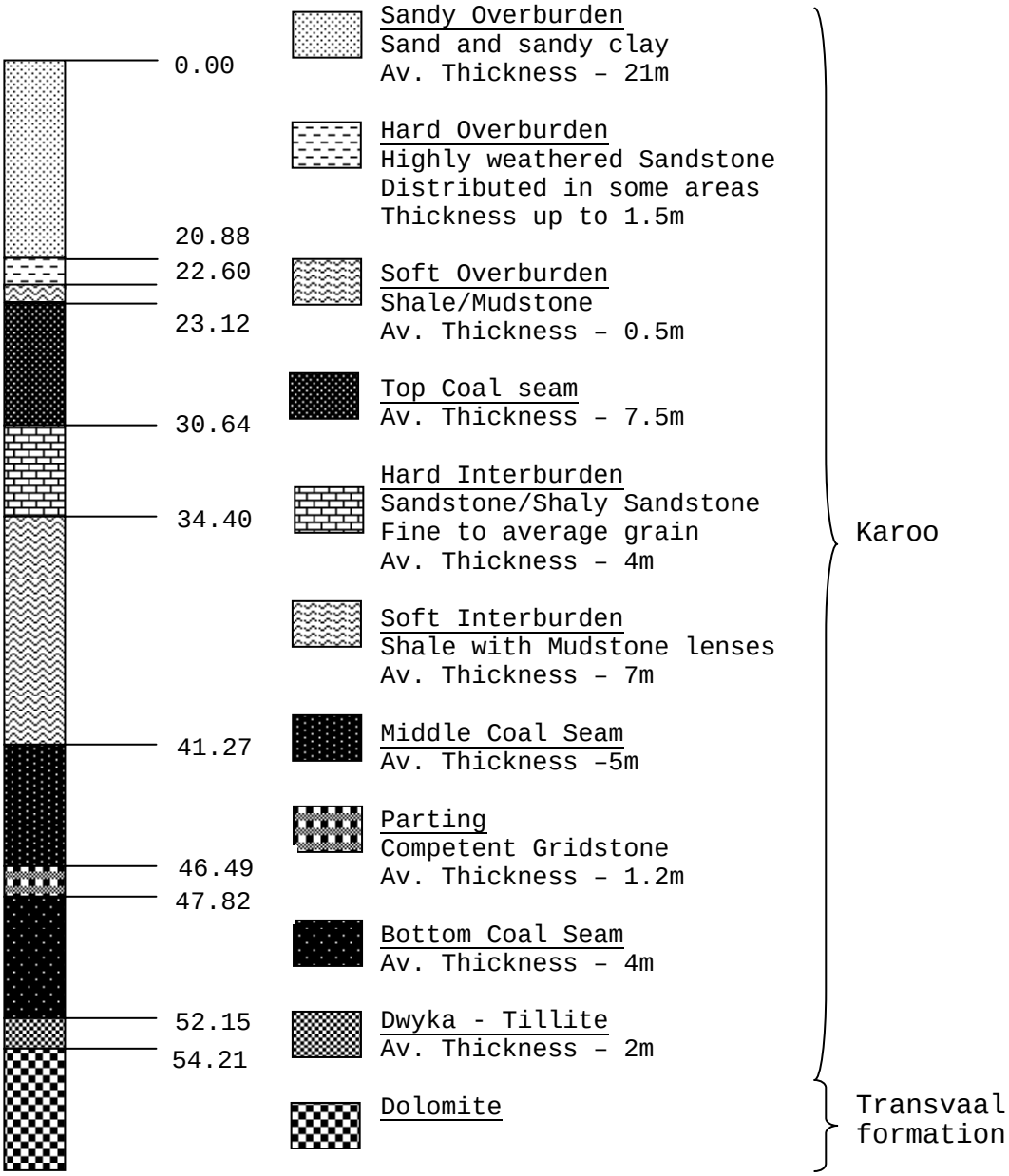

Figure 1.3

Representative stratigraphic column (after Mattushek, 1985)

The geological sequence that appears in Figure 1.3 is reproduced after Mattushek (2005), showing the representative stratigraphic column in which slope failure examples taken from Colliery "A" will be described.

1.1.2 Slope failures in complex geotechnical conditions

Opencast Colliery "A" mines three coal seams with an average total thickness of approximately 16m. Figure 1.3 presents the colliery stratigraphic column. A map of Colliery A showed old coal pillars, left in some areas in the middle coal seam, in other areas, the bottom coal seam, and sometimes superimposed upon one another in both seams. The upper coal seam was never mined.

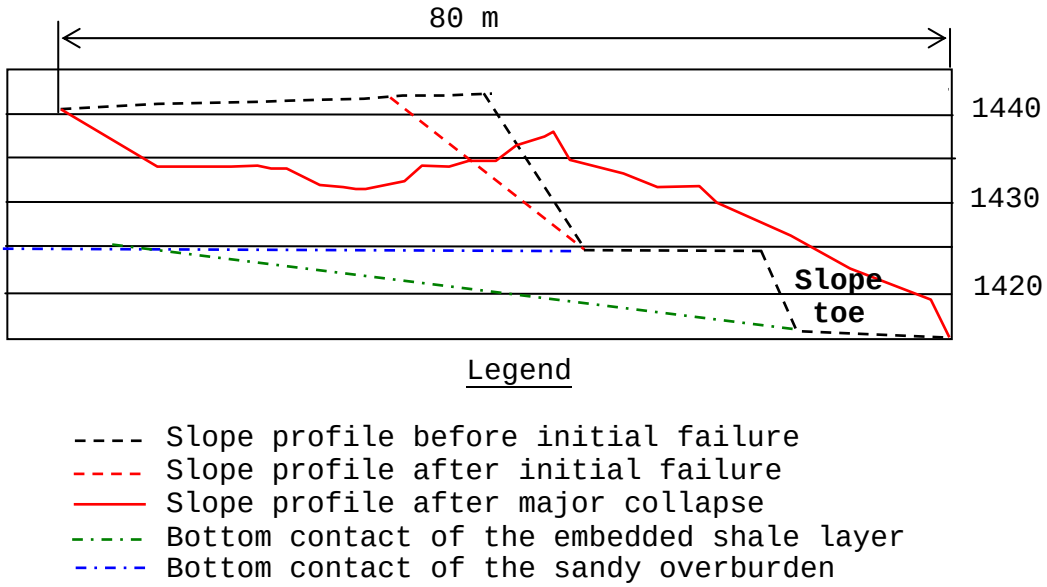

Figure 1.4

Initial and main failure profile in Pit "A-1" (after SRK – 1995)

Two slope failures took place during different seasons and in different pits but in both cases the strata dip towards the pit. The widely used computer program "SLOPE/W" developed by Geo Slope International particularly for circular and blocky failure, aided the failure analysis undertaken by the author.

The first case of slope failure took place in pit "A-1" in an undulated stratum at the shaly contact between the shaly interburden and the middle coal seam with a dip angle of 10^0 to 12^0 towards the pit. The top coal seam in the area was very thin (in the range of 1m). The failure took place in two stages: the initial failure (involving only the sandy overburden) and the major collapse, which slipped along the bottom contact of the shale layer above the middle coal seam. The slope profiles before and after failure can be seen in Figure 1.4. Owing to the calculated factor of safety (FOS=0.72), the initial failure can be recognised as probably circular. SLOPE/W outputs showing initial failure profiles for circular and blocky failure appear in Figure 1.5.

The major collapse followed the cleaning operations that took place after the initial failure, when the slope profile had a lower slope angle than it had prior to failure (compare Figures 1.5 and 1.6). The major failure indicates a multi-planar or blocky type of failure, but the applied block-specified technique used for the FOS calculation was not successful, because the calculated FOS value was higher than unity. SLOPE/W outputs are shown in Figure 1.6. Mine plans did not show any underground mining activities in the area underneath the failure.

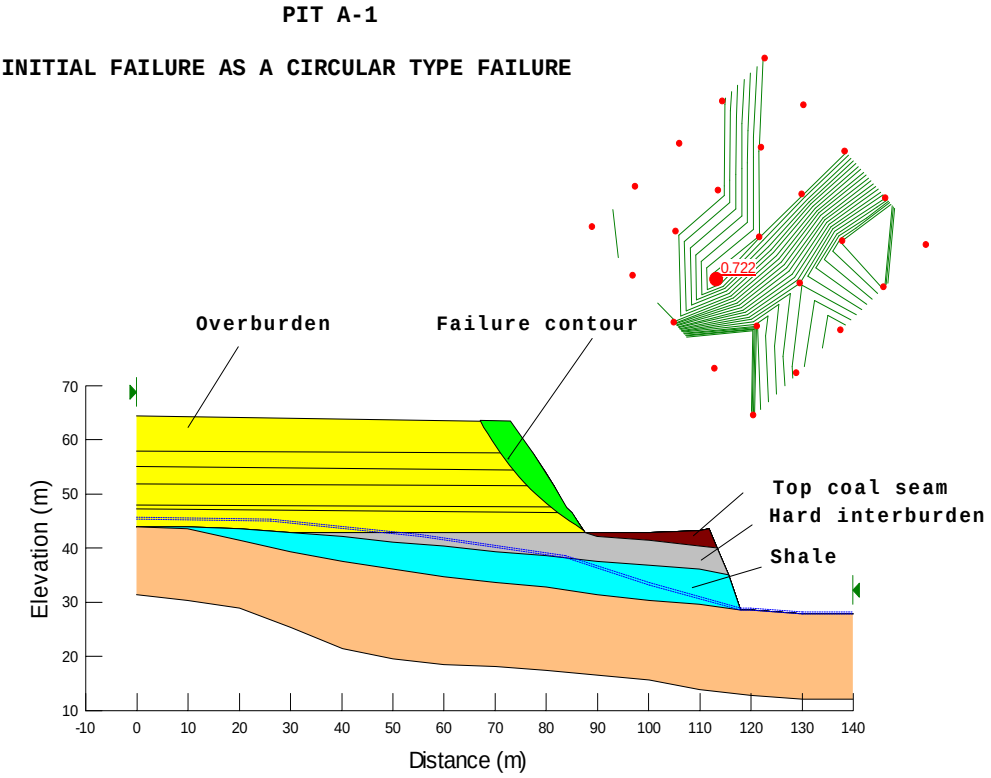

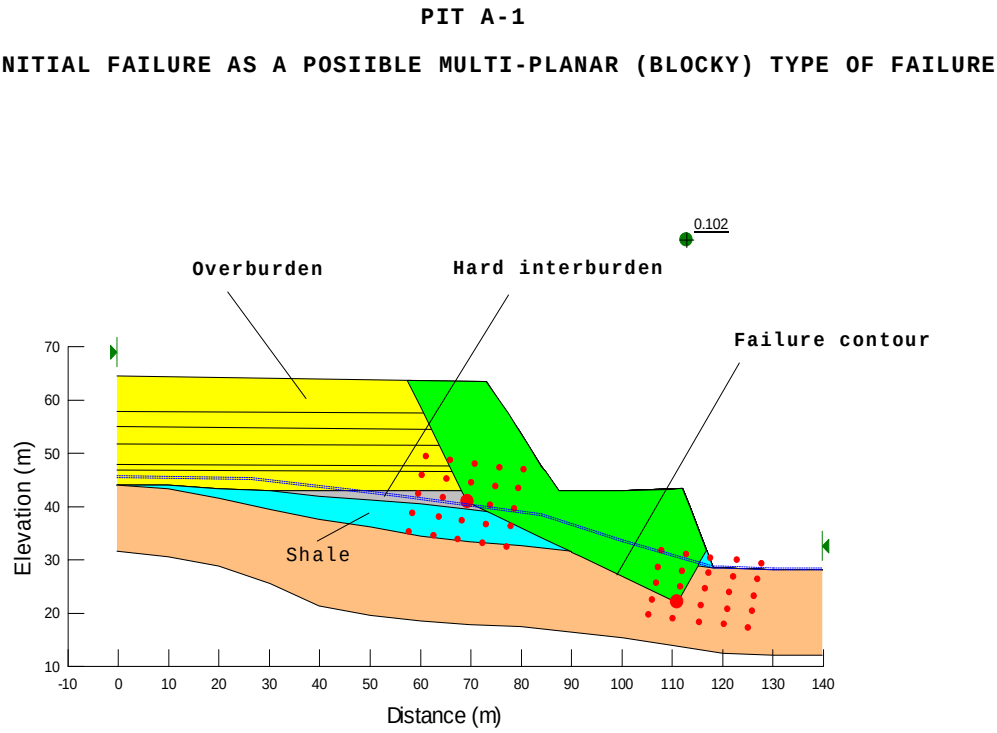

Figure 1.5

Theoretical failure profiles which resulted in initial collapse of sandy overburden – Pit A-1 (note higher slope angle in sandy overburden compared with Figure 1.6)

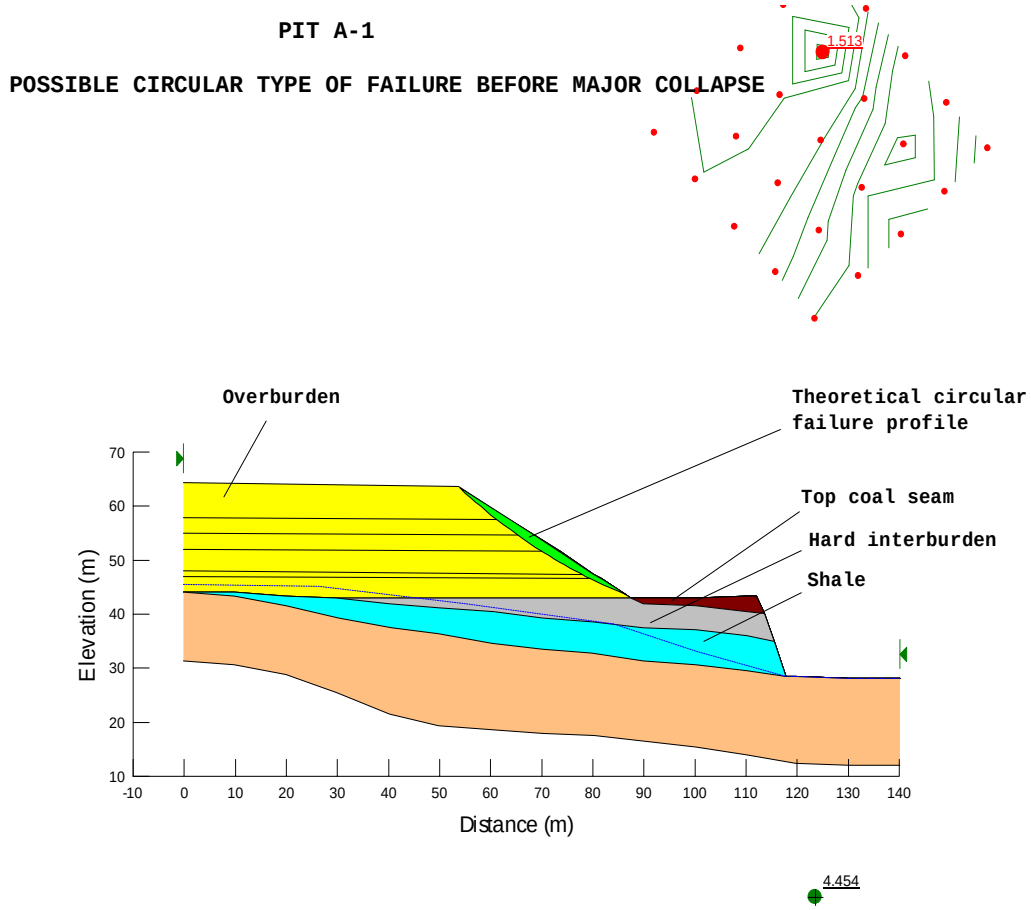

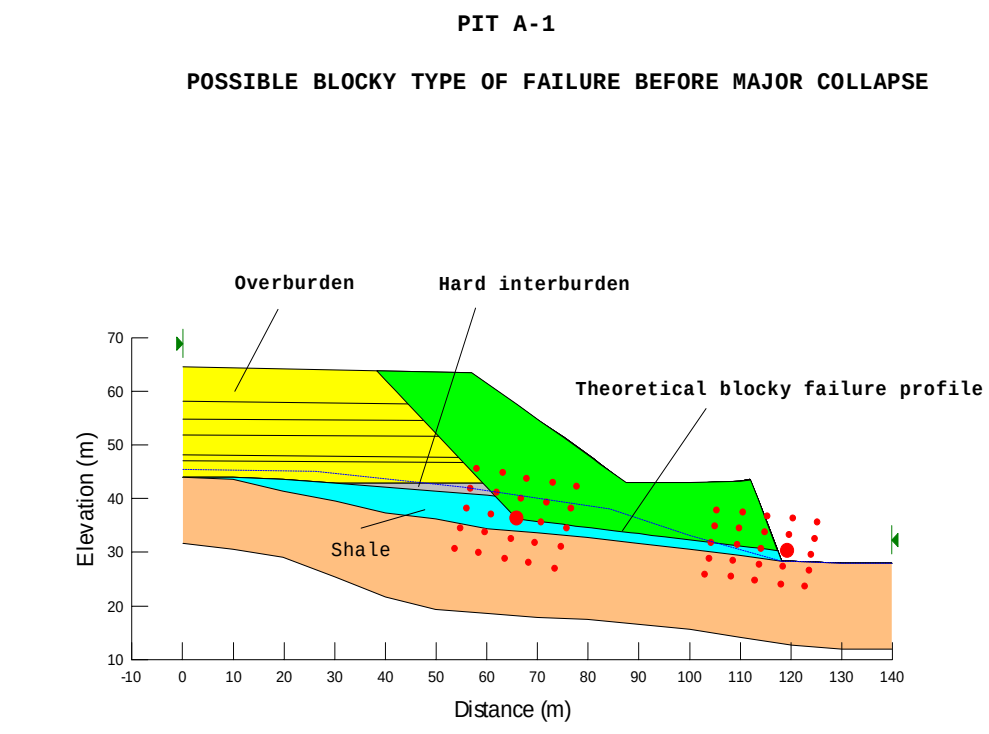

Figure 1.6

Theoretical failure profiles for final major slope collapse after the initial failure had been cleared– Pit A-1 (note lower slope angle in sandy overburden)

The second slope failure took place in Pit “A-2” of the same colliery. Figure 1.7 presents the slope profile before and after the failure, while Figure 1.8 shows possible failure mechanisms. Spoils with heights of 20m to 25m were dumped at a distance of approximately 20m behind the slope crest. Any joints that might have triggered wedge failure were not observed in the area.

Without any visible indications or warnings of impending failure, the slope collapsed, and this failure involved the spoils, overburden, top coal seam, and interburden between the top coal seam and the middle coal seam.

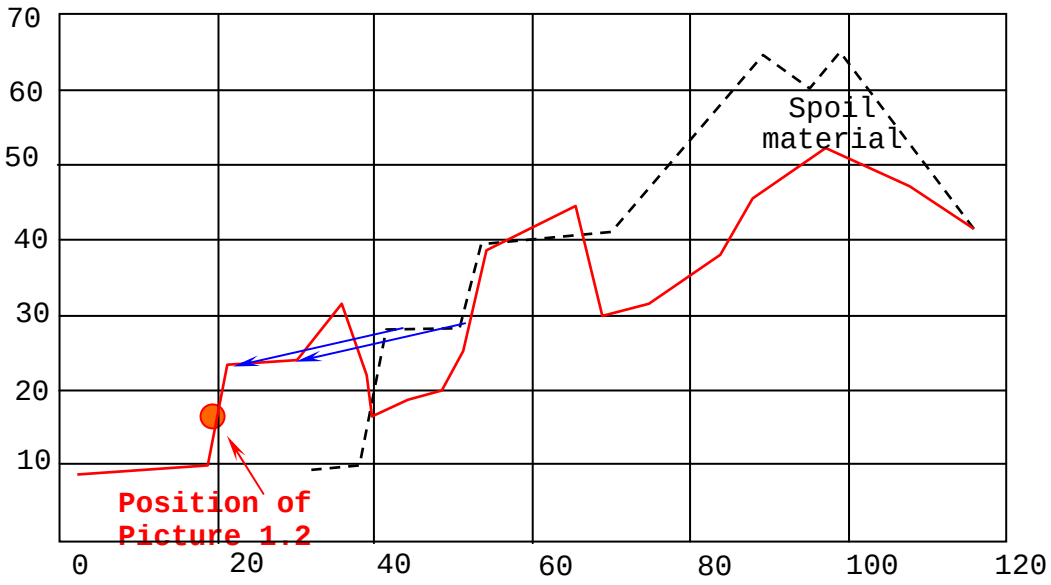

Figure 1.7

Slope profile before failure (marked with dotted black line) and after failure (marked with red line). Blue arrows indicate movements of the face block, while the red line shows valley formation behind the face block

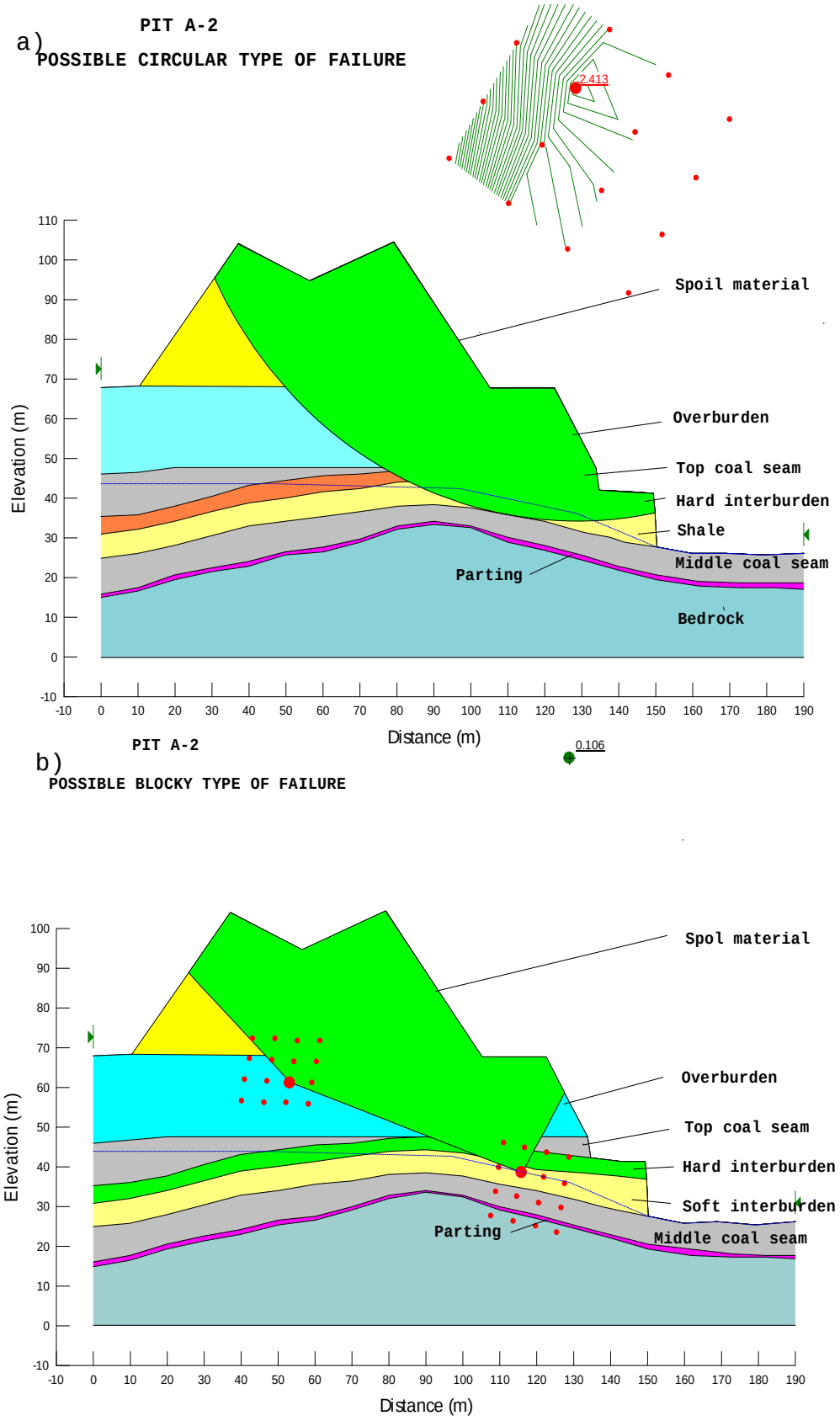

Figure 1.8

Possible circular (a) and blocky (b) type of failure at Pit–A2

After the cleaning operations, the failure surface was clearly observed on the contact between the soft interburden and the middle coal seam (Figure 1.9) which had an average dip angle of 16^0 towards the pit. The estimated FOS for the circular type of failure (Figure 1.8a) was between 2.4 and 2.6 depending on the method of calculation (Ordinary, Bishop, Janbu, Spencer or Morgenstern-Price).

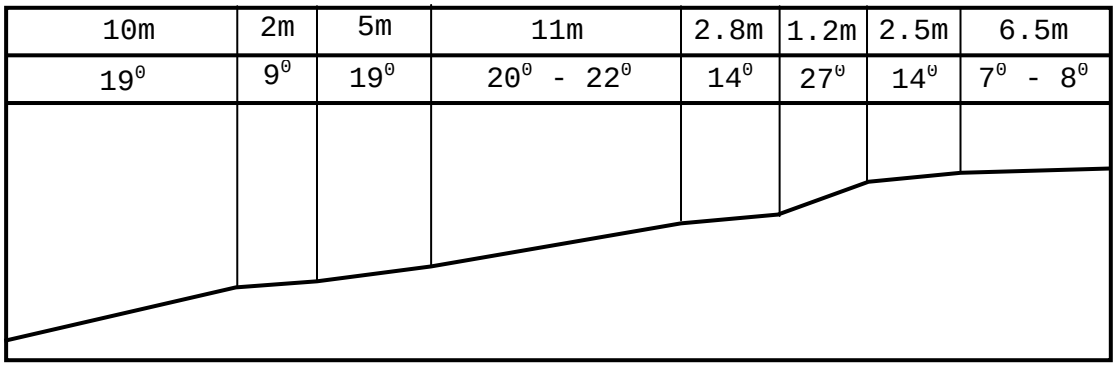

Figure 1.9
Profile of the failure surface, measured after cleaning operations

The blocky type of failure (Figure 1.8b) had a lower FOS for the profile, varying between 0.2 and 1.2. From these results and the derivative profile of the failure mass the author concludes that the failure must have been of a “blocky” type. As with the previous slope failure example in Pit A-1, there are problems with the application of the “Block Specify” in SLOPE/W because of the complexity of the slope profile. For instance, one of the most reliable calculating techniques, namely the Morgenstern-Price method, for blocky failure calculations, gives a very low safety factor value (FOS=0.11 to 0.14). The other methods, such as the Janbu and Bishop indicated slightly higher safety factors around FOS=0.15, while the Ordinary method

yielded a FOS of 1.198. All except the Ordinary Method therefore failed to provide credible slope safety factors, even though it was clear at the mine that some sort of blocky mechanism was responsible for the major collapses in both pits.

Picture 1.2
Face of the failed slope profile in Pit A-2, which does not indicate any significant structural damage to the shale

Picture 1.2 shows the front side of the failed blocks for the second slope failure. There is no significant structural damage, despite the fact that the material is shale, which had been thrust forward some 20m. The location of the picture is shown in Figure 1.7. If there were any joint sets which might have triggered wedge failure, and which were missed by the author, then the downward movement of the spoil material and almost horizontal movements of the other points in the slope profile are kinematically impossible for the wedge failure mode. Furthermore, wedge failure cannot

explain the valley formation in the post-failure profile i.e. definite downward movement of parts of the slope behind the forward thrust of the slope face, see Figure 1.7.

The third slope failure took place in Colliery “B” with similar stratigraphic column shown in Figure 1.3. The slope was composed of strata dipping 5^0 to 9^0 towards the pit. This failure was smaller than the previous two, but was notable in that it provided an opportunity to see the failure type between the blocks. The failure occurred in an 8m-thick coal seam at 25m depth with a similar overburden shown in Figure 1.3.

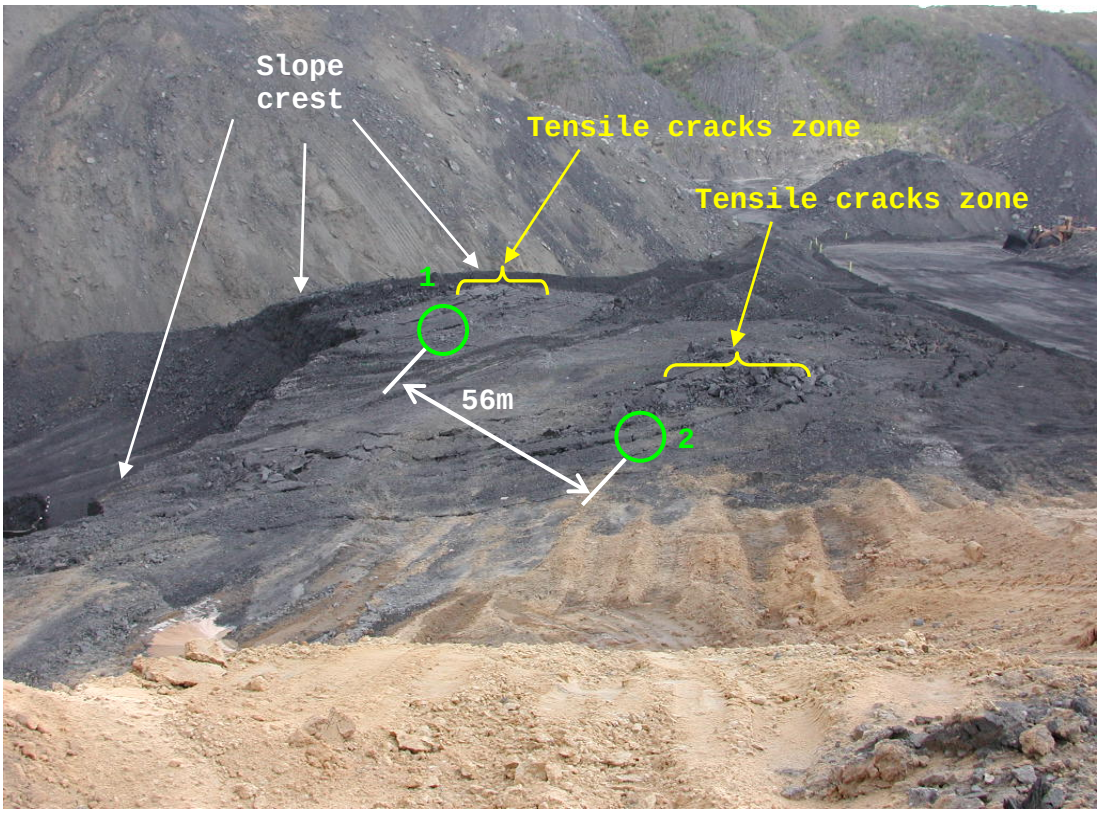

Picture 1.3
Panoramic view of the cleaned coal seam after the movement, showing tensile and shear crack zones

The failure indicated only horizontal movement toward the pit along the contact between 0.6m thick clay layer the coal seam. When the failed overburden was removed, two fracture zones could be seen in the coal seam (Picture 1.3) - a shear zone and a tensile zone. Pictures 1.4 and 1.5 are detailed pictures taken at the shear and tensile zones respectively. Measurements of the slope profile before and after the failure were not made available to the author, so no further analysis of this failure is possible in the thesis.

1.1.3 Common features of the failures

There are four features common to the failures. The first one is related to the post-failure profile, similar to that reported by Boyd (1983) in Figure 1.1. The failure mode has horizontal movement towards the pit by an almost undisturbed front block (passive block) and vertically downward movement of the block behind it (active block), with a final elevation significantly lower than that of the original slope profile.

The second feature of the failures is that in all cases the slope is situated on an undulated stratum with strata dipping towards the pit. The failure surface is at the contact between shale that overlies the second coal seam, i.e. the contact between a relatively weak and relatively strong layer respectively.

The third feature is that all failures daylighted at the toe of the slope, unlike the SLOPE/W failure planes for the blocky type of failure, which are predicted not

to approach the toe of the slope (see Figures 1.6b and 1.8b).

The fourth feature common to the failures is the presence of almost vertical tensile fractures (indicating tensile failure) above the crest of the undulated strata formations. These fractures are often difficult to see because they are usually covered by debris but, whenever access is available, for example after cleaning operations (as in Picture 1.3), they can be seen. In this case, it appears that tensile fractures may have persisted from surface behind the slope crest, into the middle coal seam.

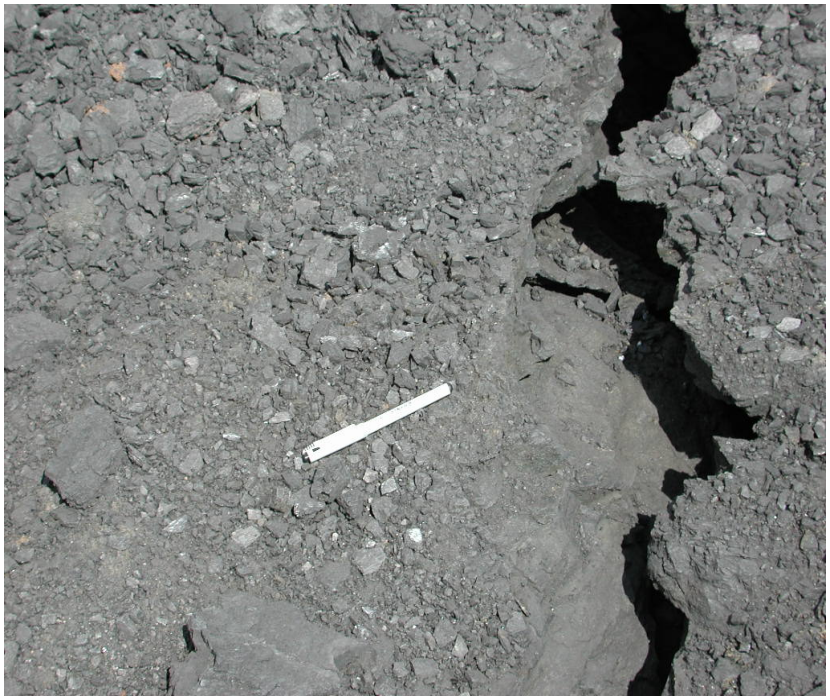

Picture 1.4

Open tension crack in the coal seam on the sheared block side (closer to the slope crest)

Picture 1.5

Tensile type of failure at the coal seam on the sheared block side, further from the formation crest

In this thesis, specific terminology will be used to facilitate discussion. Figure 1.10 presents a visualisation of the terminology that will be used in this thesis. It is necessary because in South Africa, for instance, the term “highwall” refers to the slope where excavation processes have taken place and “lowwall” refers to the dumped overburden debris in a pit, behind the highwall. In Australia the term “highwall” refers to a certain method of opencast mining. To avoid any misunderstanding and confusion the terminology used in this thesis is shown in Figure 1.10.

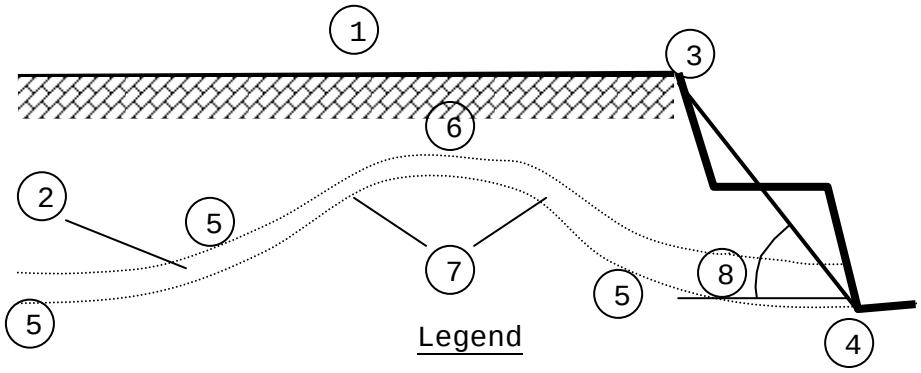

1 – Natural ground surface
2 – Weak embedded shale layer, or old coal pillars
3 – Crest of the slope
4 – Toe of the slope
5 – Toe of the undulated strata formation
6 – Crest of the undulated strata formation
7 – Limb of the undulated strata formation
8 – Slope angle

Figure 1.10

Visualisation of the terminology used in this thesis

1.2 THESIS OVERVIEW

The above discussed highwall failures (Section 1.2.2, pp. 10-17) pose some questions:

- What is the role of an undulated strata formation in the slope failures?
- What is the role of the embedded weak layer in terms of slope-stability when an undulated strata formation is present in the slope profile?
- What failure type occurs behind the slope crest in such conditions?
- What failure type exists along the embedded weak layer contact surfaces?
- How does a flatter slope angle cause major collapse in the same geotechnical conditions?

Poisel and Eppensteiner (1988) investigated failure modes at the edges of horizontal hard rock slabs lying on a soft, incompetent base. They found the existence of a tensile stress state in hard rock at the contact between hard and soft layers but they did not investigate the stress state in a multi layered system dipping toward a pit.

The failures discussed in Section 1.2.2 clearly show features that cannot be accounted for by the limit equilibrium methods, which assume far simpler conditions and geometries than are usually encountered in reality. The following features of the failures are therefore investigated in this thesis:

- The virgin stress state in undulated strata;
- The stress changes induced by cutting a slope in the undulated strata;
- The effects of the presence of a weak layer in the strata, either in the form of a shale layer or a mined coal seam in which pillars have been left behind;
- The role that different mineral constituents may play in fracture formation in a weak layer.

Site observations will be combined with the results of research carried out for the purpose of proposing a block thrust failure mode. Slope-stability safety factors will be computed for predicting more accurately the potential of slope failure in complex geotechnical conditions.

The discussion of the investigated features and research objectives is continued in the remaining chapters of this thesis.

CHAPTER 2
NUMERICAL MODEL OF GEOTECHNICAL CONDITIONS AND STRESS BEFORE MINING

2.1 SUMMARY

In this chapter, the virgin stress state in a rockmass containing undulated strata is analysed using the finite difference method, FLAC^{2D} (Itasca, 1999). The modelled strata undulations have limb dip angles of 5^0 and 15^0, while a literature survey reveals that a horizontal to vertical stress ratio of 2 will be reasonable to assume for the model. The chapter presents examples of the stress state on a horizontal profile line 30m deep for the unmined state. The model applies the “ubiquitous joints” model in FLAC to model the shale layer overlying the top and middle coal seams so that the plane of weakness lies parallel to sedimentation. The results show a concentration of the vertical component and a decrease in horizontal stress component at the undulated formation crest before mining. In the virgin state, shear stress is developed along the limbs of the undulated strata as a result of undulation.

2.2 INTRODUCTION

Analysis of geotechnical problems with the use of the Finite Difference method has been widely accepted in the research field for many years. Unfortunately, its regular use in geotechnical practice for stress analysis and its influence on predicting slope stability still remains limited. The reason for this lack of application is not entirely clear; however, practicing engineers are often sceptical of the need for such complexity, especially in view of the poor quality of soil and rock property data often available from routine site investigations. Although this scepticism is often warranted, there are certain types of geotechnical problems for which the finite difference approach offers real benefits. The challenge for an experienced engineer is to know which kind of problem would benefit from finite difference treatment and which would not. As a guide, Stead et al. (2001) presented a detailed review of all calculating techniques and the particular application of these techniques to slope stability analyses.

In general, linear problems such as the prediction of settlements and deformations (Barla and Chiriotti, 1995), the calculation on flow quantities due to steady seepage (Andrade et al., 2000), or the study of transient effects due to consolidation (Carranza-Torres et al. 1997) are highly favourable to solution by the finite difference method. Traditional approaches involving charts, tables, or graphical methods will often be adequate for routine problems, but the finite difference approach may be valuable if difficult geometries or material variations are encountered. Such

cases are not normally covered by traditional solutions, which is the case with a state of stress in a slope profile with an embedded weak layer and defined anisotropy near an inclined surface.

2.3 MODEL DEVELOPED FOR VIRGIN STRESS ESTIMATION

The rock properties used in this development are defined by six parameters, and shown in Table 2.1. Following shear test results (Karparov, 1998), it was estimated that the shale specimens would have approximately 30% lower shear strength parallel to bedding, compared to the shear strength normal to bedding. For simulating this anisotropy, the application of the "ubiquitous joints" model in FLAC (Itasca, 1999) has been used with the properties set out in Table 2.2. In this model, which accounts for the presence of an orientation of weakness in a FLAC Mohr-Coulomb model, yield may occur in either the solid or along the weak plane, or both, depending on the stress state.

Table 2.1 Geotechnical properties of rock in slope

	Shale	**Sandstone**
Bulk modulus – Pa	4.5E+09	5.9E+09
Shear modulus – Pa	2.3E+09	5.2E+09
Tensile strength - Pa	3.5E+06	5.5E+06
Cohesion – Pa	0.44E+06	0.70E+06
Friction angle - deg.	14	22
Density - kg/m^3	2700	2600

The use of this model was very important to the stress analysis and the type of failure in a slope profile. For this reason, the model was firstly investigated by comparing calculated results from FLAC simulating the uniaxial compressive test with a theoretical development in Jaeger and Cook (1979), in order to confirm the validity of the model with the “ubiquitous joints” option.

The uniaxial compressive strength of a shale sample with a defined plane of weakness is a function of the angle formed by the major principal stress and the plane of weakness. In FLAC, this behaviour was modelled by considering the sample as a continuum with a plastic anisotropy in the direction of the weakness. The rock sample has a height to width ratio of 2 (five zones in horizontal and ten zones in vertical direction) with the weak plane properties given in Table 2.2 below.

Table 2.2 Ubiquitous joint properties

Tensile strength (σ_{tj})	1.0 MPa
Cohesion (c_j)	0.1 MPa
Friction angle (ϕ_j)	9^0
Dilation angle (φ_j)	0^0

It is difficult, if not impossible, to correlate the results of different types of direct and indirect tensile tests on rock using the average tensile strength as the basic material property. Hardy (1973) was able to obtain good correlation between the results of a range of tests involving tensile fracture when the apparent surface energy was used, based on the Griffith (1924) theory for fracture propagation, as the unifying material property. The Griffith theory predicts that

the uniaxial compressive stress at the crack extension will always be eight times the uniaxial tensile strength. This does not agree with laboratory results, which have given the widely accepted tensile strength as one-tenth the uniaxial compressive strength. The tensile strength used in the FLAC model is therefore assumed to be one-tenth the uniaxial compressive strength.

The calculations are performed under plane strain conditions where the plane-of-weakness model (Jaeger and Cook, 1979) predicts that slip will occur in a triaxial test, provided that $\left(1-\tan\phi_j \tan\beta\right)>0$ and:

$$\sigma_1 = \sigma_3 - \frac{2\left(c_j + |\sigma_3| \tan\phi_j\right)}{\left(1-\tan\phi_j \tan\beta\right)\sin 2\beta} \qquad (2.1)$$

where β is the angle formed by the direction of σ_1 and the joint.

For those combinations of c_j, ϕ_j, σ_3 and β for which Equation 2.1 is not satisfied, slip in the joint cannot occur, and the only alternative is the failure of the rock material which, according to the Mohr-Coulomb failure criterion, will occur for

$$\sigma_1 = \frac{1+\sin\phi}{1-\sin\phi}\sigma_3 - 2c\sqrt{\frac{1+\sin\phi}{1-\sin\phi}} \qquad (2.2)$$

where c is intact material cohesion, and ϕ is the intact material angle of internal friction.

In the uniaxial compression test, σ_3=0, so Equations 2.1 and 2.2 can be rewritten as:

$$\sigma_1 = \frac{-2c}{\left(1 - \tan\phi_j \tan\beta\right)\sin 2\beta} \tag{2.3}$$

and

$$\sigma_1 = -2c\sqrt{\frac{1+\sin\phi}{1-\sin\phi}} \tag{2.4}$$

The maximum pressure for a uniaxial compressive test (σ_c) of a rock sample with a weak plane will then be:

$$\sigma_c = \begin{cases} \min\left[2c\sqrt{\dfrac{1+\sin\phi}{1-\sin\phi}},\ \dfrac{2c_j}{\left(1-\tan\phi_j \tan\beta\right)\sin 2\beta}\right] & \text{if } \left(1-\tan\phi_j \tan\beta\right) > 0 \\ 2c\sqrt{\dfrac{1+\sin\phi}{1-\sin\phi}} & \text{if } \left(1-\tan\phi_j \tan\beta\right) < 0 \end{cases} \tag{2.5}$$

The FLAC model is loaded with constant velocity boundaries at the top and bottom of the model until failure occurs, and then the failure stress and type of failure mode are noted. Combined damping is used because velocity vectors are all non-zero in the final state (Itasca, 1999).

The grid is the same for all the values of β, because the material property joint angle, “jangle”, controls the inclination of the joints in this model. Fairly accurate results are obtained with only 50 elements.

The effect of the variation of β is calculated every 5^0 from 0^0 to 90^0. For this test, the failure state is reached within 4000 calculation steps for the applied

velocity loading condition. This occurs for either failure along the weak plane or within the intact material. The *FLAC* solution at each value of β is then determined at the end of each 4000-step increment.

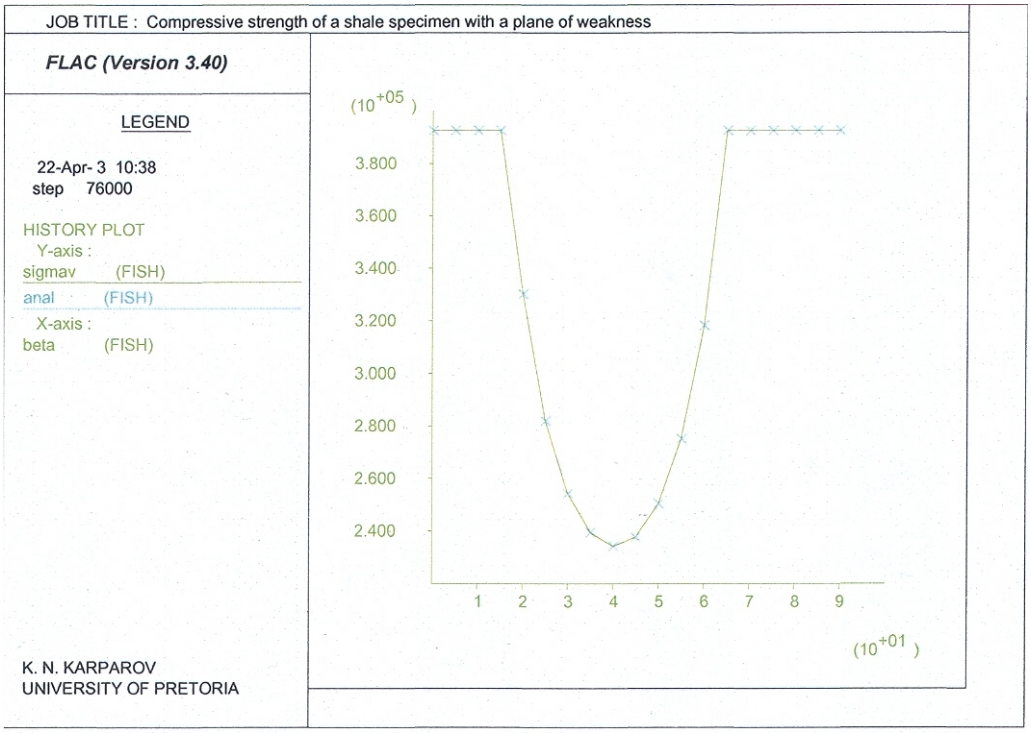

Figure 2.1

Comparison of uniaxial compressive strength values- "ubiquitous" joints model (cross) versus analytical solution (line)

A comparison of FLAC's "ubiquitous" joint model (Figure 2.1) with the analytical solution shows excellent agreement with the error below 1% for all values of β. This confirms the applicability of using the ubiquitous joints for the slope stability modelling. The input file for the vertical stress comparison between the FLAC "ubiquitous" joints model and the theoretical development in Jaeger and Cook (1979) can be seen in A1.1 (Appendix 1). It is concluded that the "Ubiquitous Joint" model in FLAC will adequately model the shale layers present in the geological succession.

2.4 ESTIMATION OF HORIZONTAL TO VERTICAL STRESS RATIO

Skempton (1961) states that Samsioe first put the idea forward in the 1930's that the k-ratio (k), defined as the ratio between the horizontal and vertical stresses in soil or rock, could be larger than unity. By reconstructing the geological history of London clay in Bardwell, Skempton (1961) showed that in this case, k > 2.5 and that the 10-15m thick upper layer of the subsoil is at the passive limit state of stress (cf. Terzaghi, 1961). Lambe and Whitman (1979) concede that in overconsolidation, the k – ratio can reach as high a value as 3.

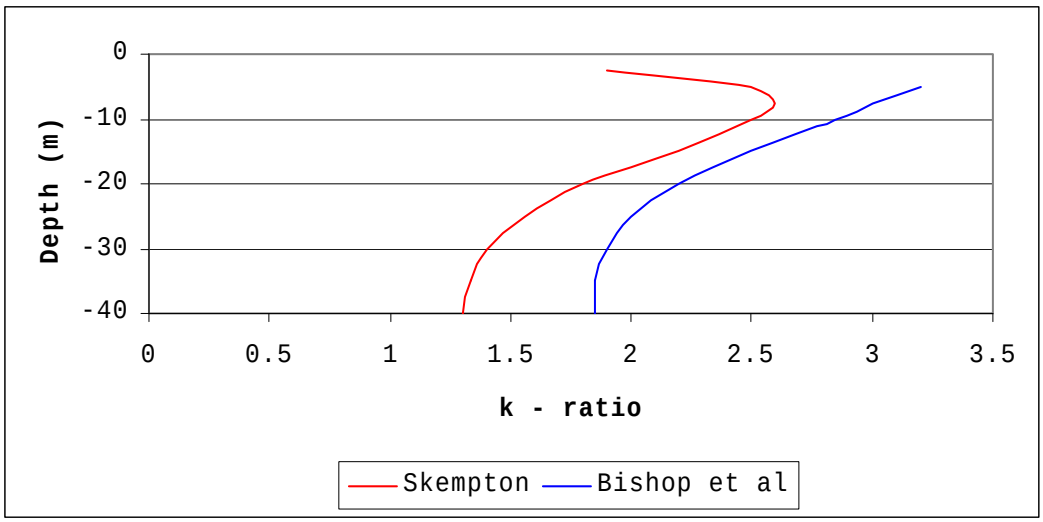

Figure 2.2
Variation of the k - ratio with depth in overconsolidated London clay, measured in a laboratory using undisturbed samples (Skempton, 1961; and Bishop et al., 1965)

The results of Skempton (1961) and Bishop et al. (1965) are reproduced in Figure 2.2, where it can be seen that the higher k–ratio value (k > 2) is observed at a depth

of 10-15m, while at a depth of 30-40m it has a value of between 1.5 and 2.0.

Brooker and Ireland (1965) claim that the magnitude of *k* is not only a function of the overconsolidation ratio but also a function of the value of the angle of internal friction as well. For an overconsolidation ratio > 8, the effect of the angle of internal friction is not certain. According to Ladd (1964), *k* becomes greater than unity for overconsolidation ratios > 2.5 - 4.5.

Broms (1971) ranged in situ k-ratios between 0.9 and 1.5, and in the laboratory between 0.45 and 2.0 by compacting loose soils behind a supporting wall. A similar effect was also observed during pile driving, even for piles of constant diameter along their whole length. Bassett (1970) estimated that *k* increases from 1 to 3.5 in the course of the process.

By applying the finite element method, Malina (1969) succeeded in numerically determining the effect of overconsolidation on the magnitude of *k*. He reports that in the vicinity of the surface, the state of stress is close to passive; this finding is in agreement with an analysis published by Skempton (1961).

In the only reference relevant to the coal mine in question, van der Merwe (2002a) mentions the applicability of a k–ratio of 2 in South African coal mines, and discusses the issue of roof stability in underground coal extraction (van der Merwe, 2002b). Because of the varied *k*-ratio estimates above, the fact

that nearly all data refers to clays in civil engineering scenarios, and that there is virtually no k-ratio data for surface mines excepting van der Merwe's (2002a) results, the author has decided to apply a k-ratio of 2 in all models in this thesis. This decision is reviewed in Chapter 3, where the effects of the presence of a mined slope are modelled.

2.5 GRID DEVELOPMENT FOR A MODEL WITH UNDULATED STRATA

In order to undertake objective analyses of virgin stress before mining, it is necessary to develop a model that contains the essential features of the geological structure. Requirements for a reasonable model of the undulating strata in the mine are as follows:

- The layers should dip smoothly without any sharp kinks causing stress concentrations.
- The strata should become flatter with decreasing depth, eventually becoming horizontal on the surface (this is a feature of the sedimentation overlying the undulating dolomitic palaeo-surface described in Chapter 1).
- The layers should be thinner in the crests of the undulated strata formation, and thicker in the troughs, as was observed at the colliery.

These three grid conditions should be constructed in the centre of the model to avoid the influence of boundary conditions, and at the same time, to allow space for the slope face (highwall) to approach the undulated surface. A FISH function (Itasca, 1999) with

boundaries as shown in Figure 2.3 was written to fulfil the above-mentioned three requirements for the case of 15^0 limb inclination of the undulated strata formation. The FLAC input file with FISH function can be seen in Appendix 1, Section A1.1.2.

Figure 2.3
Boundary of FLAC model with angulated surface, creating 15^0 strata inclination at 30m depth along profile line A-A, and flat to near-flat strata at surface

The function's major advantage is its capability to place this formation at any point on the bottom boundary of the model and control its altitude to achieve the required inclination at a chosen depth. At the bottom boundary the inclination of the rows of finite difference zones are much steeper, but their inclination gradually decreases closer to the ground surface, where they are horizontal. The required dip angle of the rows (representing sedimentary layers) in the grid is achieved at a depth of 30m. Finally, the rows above the crest are thinner, compared to the rows above the "troughs", which are here modelled by the ends of the FISH-generated domical structure.

2.6 VIRGIN STRESS DISTRIBUTION IN MODEL

To verify the reliability of the new grid for its further application, a model with homogeneous material was run first. The undulated strata formation was chosen to have maximum limb inclination angles of 5^0 and 15^0 at the intersection with the horizontal line A-A at a depth of 30m (See Figure 2.3). The finite difference grid consists of 25000 1m x 1m zones, which correspond to 250m in length and 100m in height respectively, with the undulated strata formation positioned between 130m and 230m from the left model boundary. The trial run of these examples used geotechnical parameters for massive sandstone (Table 2.1), a k-ratio of 2 and an unmined ground surface. Such a long model has been chosen to accommodate the undulated strata and for modelling an advancing excavation cut approaching this formation.

To evaluate the magnitude of stress variations induced by the geological conditions, a stress concentration coefficient for vertical and horizontal stress components was used, which has the form of:

$$k_{\mathrm{V}}^{*} = \frac{\sigma_{\mathrm{V}}^{\mathrm{F}}}{\sigma_{\mathrm{V}}} \quad \text{or} \quad k_{H}^{*} = \frac{\sigma_{H}^{F}}{\sigma_{H}} \tag{2.6}$$

where k_V^* and k_H^* are stress concentration coefficients for vertical and horizontal stress components respectively; σ_V^F and σ_H^F are vertical and horizontal stress components calculated by FLAC; and σ_V and σ_H are the virgin vertical and horizontal stresses. According to Ugular (1999), this coefficient can be applied as long as the shape variation is gradual,

which is satisfied by the undulated formation created with the FISH function. Changes in layer thicknesses together with a dip angle on the top and bottom contact surfaces between the shale and middle coal seam are set out in Table 2.3.

The virgin stress components calculated in the FLAC model were compared with expected results using the relationships $\sigma_V = \rho g h$ and $\sigma_H = 2\sigma_V$, with good agreement obtained away from the undulating strata formation.

Figure 2.4 shows the basic characteristics of the stress distributions along the profile line A-A shown in Figure 2.3, assuming an undulating homogeneous sandstone formation. Figure 2.4a gives an example of vertical stresses at 30m depth for 5^0 and 15^0 limb inclinations. The figure shows that there is a high stress region at the formation's crest. At the trough of the undulated strata a decrease in vertical stress is present. From the figure it can be seen that the stress concentrations are a function of the strata inclination angle. All the vertical stress plots for different model geometries are shown in Appendix 2, Figures A2.1 and A2.2.

Table 2.3 Seam thickness and layer inclination variations taken from the trough to the crest of the undulated strata model

Distance from the trough (m)	UGS with 5^0 limb inclination					UGS with 15^0 limb inclination				
	Thickness at the trough 2m	Thickness at the trough 8m	Dip of strata on contact (deg)			Thickness at the trough 2m	Thickness at the trough 8m	Dip of strata on contact (deg)		
			Bottom	Top 2m thick	Top 8m thick			Bottom	Top 2m thick	Top 8m thick
0	2.00	8.00	5.15	5.15	4.01	2.00	8.00	15.65	14.58	11.87
2	1.98	7.95	5.15	5.15	4.01	1.96	7.85	15.65	14.58	11.87
4	1.98	7.90	5.71	4.58	4.01	1.92	7.70	15.65	14.58	11.32
6	1.96	7.85	5.15	4.58	3.44	1.89	7.55	15.12	14.04	11.32
8	1.95	7.80	5.15	4.58	4.01	1.85	7.41	15.12	14.04	11.32
10	1.94	7.76	5.15	4.58	3.44	1.82	7.27	14.58	13.50	10.76
12	1.93	7.72	5.15	4.58	3.44	1.79	7.14	14.58	12.96	10.21
14	1.92	7.67	4.58	4.01	3.44	1.75	7.00	13.50	12.96	10.21
16	1.91	7.62	4.58	4.01	3.44	1.72	6.87	12.96	11.87	9.65
18	1.90	7.58	4.01	3.44	3.44	1.69	6.75	12.41	11.32	9.09
20	1.89	7.55	4.01	3.44	2.86	1.66	6.64	11.87	10.76	8.54
22	1.88	7.51	3.44	3.44	2.86	1.63	6.53	10.76	10.21	7.97
24	1.86	7.47	3.44	3.44	2.86	1.60	6.42	10.21	9.65	7.97
26	1.86	7.45	3.44	2.86	2.29	1.58	6.33	9.09	8.54	6.85
28	1.85	7.42	2.86	2.86	1.72	1.56	6.25	8.54	7.97	6.28
30	1.84	7.39	2.29	2.86	1.72	1.54	6.17	7.41	7.41	5.71
32	1.85	7.37	2.29	1.72	1.72	1.53	6.10	6.85	6.28	5.15
34	1.84	7.35	1.72	1.72	1.15	1.51	6.04	5.71	5.15	4.01
36	1.83	7.32	1.15	1.15	1.72	1.49	5.98	4.58	4.58	4.01
38	1.83	7.31	1.15	1.15	1.15	1.49	5.94	4.01	3.44	3.44
40	1.83	7.31	1.15	1.15	0.57	1.48	5.91	3.44	2.86	2.29
42	1.82	7.29	0.57	0.57	0.57	1.47	5.88	2.29	1.72	1.72
44	1.82	7.29	0.57	0.57	0.57	1.46	5.86	1.15	1.15	1.15
46	1.82	7.28	0.00	0.00	0.00	1.46	5.85	0.00	0.00	0.00
48	1.82	7.28	0.00	0.00	0.00	1.47	5.85	0.00	0.00	0.00

a)

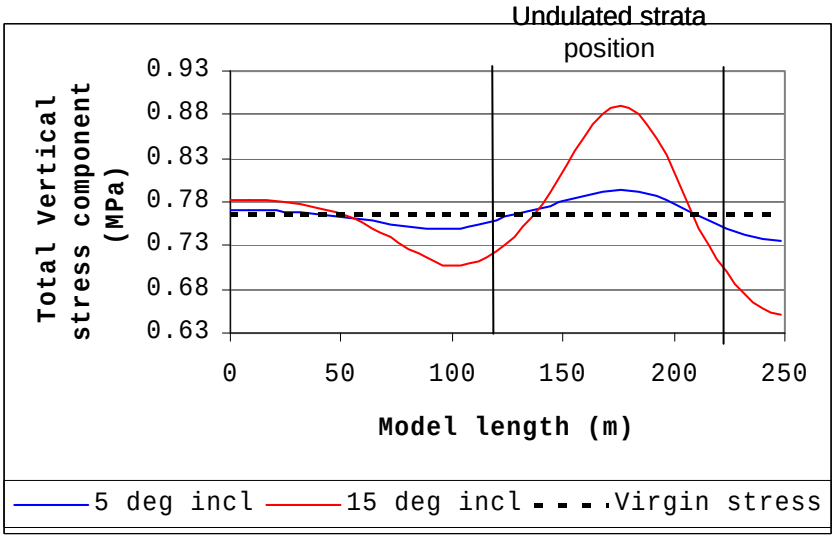

b)

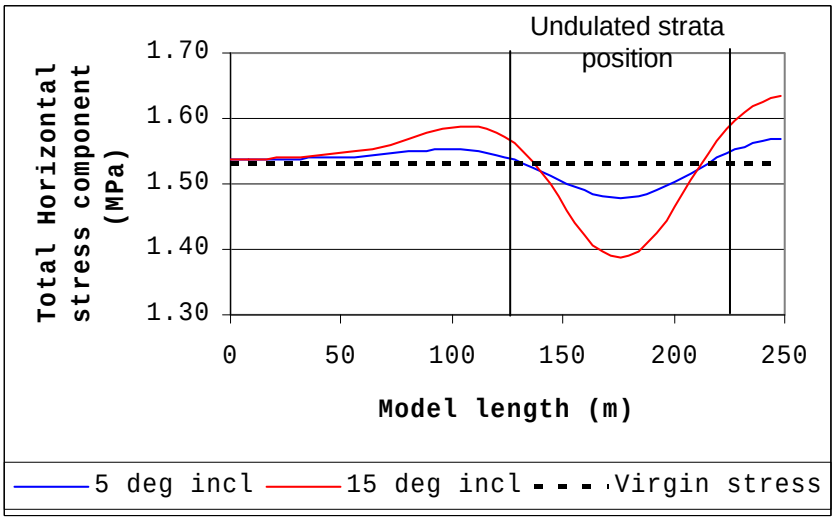

c)

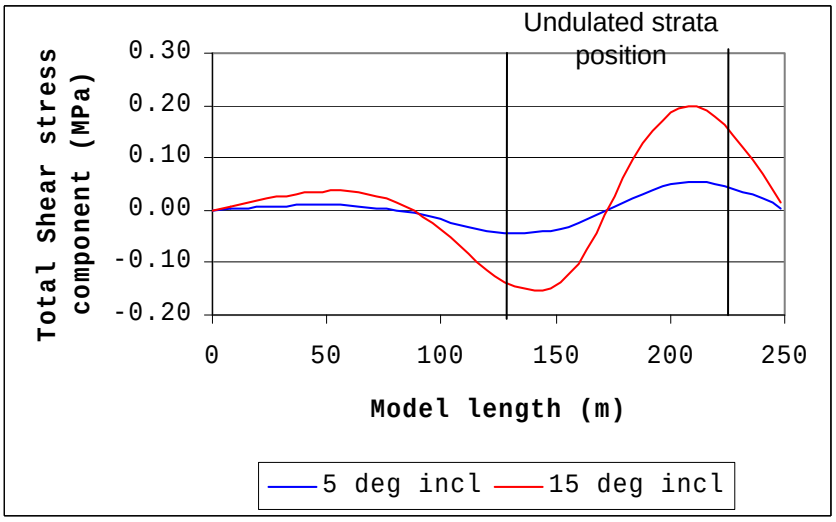

Figure 2.4

Stress state along horizontal line at 30m depth

Such an increase in vertical stresses was calculated by Timoshenko (1934) using the theory of elasticity for pressure between two spherical bodies in contact, as a sphere with smaller diameter is in contact with and enclosed by sphere with larger diameter. Depending on the radius of spheres (in our case, changes in a layer's thickness) and their elastic constants, the vertical stress can increase up to 25% for a depth of 30m. Elastic properties were taken from Table 2.1 and the applied compressive force was equal to 765180N, corresponding to a depth of 30m. The calculated results can be seen in Table 2.4, where the percentage difference between Timoshenko's model and the stresses calculated by FLAC is less than 5%.

Table 2.4 Comparison of the stress calculated by FLAC and the re-worked Timoshenko's model

UGS* incl. (..^{0})	Radius R_1 (m)	Radius R_2 (m)	Stress after Timosh-enko	Calc. str. by FLC	Differ (%)
5	431.4	439.9	0.811 Mpa	0.793 MPa	-2.1
15	122.1	122.8	0.869 Mpa	0.896 MPa	3.2

* Undulated ground surface

Figure 2.4b shows the horizontal stress component. The low-stress region can be seen at the formation crest while the high-stress region can be seen at the formation lows.

Figure 2.4c shows the shear stress results. Pre-existing shear stress in virgin stress conditions on the limbs of the undulated formation have values of approximately 0.05MPa and 0.15MPa for layers inclined at 5^0 and 15^0 respectively. The non-zero shear stresses

develop purely as a result of the presence of the inclined layers in the geological succession, and are not tectonic in origin.

For the pre-existing shear stress verification along the limbs of the undulated strata, a shale core from the mine was cut parallel to bedding, glued on thin glass, and polished to form a thin section. Under the binocular microscope and normal lighting (Picture 2.1), the original grain direction is visible and marked with the red line S0. “CS” zones (marked with green) indicate post-sedimentation shear stress development. Using the rotating polariser as a tool for structural analysis permits the simultaneous examination of features such as grain size, grain shape, grain identity and the *c*–axis (Fueten and Goodchild, 2001).

The newly developed carbon crystals (Picture 2.2) with a direction of approximately 45^0 to the direction of the sedimentation (shown by the dotted yellow lines marked S1) are the result of the existence of the post-sedimentation shear, which also confirms the shear stress along the limb of the undulated stratum in virgin conditions.

The stress concentration coefficients for vertical and horizontal stress components, calculated from Equation 2.6 (p. 37), are presented in Figure 2.5. The figure shows that the horizontal stress component decreases in magnitude by 4% at the crest of the undulated strata formation at a 5^0 inclination, and by 10% at a 15^0 inclination, while the vertical stress component increases by 4% and 16% respectively for the same limb inclinations.

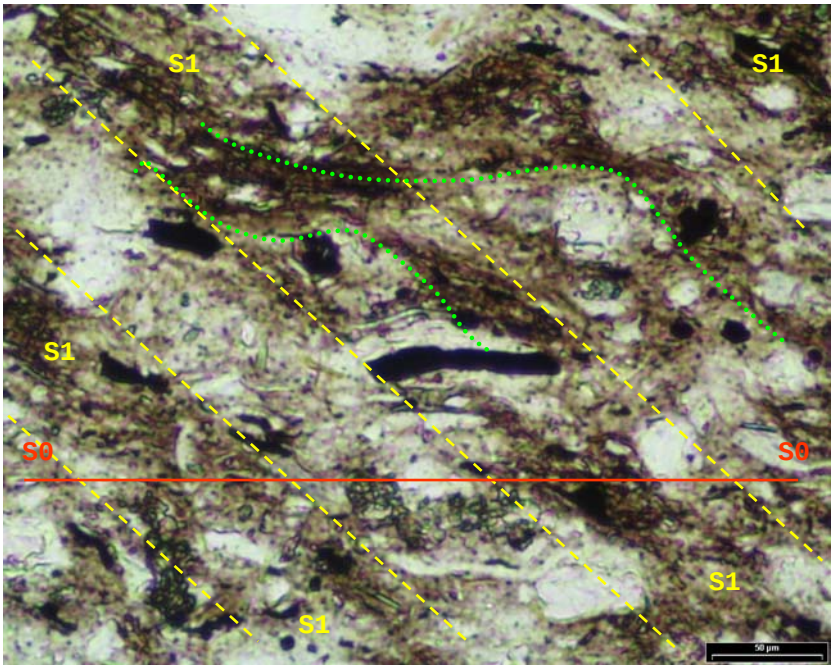

Picture 2.1

Microscopic picture of a shale specimen from undulated stratum showing shear bands and carbon flakes orientated parallel to sedimentation direction S0

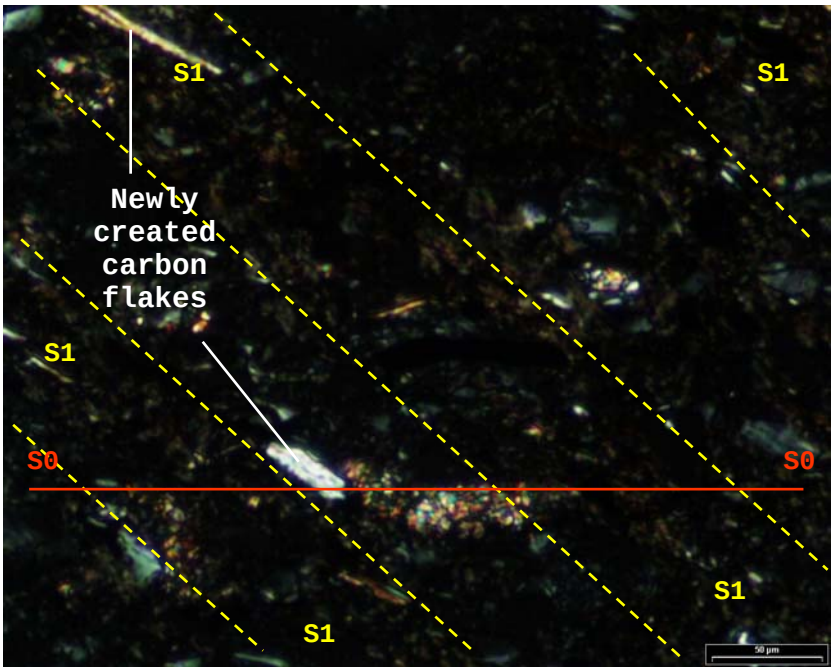

Picture 2.2

Carbon flakes at 45° to bedding direction S0

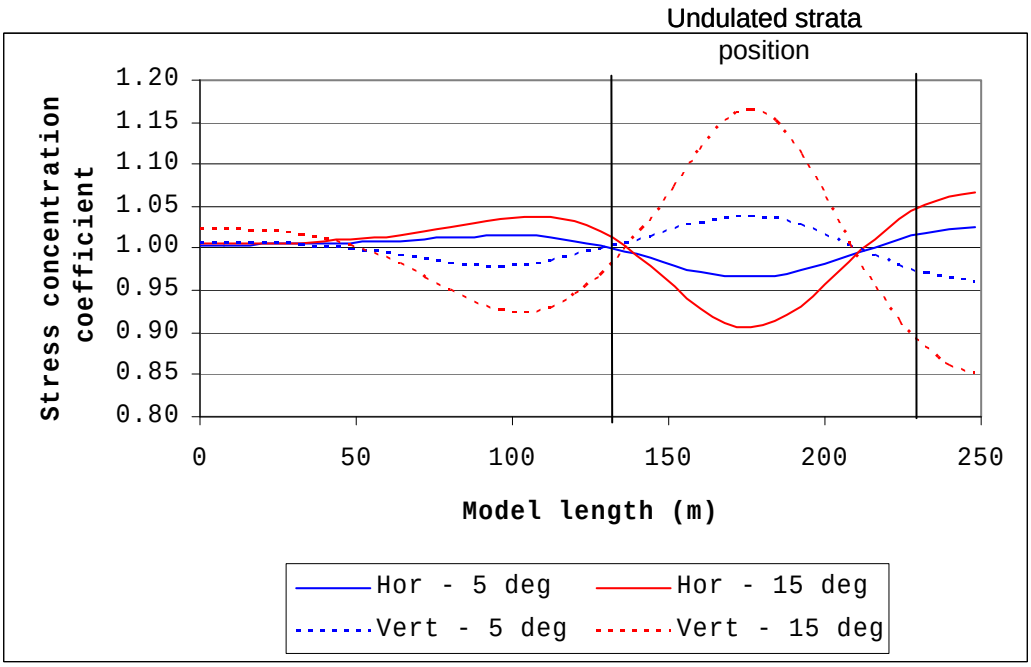

Figure 2.5

Horizontal and vertical stress concentration coefficients along horizontal line at 30m depth

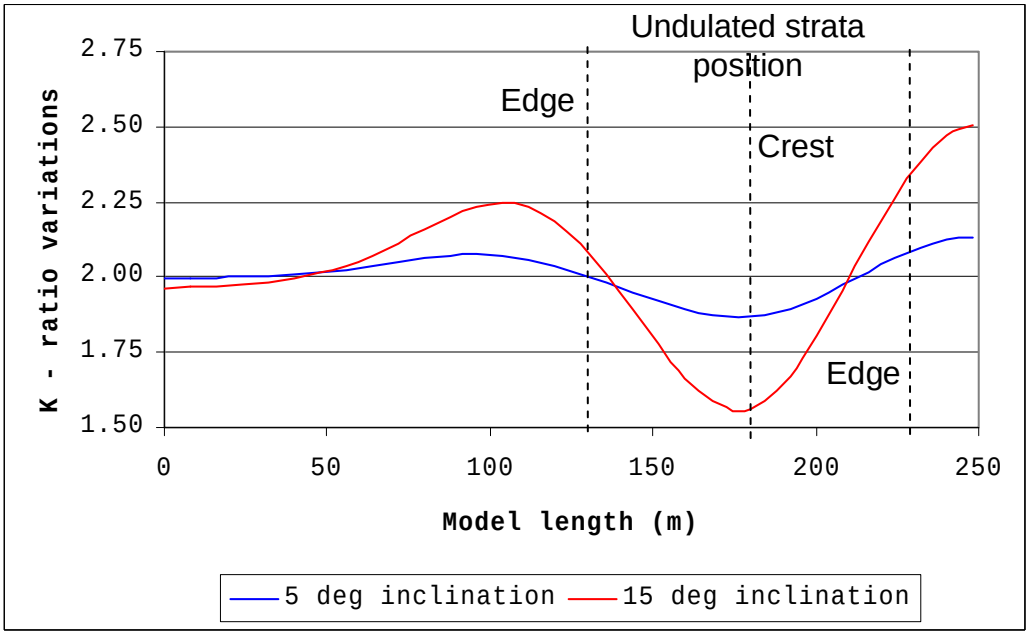

Figure 2.6

K-ratio variations along horizontal line at 30m depth

Because of the vertical stress increases and horizontal stress decreases, the k-ratio drops to a value of 1.6 at the crest because of the increased vertical and reduced horizontal stresses. In the troughs of such formations, the opposite is observed; an increase in horizontal stresses and a decrease in vertical stresses can be observed, which consequently increases the k-ratio by about 10% (Figure 2.6).

In summary, there is an increase in vertical stress components and a decrease in horizontal stress components above the crest of the undulated formation. Vertical stresses are more sensitive to the changes in the dip angle of an undulated strata limb than horizontal stresses. Shear stress can be expected to develop along the formation limbs and to reach zero at the crest. This fact raises two questions about the reliability of the well-known equilibrium methods for slope stability analysis: the first, about the weight of the slices across such strata; and the second about the magnitude and distribution of interslice forces (for instance sinusoidal or trapezoidal) and their directions.

The effect of the undulating strata on the inclination of the principal stress direction and the principal stress magnitude appear in Figures 2.7 and 2.8 respectively. The principal stress angle varies as a result of the limb inclination, as the steeper undulated strata formation creates higher angle variations compared to the flatter formation (Figure 2.7). It is seen that both graphs have “zero” value at the formation crest, which confirms the higher value of the horizontal stress component compared to the

vertical stress component. Therefore, we can draw the conclusion that the principal stress directions tend to follow the bedding. This conclusion is another confirmation of the existence of shear stress along the horizontal line A-A shown in Figure 2.3. The pre-existing shear along the undulating strata limbs would not have been included in the traditional slope stability analyses, which assume the overburden weight for the vertical stress, and an assumed k-ratioto estimate the horizontal stress.

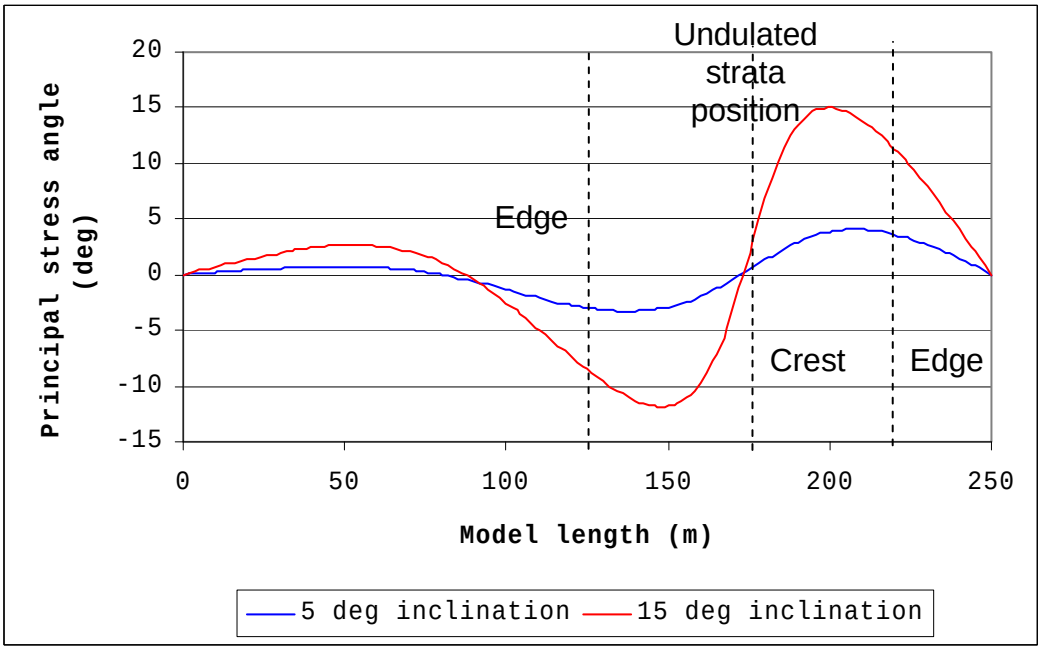

Figure 2.7

Principal stress angle variations along horizontal line at 30m depth

The magnitude of the principal stress variations (Figure 2.8) is also influenced by the formation limb inclinations. The steeper limbs create higher principal stress variations compared with the flatter limb inclinations.

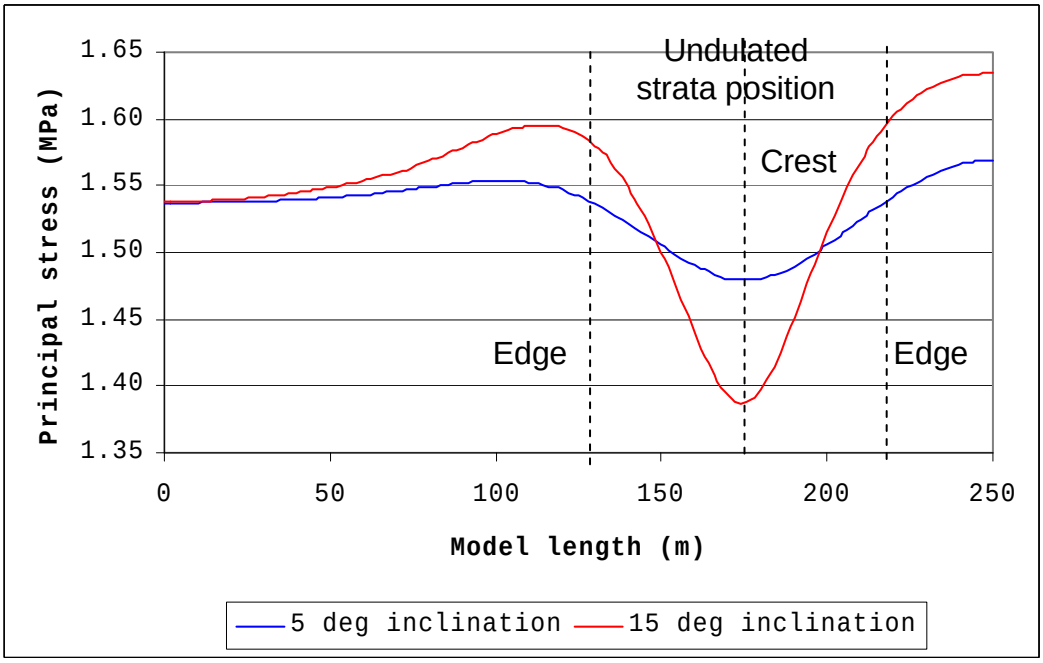

Figure 2.8
Major principal stress magnitude variations along horizontal line at 30m depth

2.7 VIRGIN STRESS ON AND ABOVE SHALE-COAL CONTACT

Failure in the mine took place on the bottom contact of the shale layer (i.e. at the top of the middle coal seam) when the strata were dipping toward the pit. This section concentrates on the virgin stress state along this contact, and along a vertical line above the crest of the undulating formation.

Figure 2.9 presents part of the model showing the shale layer, indicating the future slope position and the two profile lines for the representation of virgin and post-mining stress state data. The thickness of the embedded shale layer (h) in the first run of the model was 2m and, in the second run, 8m with an overburden thickness (H) of 28m and 22m respectively. In figure

2.9, the mine slope angle β has been given two values – 70^0 and 90^0, and the effects of slope angle will be investigated in Chapter 3. The strata inclinations on the limb, defined by α in the slope profile are 5^0 and 15^0.

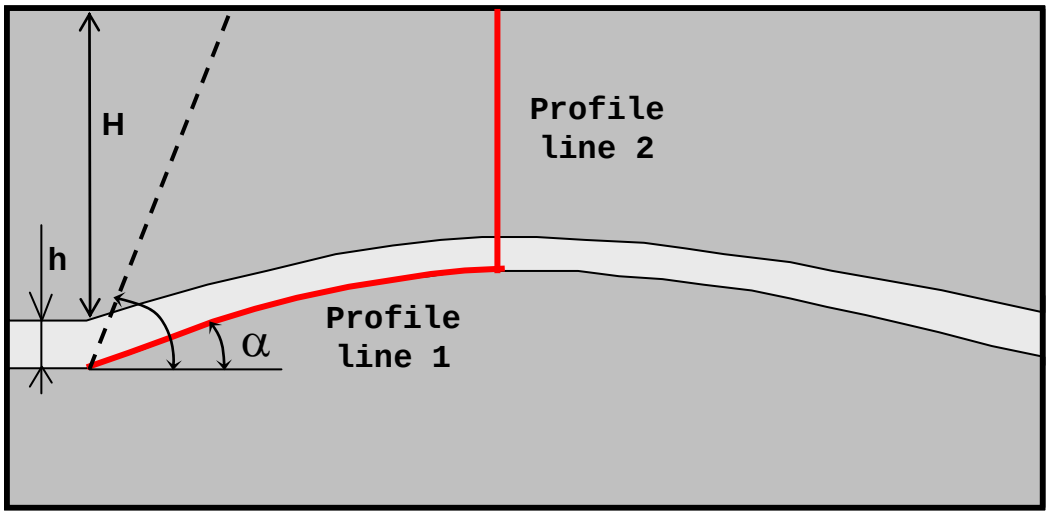

Figure 2.9
Definition of profile lines and model parameters for undulating strata

Turning to the virgin stress along profile line 1 on the contact, the plots given in Figure 2.10 indicate that the vertical stress is influenced by the presence of the undulating strata. Using equation 2.6, and expressing this stress as a dimensionless stress concentration factor produces the result shown in Figure 2.11. In the figure the formation with steeper limbs causes a higher stress concentration at the crest compared to the the formation with the flatter limbs. The shale thickness is insignificant according to the model results.

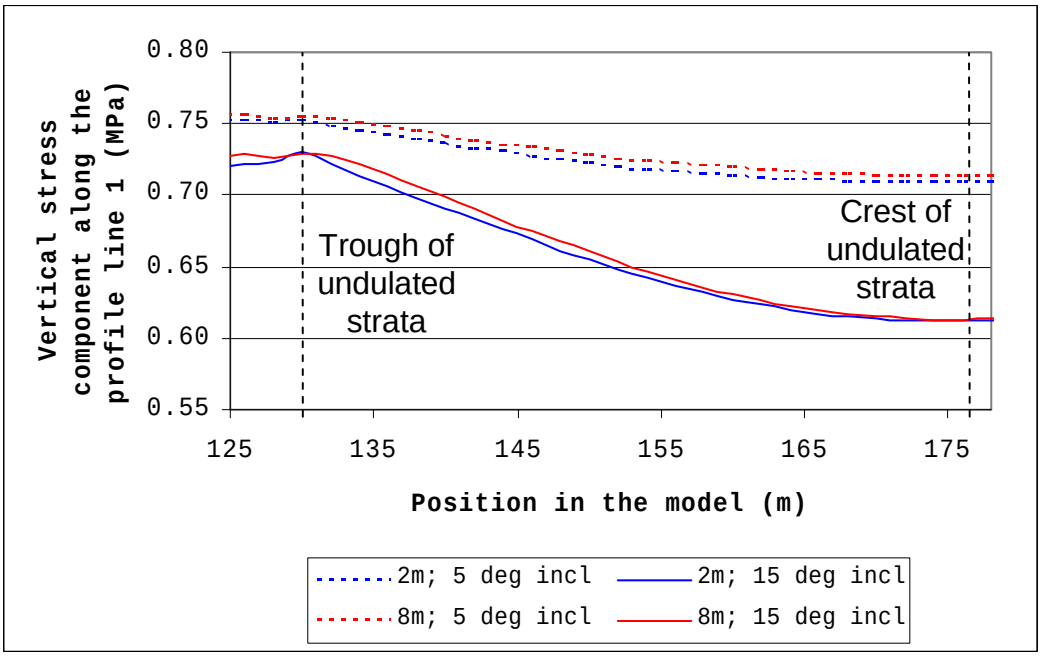

Figure 2.10

Vertical stress component before mining along a profile line set at the shale-middle coal seam contact

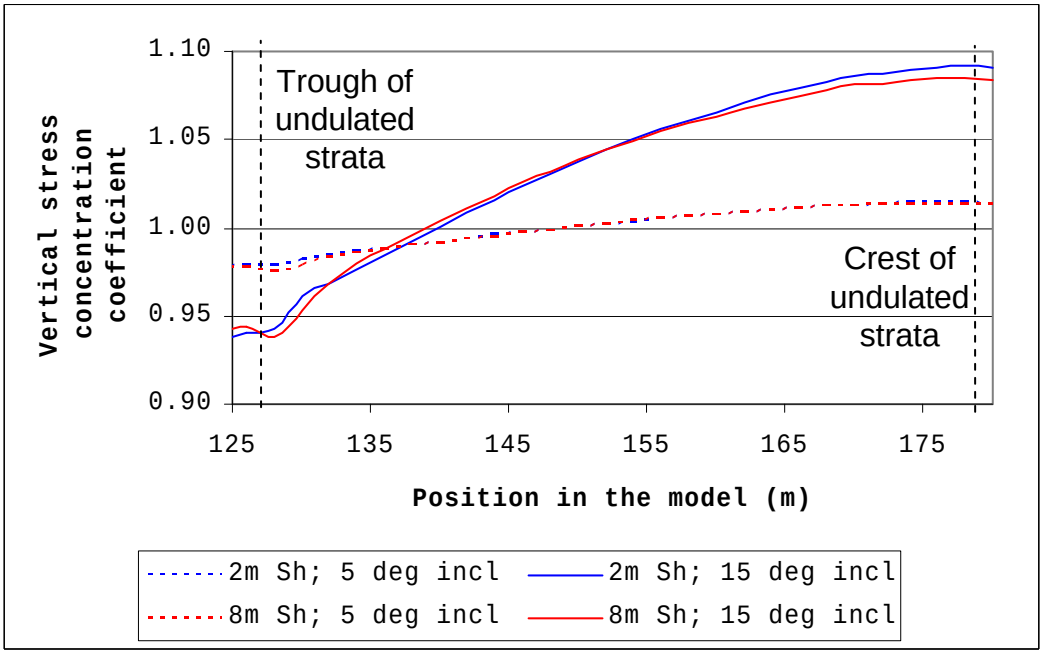

Figure 2.11

Vertical stress concentration factor before mining along a profile line on the shale-middle coal seam contact

The virgin vertical stress component distributions computed for all possible scenarios appear in Appendix 2, Figures A2.27-A2.30.

Figure 2.12 presents horizontal stress components along profile line 1 in virgin stress conditions. Along the formation limb, layers with a steeper inclination angle have lower horizontal stress in the formation crest compared to the formation with flatter inclination. This lower horizontal stress is the result of the smaller depth of the formation crest in the model with steeper limbs compared to the crest depth of the flatter formation.

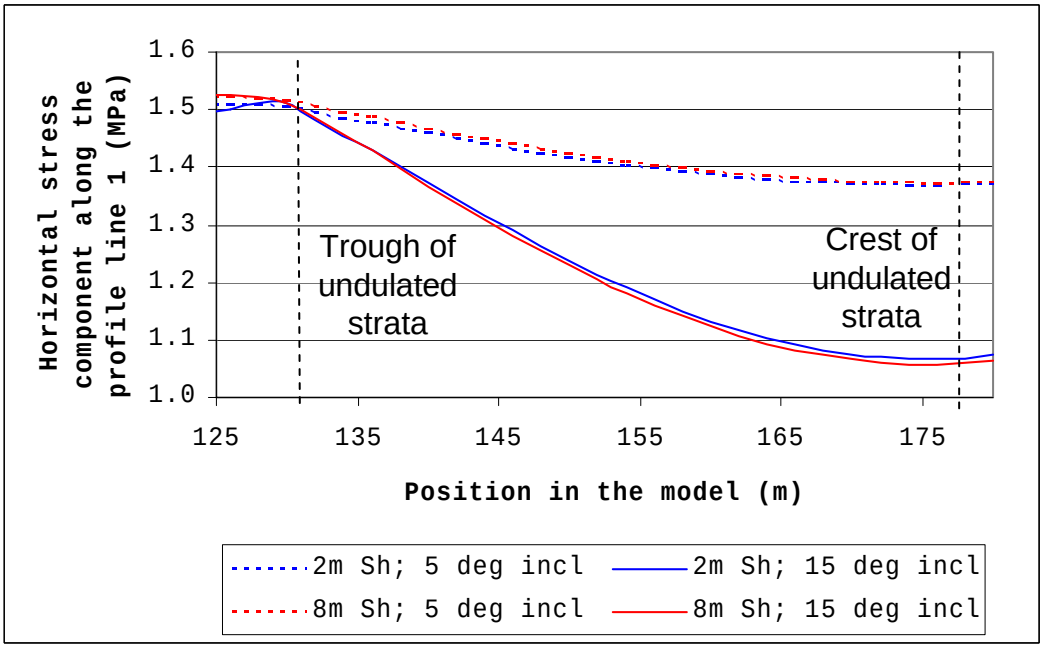

Figure 2.12
Horizontal stress component before mining along the profile line set at shale-middle coal seam contact

If we compare the layers with different thickness along the formation limb, the thicker shale layer has a lower horizontal stress component at the crest compared to the thinner layer. Equation 2.6 is used again to

investigate the undulated strata formation influence on concentrating the horizontal stress component in virgin conditions

Figure 2.13 presents the plot of these stress concentration coefficients. In the figure the horizontal stresses are reduced by 10% to 30% at the formation crest for a 2 m and 8 m thick layer respectively.

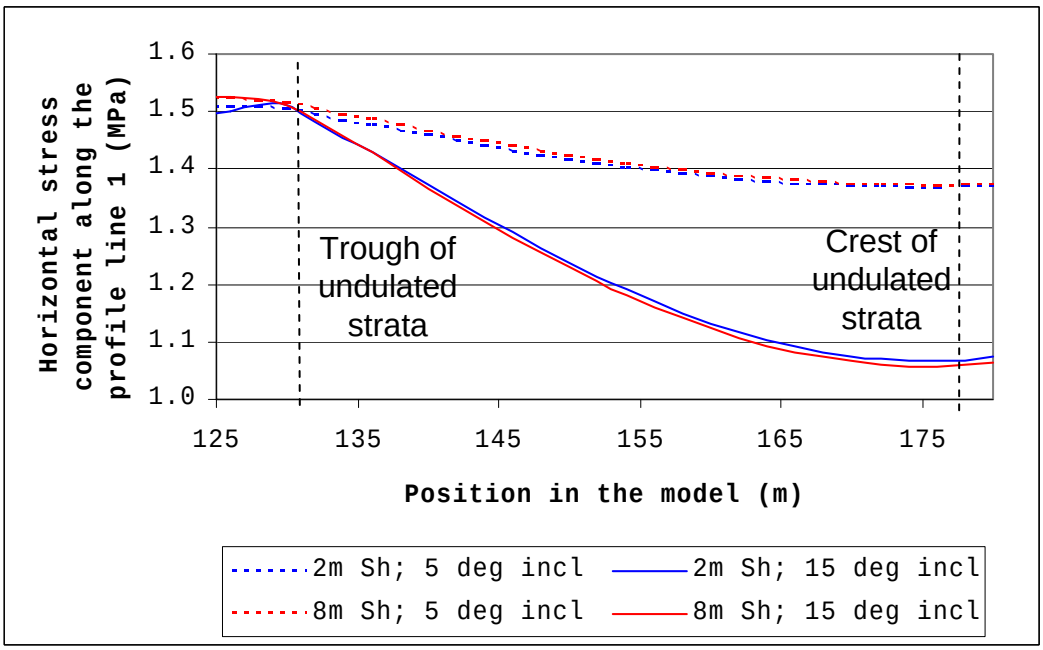

Figure 2.13
Horizontal stress concentration factor before mining along the profile line set at the shale-middle coal seam contact

The thicker embedded layer has a higher offloading effect in the crest of the undulating formation compared to the formation with the thinner embedded layer, while there is little effect on the horizontal stresses in the trough.

Therefore, we could say that the formation crest is subject to about 1% to 9% increased loading of the vertical stress component and 10% to 30% offloading of the horizontal stress component for limb angles of 5° and 15° respectively. This means that the virgin stress state is closer to lithostatic conditions for virgin stresses with a k-ratio of 2 because of the presence of the formation.

The horizontal stress component distribution in the model with a 2m and an 8m embedded shale layer and limb inclinations of 5^0 and 15^0 are detailed in Figures A2.31-A2.34, Appendix 2. Like Figure 2.13, all these figures show the presence of an induced tensile horizontal stress above the formation crest.

There is no closed-form method to calculate the shear stress component in virgin stress conditions, but it is reasonable to assume that the vertical and horizontal stress components are the principal stresses. Therefore, shear stresses must develop along the limbs of the undulating palaeosurface and in the inclined sediments overlying it.

Figure 2.14 shows plot of the shear stress component along the profile line at the base of 2m- and 8m-thick shale layers. It can be seen that the profile with the thicker embedded shale layer always has lower shear stress along the profile line compared to the profile containing the thinner layer. The highest shear stress develops at the formation toe, while the steeper limb inclination has a higher shear stress component than the to the flatter limb.

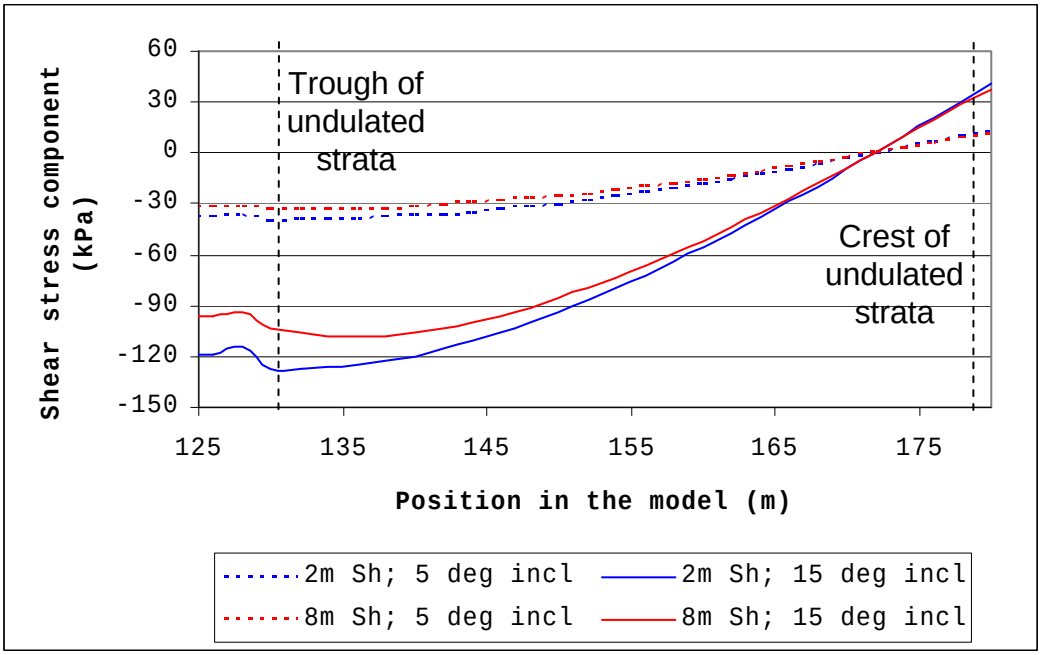

Figure 2.14

Shear stress component before mining along a profile line set at the base of the weaker layer

Theoretically, at the formation crest we should not have any shear stress, which is not confirmed by Figure 2.14 but this shear stress is very low (in the range of 10-20kPa) and can be ignored. In the formation trough there is a maximum shear stress component which is influenced by the limb inclination. The shear stress components for all possible scenarios appear in Figures A2.35-A2.38, Appendix 2.

Considering stress above the undulating formation, Figure 2.15 shows a plot of the virgin horizontal stress component along a vertical profile line (profile line 2, see Figure 2.9) above the crest of the undulating formation. The model predicts that a small tensile stress develops close to the ground surface above the formation crest in virgin conditions. The tensile zone depth is roughly proportional to the limb

inclination angle, as the steeper undulated strata formation creates a larger tensile zone at surface.

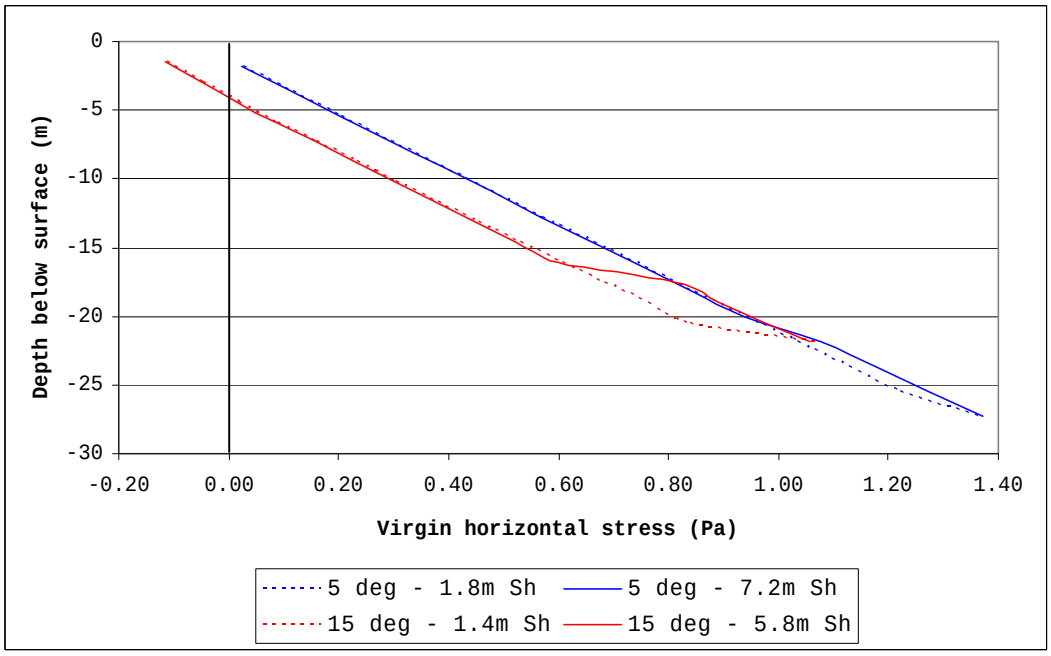

Figure 2.15

Horizontal stress component in virgin stress conditions along a vertical profile line above formation crest

In Figure 2.15, the tensile stress on the surface created by the flatter formation is shown to be in the range of 19 – 21kPa and cannot be seen because of the scale, whereas the tensile horizontal stress above the crest bounded by steeper limbs is of the order of 100kPa.

2.8 CONCLUSIONS

In conclusion the following have been noted:

- The ubiquitous joint model was tested and shown to be in agreement with the theoretical development by Jaeger and Cook (1979). Hence, it is included in the model.

- The FISH function produces an adequate model profile for the undulating formation structure at the desired depth of interest, and along the shale-middle coal seam contact.
- Stress deviations from simple models for horizontal and vertical stresses are the result of model geometry and not of tectonic stress.
- Differences in stress distribution are almost wholly the result of the geological structure, not the strata composition, i.e. whether the succession is homogeneous sandstone, or a combination of sandstone, shale, and coal.
- Stress deviations both in direction and magnitude are significant all along the limbs of the undulated strata formation, and become increasingly so with increasing limb inclination.
- The concentration of the vertical stress component at the crest is confirmed by Timoshenko (1934).
- Shear stresses develop along the limbs in virgin conditions because of the limb inclination, and this is supported by the photomicrographs in Pictures 2.1 and 2.2.
- Conditions for the development of a horizontal tensile stress on surface above the formation crest are favourable, although it is unlikely that it would exist because of weathering and sedimentation processes through geological time.
- The inability of existing slope stability methods to explain the failures observed in Chapter 1 suggests that the non-uniform virgin stress state predicted by the model must persist to some degree in the strata.

These results are all used in subsequent analyses to establish the stability of a mined slope in undulating strata.

CHAPTER 3
STRESS STATE IN THE SLOPE AFTER MINING

3.1 SUMMARY

This chapter deals with the stress state of a slope profile situated above undulating strata such that the strata dip towards the toe of the slope. A relatively weak layer is present in the succession, and could be either a shale layer in sandstone or coal pillars left underground. It is shown that direct application of the Mohr-Coulomb shear failure criterion does not give satisfactory results in specific conditions when the artificial cut is made above the trough of the undulated strata. Attention is drawn to the stress difference between the virgin conditions and after slope excavation, as modelled by FLAC. The general case is discussed in Appendix 1.2. Profile lines along the bottom contact between the embedded shale layer and the sandstone aid all discussions where failures were observed in the colliery slopes. The existence of a negative stress difference along the bottom contact of the shale is demonstrated, which indicates stress relaxation in the shale layer compared to the virgin conditions. In the case of underground pillars we have a decrease of the vertical pillar stress difference, indicating decreased loading on the pillars during surface mining, compared with the pillar stresses after underground mining was complete. It is standard surface mining practice to buffer-blast the pillars from surface, to remove the possibility of later pillar collapse once the slope has been cut. Buffer blasting

is tantamount to pillar collapse, and since it does not cause slope instability, it is concluded that collapsed pillars at the slope toe will almost certainly not be responsible for slope instability.

3.2 INTRODUCTION

Chapter 2 dealt with pre-mining stress variations along three profile lines in undulating strata (see Figures 2.3 and 2.9). As was pointed out in Chapter 1, in all cases, the failure surface responsible for the slope instabilities was observed on the bottom contact between the shale layer and the relatively stronger middle coal seam underlying it. It is widely accepted that the stress component normal to the failure surface is the main parameter governing the failure. For this reason, this chapter concentrates on this stress component.

This chapter starts with an analysis of the effect of a high k-ratio on the failure potential in a cut slope on the shale-middle coal seam contact, and then continues with a discussion of slope profile scenarios with limb inclinations of 5^0 and 15^0.

3.3 EFFECT OF HIGH K-RATIO ON FAILURE POTENTIAL

In Section 2.4, we discussed the reasons for the choice of the k-factor, and settled on k=2 for all model analyses. The virgin stress state in any failure scenario is a very important parameter, and the question now is: will a virgin stress state in which

the horizontal stress is twice the vertical stress favour failure along the contact surface between the shale layer and the middle coal seam once a mined slope is present?

In order to answer this question, a mined slope with single terrace 30 m high, and slope angle of 70^0 was modelled using DIGS (Discontinuity Interaction and Growth Simulation, CSIR, 1996). This code, based on a boundary element method, simulates fracture propagation in a homogeneous body, assuming one of the fracture propagation modes (e.g. tensile, or shear). The code was set to model shear failure in a homogeneous mudstone with properties listed for the shale in Table 2.1, since the model cannot take account of the anisotropic laminated nature of shale.

The model geometry was kept as simple as possible, with the pure objective of answering the above question, rather than developing a complex geometry that was similar to the pre-failure geometries seen in Chapter 1. In the three scenarios modelled the virgin k-ratio was set at 0.5, 1.0, and 2.0 (see Figure 3.1).

Firstly, the model predicts the formation of a shear fracture that propagates from just below or just above the toe of the slope, backwards into the slope, curving upwards towards the surface. This is similar to a circular failure mechanism. As the *k*-ratio increases above 1.0, the predominantly circular failure mechanism becomes flatter and lies closer to the failure surface on the top contact of the middle coal seam observed at the coal mine.

a)

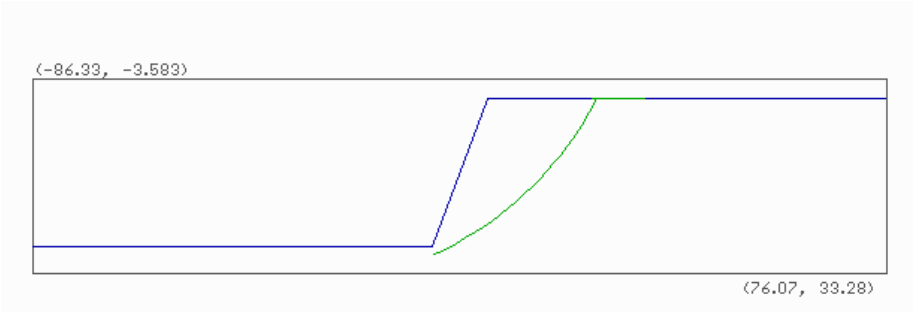

b)

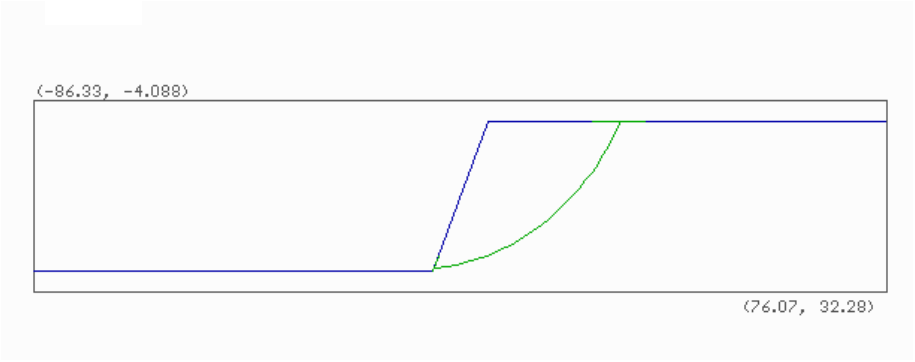

c)

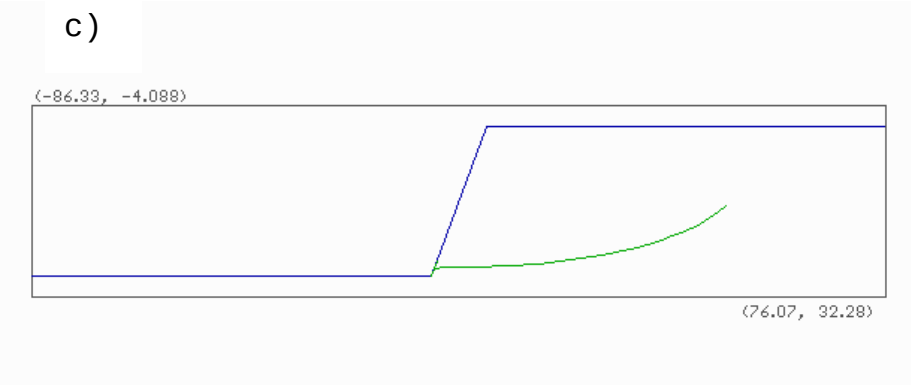

Figure 3.1

Shear fracture propagation in homogeneous slope profile with virgin stress ratio of: a) k=0.5; b) k=1.0 and c) k=2.0

This model does not confirm absolutely that failure along the shale-middle coal seam contact will actually take place, because of its geometric simplicity, and inability to model undulating anisotropic strata. However, it does confirm that shear failure is more likely on the shale-coal contact when the virgin k-ratio is 2, than when the k-ratio is 0.5.

3.4 SIMPLIFIED FLAC MODEL FOR MINED SLOPE

Because of the complex geotechnical conditions, the FLAC^{2D} code (Itasca, 1999) was used to model stress conditions in the slope after a mining cut had been made. Rather than modelling the influence of every variable in the slope geometry, the author has relied on earlier studies in the literature for simple guidelines. Hoyaux and Ladanyi (1972) and Stacey (1970 and 1973) presented some valuable results regarding the stress distribution in a slope and the influence of the slope angle. Kitahara et al (1986) investigated in more detail the original stress state, which could have high horizontal values. Jiang and Xie (1988) investigated the stresses in a slope profile due to the dip of the strata. Griffiths and Lane (1999) presented examples of finite element slope stability analysis and compared it to the other solution methods. Despite their achievements regarding the stresses in a slope profile, the Griffiths and Lane (1999) models have horizontal strata with a constant thickness, which is uncommon in nature.

Owing to the inhomogeneous native rock structure typical of natural situations, there are differing

responses to the stress changes in different layers as a result of mining activity. These stress changes depend on the ratio of horizontal to vertical stresses, which also vary with depth. The important role of rock failure in slope stability analysis is also dependent on the accuracy of the model used. None of these effects can be adequately accounted for in the equilibrium methods discussed in Chapter 1, and none of the analyses described above are directly applicable to the problem at hand because they all assumed geotechnical simplicity to facilitate the analyses.

The mining cut to the middle coal seam is 45m wide (standard mining practice) and it is assumed that this is wide enough to nullify any effects of the slope on the other side of the cut. The model (as with the DIGS model above) therefore consists of a mine cut beginning at the left boundary, extending to a simplified mine cut slope in the middle of the model, with the original ground surface extending from the slope crest to the right-hand model boundary.

The mine slope is simplified to a single terrace slope, unlike the complexity of the mine slope profiles shown in Chapter 1. The reason for this is to develop a simple, yet viable finite difference model that can be used to investigate the influence of the geotechnical conditions in the slope, rather than the influence of mining details. The simplicity of the slope does not mask any critical details in the post-mining stress in the slope. The depth of the cut was assumed to be an average 30 m, similar to the dimensions of the slopes that failed. The simplified FLAC model has the same height, length and number of zones as the model

presented in Chapter 2. Once the effect of a simple cut and the geotechnical conditions on the post-mining stress state became known, more complex models which take mining details into account were developed. These models appear and are analysed in Chapter 6.

The undulating strata model under the slope occupies approximately 100m of the total 250m-grid length, which was designed to avoid any influence of the model boundaries on the stress state around the slope profile. There is one disadvantage to this model. During the course of application the FISH function does not accept any further “generate” commands, disregarding further changes in zone size or their coordinates for the purposes of mining slope simulation. Therefore, any slope face creation has to be done with line generation. After the “adjust” command, some of the zones might not have acceptable FLAC geometries, which causes grid failure and, as a consequence, failure of the model.

This event can be avoided by increasing the number of zones in the model, therefore improving approximation. More zones will reflect in longer runtime, however. The other option is to change coordinates on the crest of the slope and from there on the generated line, which will result in a slope angle of 69.5^0 or 71^0, instead of the intended 70^0.

Profile Line 1 (see Figure 2.9) is placed on the contact between the shale and the middle coal seam, and covers the 48m distance between the trough and the crest of the formation, where the failure surfaces were observed (Figures 1.1 and 1.8). The slope toe is

situated directly above the trough so that the strata in the slope dip toward the pit, as seen at the coal mine. Profile Line 2 is vertical and spans the distance between the shale-coal contact at the crest, and surface (Figure 2.9).

The properties for sandstone and shale listed in Tables 2.1 and 2.2 in Chapter 2 were used in the model for the appropriate strata in the geological succession. The properties of the middle coal seam are those listed in Table 3.1.

Table 3.1 Coal properties applied in the FLAC model

Geotechnical parameters	Properties
Bulk modulus – Pa	2.0E9
Shear modulus – Pa	8.5E8
Tensile strength – Pa	2.0E6
Cohesion – Pa	4.0E5
Friction angle – deg	27
Density – kg/m^3	1500

3.5 STRESS STATE IN THE SLOPE PROFILE AFTER MINING

The previous chapter developed a model of the expected virgin stress state in unmined ground, and the effects of an undulating formation on the stress state. This section will explore the stress state and possible failure modes in the mined slope using the Mohr-Coulomb failure criterion. Figures 3.2 and 3.3 demonstrate failure modes in the profile with a 70^0 slope and a 2m-thick embedded shale layer in flat strata and strata with a 5^0 limb inclination.

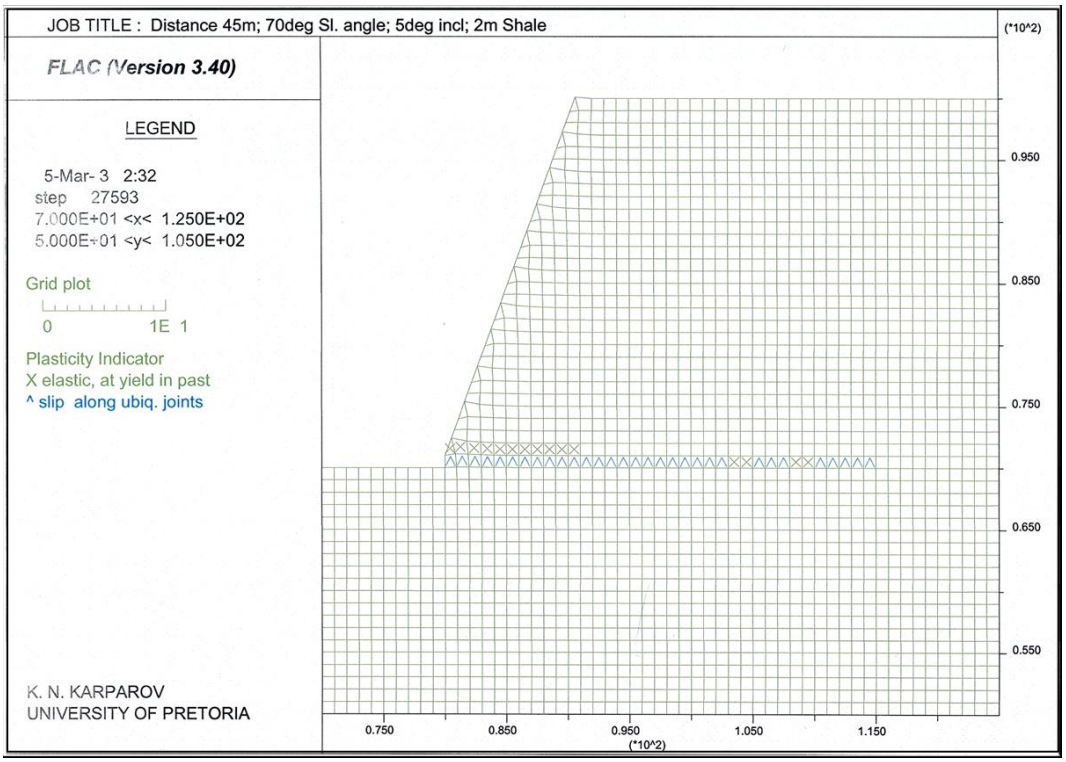

Figure 3.2

Failure in profile with flat strata

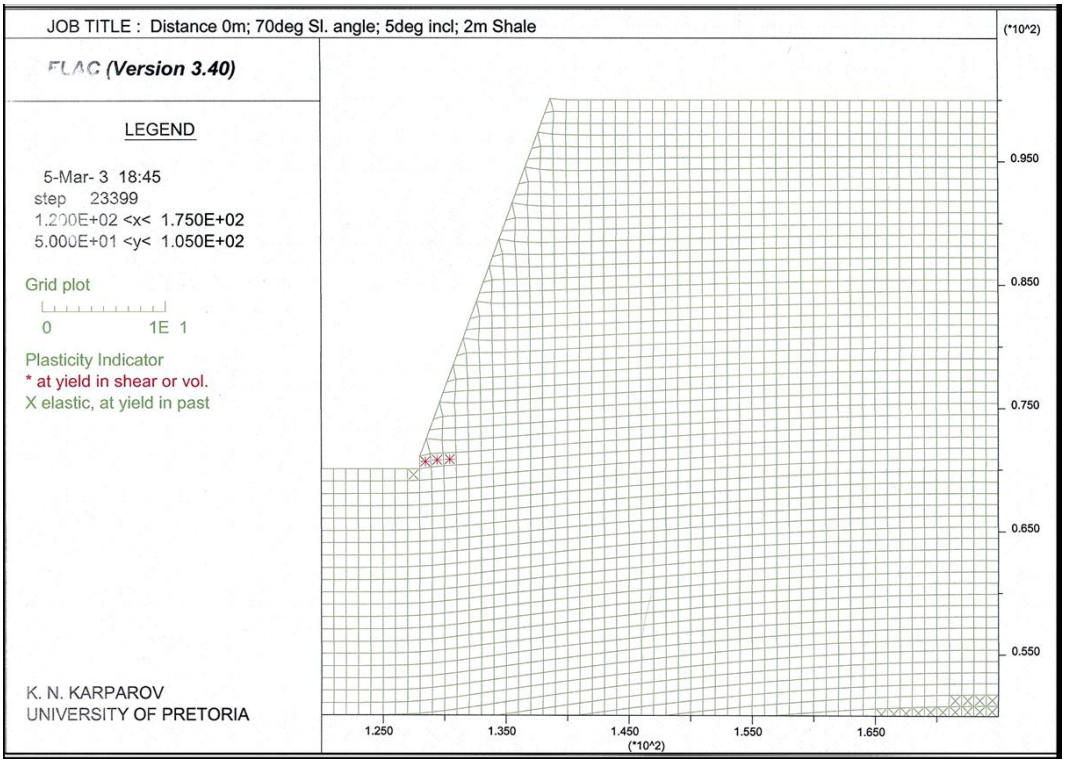

Figure 3.3

Failure in a slope with strata dipping at 5^0

In the flat layer scenario (Figure 3.2) we have an indication for slip along the weak bedding direction of approximately 30-35m, starting from the toe of the slope. The slope model shows some plastic deformations in the upper half of the embedded layer. Field observations show only layer swelling in such cases (Picture 1.1). In the case of the slope profile above the undulated strata (Figure 3.3), we have only plastic deformations in the first few metres from the toe of the slope.

Other slope profiles exhibit similar behaviour and their characteristics are given in Appendix 2 (Figures A2.7 to A2.10). Profiles with a vertical slope, which also exhibit the same behaviour, appear in the appendix (Figures A2.11-A2.16).

The major purpose of the failure models shown above and in Appendix 2 is to demonstrate that even when using a geotechnical model that contains the complexity of conditions seen at the mine, failure analyses produce inadequate results at best, and at worst, may be misleading (see Figures 3.2 and 3.3). Since the Mohr-Coulomb failure criterion was used in both models (the former demonstrating also slip along ubiquitous joints), they demonstrate that for failure to occur along the shale-coal contact, other mechanisms must also be involved. This is investigated in Chapter 4.

In Chapter 2 it was shown that induced stress differences in virgin conditions are caused by the undulated strata formation in the model. The influence of the presence of a mining cut is investigated in the following discussion. Figure 3.4 presents the vertical

stress difference (discussed in Appendix A1.2) along the profile line for a limb inclination of 15^0. It can be seen that there is a net tensile stress difference for some 30m into the slope from the toe for the 70^0 slope. The net induced tensile stress difference extends for a distance of only 10-12 m into the slope in the case of the vertical mine slope.

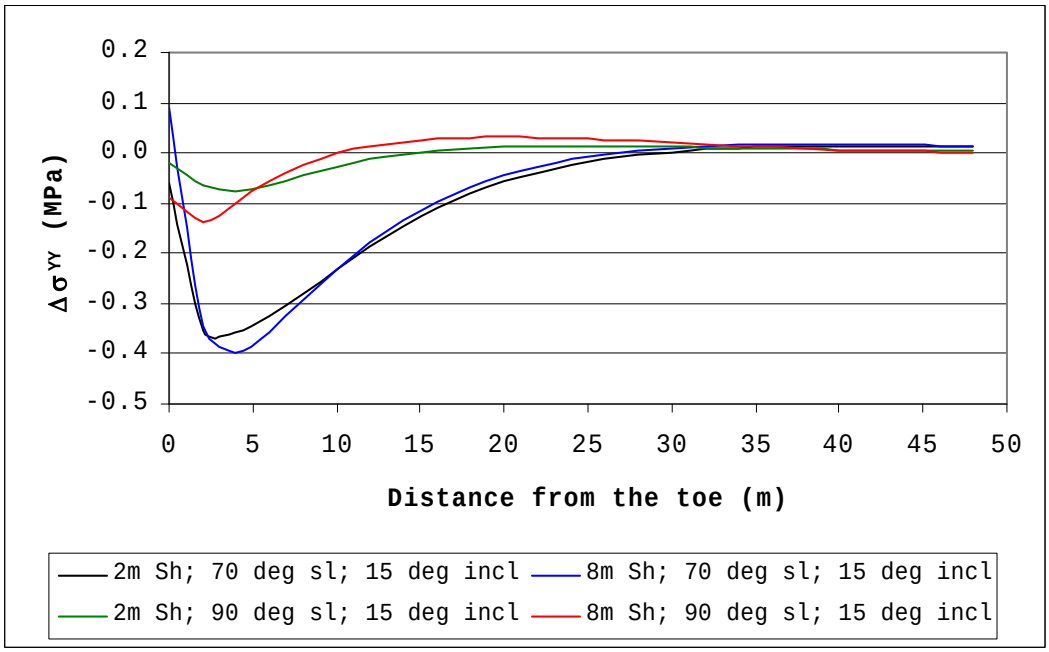

Figure 3.4

Vertical stress difference along profile line at shale–middle coal seam contact

The thickness of the shale layer has a less significant effect than the mine slope angle as demonstrated in Figure 3.4. Some compressive $\Delta\sigma_{YY}$ values develop in the first 1-2m from the toe of the slope, and are the result of the material failure there. The distances for which tensile $\Delta\sigma_{YY}$ values persist along the base of the shale layer for different cases are summarised in Table 3.2.

The results for the model with 5^0 limb inclination can be seen In Figure A3.2, Appendix 3, and are summarised in Table 3.2 below. The stress differences are mainly tensile for the profiles with flatter slope angles, and varying for different layer inclinations, and thicknesses. The resultant vertical stress component plots along the profile line can be seen in Figure A3.1, Appendix 3. It is concluded that the mining geometry is the dominant factor influencing the change in vertical stress along the profile line, and that the geotechnical factors such as layer thickness and limb inclination have relatively lesser influences.

Table 3.2 Distance that induced tensile stress $\Delta\sigma_{YY}$ persists into the slope along base of weak layer

Slope angle	5^0 Layer inclination	15^0 Layer inclination
2m thick shale layer		
70^0 slope angle	36m	26m
90^0 slope angle	20m	12m
8m thick shale layer		
70^0 slope angle	30m	24m
90^0 slope angle	8m	8m

The induced horizontal stress components along the shale-coal contact appear in Figure 3.5. They are the difference between the virgin values (Figure 3.10) and the resultant horizontal stress component (Figure A3.3, Appendix 3). In Figure 3.5 $\Delta\sigma_{XX}$ is shown only for the case of slope profiles with 15^0 limb inclination. In the figure all $\Delta\sigma_{XX}$ values have a negative sign for the slope profiles, indicating offloading along the whole profile line. The flatter formation exhibits similar results, which can be seen on Figure A3.4, Appendix 3.

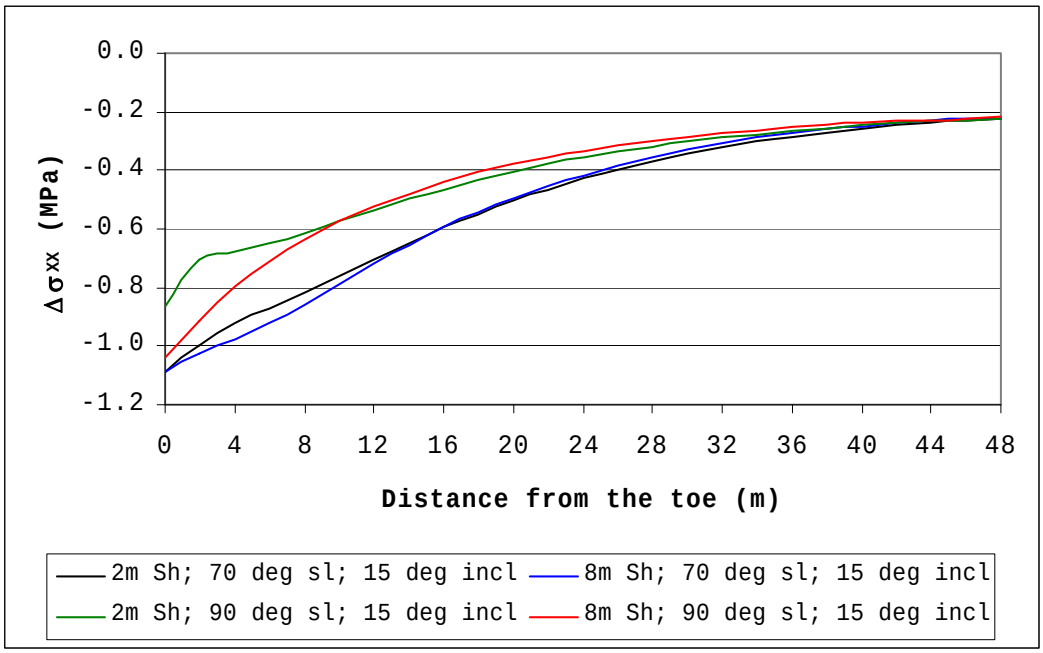

Figure 3.5
Horizontal stress difference along profile line at shale–middle coal seam contact

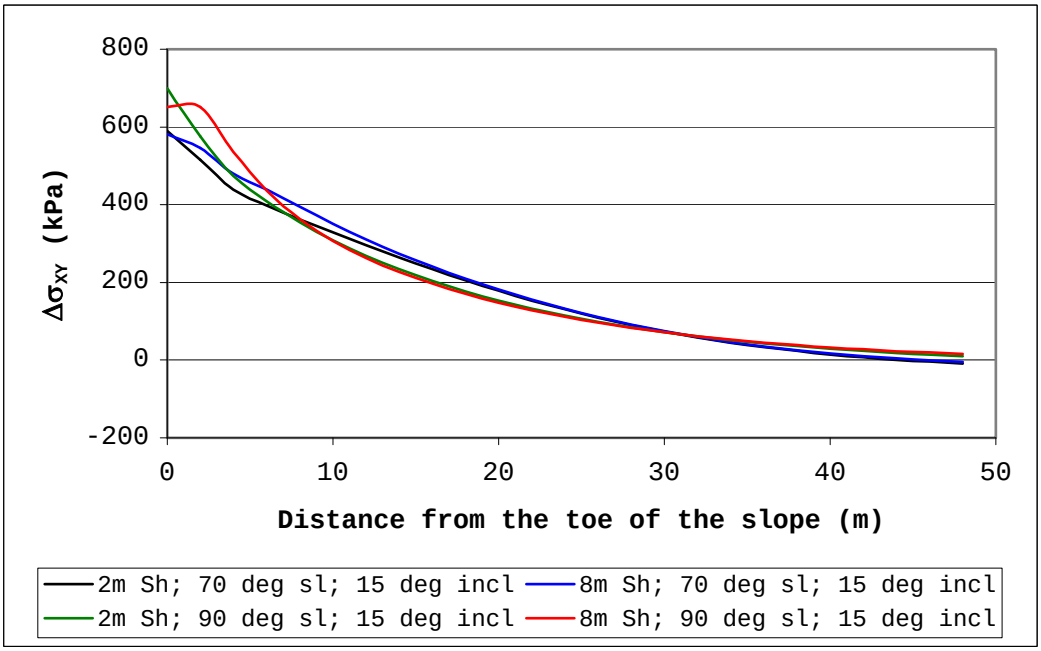

Figure 3.6
Shear stress difference along profile line on shale–middle coal seam contact

Figure 3.6 shows a plot of the shear stress difference induced by the presence of the mined slope. Firstly, it shows that there is a reversal in the sense of shear along the profile line until at least 30 m into the slope (compare Figures 2.14 and 3.6, noting that the toe of the slope coincides with the trough of the undulating formation), and that the magnitude of the induced shear stresses are much larger than those induced by the formation in virgin conditions. The induced shear stress results for the mined profiles with flatter formations in the model can be seen in Figure A3.6, Appendix 3.

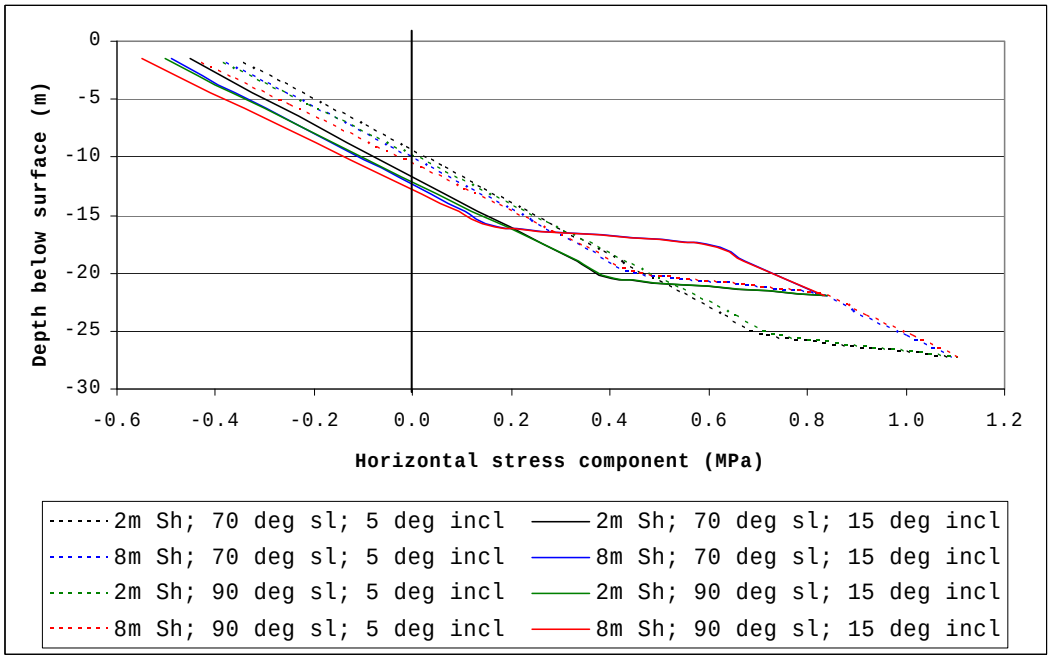

Figure 3.7
Horizontal stress component along a vertical profile line above the formation crest

Figure 3.7 presents a plot of the horizontal stress component along the vertical profile line above the crest of the formation when mining activities have taken place (refer to Figure 2.9 for position of

vertical profile line). There is a significant increase in the tensile stress component together with an increase in the tensile zone depth for all scenarios considered. Both the virgin and post-excavation stress states together with the tensile zone depth at the crest of the undulated strata formations are listed in Table 3.3 below. The significance of these results is that conditions conducive to surface tensile cracking are generated by a combination of mining and the subsurface geological structure.

Table 3.3 Maximum tensile stress and tensile zone depth along vertical line above formation crest

Slope angle (...^{0})	**Virgin stress (before mining)**		**Stress after mining**	
	Maximum Tensile stress (MPa)	**Tensile zone depth (m)**	**Maximum Tensile stress (MPa)**	**Tensile zone depth (m)**
5^0 limb inclination, 2m-thick shale layer				
70	-0.019	0.76	-0.399	8.73
90			-0.437	9.11
15^0 limb inclination, 2m-thick shale layer				
70	-0.140	3.42	-0.491	11.01
90			-0.533	11.39
5^0 limb inclination, 8m-thick shale layer				
70	-0.021	0.76	-0.433	9.49
90			-0.481	9.87
15^0 limb inclination, 8m-thick shale layer				
70	-0.143	3.42	-0.529	11.77
90			-0.579	12.15

Mining in particular brings about a significant increase in the magnitude of the maximum tensile stress as well as the depth to which it penetrates. The depth of the tensile zone and the magnitude of the maximum tensile stress are also influenced by the shale thickness, and in the case of the mined situation, slightly by the slope angle, but these factors are insignificant.

A little more detail on the horizontal stress state at surface is investigated next, because it will provide information on the potential for the formation of vertical tensile cracks behind the crest of the mined slope. These results are model predictions, and must not be assumed as guaranteed tensile horizontal stress at surface; the actual total stress at the surface will undoubtedly be neutral or slightly compressive, since surface soils would not be able to sustain any other stress state. Soils cope with induced tensile stresses by allowing the formation of tensile cracks commonly seen behind mining slope crests.

The results shown in Figures 2.15, 3.7, and 3.8 are specific to the modelled formation, since the depth of the formation below surface will have a strong influence on the surface tensile stress (i.e. if the formation were buried at a much greater depth than the modelled 30 metres, it should induce no horizontal tensile stress in the soils on surface or just below surface). Finally, we can assume that the thickness of the shale layer does not influence the horizontal stress component on the surface and that only the limb inclination does.

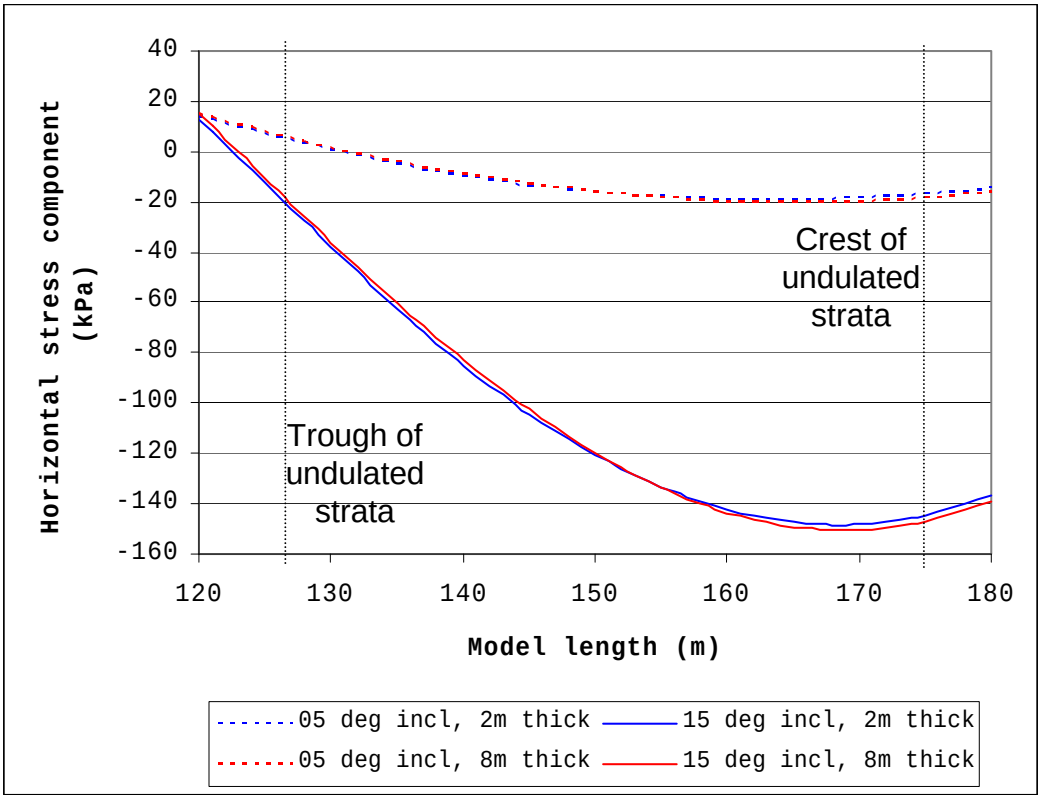

Figure 3.8
Horizontal stress component at surface

Thus far, all stresses have been expressed in terms of vertical and horizontal coordinates. Figure 3.9 shows the value of the stress difference ($\Delta\sigma_N$) normal to bedding along the shale-middle coal seam contact (see Figure 2.9) as calculated using Equation A1.9 (Appendix 1). In the figure, the $\Delta\sigma_N$ value has a negative sign, indicating a stress relaxation along the profile line for all cases.

The undulated strata formation with steeper limb inclination creates three to four times higher induced tensile ($\Delta\sigma_N$) values than the formation with flatter layer inclination. If we compare the graphs of the cases with different thickness of the layers then we

see that the thicker shale layer expresses slightly higher $\Delta\sigma_N$ in the first few metres than the profiles with a thinner shale layer.

The other most obvious difference between the graphs in Figure 3.9 is the comparison between $\Delta\sigma_N$ values of the profiles along the limb with different dip angles. The undulated strata formation with a flatter inclination angle exhibits smaller differences between the $\Delta\sigma_N$ values of the profiles with identical slope angle and layer thickness than the steeper formation does.

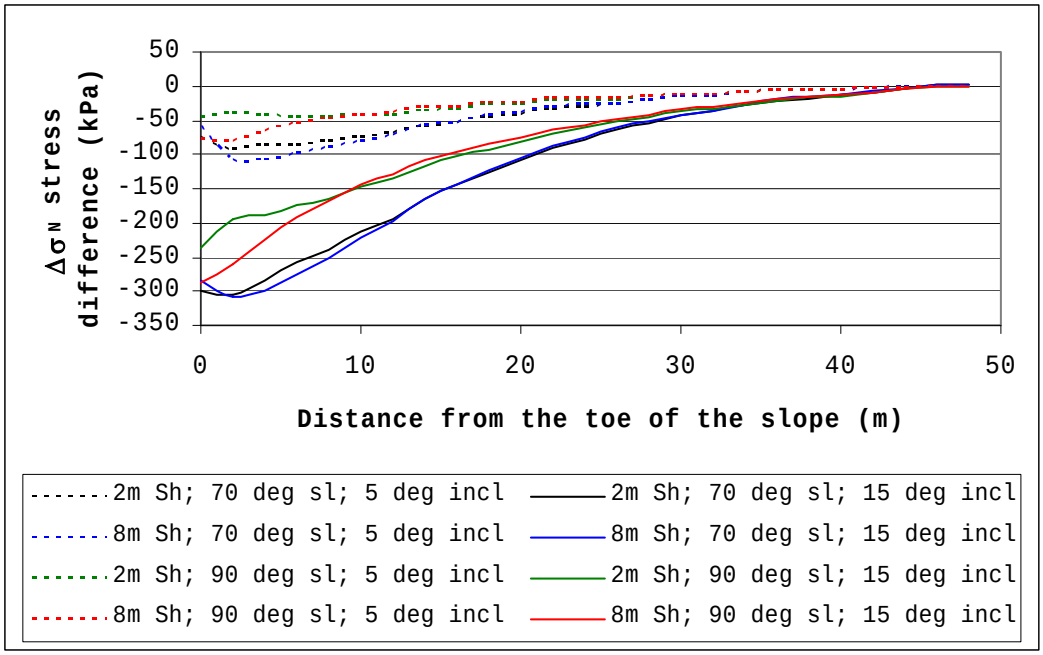

Figure 3.9

Induced stress changes normal to shale contact

The profiles with a vertical slope angle create a lower tensile difference than the profiles with a flatter slope angle in all investigated profiles. The figure shows that the stress difference normal to bedding is more or less proportional to the limb inclination.

These findings explain to some extent why a second collapse follows the initial slope failure that resulted in a reduction of the slope angle (see Example 1 in Chapter 1). From the stress difference results in Figure 3.9 we can conclude that the failures are related to stress relaxation normal to the strata. This aspect is investigated further in Chapter 4.

3.6 INVESTIGATION OF POTENTIAL PILLAR INSTABILITY AS A RESULT OF OPENCAST MINING

The current coal mine extracts all coal seams whether they were mined underground previously or not. As a result, the highwall slopes are cut above previously mined areas on the middle and bottom coal seams. The top seam was never mined by the underground coal mine. The highwall failures, presented in Chapter 1, appeared in areas where the underground mining activities didn't take place. For this reason, both highwall failures (discussed in Chapter 1) can not be associated with any influence on underground pillars. Hence, the following investigation of pillar instability as a result of opencast mining will discuss only the variations of the average induced pillar stress as a result of open cast mining.

The underground mining was exclusively bord and pillar, with pillar widths varying between 6.7 and 7.8m, and the bords averaging 6.7m in width for both seams. There was little data on average mining height in the old underground mine so an average of 3.5m, based on the stratigraphic column shown in Figure 1.3 and the previously used mining method "drill and blast", was

used. This assumes that either the middle or bottom coal seams were mined or if both were mined, they were mined to a height of approximately 1.5m each to leave a sufficiently thick middle parting. These mining parameters at about 45m depth give an approximate pillar safety factor ranging between 1.9 and 2.2, after the Collieries Research Laboratory (1972), which is based on the Salamon-Munro pillar strength formula. The extent of pillar failure prior to the open cast mining is not known, so it is likely that the average pillar safety factor was in the above calculated ranges.

The opencast pillar extraction sequence is shown in Figure 3.10, (deliberately omitting the buffer blasting step before cutting the slope, see below for description of buffer blasting) where the pillar numbering, and the profile line position at pillar mid-height, is shown. All the analyses of slopes established above mining on the middle coal seam assume the worst stability case in which the pillars remain intact after the slope has been cut. In reality, the mine practices buffer blasting, in which the pillars on the mined seam are shattered by drilling and blasting them from surface before the mine pit slope is cut. The reasons for carrying out buffer blasting are threefold:

1. buffer blasting will help to extinguish any pillars that might be burning through a process of spontaneous combustion;
2. if the pillars are still intact and not burning spontaneously, shattering them minimises the possibility that they could ignite spontaneously

when they are exposed to oxygen and water once the slope has been cut;

3. if pillar collapse below a slope were allowed after a slope had been cut, it could severely affect mining machinery both behind the slope crest and in the pit, and also affect spoil piles dumped behind the slope crest (see for example Figures 1.7 and 1.8).

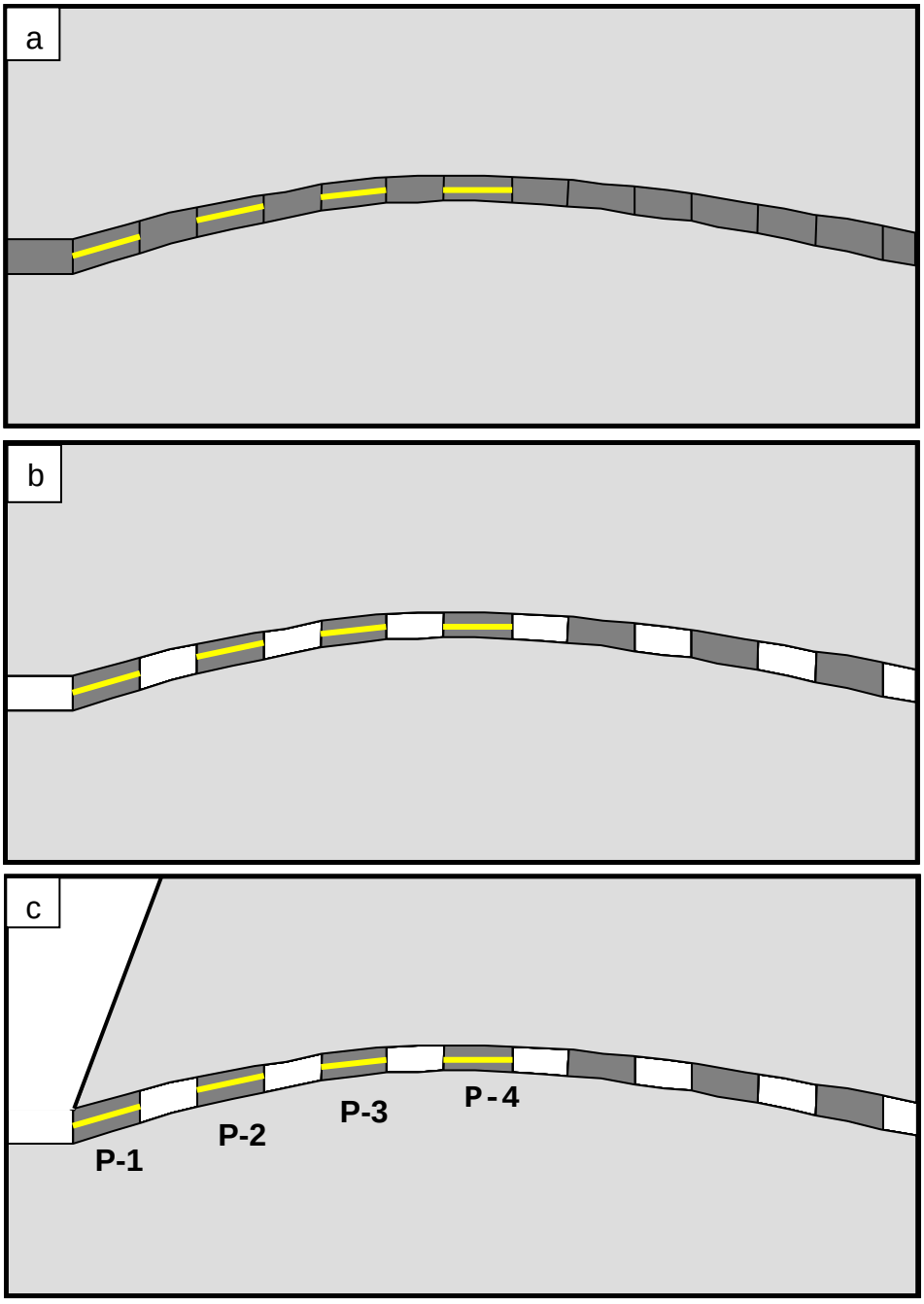

Figure 3.10

Profile lines (marked with yellow) for pillar stress analysis: a) virgin stress state; b) coal seam mined underground; and c) opencast exposure of coal pillars together with their numbers

Buffer blasting can only be carried out on the middle and bottom coal seams, because the top coal seam was never mined. If the buffer blasting is carried out perfectly, it would result in a layer of broken coal between 1.6 and 1.8m thick assuming a 1.6 swelling factor, 3.5m mining height, and areal extraction between 72 and 75% respectively. In all analyses, only a single mined seam was modelled.

In the pillar stress analyses, the average stress values along the pillar profile line are used, and the discussion that follows includes only results for the pillar geometry with a safety factor of 1.9, because the slope profile with pillar safety factor 2.2 shows similar results. These latter results appear in Appendix 3.

Table 3.4 Average inclination angles of the profile lines in the pillars

Pillar number	Profile line inclination angle (FOS=1.9 pillars)		Profile line inclination angle (FOS=2.2 pillars)	
	5^0	10^0*	5^0	10^0*
1	5	10	5	10
2	5	8	5	7
3	3	4	2	4
4	1	1	0	1

*The coal seams were not mined if the limb inclination was greater than 10^0.

Since the pillar profile lines are at different inclinations in each pillar, Table 3.4 shows the average inclination angles of the profile line at each pillar.

The effects of strata inclination on pillar stability are shown in Figures 3.11 and 3.12 using pillars with a safety factor of 1.9. The worst-case 90° slope angle has been used for this purpose (the slope above the middle coal seam in Figure 1.7 was actually 80°). As a two-dimensional program, FLAC assumes out-of-plane continuity of the profile. In order to account for the presence of bords around the pillars in both horizontal directions, the vertical pillar stress was doubled while out-of-plane stresses (horizontal and shear) were taken as calculated by FLAC.

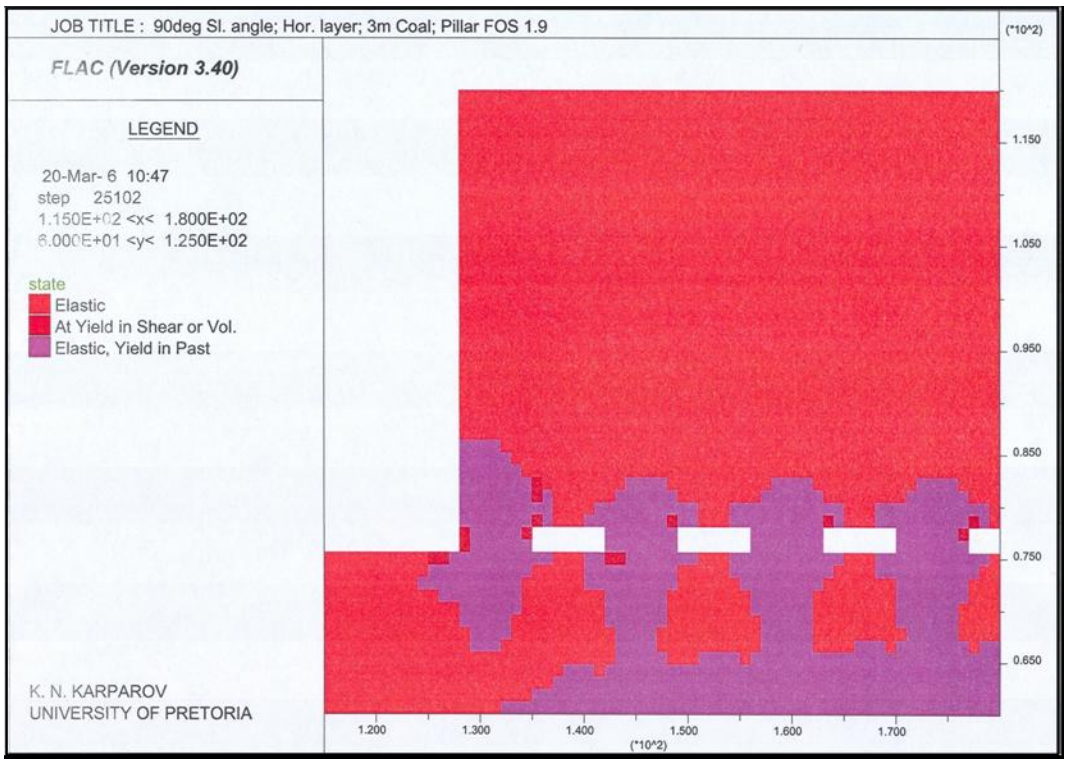

Figure 3.11

Pillar failure in flat strata below 90° slope

The model predicts some shear failure in the two pillars closest to the toe, with virtually no damage to pillars deeper in the slope. The slope overburden is in the elastic regime and damage to the enclosing strata due to the pillar failures is not present.

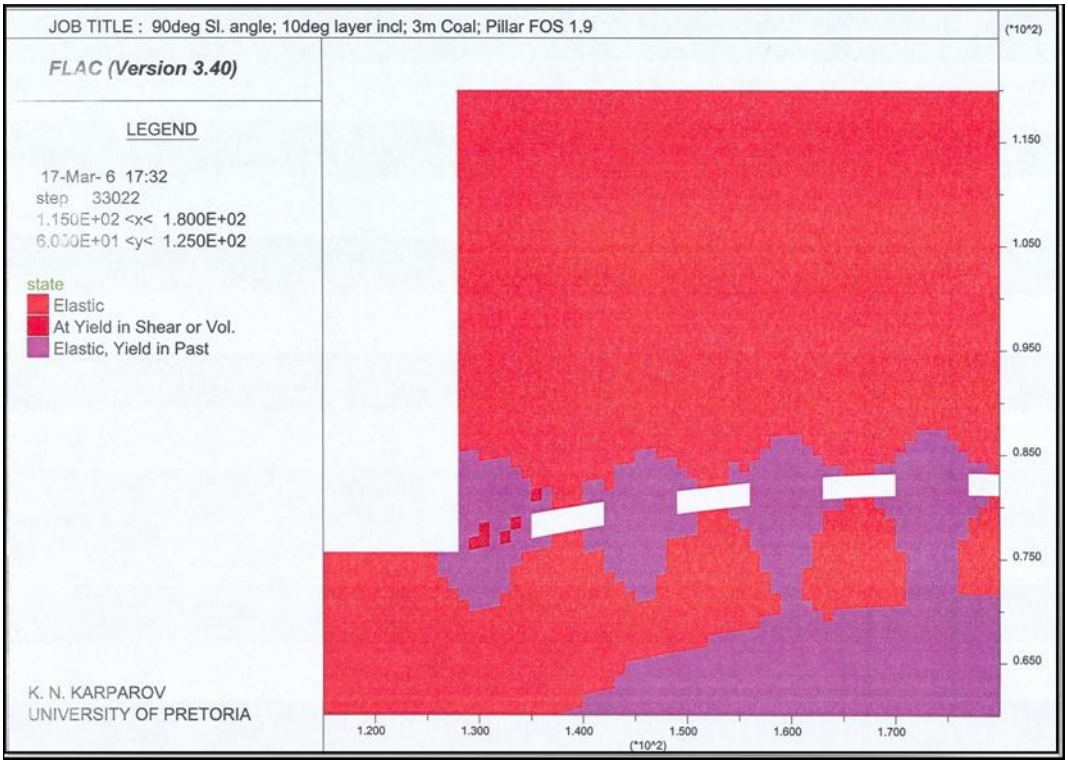

Figure 3.12
Pillar failure in inclined strata below 90° slope

Figure 3.12 shows the slope profile in inclined strata. In this case, only the pillar at the slope toe indicates some shear failure. Comparing this with the pillar failures predicted in flat strata, it appears that the pillars in the inclined strata may be more stable. This is probably because the coal layer thins on the limbs, giving the pillars a better width to height ratio if bord and pillar dimensions remain the same. Figures A2.17–A2.26 in Appendix 2 show pillar failure in all other possible scenarios.

For evaluation of underground pillar stability as a result of opencast extraction, the author uses induced stress components along the pillar mid-height between these two cases. The reasons for using underground

pillar scenario as a base for opencast extraction can be summarised as:

- Underground mining had taken place long time (about 30 years) before opencast mining. During this period, the stress state has achieved its balance and all possible deformations have taken place. One of these deformations is pillar scaling, which can be seen whenever the pillar is daylight in the toe of the slope.
- Both FLAC models (underground coal pillars with and without artificial slope) are with the same properties of strata and assumptions (regarding k-ratio). Hence, the stress state difference along the pillar mid-height is only result of the opencast extraction.
- Using induced stresses between both stages (FLAC models before and in time of opencast extraction) diminishes possible mistakes in the models regarding coal pillar properties (affected by scaling) or possible roof failures in bords.

Figure 3.13 presents a plot of the stress difference of the average vertical stress component ($\Delta\sigma_{YY}$) for the first four pillars in the slope profile at pillar mid-height. In the figure, the profile slope angle influences the average induced pillar vertical stress only in the first three pillars from the mining slope toe. The profile with a vertical slope angle has lower $\Delta\sigma_{YY}$ than the profile with a flatter slope angle. The slope profiles with steeper layer inclinations have lower $\Delta\sigma_{YY}$ values than the profiles with flatter strata inclination.

Since $\Delta\sigma_{YY}$ values always have a negative sign, the pillars undergo a decrease in vertical loading when the open cut approaches. Similar results hold for the pillar geometry with a safety factor of 2.2 (Figure A3.7, Appendix 3).

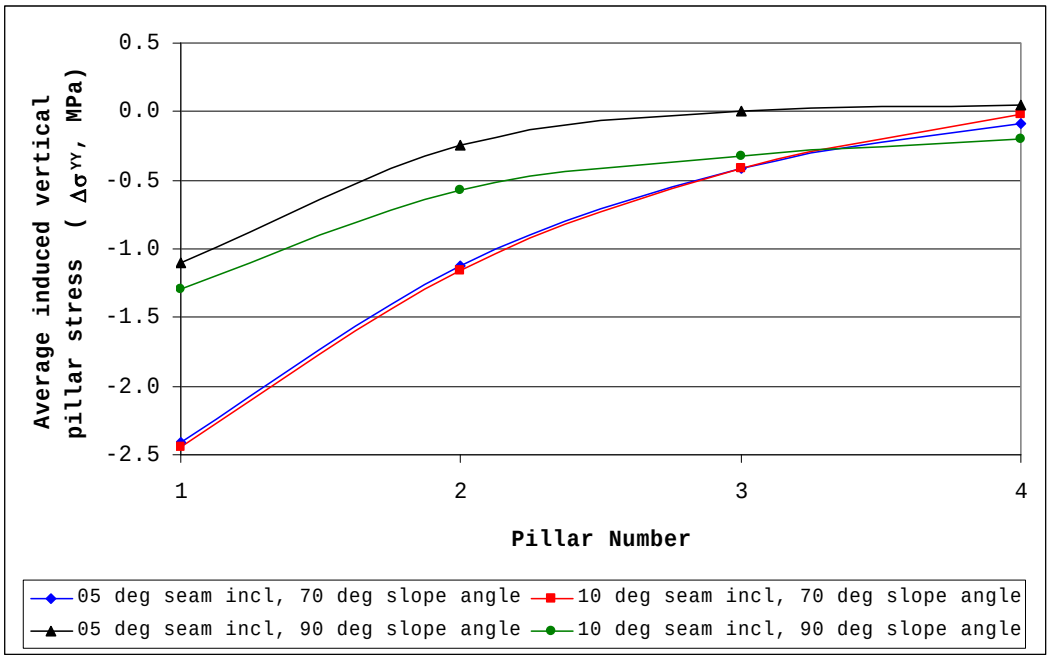

Figure 3.13
Induced vertical stress change in pillars at the base of the mined slope

Figure 3.14 shows a plot of the horizontal stress component difference ($\Delta\sigma_{XX}$) along the profile line. The graphs of the slope profiles with a pillar safety factor of 2.2 appear in Figure A3.8, Appendix 3. All values on $\Delta\sigma_{XX}$ are negative, which means a relaxation from the underground conditions. In Figures 3.13 and 3.14, it is seen that when the pillars approach the formation crest the average vertical and horizontal stress differences ($\Delta\sigma_{YY}$ and $\Delta\sigma_{XX}$) decrease in value in approximate proportion with the decreasing strata

inclination. The slope angle is insignificant for pillar numbers 2, 3 and 4 when considering induced horizontal stresses in the pillars.

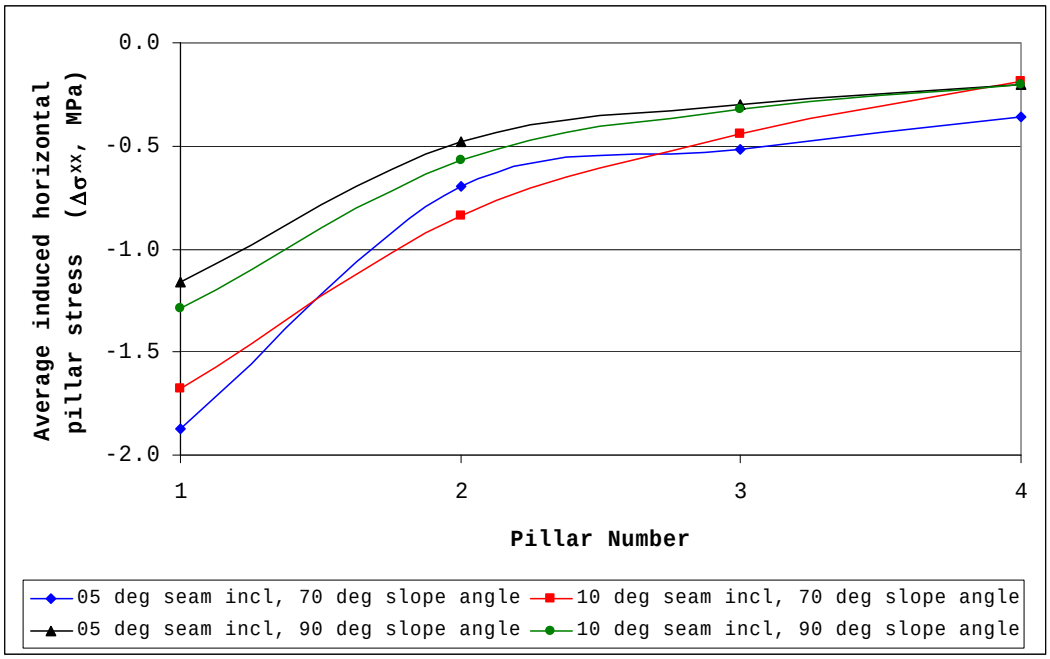

Figure 3.14
Induced horizontal stress change in pillars at the base of the mined slope

Along the formation limb shear stress changes ($\Delta\sigma_{XY}$), shown in Figure 3.15, do not differ significantly between the profiles with different layer inclinations. It is seen that opencast extraction of underground pillars increases the shear stress component in pillars. If we compare the profiles with different slope angles then the profile with the vertical slope maintains higher $\Delta\sigma_{XY}$ than the profile with flatter slope angle. Exception makes only pillar number one which has almost the same $\Delta\sigma_{XY}$ value in the profile with flatter slope angle profile compared to the profile with vertical slope angle at formation with flatter layer inclination. Comparing the shear stress

component difference from the graphs with different layer inclinations, the steeper formation has lower induced shear stress values than the formation with flatter limb inclination. Shear stress changes for the profiles with pillar safety factor 2.2 appear in Figure A3.9, Appendix 3.

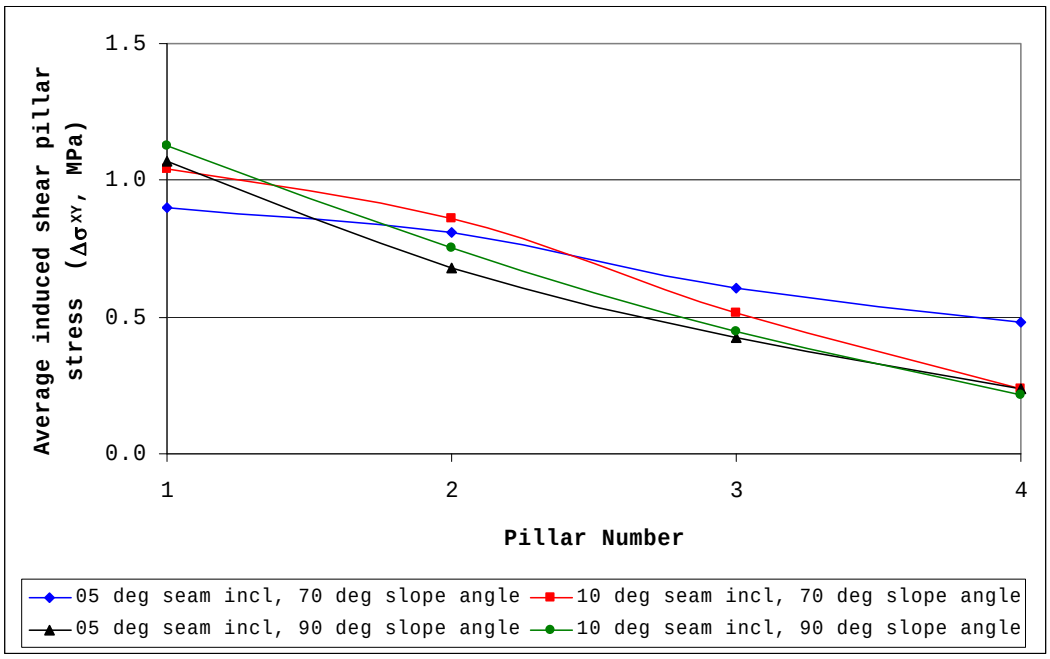

Figure 3.15
Induced shear stress change in pillars at the base of the mined slope

Shen and Duncan Fama (1999) investigated the highwall mining experience in Australia, where mines using the Continuous Highwall Mining System create rectangular entries, usually 3.5m wide, with a distance of 2.5m between entries. Every 3 to 5 entries, barrier pillars 5-8m wide are left. In this situation, mainly roof failures were observed, while subsided zones and highwall failures also occurred, but more rarely (Shen and Duncan Fama, 1999).

Generally, the Australian pillar safety factors are lower than for this study, so we can draw the conclusion that the highwall failures as a result of opencast pillar extraction in the South African coal mine are unlikely, and become extremely improbable because of the buffer blasting of pillars prior to slope excavation. Although the pillar model appears stable as modelled, it will be more stable if the buffer blasted pillars were modelled as a 1.6-1.8m cohesionless coal seam with zero tensile strength. The bulk and shear moduli would be about half the values given in Table 3.1, while the density would be reduced to 1000kg/m^3 because of the bulking factor. A lithostatic stress state would also have to be modelled within the coal seam, which would be impossible in FLAC if other parts of the profile are not in a lithostatic stress state. Finally, buffer blasting has been confirmed by experience at the mine as being effective in maintaining slope stability in slopes above pillars, so it is concluded that the pillars have played no role in the slope collapses observed on the shale-top coal seam contact, since all major failures described in Chapter 1 were on the contact between the shale and the unmined middle coal seam.

3.7 CONCLUSIONS

The following conclusions can be drawn from the simple models tested in this chapter:

- Stress relaxation normal to bedding occurs when the mine slope has been cut.

- Normal pillar stresses are reduced by the slope, but this relaxation is insufficient to cause pillar instability.
- Observations at the mine showed that no mining took place in coal seams inclined at 10° or more, and that the top coal seam was never mined by the underground mine.
- The models help to confirm that pillars below slopes will probably not have an effect on slope stability.
- The models used are unable to completely explain why major slope failures occurred in slopes located above unmined ground, but their results can be used as input for the development of a proposed block thrust mechanism described in Chapters 5 and 6.

Since the models on their own are unable to confirm slope failure above unmined undulating coal seams, investigation into the mechanisms through which failure can eventually result along the shale-middle coal seam contact are indicated, and are discussed in Chapter 4.

CHAPTER 4
MECHANISM OF FAILURE SURFACE GROWTH IN SLOPE AFTER MINING

4.1 SUMMARY

This chapter deals with possible mechanisms of fracture extension and coalescence that must take place along the shale-middle coal seam contact to result in the observed mine slope collapses. Fracture extension is encouraged by stress relaxation normal to sedimentation due to open pit mining, discussed in the previous chapter. Many authors state that fracture initiation and possible extension are related to the pore size of the rock. The shales, which represent the weak layers in the slope profile, have very low porosity, ranging between 3% and 6%. Microscope study of thin sections together with X-ray analysis agree that the shales in the succession are polyminerallic, laminated rocks, which include minerals both stronger and weaker than the surrounding muddy matrix. The most important of these minerals appear to be quartz and carbon, which appear as fragments and flakes usually larger than the grain size of the matrix in which they are set.

The significance of these minerals and their distribution is studied using of the Dugdale-Barenblatt analysis model (Dugdale, 1960; Barenblatt, 1962), in which collinear flaws represented by the carbon flakes coalesce to form a failure surface favourable to eventual slope collapse. Instead of a completely damaged zone with finite size, the model assumes that a

fracture process zone of macroscopically negligible width forms ahead of the tip of a Mode-I flaw, represented by the carbon flakes. Under the assumption of plane stress, a periodic array of collinear flaws (carbon flakes) with equal length is taken as an example of analysis. The critical length of the fracture process zone is assumed to be a rock constant, as is verified by the analysis of the increased distance between the flakes. The flaw coalescence is attributable to two causes: flaw propagation due to the mining-induced stress changes; and the linking of fracture process zones due to the small distance between neighbouring flakes, which promotes the development of the failure surfaces seen in the slope collapses.

4.2 INTRODUCTION

When rock is loaded to failure, cracks nucleate and propagate from pre-existing inhomogeneities, which can be in the form of pores, fractures, inclusions or other defects. The first plausible theoretical description of crack initiation and propagation in solids appeared in the early 1920s (Griffith 1921, 1924). Systematic theoretical and experimental investigations of crack initiation, propagation, and interaction in rock began in about the middle of the twentieth century and have continued since (Hoek and Bieniawski, 1965; Peng and Johnson, 1972; Hallbauer et al, 1973; Tapponnier and Brace, 1976; Olsson and Peng, 1976; Kranz, 1979; Batzle et al., 1980; Dey and Wang, 1981; Wong, 1982; Nemat-Nasser and Horii, 1982; Steif, 1984; Horii and Nemat-Nasser, 1985 and 1986; Ashby and Hallam, 1986; Sammis

and Ashby, 1986; Kemeny and Cook, 1987). It is recognised that under the combined action of tension and shear loading, both tensile and shear stress concentrations can develop at pre-existing inhomogeneities in rock. As the tension applied to the rock further increases, tensile cracks will be initiated. In the shear sliding crack model, this tensile crack is known as a "wing crack", which initiates from the tip of a pre-existing fracture and grows progressively in the direction normal to maximum tension. In the early stages, when the wing crack is short, the stress field around the pre-existing fracture from which it grows dominates the growth. As the crack extends, it starts to interact with neighbouring microcracks, and this interaction ultimately leads to crack coalescence and final failure of the sample (Ashby and Hallam, 1986).

Owing to the importance of the near crack-tip field in fracture behaviour, crack-inclusion interaction studies have received a great deal of attention in fracture mechanics (Lipetzky and Schmauder, 1994; Lipetzky and Knesl, 1995; Papaioannou and Hilton, 1974; Wang et al., 1998; Tamate, 1968; Helsing, 1999; Muller and Schmauder, 1993; Sih et al., 1970). Most of the studies use numerical approaches, such as the finite element method (Lipetzky and Schmauder, 1994; Lipetzky and Knesl, 1995; Papaioannou and Hilton, 1974), the boundary element method (Lipetzky and Knesl, 1995; Wang et al., 1998), and the singular integral equation method (Tamate, 1968; Helsing, 1999; Muller and Schmauder, 1993). A wide range of crack and inclusion geometries have been investigated by these numerical

analyses to show the effects of inclusion shape, size, location and stiffness in the near crack-tip field.
Some important work has been carried out using the numerical simulations of crack propagation and coalescence between multiple crack-like flaws. Using the Displacement Discontinuity Method (DDM), Scavia and Castelli (1996) and Scavia (1999) conducted some preliminary work, using a numerical technique to investigate the mechanical behaviour of rock bridges in material containing two and three crack-like flaws. In these studies, a series of numerical analyses was carried out to evaluate the influence of overlapping so as to identify a critical value for the resistance of the rock bridge between two cracks. The results show that direct and induced tensile crack propagation can occur in both stable and unstable conditions depending on flaw spacing and applied confining stresses. Vasarhelyi and Bobet (2000) have used the displacement discontinuity model, FROCK, to model crack initiation, propagation, and coalescence between two bridged flaws in gypsum under uniaxial compression. Their simulations reproduced the types of coalescence observed in the experiments, and they predicted an increase in coalescence stresses with increases in the bridged length. These inclusions have different shapes and stiffnesses, which affect the crack-tip field. The extent to which the near-tip field will be reduced or increased by the loading is dependent both on the stiffness difference between the inclusion and matrix and the inclusion geometry.

In most brittle and quasi-brittle materials such as concrete and rocks, damage evolution is typically attributable to nucleation, propagation, and

coalescence of microcracks. This process is very often anisotropic depending upon, for example, the loading history of external stresses. Several phenomenological and micromechanical damage models have been established for microcrack-weakened materials, for example Nemat-Nasser and Horii (1993), and Krajcinovic (1997).

To analyse and describe the fracture of various materials subjected to mechanical loads, various different methods have been developed. Among others, the Dugdale-Barenblatt (D-B) model, sometimes also referred to as the “cohesive strip model”, has proved its usefulness in many applications. Initially developed to consider the mode-I plane-stress crack problem of ductile materials (Dugdale, 1960; Barenblatt, 1962), the D-B model has been extended to many other cases, for example, mixed mode cracks, fatigue, creep, damage and interface cracks (Janson, 1977; Yu and Fan, 1992; Mou and Han, 1994; Zhang and Gross, 1994; Becker and Gross, 1988).

Janson (1977) first introduced the concept of continuous damage into the D-B model and considered the damage in a narrow plastic zone ahead of a crack tip. Yu and Fan (1992) modified Janson's model by assuming that there is a narrow damage zone and a narrow plastic zone ahead of the crack tip. Adopting a damage model based on the hypothesis of incremental complementary energy equivalence, Mou and Han (1994) calculated the damage distribution near a crack tip. Zhang and Gross (1994) investigated a cohesive damage zone model of the D-B type for a mode-III crack in a power-law hardening material. Andersson (1977) presented a cohesive damage model consisting of a row of voids developed ahead of a

macrocrack tip to simulate the extension of the crack. For quasi-brittle materials, Feng and Yu (1995) investigated the effect of damage on fracture behaviour at a crack tip. It was pointed out that analogously to the plastic strip in a metal sheet (Dugdale, 1960); a fracture process zone is formed ahead of the crack tip in a solid.

As was mentioned above, coalescence of microcracks always occur in a quasi-brittle material before a fatal macroscopic crack forms. However, investigations on the coalescing process of microcracks are still very limited. In this chapter, the coalescence of interacting multiple collinear flaws in a rock is studied by using the analysis method of the Dugdale-Barenblatt model. As is usual for tensile failure, wing cracks at the end of the pre-existing flaw diminish their effects and become flatter in the case of randomly distributed flaws (Al-Ostaz and Jasiuk, 1997).

4.3 INITIAL FLAW FOR CRACK INITIATION AND BINOCULAR MICROSCOPE OBSERVATIONS

Micromechanical modelling of instability, mainly in underground mining, followed the development of analytical and computational fracture mechanics during the last four decades (Cherepanov, 1998), which allowed the understanding of the mechanisms and consequences of fracture initiation and growth. Observations of failure in physical experiments with cavities in brittle rocks (Santarelli and Brown, 1989; Ewy and Cook, 1990; Haimson and Song, 1993, 1998; Okland and Cook, 1998) suggest two main failure modes depending on the rock

microstructure: (a) microcrack accumulation; and (b) extensive fracture growth. A number of micro-mechanical models have been proposed with respect to these mechanisms. Shen et al. (1997) considered shear fracture development on the basis of the growth criterion that they had introduced prior to their work (Shen et al., 1993; Shen et al., 1994). Zheng et al. (1989) and Zheng (1998) considered borehole cross-section evolution based on a specially developed numerical scheme that mimics fracture of rock structural elements (spalls or chips).

Similarly, a number of works have considered buckling of layers (pre-existing or formed due to crack growth) as the main mechanism of borehole instability. These models were based on the micro-mechanical parameter of layer thickness, although the question of the layer appearance was usually left aside. This approach originated in composite mechanics for modelling delamination in compression (Kachanov, 1988) and is based on identifying the failure stress required for buckling of a thin surface layer of compressed material. In rock mechanics, this approach was adopted by Germanovich (1984, 1997) for modelling thermal spalling. Ortlepp and Stacey (1994), Bazant and Xiang (1997), van den Hoek et al. (1994) and Vardoulakis and Papamichos (1991) implemented the buckling approach for modelling rockbursts and breakouts. Although from different positions, Papamichos and Vardoulakis (1989) and Dyskin and Germanovich (1993) considered the coupling effect of surface instability and normal traction applied to the body surface and/or to the sides of the crack parallel to the surface. Bazant et al. (1993) proposed a model of borehole instability

based on simultaneous buckling of a package of layers of equal length. Bazant and Xiang (1997) subsequently used this approach to model shear bands consisting of slim columns (beams) between the locally growing cracks. Their approach seems to be adequate in the case of pre-existing layers with weak or no inter-layer cohesion.

Several authors have studied the influence of grain size on rock strength. Hugman and Friedman (1979) have shown that ultimate strength is inversely proportional to mean grain size in carbonate rocks such as limestones and dolomites. Olsson (1974) has also observed this trend in marble and has shown that the stress difference at failure is linearly proportional to the inverse square root of the mean grain size ($d^{-1/2}$). He suggested that the Petch theory (Petch, 1953) on the relation between yield stress and grain size in metals is also valid in polycrystalline aggregates, such as carbonate rocks. Fredrich et al., 1990, later confirmed a Petch relation in a variety of carbonate rocks of varying mean grain sizes.

It is commonly assumed that mean grain size in crystalline rocks (Fredrich at al., 1990; Wong et al., 1995) is a good measure of the initial Griffith flaw size in the material. With remote stress application, stress concentrations develop at the tips of the flaws, and maximum concentrations evolve at the crack tips, which are inclined at a critical angle with respect to the principal stress axes. Hatzor and Palchik (1997) have shown in heterogeneous dolomites that grain boundaries function as initial Griffith flaws

(Griffith, 1921; Bieniawski, 1967) in low-porosity rock (porosities ranging between 3-4%).

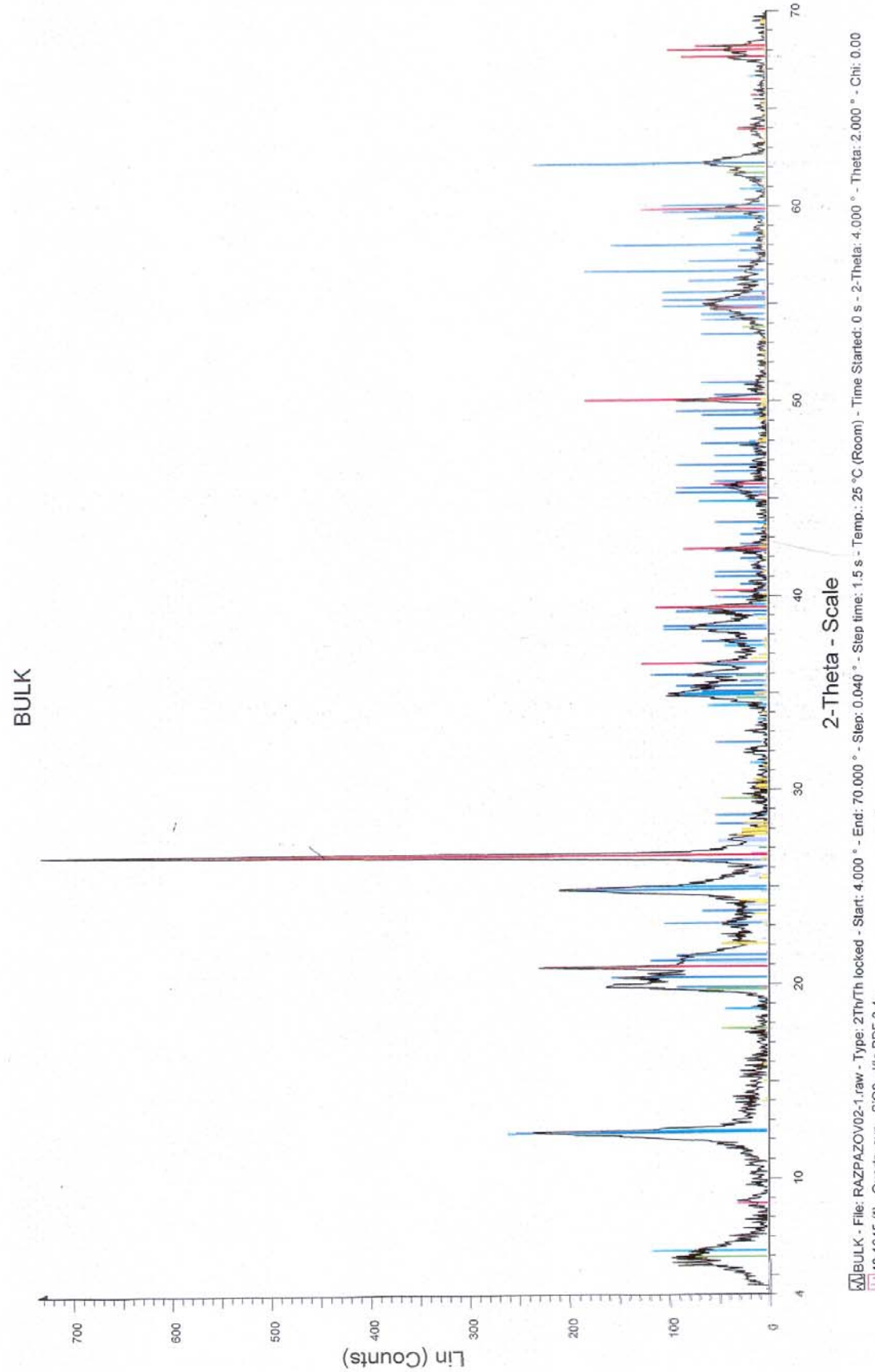

Figure 4.1 Example X-ray analyses of a shale specimen, showing the polymineralic character of the rock

X-ray analyses (Figure 4.1) of a shale specimen were conducted by the author to define minerals involved in the embedded shale layer. It was shown that the inclusion minerals, which form part of the investigated shale structure, are mainly quartz grains and carbon flakes, distributed in a mudstone matrix consisting of montmorillinite, kaolinite, muscovite, microcline and albite.

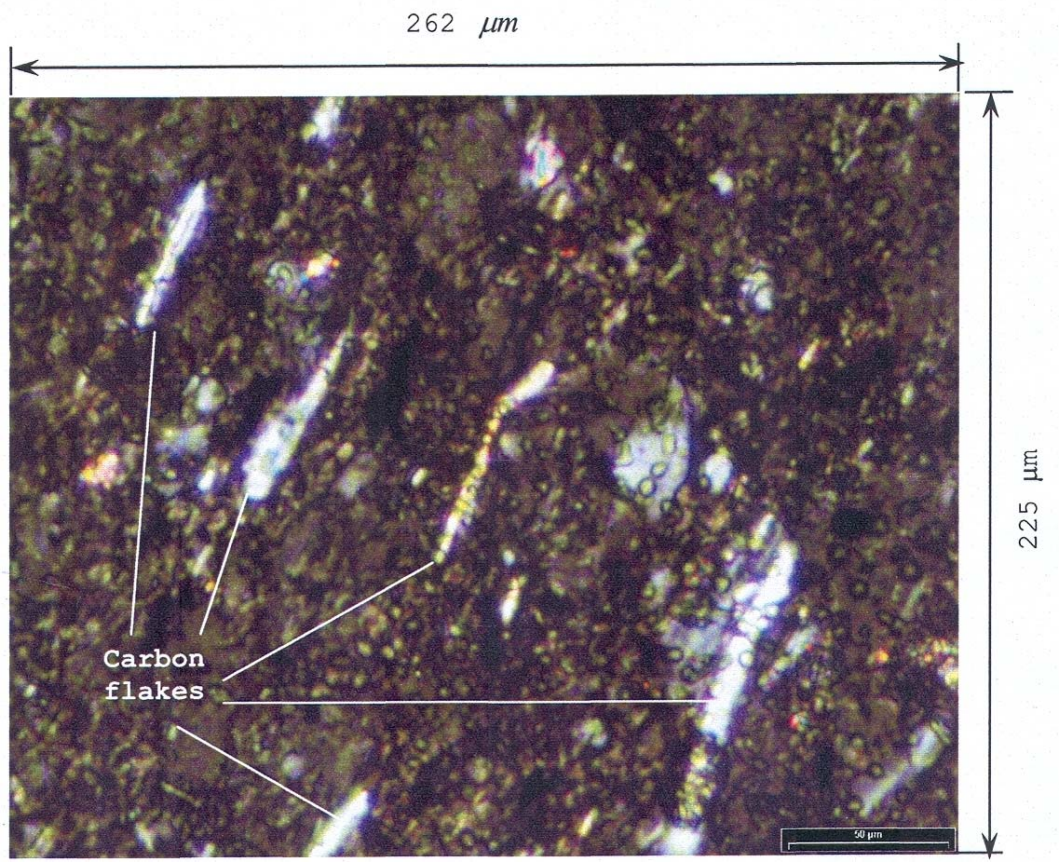

Picture 4.1
Symmetrically distributed carbon flakes in the shale specimen

For the detailed microscope measurements, thin sections of the shale layer were prepared. Of prime interest was the orientation of the carbon flakes in relation to the limb and highwall position. For these reasons an orientated diamond drill core of a shale layer situated

on the limb of an undulated strata formation was taken. The thin sections of shale specimens were cut parallel to the sedimentation and glued to the thin glass plates. After this, the glued shale material was polished to the thickness of about 30 μm and studied under a binocular microscope.

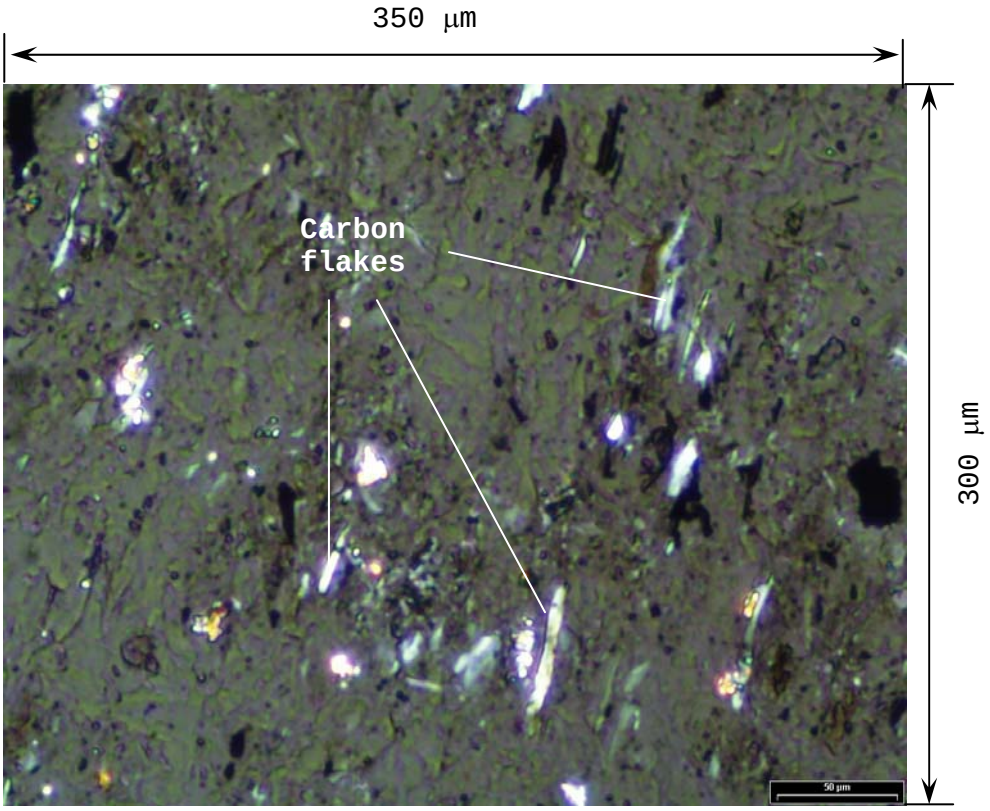

Picture 4.2

Carbon flakes with a length of between 8 μm and 21 μm

It was estimated that carbon flakes are parallel to sedimentation and symmetrically distributed in relation to each other (Picture 4.1) with an orientation almost normal to the highwall position and parallel to the limb inclination. As the flake lengths vary between 40 μm (Picture 4.2) and 110 μm (Picture 4.3), the average length was calculated to be 66 μm. The average thickness of the carbon flakes was measured at 5 μm.

The distance between the neighbouring flakes varies between 60 μm and 120 μm, with an average distance of 85 μm.

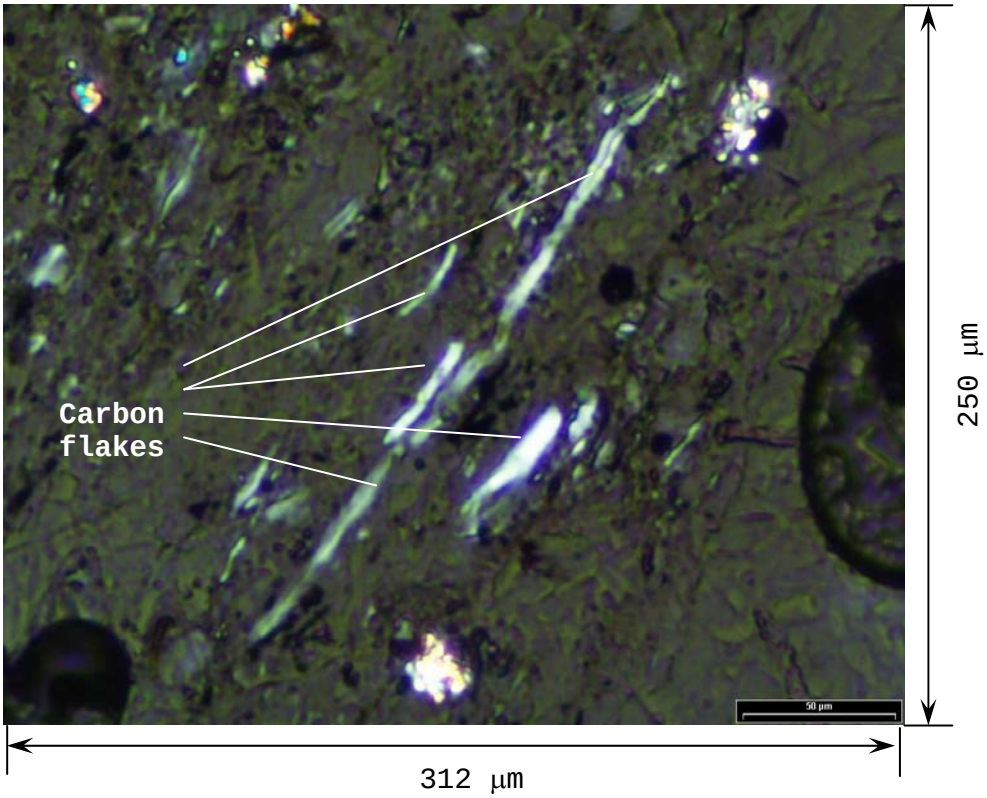

Picture 4.3

Carbon flakes with a length of between 30 μm and 190 μm

The second most common inclusion mineral in the shale is quartz, shown in Picture 4.4. It was estimated that average diameters of quartz grains are approximately 40 μm and that they are distributed randomly through the matrix at distances of between 110 μm and 230 μm apart. Hatzor and Palchik (1997) investigated the influence of grain size and porosity on crack-initiation stress and concluded that crack-initiation stress decreases from low porosity-high grain size to high porosity-high grain size. Their assumption of the

sliding crack mechanism in polycrystalline aggregates leads to the expectation that crack initiation and ultimate stress are linearly related to the inverse square root of the mean grain size, since existing grain boundaries are assumed to function as initial flaws, and therefore as stress concentrators (Petch, 1953). The longer the initial crack, the higher stress concentration and, therefore, the lower the remote stress level required for fracture initiation.

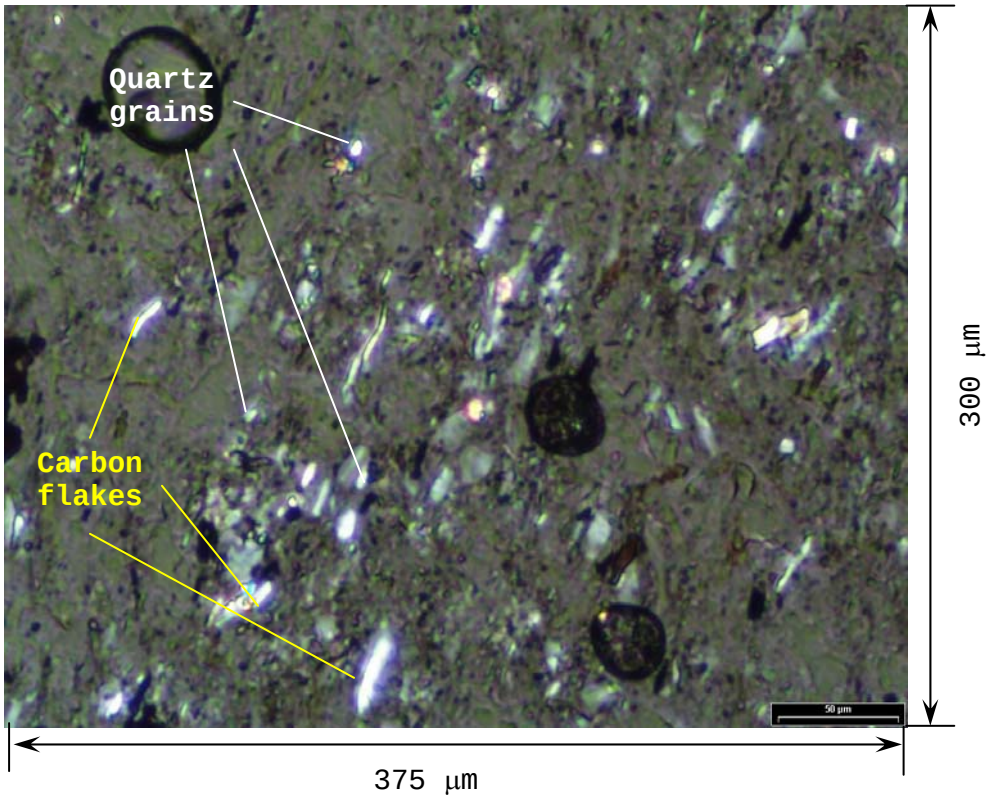

Picture 4.4

Carbon flakes and quartz grains in muddy matrix

4.4 MODE OF INTERACTION

As we observed, the carbon flakes and the quartz grains follow a certain loose order of distribution. As the most frequently seen inclusions in the shale thin sections, they definitely play an important role in the fracture-propagation process. It is assumed that the crack-inclusion separation and the size of the inclusion are small compared to the crack length, the outer end of which can be seen in every slope face. In the previous section we observed that the most common inclusions (carbon flakes and quartz grains) have different shapes, and will have different elastic moduli, to each other and the mud matrix. On the basis of smaller Poisson's ratio variations in rock and for model simplicity, it is assumed that the Poisson's ratios are the same and that the bonding between matrix and inclusions is perfect. Therefore, the crack is subjected to a remotely induced tensile stress field (see Chapter 3) specified by the applied stress-intensity factor, K_0. The near-tip field has the same classical form but its stress intensity factor, K_{tip}, is different, affected by nearby inclusions and the difference has the form of:

$$\Delta K_{tip} = K_{tip} - K_0. \qquad (4.1)$$

If we take into account the stress intensity factor for a single crack in a tensile stress field perpendicular to the crack line (Whittaker et al., 1992):

$$K = \sigma\sqrt{\pi c} \qquad (4.2)$$

where K is the stress intensity factor, σ is applied stress and c is the half of the crack length, then we can write Equation 4.1 as:

$$\left(\sigma_0 + \Delta\sigma_{tip}\right)\sqrt{\pi c} = \sigma_{tip}\sqrt{\pi c} \tag{4.3}$$

where the symbols σ_0, σ_{tip} and $\Delta\sigma_{tip}$ are the remote induced tensile stresses, the near-tip tensile stress, and the difference between them respectively. We can further simplify Equation 4.3 to:

$$\sigma_0 + \Delta\sigma_{tip} = \sigma_{tip} \tag{4.4}$$

where a negative value of $\Delta\sigma_{tip}$ predicts a toughening increment due to the shielding effect of the inclusions, and a positive $\Delta\sigma_{tip}$ means a weakening effect.

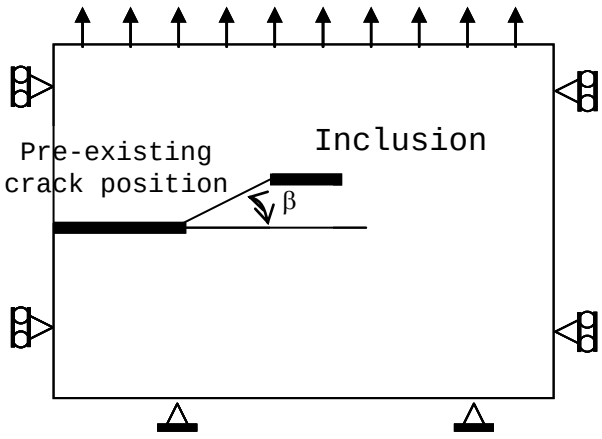

Figure 4.2
Applied boundary and stress conditions of the FLAC model for pre-existing crack and inclusion interactions (not to scale)

To investigate the interaction inclusions should have with an existing crack, the sizes of quartz grains and carbon flakes, discussed above, were taken into account. The microscope observations show that the angles between three carbon flakes and three quartz grains are not more than 12^0 and 15^0 respectively, shown by β in Figure 4.2.

FLAC was used for near-tip stress determination (model shown in Figure 4.2). Input values appear in Table 4.1, where the elastic moduli for the mudstone matrix and carbon flakes respectively come from van der Merwe (1998) and Markgraaff (1986). Both inclusion types were modelled at horizontal distances of 50, 100, 150, and 200 μm from the crack tip, while the angle β between the pre-existing crack plane and the inclusion centre-line, varies from 0.5^0 to 16^0.

Table 4.1 Input values for quartz grains and carbon flakes

	Mudstone matrix	Quartz grain	Carbon flake
Elastic modulus – E, GPa	7	70	4
Poisson's ratio - ν	0.25	0.25	0.25
Radius – R, μm	-	20	-
Length/width – l/W, μm	-	-	66/5
Distance from the cr. tip, μm	100, 150, 200 and 250		

In the models, the maximum zone length: width ratio of 10 was used to model the elongated shape of the cracks and carbon flakes. Taking this into account, the half crack was modelled by null zones. The pre-existing crack length was assumed to be 60 times the length of the carbon flake.

As the inclusion size is in the range of microns, the entire FLAC model was given dimensions of 1000 μm by 1000 μm (1 by 1 mm). The far-field stress was modelled with an applied pressure at the top boundary, normal to the X-axes and with a negative sign (to simulate tensile conditions). The inclusion position was modelled as defining certain zones into the model with the inclusion's properties, as shown in Table 4.1. The boundary conditions and the applied load are shown in Figure 4.2.

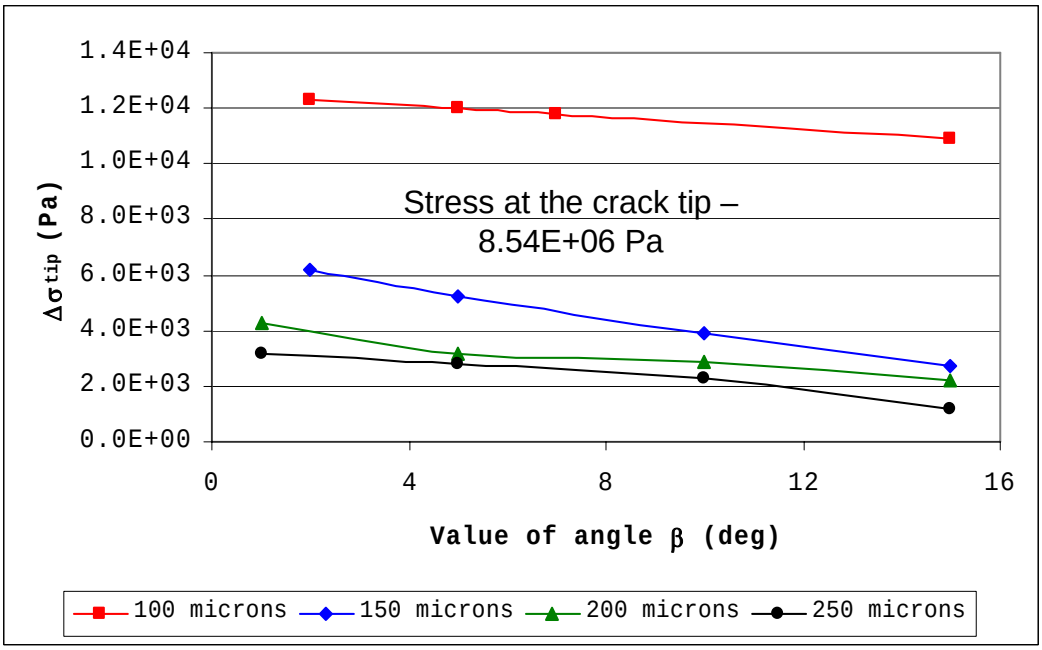

Figure 4.3

$\Delta\sigma_{tip}$ changes at the crack tip with carbon flake inclusions, according to the value of angle β and distance from pre-existing crack tip

Figures 4.3 and 4.4 present a plot of the FLAC model results for the $\Delta\sigma_{tip}$ interaction between the crack tip and carbon flakes and quartz grains respectively. These figures show only the results regarding the position of

the inclusions above the crack plane. If the inclusion is below the crack plane, the calculated stress difference is slightly lower compared to the inclusion's position above the plane. This difference can be explained by body forces in the material, but in both cases the stress difference ($\Delta\sigma_{tip}$) has the same sign.

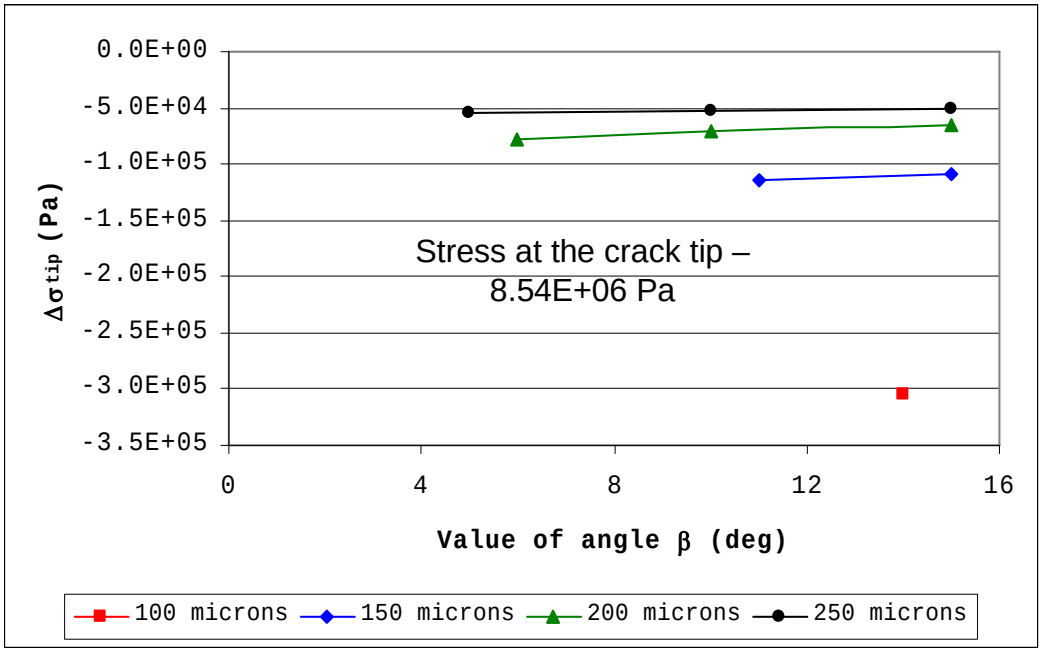

Figure 4.4

$\Delta\sigma_{tip}$ changes at the crack tip with quartz grain inclusion, according to the value of angle β

It can be seen (Figure 4.3) that all calculated results are positive and we can say that the carbon flakes weaken the mudstone matrix. In the figure, $\Delta\sigma_{tip}$ decreases with the increase in distance between the near flake end and the crack tip. From the all-modelled flake positions, $\Delta\sigma_{tip}$ has a maximum value at the lowest angle β in relation to the crack plane. These analyses are confirmed by the shale anisotropy, where

the elastic modulus normal to bedding is lower than the modulus parallel to bedding.

The quartz grains toughen the crack tip by inducing a negative value for $\Delta\sigma_{tip}$. Crack tip strengthening is much higher when the grain is closer to the crack tip (Figure 4.4) and this effect appears independent of the angle β between the grain and the fracture plane for the distances and angles investigated.

Figure 4.5 presents $\Delta\sigma_{tip}$ variations when the carbon flake (Figure 4.5a) and quartz grain (Figure 4.5b) are co-linear and at different distances from the pre-existing crack tip. There is general agreement between Figures 4.3 and 4.4 and Figures 4.5, and we can conclude that the presence of carbon flakes in the matrix will encourage fracture propagation, while the quartz grains will impede fracture propagation.

Therefore, any fracture propagation due to the remote induced tensile stress condition will involve more–or-less collinear carbon flakes, which behave as if they were cracks. If carbon flakes are distributed in the matrix in such a way that lines joining them are less than 12^0 inclined to the overall direction of the flakes, the interaction effects described above remain significant. This finding is valid only for the defined average flake size and average distance between flakes.

(a)

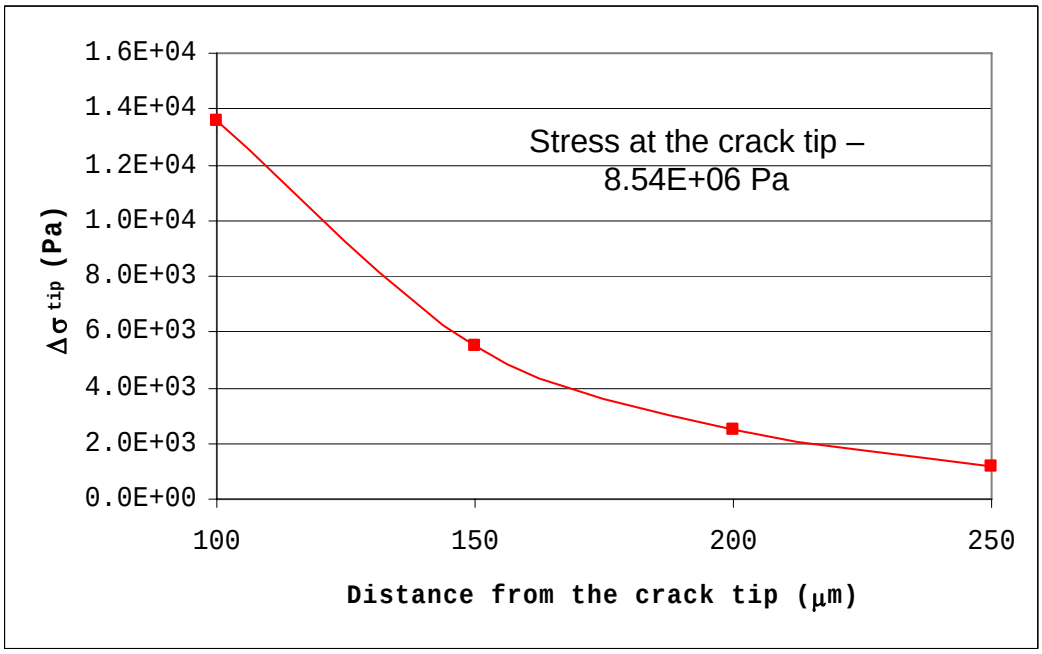

(b)

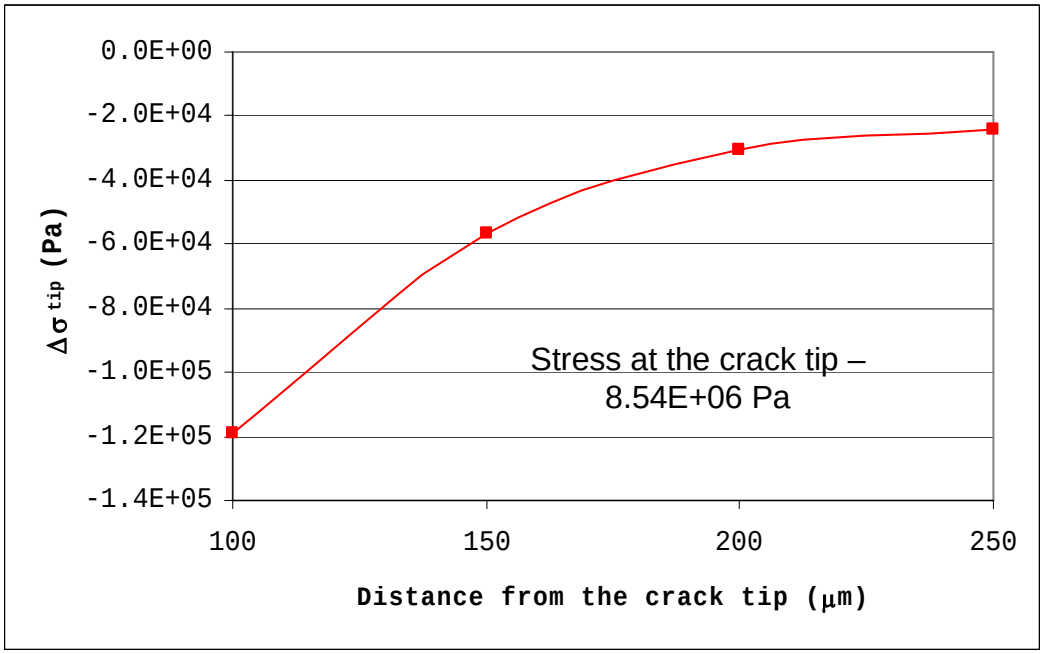

Figure 4.5

$\Delta\sigma_{tip}$ variation versus distance between the crack tip and a collinear carbon flake (a) and collinear quartz grain (b)

4.5 DEVELOPMENT OF SINGLE CARBON FLAKE-BASED CRACK MODEL FOR SHALE-COAL CONTACT

If the failure process is encouraged by the presence of carbon flakes in a mudstone matrix, then what remote stress condition has to be satisfied to induce the formation of a slip surface along the shale-coal contact? In this section, the general features and properties of cracks are gathered together into a simple crack model for the shale, and then this is extended to a row of collinear cracks in the next section.

Experimental observations suggest that one of the mechanisms of skin (strain) rockburst caused by tensile (splitting) fractures propagating, parallel to the major principal compressive stress direction (Fairhurst and Cook, 1966; Horii and Nemat-Nasser, 1985; Haimson and Herrick, 1986; Haimson and Song, 1993 and 1998; Van den Hoek et al, 1994 and Okland and Cook, 1998). These experiments refer to the splitting type of brittle fracture in compression, supporting a model in which a single crack extends, leading to failure. There are also observations which imply that there exist localized zones of multiple extensile cracks arising due to the interaction at the grain scale (Myer et al, 1992). These interactions result in an en echelon arrangement of growing cracks and might lead to structures characteristic for another common type of failure in compression, that is, oblique fracture (Germanovich et al, 1994). All these failures are more strain related and can not be explained with the stress-based criteria (e.g. Mohr-Coulomb, or Griffith). Stacey’s (1981) simple extension strain criterion for

fracture of brittle rock is empirical, as is the widely used criterion of Hoek and Brown (1980). Neither of these have any basis for general applications, unless there are observations and measurements to back an engineering judgement of failure. Failure criteria and their development lie beyond the scope of this thesis, and will not be considered any further. The author applies some fracture mechanics principles to achieve some practical results, in the hope of developing a plausible mechanism of fracture development along the shale – middle coal seam contact in the slope. This analysis begins first with a standard fracture mechanics approach, and then proposes a relaxation mechanism in a polyminerallic rock that could account for tensile failure even though the total stress state remains compressive.

In rocks, the crack-tip process zone is non-linear and is caused by the initiation and propagation of the microcracks in the immediate vicinity of the crack tip. Consequently, this zone is described as a microcracking zone, which appears and behaves in a similar way to the plastic zone in metals. It is actually a modification of Dugdale's (Dugdale, 1960) crack model originally developed for metals. Since there are no sound theoretical models available to fully describe the shape and size of the crack-tip fracture-process zone in rocks, the approximate models developed to describe the plastic zone in metals are often used.

Schmidt (1980) suggested a maximum normal stress criterion to describe the shape of the crack-tip fracture-process zone in rock. This criterion is based on the assumption that the formation of the fracture-

process zone takes place as a result of excessive tensile stress, i.e. when the local maximum principal stress in the vicinity of the crack tip reaches the ultimate uniaxial tensile strength of the rock. Thus

$$\sigma_1 = \sigma_t \tag{4.5}$$

where σ_t is the uniaxial tensile strength taken as positive to be consistent with the formulation of the crack-tip fracture-process zone.

It is known from the ISRM "Suggested methods for determining fracture toughness of rock" (Ouchterlony, 1988) that the testing results for fracture toughness generally should be corrected by a formula such as:

$$K_{IC} = \sqrt{\frac{1+p}{1-p}} K_q \tag{4.6}$$

in which K_q is the fracture toughness calculated using the linear elastic formula and p is a non-linear plasticity factor, which has been the subject of study of rock fracture toughness in recent years (Ouchterlony, 1988).

To calculate the plasticity factor, p, several unloading-reloading cycles must be conducted in the fracture-toughness testing process of rock according to the ISRM methods (Ouchterlony, 1988). The p factor represents the ratio of irreversible deformation and is calculated as shown in Figure 4.6:

$$p = \frac{\Delta\delta_i}{\Delta\delta_p} \tag{4.7}$$

It was found by experiment that the p factors for metal specimens were close to zero when their diameters were small (Barker, 1979). The p factors of rock specimens are typically larger than 0.10 (for coal – 0.32; sandstone – 0.28; quartz – 0.16; norite – 0.18, after Karparov, 1998). Because of the friability of the shale layer above the coal, it was not possible to obtain a reliable p factor in the laboratory. The p factor was found to be a constant for rock specimens with diameters over 30mm (Whittaker et al., 1992).

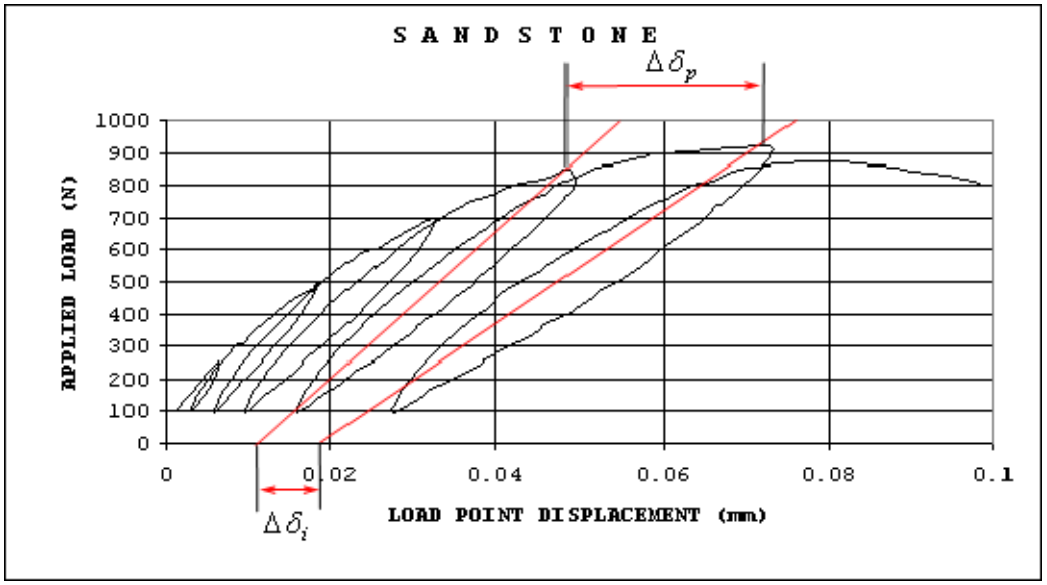

Figure 4.6
Calculation on plasticity factor "p" for sandstone specimen (after Karparov, 1998)

According to the micromechanical damage theories for brittle and semi-brittle materials (Krajcinovic, 1997; Nemat-Nasser and Horii, 1993; Dugdale, 1960; Barenblatt, 1962; Janson, 1977; Yu and Fan, 1992; Mou and Han, 1994; Zhang and Gross, 1994; Becker and Gross, 1988; Andersson, 1977; Xia et al, 1995; Feng and Yu, 1995), there exists a distributed damage zone around a

crack tip, where some microcracks that satisfy a specific growth criterion propagate in a stable manner.

The cohesive crack model is based on the assumptions made by Labuz et al. (1987), Ingraffea and Gerstle (1984), and Carpinteri et al. (1986). In general, the stress-strain relation of such a material can be divided into three stages: linear elasticity, plastic behaviour, and strain softening. In some papers (Bui and Ehrlacher, 1981; Bui et al., 1984; Hao et al., 1991), a completely damaged fracture process zone with a specific shape, and which cannot sustain any small stress, was assumed.

When the applied load reaches a limit value, damage will be localised in the direction perpendicular to the maximum principal stress. Once the damage localisation occurs, the stresses near the crack tip will be partly released. Instead of the completely damaged zone with finite sizes, therefore, the fracture process zone reflects some more realistic features of damage at the crack tip in rock. Moreover, less energy will be dissipated during the crack propagation with a fracture-process zone than with a completely damaged zone of a specific finite width (Feng and Yu, 1995).

The crack damage stress is generally referred to as the stress at onset of dilation. Until this stress level is reached, the rock volume decreases. When the crack damage stress has developed, the material volume begins to increase (Bieniawski, 1967; Schock et al., 1973; Brace, 1978; Paterson, 1978; Brady and Brown, 1993). Martin and Chandler (1994) and Eberhardt et al. (1999)

have used the term "crack damage stress σ_{CD}" and have shown that rocks become critically damaged at σ_{CD}, which is significantly lower than the failure stress.

Using an elastic-rapid damage model, for example, Bui and Ehrlacher (1981) obtained the solution of damage for a steady-state propagating crack shown in Figure 4.7b. Their solution is equivalent to the configuration of a steadily extending notch in an infinite sheet. Generally, the shape of the carbon flakes is not the same (see Figure 4.7a). Even if carbon flakes have a similar shape in their original state, they will not keep this shape during fracture initiation and propagation due to the chaotic microstructural disorder of grains in the rock matrix.

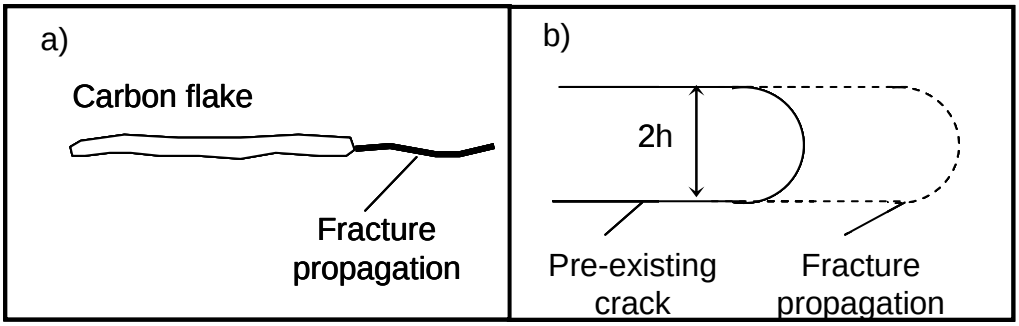

Figure 4.7
(a) Fracture propagation in the rock specimen from carbon flake, which behaves like a pre-existing crack; (b) Model of steady state fracture propagation after Bui and Ehrlacher (1981)

For the shale, a notional crack with an effective crack length is assumed equal to the average carbon flake length of 66μm. This effective crack length consists of a tensile free point (true crack length) and a length

of fracture-process zone over which a cohesive stress, tending to close the crack, is distributed. Such a hypothesis is often referred to as a "fictitious crack".

This study uses additional assumptions regarding the remote stress distribution over the grain boundaries and grain orientation, due to the bedding inclination on the undulated strata formation limb:

1. The carbon flake orientation is parallel to the bedding.
2. Taking into account flake size and stress changes in a slope profile, it is assumed that a remote tensile stress difference ($\Delta\sigma_N$) is a constant and is uniformly distributed over a large number of grains.
3. The material in the fracture-process zone is partially damaged but still able to carry stress $\sigma(x)$, which is transferred from one surface to the other of the rock, while the material outside the fracture process zone is assumed linearly elastic.
4. The fracture process zone starts to develop when the stress difference $\Delta\sigma_N$ normal to bedding reaches the tensile strength σ_t and the corresponding true crack-tip opening displacement δ_t is zero. With increasing δ_t, the stress is decreased until zero and the corresponding δ_t reaches a critical value δ_c. Such a phenomenon of decreasing stress with increasing deformation is known as strain-softening behaviour (Hilleborg, 1985) or tension-softening behaviour (Horii et al., 1987; Leung and Li, 1987).

5. The closing cohesive stress is a function of true crack-tip opening displacement δ_t, i.e. $\sigma(x)$, which is the Dugdale crack model where the closing cohesive stress $\sigma(x)$ is assumed to be a constant, having the value of the yielding strength.
6. The overall stress intensity factor at the notional crack tip no longer exists, i.e. the stress singularity at the notional crack tip disappears.

To determine conditions favourable for crack propagation, it is essential to choose an appropriate fracture parameter and thereby to establish an applicable fracture criterion (see Figure 4.8). Before loading, the crack length is $2a$. From the above discussion, it can be seen that damage localisation occurs ahead of the two tips of the crack in tension.

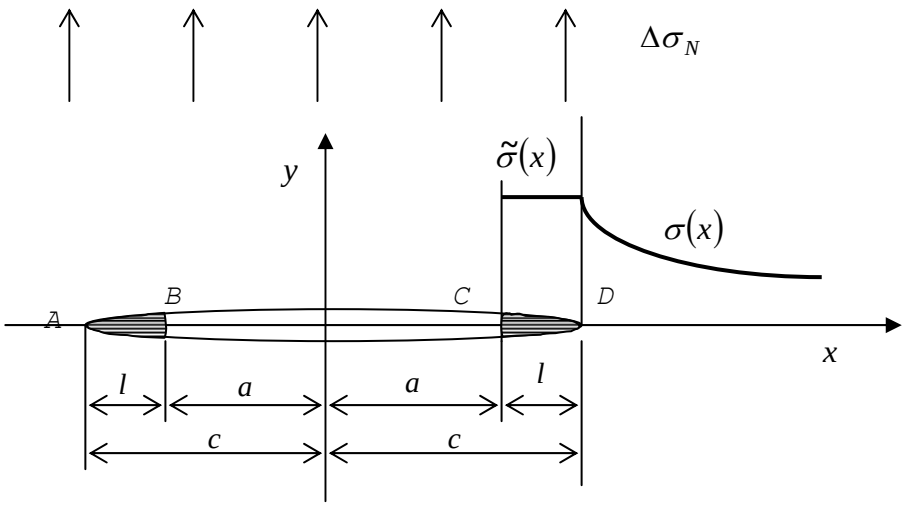

Figure 4.8
Fracture-process zone localisation of a flaw under tension

The material in the fracture-process zone experiences a stress drop and strain softening but still has a

certain amount of residual strength to maintain the stresses. Thus, the equivalent crack length is $2c = 2(a+l)$ with l denoting the length of the fracture-process zone. The normal stress in the ***y*** - direction along the ***x*** - axis is expressed as:

$$\sigma_{yy} = \begin{cases} \tilde{\sigma}(x) & (a \le x \le c) \\ \sigma(x) & (x > c) \end{cases} \qquad (4.8)$$

The compatibility condition of deformation requires at x=c that $\tilde{\sigma}(c) = \sigma(c)$, that is, the stress $\Delta\sigma_N$ is continuous. In D-B models, the material-specific decreasing tensile stress versus the increasing displacement difference between the zone faces usually characterises the cohesive damage zone. According to Schmidt (1980 – given in Equation 4.5), it will be assumed that the tensile stress remains constant at the value σ_{tt}, equal to the strength σ_t within the cohesive zone, that is,

$$\tilde{\sigma}(x) = \sigma_t \qquad (a \le x \le c) \qquad (4.9)$$

Under the external tensile stress $\Delta\sigma_N$ (discussed in Chapter 3), the stress intensity factor of the equivalent crack with length $2c$, Equation 4.2 can be written by analogy as:

$$K_I^N = \Delta\sigma_N \sqrt{\pi c} \qquad (4.10)$$

By requiring that the stress intensity factor at the fictitious crack tips ($x = \pm c$) disappears, that is,

$$K_I^N + K_I^D = 0 \tag{4.11}$$

In the linear elastic fracture mechanics, the stress intensity factor is often adopted as the control parameter for determining the crack propagation. Then, the fracture criterion for a mode-I crack is

$$K_I^N = K_{IC} \tag{4.12}$$

with K_{IC} being the matrix fracture toughness. For a crack of length $2a$ in an infinite plate under an external tensile stress (Figure 4.8), the critical stress corresponding to the crack propagation is obtained as

$$\sigma_N^c = \frac{K_{IC}}{\sqrt{\pi a}} \tag{4.13}$$

The fracture criterion given by Equation 4.12 has been extensively used (Broek, 1996; Kanninen and Popelar, 1985). The corresponding fracture criterion takes the form

$$l = l_c. \tag{4.14}$$

4.6 PERIODIC COLLINEAR CRACK MODEL FOR SHALE-COAL CONTACT

The following problem to be considered is that of a periodic row of co-linear carbon of equal length $2a$ (the length of the average flake) in an infinite space subjected to a remote induced tension, $\Delta\sigma_N$ (discussed in Section 3.8), and shown in Figure 4.9.

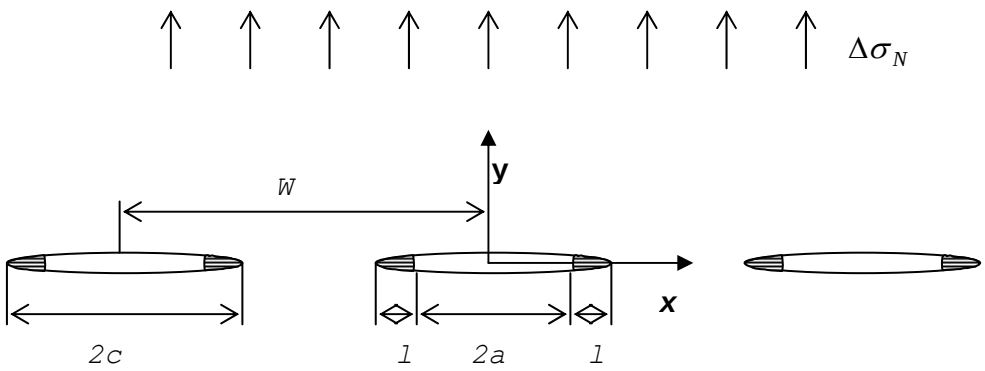

Figure 4.9
Simplified model of a periodic row of collinear carbon flakes in shale

The stress intensity factor at each flake tip caused by the remote induced tension is (Tada et aI., 1985).

$$K_I^N = \Delta\sigma_N \sqrt{W \tan\frac{\pi c}{W}} \qquad (4.15)$$

where $c = a + l$ denotes the half-length of the equivalent flakes, and l the length of the fracture process zone. When each flake is subjected to two pairs of symmetrical concentrated forces, $-\sigma_t d\xi$, normal to the crack surfaces and acting at $x = \pm\xi$, the stress intensity factor at each crack tip is (Tada et al., 1985)

$$dK_I^D = -2\sigma_t\, d\xi \cos\frac{\pi\xi}{W}\sqrt{\frac{1}{W}\tan\frac{\pi c}{W}}\left[\left(\sin\frac{\pi c}{W}\right)^2 - \left(\sin\frac{\pi\xi}{W}\right)^2\right]^{-\frac{1}{2}} \qquad (4.16)$$

By integration (see Appendix 1 – A1.3.1), the stress intensity factor induced by the stress σ_t in all the fracture-process zones is:

$$K_I^D = -2\sigma_t \sqrt{\frac{1}{W}\tan\frac{\pi c}{W}} \int_a^c \cos\frac{\pi\xi}{W}\left[\left(\sin\frac{\pi c}{W}\right)^2 - \left(\sin\frac{\pi\xi}{W}\right)^2\right]^{-\frac{1}{2}} d\xi$$
$$= -\sigma_t \sqrt{W\tan\frac{\pi c}{W}}\left[1 - \frac{2}{\pi}\arcsin\frac{\sin(\pi a/W)}{\sin(\pi c/W)}\right]. \qquad (4.17)$$

Substituting Equation 4.15 and 4.17 into the finiteness condition of Dugdale:

$$K_I^N + K_I^D = 0, \qquad (4.18)$$

the length of the fracture-process zone is obtained as (see Appendix 1 – A1.3.2)

$$l = \frac{W}{\pi}\arcsin\frac{\sin(\pi a/W)}{\cos(0.5\pi\,\Delta\sigma_N/\sigma_t)} - a. \qquad (4.19)$$

With an increase in $\Delta\sigma_N$, the length of the fracture process zone increases. We can use again Equation 4.13 to calculate the critical fracture process zone length in the case of a periodic row of flakes. Then Equation 4.19 will have the form of

$$l_c = \frac{W}{\pi}\arcsin\frac{\sin(\pi a/W)}{\cos\left(\frac{K_{IC}}{2\sigma_t}\sqrt{\frac{\pi}{a}}\right)} - a \qquad (4.20)$$

From Equation 4.20 and the fracture criterion – Equation 4.14 - the critical stress of $\Delta\sigma_N$ corresponding to the crack propagation is arrived at (see Appendix 1 – A1.3.3):

$$\sigma_N^p = \frac{2\sigma_t}{\pi} \arccos \frac{\sin(\pi a / W)}{\sin[\pi(a + l_c)/W]}. \qquad (4.21)$$

Once $\Delta\sigma_N$ reaches σ_N^c, the collinear flaws propagate and begin to coalesce as a result.

It is also seen that when the length of the collinear flaws is bigger than the characteristic value

$$a_c = \frac{1}{2}W - l_c \qquad (4.22)$$

the collinear flaws may also coalesce due to the linking of two fracture-process zones, even though $\Delta\sigma_N < \sigma_N^L$. Therefore, another condition for flaw coalescence is:

$$2c = 2a + 2l = W \qquad (4.23)$$

Substituting Equation 4.19 for Equation 4.23 leads to the critical tensile stress of the fracture-process zone linking as follows (see Appendix 1 – A1.3.4):

$$\sigma_N^L = \sigma_t \frac{(W - 2a)}{W}. \qquad (4.24)$$

For a periodic array of collinear flaws of equal length in an infinite sheet, thus, the stress of flaw coalescence is:

$$\sigma_N^p = \begin{cases} \dfrac{2\sigma_t}{\pi} \arccos \dfrac{\sin(\pi a / W)}{\sin[\pi(a + l_c)/W]} & \text{for } a < a_c \\ \sigma_t \dfrac{(W - 2a)}{W} & \text{for } a > a_c \end{cases} \qquad (4.25)$$

Up to now, we have worked in the field of elasticity. The calculated critical tensile stress has to be corrected with a plasticity indicator (Equation 4.6) to be applicable to the ductile properties of most sedimentary rocks. Hence, from Equation 4.13 we can write:

$$K_{IC} = \Delta\sigma_N^P \sqrt{\pi a} \tag{4.26}$$

Combining Equations 4.26 and 4.6 we have:

$$K_q \sqrt{\frac{1+p}{1-p}} = \Delta\sigma_N^P \sqrt{\pi a} \tag{4.27}$$

and consequently

$$K_q = \frac{\Delta\sigma_N^P}{\sqrt{\frac{1+p}{1-p}}} \sqrt{\pi a} \tag{4.28}$$

Then Equation 4.25 can be rewritten in the same form by analogy as dividing the tensile strength (σ_t) by the coefficient $\sqrt{\frac{1+p}{1-p}}$. Hence, Equation 4.25 will have the form of:

$$\sigma_N^p = \begin{cases} \dfrac{2\sigma_t}{\pi\sqrt{\frac{1+p}{1-p}}} \arccos \dfrac{\sin(\pi a / W)}{\sin[\pi(a + l_c)/W]} & \text{for } a < a_c \\ \dfrac{\sigma_t}{\sqrt{\frac{1+p}{1-p}}} \dfrac{(W - 2a)}{W} & \text{for } a > a_c \end{cases} \tag{4.29}$$

These equations are applied to the carbon flakes in the mudstone matrix in the following Section.

4.7 DETERMINATION OF THE CRITICAL TENSILE ZONE LENGTH ALONG THE UPPER AND BOTTOM SHALE CONTACT SURFACES

In Chapter 3 (Figure 3.9) we calculated the normal stress difference ($\Delta\sigma_N$) along the failure surface. In this chapter (Section 4.3) we estimated the average length of carbon flakes ($66\,\mu m$) and the average distance between them ($85\,\mu m$). Hence, we are in a position to calculate the magnitude of the critical tensile stress for fracture propagation in terms of $\Delta\sigma_N$ along the potential failure plane. Because of the flaky quality of the shale under study, it was impossible to drill an intact core for the Mode-I stress intensity factor (K_{IC}) estimation. For this reason in the following calculations, the author accepts experimental results by Schmidt (1977), Bhagat (1985), and Atkinson (1987) for the shale stress-intensity factor, K_{IC}=$0.94\,MPa-m^{-1/2}$ and plasticity indicator, p = 0.33. Then, the critical fracture-process zone for the periodic crack row has the length $l_C = 4.91\mu m$ (Equation 4.20).

If we compare the critical half carbon-flake length ($70.1\,\mu m$ - Equation 4.22) with the average measured flake half length ($33\,\mu m$) then tensile fracture propagation is the result of the remote applied tensile stress. After Equation 4.29, we calculate the critical tensile stress $\Delta\sigma_N^P = 0.210MPa$ for the periodic row of flakes for the shale. Figures 4.10 and 4.11 present the plot of the stress normal to bedding and the

critical (σ_N^P) tensile stresses of the embedded shale layer in the upper and the bottom contact surfaces. The stress state shown in Figure 4.11 is the same as in Figure 3.21.

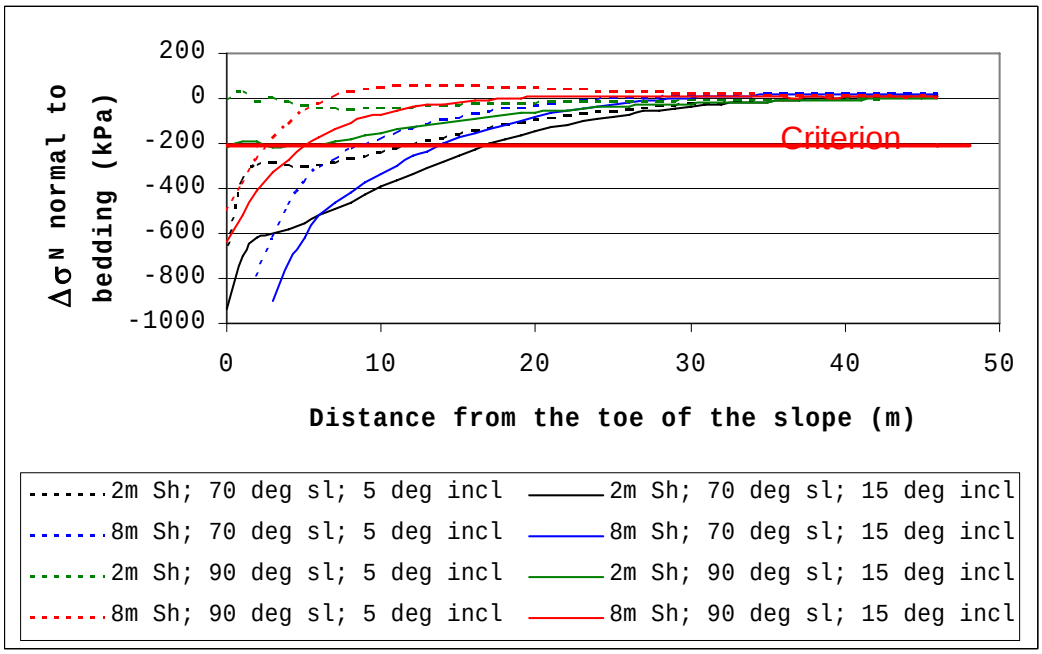

Figure 4.10

Critical tensile stress value - σ_N^P (bold red line), with the stress differences normal to bedding at the upper shale contact

Figure 4.10 shows for the upper shale contact that only the vertical slope with 2m-thick embedded layer dipping at 5^0 does not have the conditions for tensile fracture propagation due to the $\Delta\sigma_N$ value. The bottom contact is affected by $\Delta\sigma_N$ in slope profiles with a 15^0 inclination. This encourages the growth of a tensile crack along the coal-shale contact. The modelled tensile fracture lengths appear in Table 4.2.

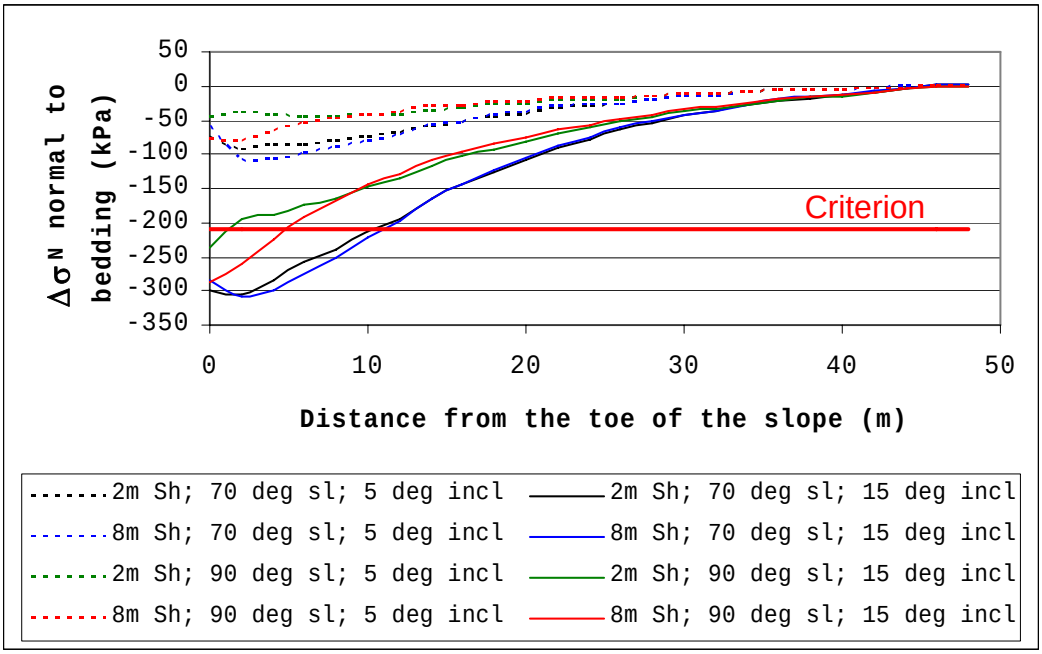

Figure 4.11

Critical tensile stress value - σ_N^P (bold red line) with the stress differences normal to bedding at the shale-middle coal seam contact

Table 4.2 Potential Lengths of the tensile fractures along the contact surfaces between the embedded shale layer with the overburden and the bedrock

	Slope angle (^{0})	5^0-limb inclination		15^0-limb inclination	
		2m thick	8m thick	2m thick	8m thick
Top contact	70	12m	8m	16m	14m
	90	0m	4m	6m	6m
Bottom contact	70	0m	0m	12m	12m
	90	0m	0m	2m	6m

The tensile fracture zone along the top contact surface is longer than that along the bottom contact surface. This is the result of the higher relaxation at the upper shale contact compared to the lower shale contact. For better visualisation, the lengths of the tensile fracture zones along the top and bottom contact surfaces can be seen in Table 4.2, which show that the slope profile with flatter slope angle creates longer tensile zones compared to the profile with steeper slope angle. This may explain why the major failure in Colliery – A1 took place after the minor failure, which had resulted in a reduction of the slope angle (see Chapter 1).

4.8 DISCUSSION AND CONCLUSIONS

The following conclusions can be drawn from the attempt to explain the genesis of the failure surface along the shale – middle coal seam contact that has been observed in all three major slope failures at the coal mine. Firstly, failure processes in solids are not well understood, and although the fracture mechanics approach has produced some excellent results, it is still unable to completely explain failure in rock. This study has approached the problem of determining if there is a possibility of generating a tensile failure surface close to, or on the bottom shale contact with the coal, in a stress regime in which the stress normal to the surface remains compressive, after there is a net relaxation as the slope is cut.

There are two points of interest concerning the development of the failure surface:

- Excavations in deep level mines become unstable once the surrounding stress has been relaxed for whatever reason (this is called unravelling), but the failure surfaces had already formed prior to the relaxation, and not during the relaxation;
- The shale thin sections were taken from the body of the shale, and not on the shale-middle coal seam contact itself, where in all likelihood, carbon flake density and alignment are likely to be increased and more consistent respectively, thereby reducing the critical tensile stress required to produce tensile failure, according to the above analysis.

The failure could conceivably start at the slope toe where stress relaxation is total, and then progress into the slope interior along the bottom contact in a mixed-mode fashion. This is perhaps more likely because the strata inclination is important: significant collapses have only taken place on limb inclinations of approximately 15°. Post-collapse observations have not been able to determine whether the failure surface formed in tensile, shear, or mixed-mode fashion, because shear displacement took place along it in all cases during the slope collapse.

Some of the outcomes in this chapter provide valuable insights, and are listed below:

- Carbon flakes weaken the mudstone matrix, and because of their weaker properties compared with the other minerals, must be involved in the genesis of the failure surface.

- As a result, we can define two regions on the failure surface: the first, where failure by whatever mechanism has developed (probably from the toe into the slope), and which is defined as the frictional region; the second, which lies beyond the first, where the normal stress relaxation is too small to permit further fracture growth, and this is called the cohesive region.
- The frictional zone length has an inverse relationship with the slope angle, i.e. it extends further into the slope interior for flatter slope angles than for steeper slope angles.
- The frictional zone length will be related to the limb inclinations, the limb lengths, and pore water pressure.
- A stress-based failure criterion has been used, but this fails because the net vertical stress remains compressive. A strain-based criterion would perhaps be more successfully applied in this case, and research to determine a suitable criterion should be initiated.

Even though this study has not been able to determine the failure mode absolutely, a fracture mechanics approach shows that even partially aligned carbon flakes will weaken the shale at the shale-middle coal seam contact, encouraging the formation of a failure surface along this contact, whose stability will ultimately depend purely on friction. No attempt was made in the analyses to predict how quickly such a failure surface will form after the mining slope has been cut. Although there are no records at the mine detailing time-spans between slope creation and slope

failure, best estimates based on experience range between two to four months (Mattushek, 2005).

The mode of fracture formation is also not detectable from the exposed failure surfaces, because subsequent slip of the overlying strata had taken place along them after the slopes had reached an unstable condition. The detailed nature of the fracture formation mechanism is not of critical importance to the outcome of the work, because we know from observation that the failure surface must form by whatever mechanism, either in part or all of the intervening period between slope formation and ultimate failure, or in the few instants before slope collapse. The actual mode and mechanism of failure surface formation continues to remain unknown, and fracture mechanics demonstrates that a stress-based approach is inappropriate.

The initial objective of this work was to explain why the accepted slope stability analysis methods were unable to predict the failures, and to produce a more reliable method of slope stability analysis in the conditions seen at the mine. In the following chapter, we accept that a failure surface grows in time along the shale-middle coal seam contact because the fracture analyses do not prohibit the formation of a fracture along the shale-middle coal seam contact, and DIGS modelling favours the formation of a fracture near the contact. Because of either progressive or sudden weakening of the contact, a sufficiently large frictional region must form to allow eventual slope collapse.

CHAPTER 5
PROPOSED THRUST FAILURE MECHANISM FOR SLOPE STABILITY ANALYSES IN COMPLEX GEOTECHNICAL CONDITIONS

5.1 SUMMARY

In this chapter all the results of the observations, modelling, and fracture analysis come together to develop a thrust failure mechanism in which the failures in the coal mine are explained as completely as possible. The proposed mechanism is a blocky-type failure mechanism, and the blocks are defined by internal shear failures that link up with fracture formation along the shale – middle coal seam contact. These proposals agree very well with Boyd's (1983) observations on the formation of an active block boundary.

5.2 INTRODUCTION

The proposed failure mechanism is based on the polygonal failure surfaces theory by Kovari and Fritz (1978), Boyd's observations (1983 – Figure 1.1), Stead and Scoble (1983 – Figure 1.2), failure modes from Figures 1.4 and 1.5 and the shear stress analyses discussed in this chapter. From the literature it is known that sliding usually takes place on curved surfaces that can be modelled by concave-up polygonally–shaped surfaces. For such cases, Janbu (1954) and Morgenstern and Price (1967) have suggested practical methods of computation, according to which the unstable earth- or rock-mass is divided up into vertical strips or slices. The Kovari and Fritz (1978)

polygonal failure surfaces theory is based on certain assumptions regarding the distribution and slope of the internal contact forces, as well as the hypothesis of limit equilibrium. Their method is based upon the physical requirement that sliding on a polygonal surface is only possible kinematically if a sufficient number of internal shear surfaces can develop. For the sake of simplification, only continuous shear surfaces starting from the intersection lines of the polygon-sliding surface are assumed. Thus, as shown in Figure 5.1, the slide of a mass on three surfaces must be accompanied by at least two internal shear surfaces. For n external sliding surfaces ($n-1$) such interfaces are required.

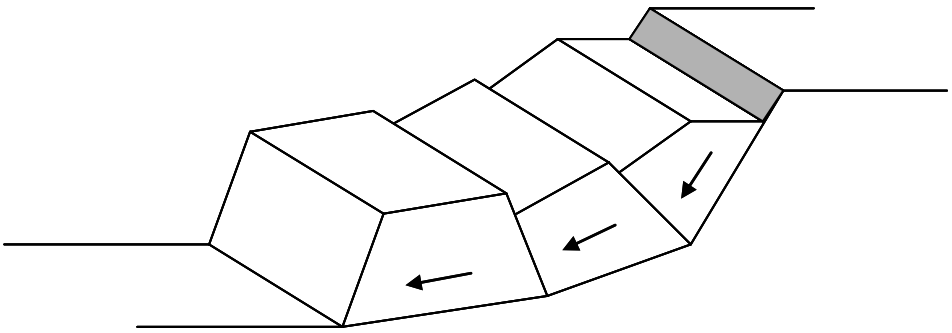

Figure 5.1
Kinematics of a slope failure for a polygonal sliding surface (after Kovari and Fritz, 1978)

The Kovari and Fritz (1978) method rests upon the following basic assumptions:

1. The blocks comprising the rock mass are each considered to be rigid.
2. The directions of the internal shear surfaces are known.

3. On the internal and external sliding surfaces (at the condition of limit equilibrium) the Mohr-Coulomb failure criterion applies, and no tensile strength is permitted. The strength parameters may be allocated different values on each sliding surface.

The direction of the internal shear surfaces is chosen from case to case on the basis of a careful investigation of the structure of the potentially sliding mass. However, for highly jointed rock, the directions of the internal slip surfaces are found by the condition of a minimum safety factor for the system. In an investigation of the stability of an earth dam, Sultan and Seed (1967) used a similar criterion.

The Kovari and Fritz (1978) method does not take into account the existence of complex geotechnical structure within the slope. It also ignores the formation of a tensile fracture behind the slope crest, which is a common feature in competent rock slopes. In their method, the internal failure surfaces are determined by careful field observation, which has an element of subjectivity introduced by observer experience.

The proposed thrust failure mechanism simplifies Kovari and Fritz's (1978) method by using only three failure surfaces as the investigated slope profile is divided into two block types: so-called "passive" and "active" blocks. The proposed method also takes into account the tensile fracture behind the crest of the slope.

5.3 DETERMINING SHEAR FAILURE ZONE DIRECTIONS IN THE SLOPE

Fracture development in rock is complex and remains poorly understood. In layered sedimentary rocks, opening-mode fractures have been observed to abut against bedding contacts (Baer, 1991; Narr and Suppe, 1991; Gross et al., 1995; Becker and Gross, 1996; Ji and Saruwatari, 1998), cross through contacts (Becker and Gross, 1996), and jog or step-over at bedding contacts (Helgeson and Aydin, 1991). Fracture termination at frequent bedding contacts can produce highly tortuous fracture paths in sediments (Tsang, 1984). By contrast, fractures that propagate straight through bedding contacts provide well-connected pathways. A potential intermediate case is a fracture that jogs or steps over a few centimetres at bedding contacts (Helgeson and Aydin, 1991). Although these three types of fracture intersection with bedding are easily recognised in the field, the mechanisms that control the development of one as opposed to another type are not yet well understood. Insight into controlling mechanisms and parameters could aid the prediction of subsurface fracture propagation.

Even in solid rock material (where jointing and other structures are insignificant), shear failure remains a complex process resulting in complex fracture structures. A common terminology for brittle shear fractures in rock is introduced below (adapted from Riedel, 1929, Sylvester, 1988, and Vermeer and de Borst, 1984) and shown in Figure 5.2. Riedel’s (1929) paper is not available, and his work is completely unknown in solid mechanics, while it is widely

referenced in geology. The reproductions of his interpretations in Sylvester (1988) and McKinnon and de la Barra (1998) are probably misleading because there is no mechanistic description of how the various fractures develop. Riedel's work should be revisited from a solid mechanics point of view, because it provides a good starting point for the interpretation, from a stress and deformation point of view, of small and large faults in rockmasses.

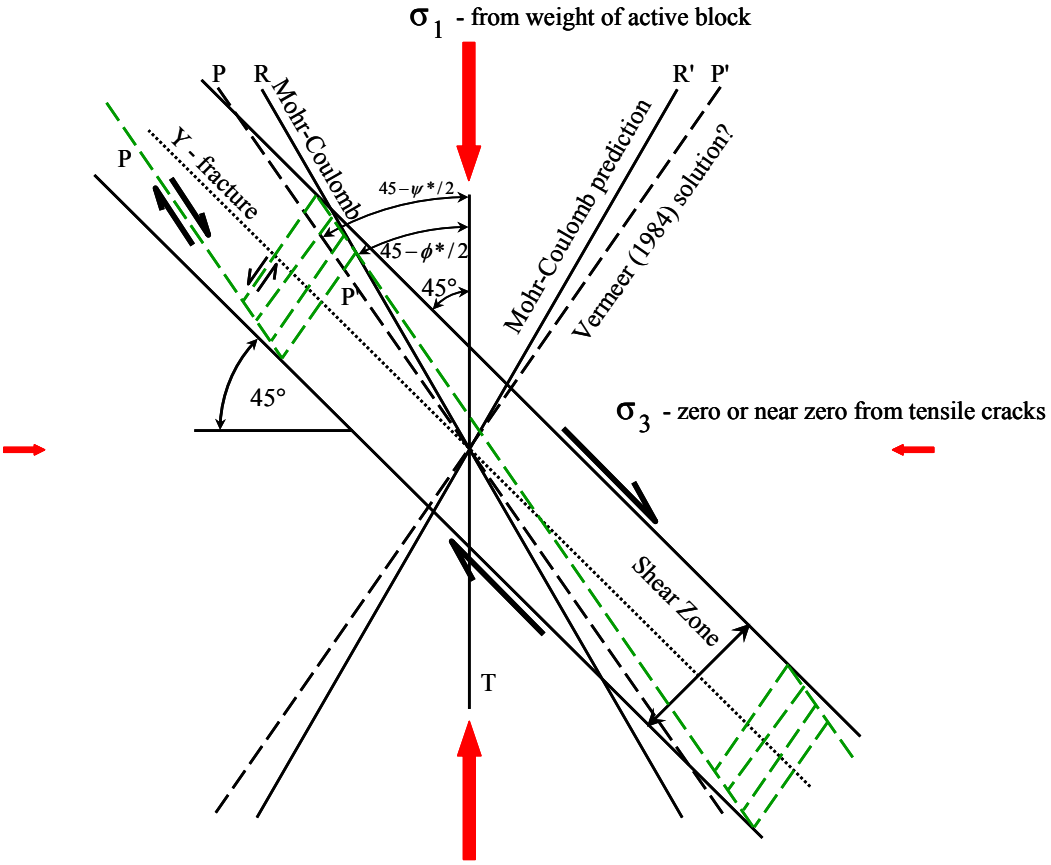

Figure 5.2

The Riedel (1929) Shear Fracture Model in green showing typical orientation relative to the major principal stress and direction of shearing

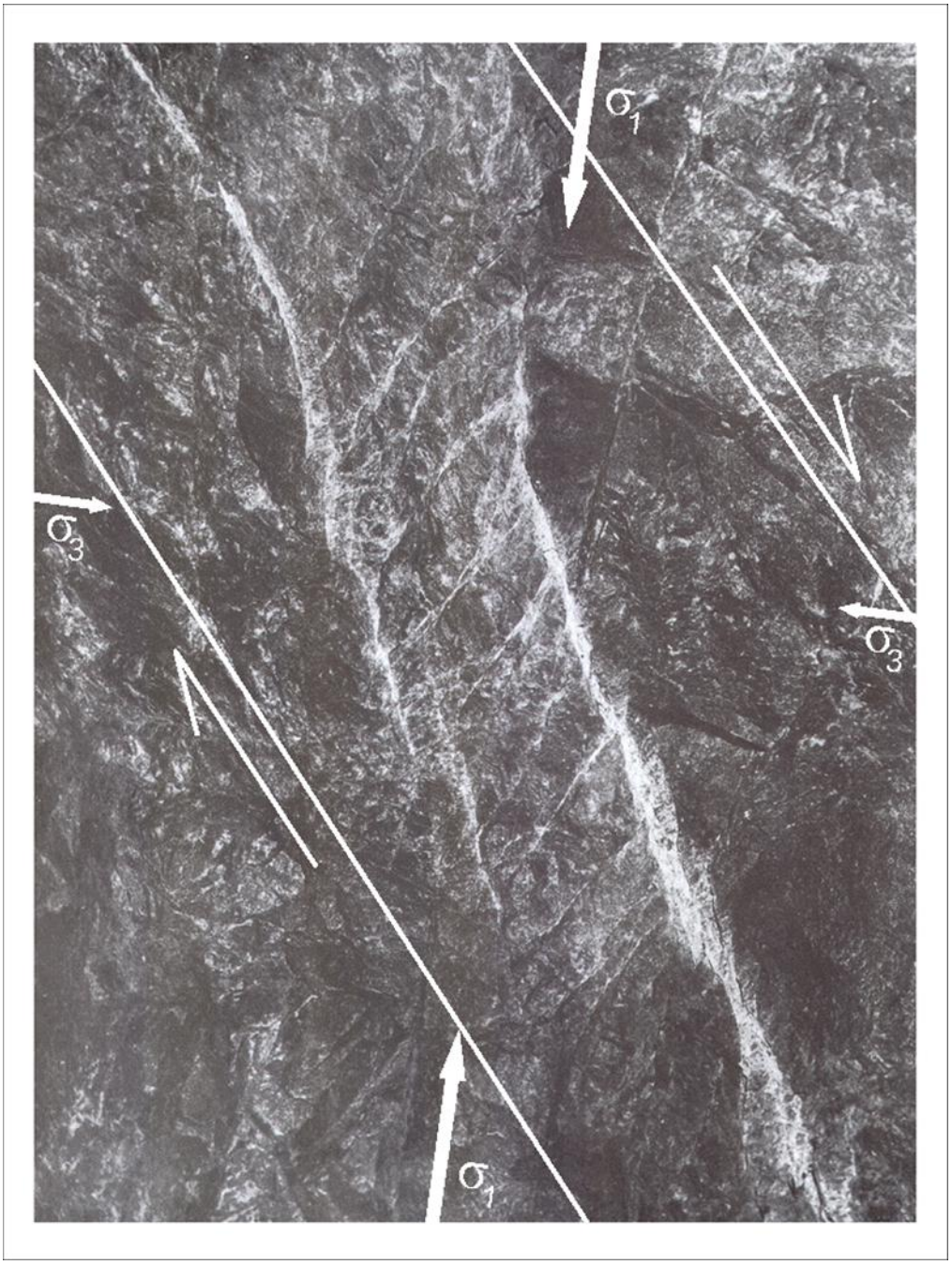

Picture 5.1

Example of a shear fracture in brittle rock in a deep level gold mine showing Riedel Structures (after Ortlepp, 1997)

The location chosen in the slope for the stress state shown is just below the modelled horizontal tensile zone, where the horizontal stresses will be small. There is no mechanistic reason for this excepting that this point has the maximum isolated block weight above it (the block is assumed to be defined by two or more tensile fractures behind the slope crest) and this should be a favourable point for the origin of shearing, where the horizontal stresses are low. The shearing fractures are also assumed to have the complexity of shearing seen in all geological materials, i.e. along faults, in mines, and in the laboratory. Since Riedel (1929) presented his shearing model, it has been widely accepted and has again and again been demonstrated to be a reliable guide for the interpretation of shear along all types of geological features.

Riedel fractures, R and R', form a conjugate set about the major principal stress direction, and are here drawn using Vermeer and de Borst's (1984) notation in which $\phi*$ is the mobilised angle of internal friction. Tension fractures, T, form in the direction of major principal stress, P fractures form symmetrically to the R fractures with respect to the shear direction (these are conjectured to be Vermeer and de Borst's 1984 solution, see equation 5.1 below), while Y fractures are those that lie parallel to the direction of applied shear displacement. All of these fracture types have been observed in nature (Tchalenko and Ambraseys, 1970; Gammond, 1983 and Ortlepp, 1997 – Picture 5.1). McKinnon and de la Barra (1998) have modelled the shear failures, and on the basis of small-strain Mohr-Coulomb theory they have found that it is not possible to

explain the formation of primary P or Y fractures. It now appears that Vermeer and de Borst's (1984) solution for non-associated flow may explain the P fractures, but this is beyond the scope of this thesis. Bartlett et al. (1981) report that all the fracture types illustrated by Riedel (1929) have been reproduced in various laboratory tests.

As mentioned above, the orientation of R and R' fractures can be deduced from the Mohr circle. For a rock with strength defined by cohesion **c** and friction angle ϕ, fracture occurs on planes oriented at $\pm(45-\phi/2)$ from σ_1 as shown in Figure 5.2. Depending on the amount of confining pressure, σ_3, tension fractures T may occur parallel to the σ_1 direction. Using plasticity theory, Vermeer (1990) have shown that for a hardening modulus h_c of zero in non-associated flow, there are two possible solutions for θ, namely:

$$\frac{\pi}{4}-\left(\frac{\phi^{*}+\psi^{*}}{4}\right)<\theta<\frac{\pi}{4}-\frac{\phi^{*}}{2} \qquad (5.1)$$

where ψ^* and ϕ^* are the *mobilised* angle of dilation and *mobilised* angle of internal friction i.e. they are some function of the strain in the material (Vermeer and de Borst, 1984). Combining the results of Riedel (1929) and Vermeer and de Borst (1984), we know that plastic shear flow in the slope must be non-associated, hence $\phi^* \neq \psi^*$, and by implication in Figure 5.2 and Vermeer (1990), that $\phi^* > \psi^*$.

The purpose of presenting all this detail is to recognise that the formation of shear zones in the slope will be complex, just as they are in any

geological material. However, Riedel's (1929) observation that the shear fracture structure is complex, contrasts with the simple observation that the *shear zone orientation* is simple, i.e. it can be assumed to lie parallel with the direction of the largest shear stress in the slope. Shear bands or fractures, however, need not occur at only one specific angle, but could occur over a range of angles in relation to the maximum principal stress direction together with the effects of anisotropy in the shale (e.g. Jaeger and Cook, 1979). Note that only one possible Riedel Shear Structure is drawn in green in Figure 5.2 in which the conjectured Vermeer and de Borst (1984) dilation solution has been applied. The other possible Mohr-Coulomb alternative is not shown for purposes of keeping the drawing clear.

To analyse the inclination of the principal stress directions and consequently to identify the shear failure zones, that may develop in the slope, three horizontal profile lines were defined at 15, 20 and 25m below surface (Figure 5.3). These profile lines were applied to the discussed in Chapters 2 and 3 scenarios of layer inclination (5^0 and 15^0) in homogeneous sandstone slope profile and slope profiles with embedded shale layer thickness from 2m to 12m on 2m intervals. These profile lines provide the reader with reference lines in Figures 5.4 and 5.5. The window chosen has to be relatively small to render the principal stress tensor representations clearly, hence the position of the window in relation to the slope profile shown in Figure 5.3.

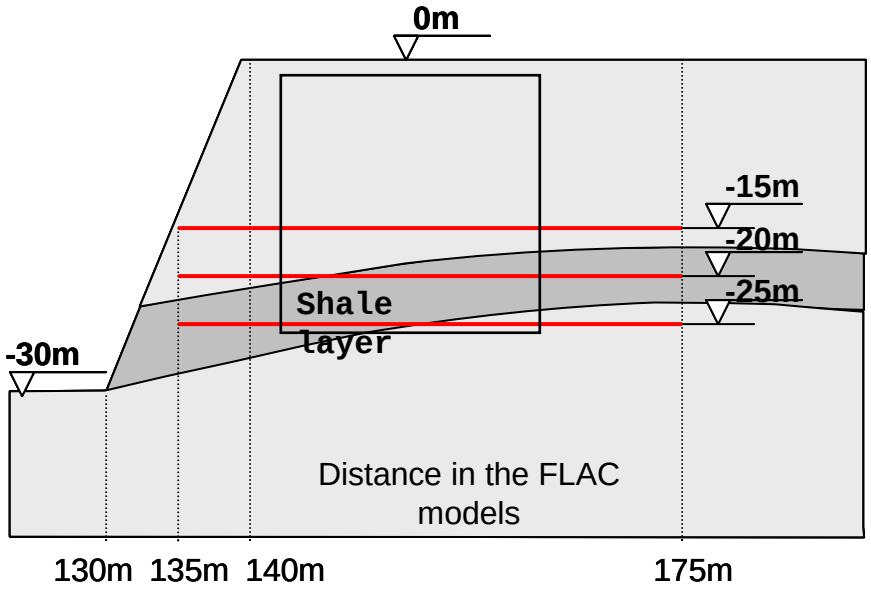

Figure 5.3

Profile line positions (marked with red) in the slope profile together with the position of the slope profile elements in the FLAC models

Figures 5.4 and 5.5 show the principal stress distributions for 6m and 8m thick shale layers respectively and 15^0 layer inclination in the models. Similar results were obtained for all the cases studied with steeper layer inclination angle in the model. The principal stress direction inclination angles of all investigated scenarios can be seen in Figures A3.10 - A3.13, Appendix 3. On these figures it can be seen that only the profiles with steeper layer (15^0 inclination angle) and 6m, 8m and 10m layer thickness have very well defined zones, along the profile line at 20m depth, with horizontal orientation of the principal stress direction inclination angle. For better presentation, these zones are tabulate in Table 5.1.

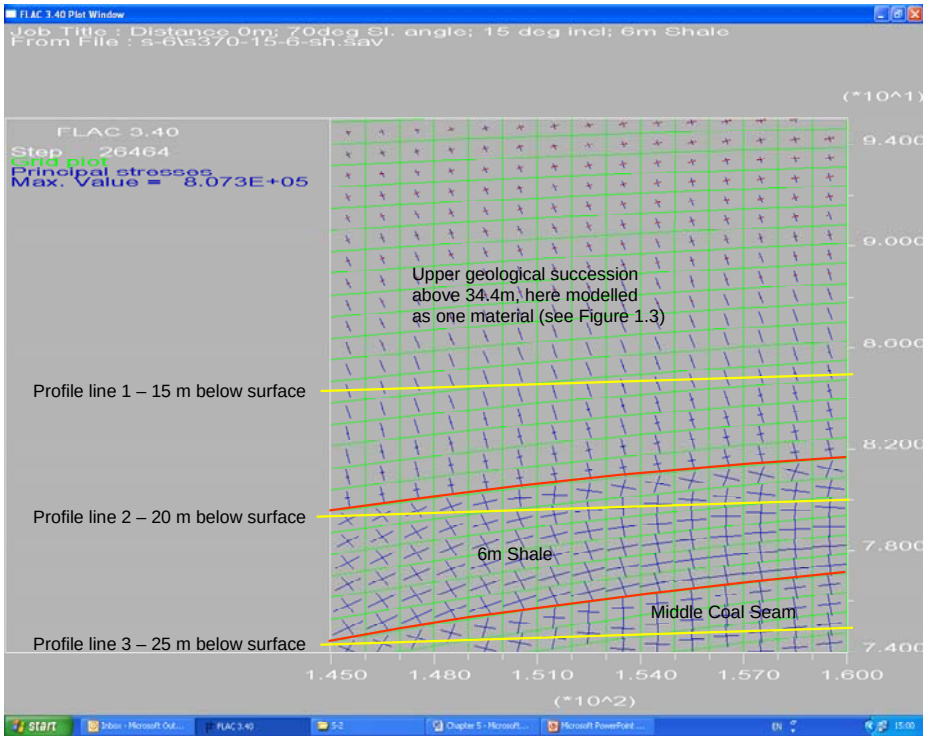

Figure 5.4

Maximum principal stress directions and inclinations in 6m thick shale and surrounding strata

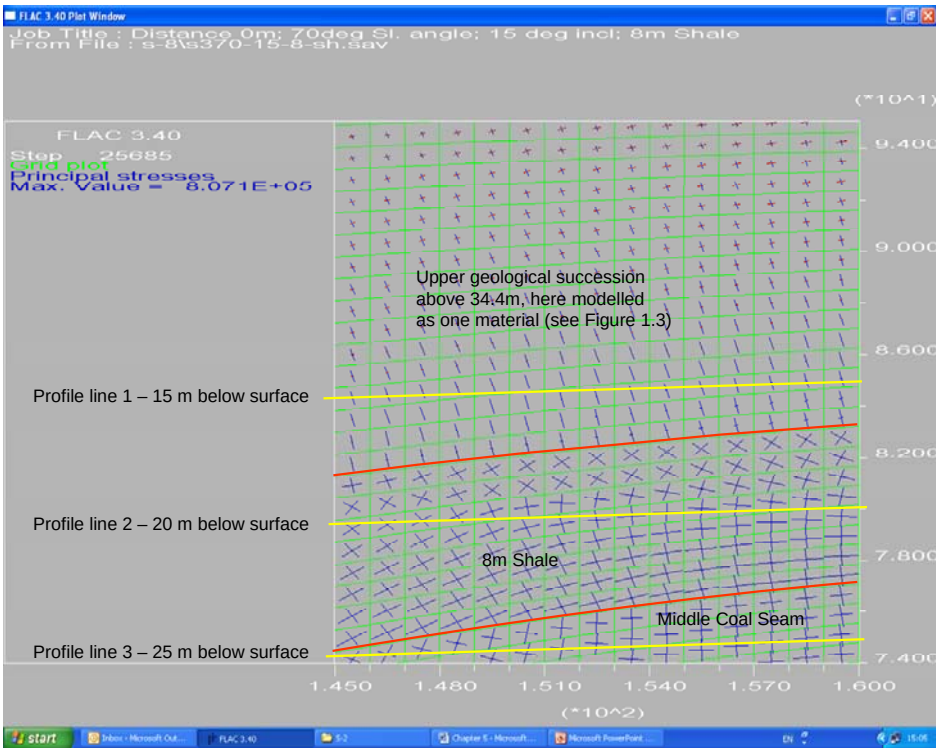

Figure 5.5

Maximum principal stress directions and inclinations in 8m thick shale and surrounding strata

Table 5.1 Points with almost horizontal principal stress direction along the profile line at 20m depth and different shale layer thickness in the slope profile

Shale layer thickness in the model (m)	Distance from the left model boundary (m)	
	First point	Second point
6	150	155
8	150	157
10	151	158

The slope profile with 15^0 layer inclination and thickest embedded shale layer (12m of thickness) exhibits only one zone on 157m from the model length at 20m depth.

Figure 5.6 shows the most likely averaged shear zone directions resulting from the principal stress distributions in Figures 5.4 and 5.5. Parts of the shear zone may even be vertical, given the inclination of the principal stress tensor near the top contact of the shale. In the solution given, the author has assumed that the shear zones are inclined at 45° to the horizontal, and that they are approximated by straight lines.

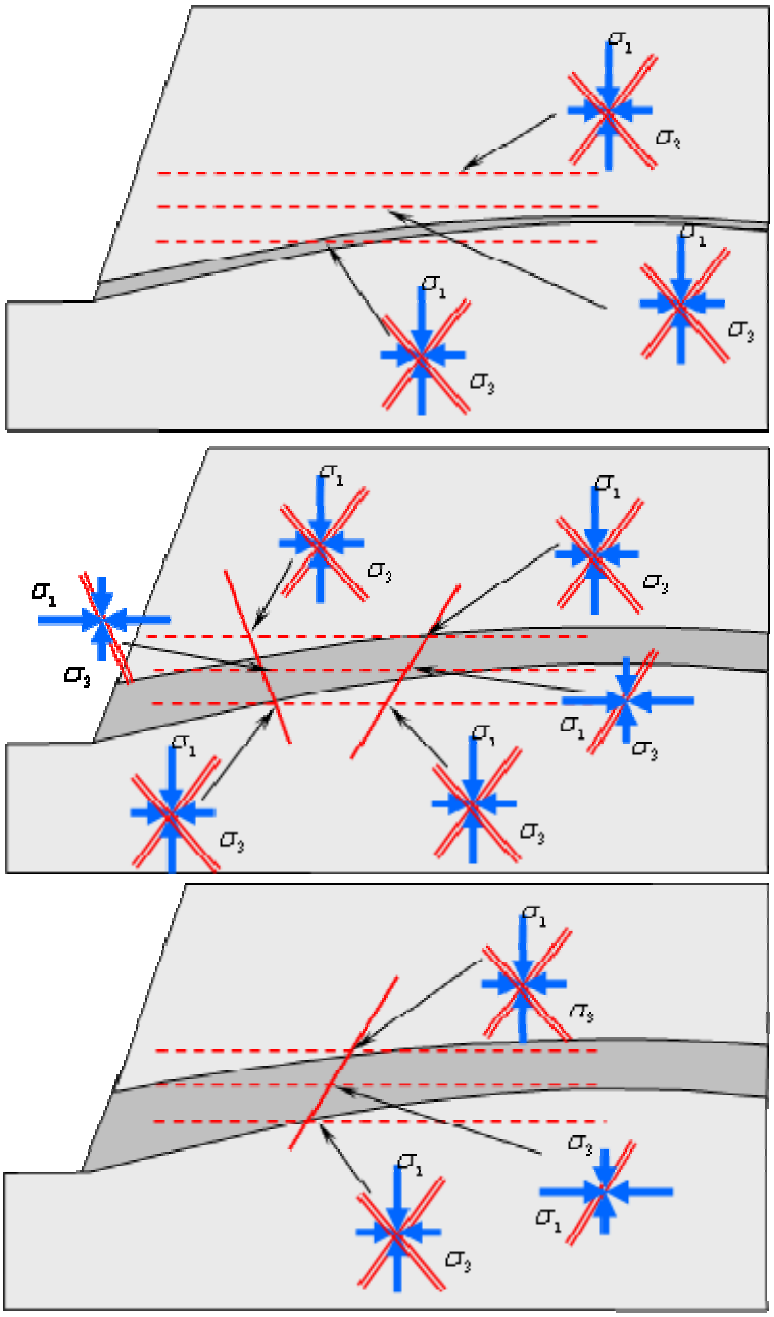

Figure 5.6

Conjectured shear zone orientations in slope profile with different shale thicknesses

There are two arguments that support the conjecture that the shear zones are angled at 45° to the horizontal:

- The FLAC model cannot reproduce failure and all its implications on the stress state in the slope;
- The principal stress orientations in Figures 5.4 and 5.5 will change with the development of the shear fractures, and will tend towards the vertical because of the block's weight.

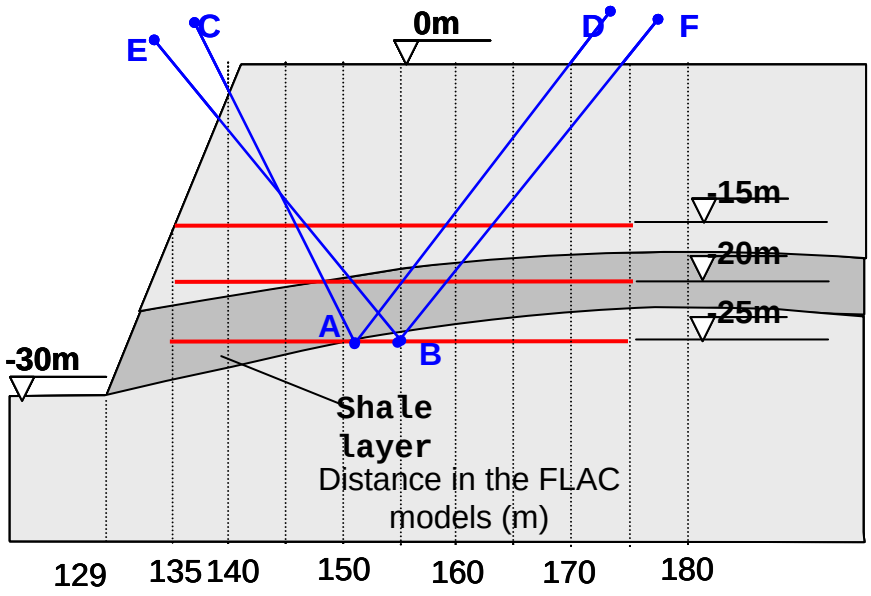

Figure 5.7

Shear failure lines (marked with blue) due to the inclinations of the principal stress direction inclination angles in Figures 5.4 – 5.6

The lines in Figure 5.7 define probable shear surfaces bounding two active blocks. The lines "*CAD*" represent lock boundaries for 6m thick shale, and lines "*EBF*" represent potential shear boundaries for slopes with 10m-thick shale. The differences between the two are not considered particularly significant, especially in the light of our approximate knowledge of slope failure mechanisms and in-situ stress states, hence the author assumes shear zones inclined at 45° to the horizontal.

5.4 ASSUMPTIONS REGARDING THE PROPOSED THRUST FAILURE MECHANISM

The proposed failure mechanism is based on the findings, definitions and assumptions set out in Chapter 4 and the previous paragraph 5.3.

1. The slope profile can be divided into two blocks – the passive and active block (after Boyd, 1983). See Figures 1.1 and 5.1.

This assumption is based on the Kovari and Fritz (1978) polygonal failure surface theory. The existence of the active block is confirmed by field observations. The modelling supports this observation by suggesting that the ground behind the slope crest tends to "slump" downwards by almost a millimetre because of the reduction of horizontal stresses because of the presence of the slope (see Figure 5.8).

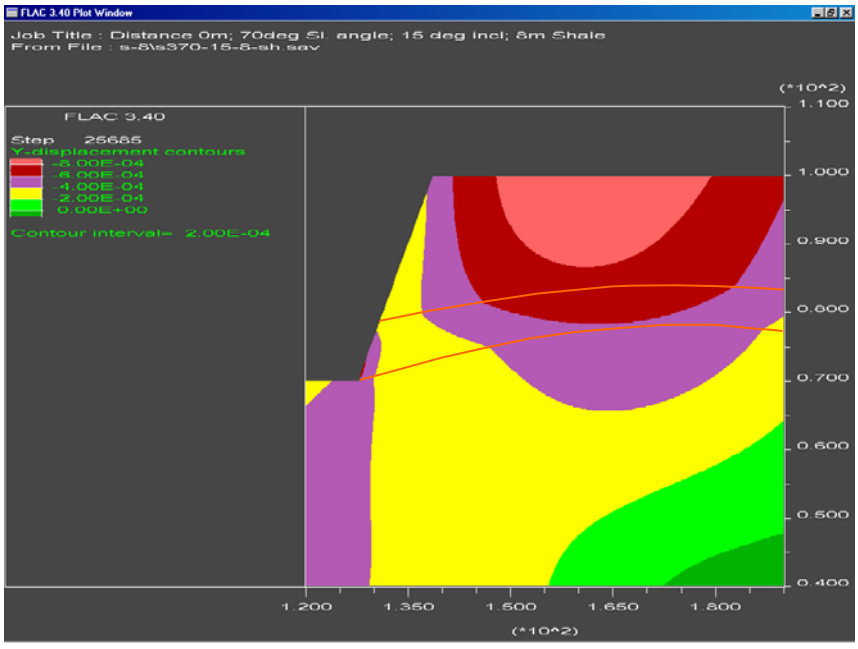

Figure 5.8

Vertical displacement contours in slope containing an 8m-thick shale layer (marked with a red line)

2. Failure takes place on the bottom contact surface of the shale with the middle coal seam, and this surface is always exposed at the toe of the slope (the mining method is to remove overburden in two stages to the top and middle coal seams respectively, and thereafter to mine the exposed coal).

This assumption is based on the site observations of the failure surface profiles (see Figures 1.1 and 1.8) and the Kovari and Fritz (1978) polygonal failure surfaces theory. As was discussed in Chapter 4, the passive block has frictional resistance along the contact surface in the area where $|\Delta\sigma_N| > |\Delta\sigma_N^P|$ and cohesive resistance when $|\Delta\sigma_N| < |\Delta\sigma_N^P|$.

3. The tensile fracture depth is equal to the depth of the induced horizontal tensile stress component.

In a series of very detailed model studies on slope failures, Barton (1971) found that the tension crack behind the slope crest was generated by small movements within the rock mass, and that it appeared after slope excavation. Although these individual movements were very small, their cumulative effect was a significant displacement of the slope surface - sufficient to cause separation of material behind the slope crest and to form tension cracks. In Section 3.5 we estimated the depth of the tensile zone above the undulated strata formation after the slope had been cut, and we assume that tensile fracture depth is equal to the depth of

the horizontal tensile stress zone, here estimated to be 10 to 12m deep (see Figure 3.7).

4. The vertical active block boundaries are defined by the vertical tensile cracks.

If a tensile zone (under different geotechnical conditions) develops in the slope profile as a result of the slope excavation, the active block sides are formed by vertical tensile fractures.

5. The active block stretches from the crest of the slope back toward the solid.

The purpose of this assumption is to determine the possibility of blocky-type failure as close as possible to the plane of weakness formed by frictional zone. This assumption is based on Figures 5.4–5.7 and A3.16–A3.19.

6. Below the tensile zone, the active block boundaries fail by shear zones formed at an angle of 45° to the horizontal, to form a wedge at the base with an angle of 90°.

The shear failure is triggered by the active block weight once its upper portion has become isolated from the rest of the slope by the vertical tensile fractures.

7. Inter-block forces are not taken into account because the failure mode consists of two blocks only. The vectors of their side forces are assumed

to be equal and opposite on opposite sides of the failure zones for equilibrium.

Instead of inter-block forces, reaction forces acting from the passive block to the active block are taken into account.

8. The shale and other rocks in the slope have low porosities (3-4%), but it is assumed that the pores are hydraulically connected.

This assumption is based on the widely accepted zero pore-water pressure at the toe of the slope (Hoek and Bray, 1981 and Hoek, 1986).

9. The analysis can be undertaken with reasonable accuracy in two dimensions, assuming unit length out-of-plane.

The proposed active and passive blocks appear in Figure 5.9 below.

5.5 PROPOSED THRUST FAILURE MECHANISM

When the artificial cut is made, fracture propagation starts as a result of rock relaxation. At this time, the vertical tensile fractures at ground surface and the possible tensile fracture (if $|\Delta\sigma_N| > |\sigma_N^P|$) at the toe of the slope along the shale-middle coal seam contact surface are formed. After their formation, the slope profile fails by shear along unbroken ligaments, as we assumed in Section 5.4. Once these fractures have formed, continued slope stability is seen to be only a

consequence of the balance of forces existing in the profile.

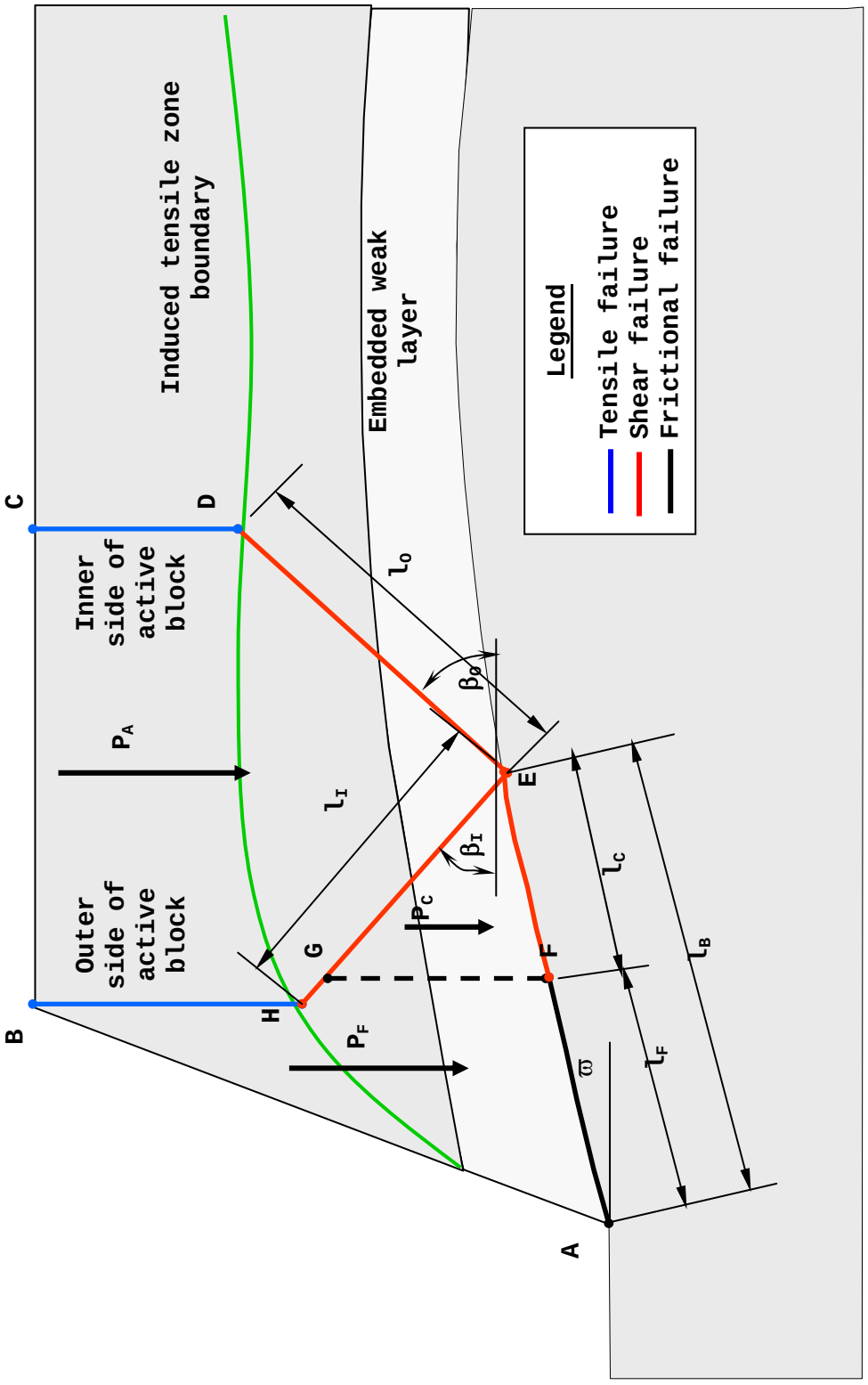

Figure 5.9 Active (B,C,D,E,G,H) and the passive (A,B,H,G,E,F) block formation with indicated lengths of the failure types at the boundary of the blocks

It is also important to recognise that this analysis considers only force equilibrium and assumes that all forces pass through the block centroids. In other words, moment equilibrium is not considered in this model because observations of the failures at the mine did not reveal any significant rotational motion in the failures.

Figure 5.9 indicates the failure length and type taken into account for the purpose of the slope stability calculations. Symbols used in the analysis are as follows:

P_A, P_F, P_C are the load of the active block and the frictional and cohesive zones of the passive block respectively.

$\bar{c}_I, \bar{c}_O$ are the cohesions of the inner and outer side of the active block respectively.

l_I, l_O are the shear failure lengths of the inner and outer side of the active block respectively.

l_F, l_C are the lengths of the frictional strength zones and the cohesive strength zones of the passive block failure surface respectively.

l_B is the length of the passive block failure surface and is equal to the sum of the lengths of frictional strength and cohesive strength zones ($l_B = l_F + l_C$).

β_I, β_O are the shear failure surface angles at the inner and outer sides of the active block respectively (assumed to be 45°).

R_P is the reaction of the passive block applied to the active block.

ϕ_{avI}, ϕ_{avO} are the average internal friction angles along the shear failure surfaces at the inner and outer side of the active block respectively.

ϖ is the dip angle of the strata.

In Chapters 2 and 3 it was mentioned that layers in the slope profile change in thickness along the undulated strata formation. For this reason, it is expected that they could have different thicknesses on opposite block sides, which means that the value of the average cohesion and friction angle will be slightly different. This level of detail is probably not appropriate in the model, so an average strata thickness is used, as shown in Figure 5.10.

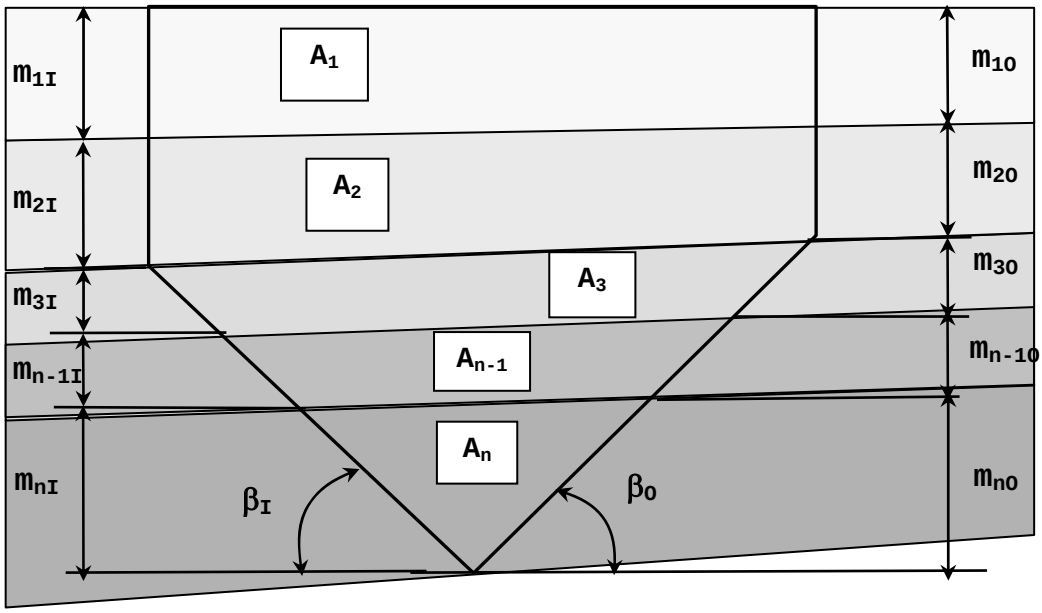

Figure 5.10

Active block, composed of different layers at average thicknesses

The average friction angle along each surface in a multi-layered medium can be expressed as the weighted average:

$$\phi_{ave} = \frac{\sum_{i=1}^{n} m_i \phi_i}{\sum_{i=1}^{n} m_i} \qquad (5.2)$$

where m_i is the layer thickness of the i^{th} layer and ϕ_i is the frictional angle of the i^{th} layer.

From the discussion in Section 5.3 and the assumptions made in Section 5.4, the shear failure surfaces are anticipated to dip at 45° to the horizontal. The tensile fracture depth has been estimated from the model, and is assumed equal to the tensile zone depth, shown in Figure 5.9. The average cohesion is calculated along the shear failure surfaces of the active block sides as the weighted average:

$$C_{ave} = \frac{\sum_{i=1}^{n} m_i C_i}{\sum_{i=1}^{n} m_i} \qquad (5.3)$$

where m_i is the failure surface length in the i^{th} layer and C_i is the cohesion of the layer intersected by the active block shear failure surface.

The active block weight for unit thickness is calculated as:

$$P_A = g \sum_{i=1}^{n} \rho_i A_i \qquad (5.4)$$

where A_i is the layer volume in the active block-profile, ρ_i is the layer density, and g is the acceleration due to gravity.

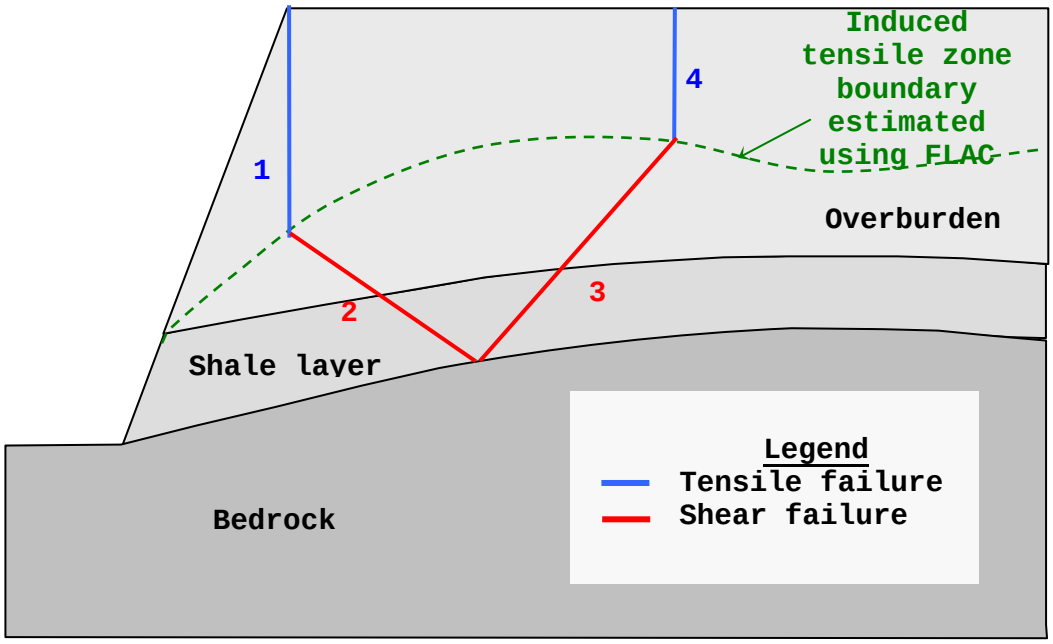

Figure 5.11

Active block construction sequence with the proposed failure types in the profile

The active block construction order (Figure 5.11) is as follows:

1. From the ground surface, at the crest of the slope, a vertical tensile fracture is drawn to a length equal to the depth of the calculated induced tensile horizontal stress zone (this is the area where tension fractures are most commonly seen).
2. A shear failure surface is drawn from the end of the induced tensile fracture downward to intersect the bottom shale contact surface at an angle of 45° to the horizontal in a direction toward the solid. This is the outer shear surface.

3. From this point, the line of the inner shear surface of the active block is drawn upward (toward the solid) to the bottom of the tensile zone at an angle of 45° to the horizontal.
4. The second vertical tensile fracture of the active block is drawn from the end of the shear failure line to the ground surface. This is the second vertical tensile crack, which would be encouraged to form because of small shear movements on the inner shear surface, and the fact that the presence of the slope has induced tensile horizontal stress below surface.

This construction is not intended to represent the sequence of development of these fractures as there is still insufficient evidence to determine exactly how the failure surfaces do grow within the slope. Once all these fractures are developed and connected, the formation of the active block is complete.

5.5.1 Calculation of the forces applied from the passive block to the failure surface

As was mentioned earlier, we have two zones along the failure surface at the passive block base, namely frictional and cohesive zones. These two zones have different shear strengths, which have to be taken into account when the resistance force developed by the passive block is computed. The passive block weight calculation is the same as for the active block.

Resisting forces at the base of the passive block are formed by the frictional strength along the failure

surface due to the block weight and the cohesive and frictional strength of that portion of the contact surface that has not yet yielded in shear. Driving forces are formed by the tangential component of the weight along the same surface. Hence, these forces can be expressed as:

$$P_F^N = P_F \cos\varpi \tag{5.5a}$$

and

$$P_F^{dr} = P_F^T = P_F \sin\varpi \tag{5.5b}$$

where ϖ is an average inclination angle of the failure surface, P_F is the passive block load above frictional zone, and P_F^N and P_F^T are the normal and tangential components respectively. The resisting force along the frictional zone will have the form:

$$P_F^{res} = P_F^N \tan\phi_E = P_F \cos\varpi \tan\phi_E \tag{5.6}$$

where ϕ_E is the frictional angle along the bedding.

Similar to the frictional zone, normal and tangential load components in the cohesive zone of the passive block can be calculated with Equation 5.7. Then the resisting and tangential forces to the failure surface will have the form:

$$P_C^{res} = c_B l_B + P_C^N \tan\phi_B = c_B l_B + P_C \cos\varpi \tan\phi_E \tag{5.7a}$$

and

$$P_C^{dr} = P_C \sin\varpi_C \tag{5.7b}$$

respectively.

5.6.2 Calculation of active block forces

Figure 5.9 shows that the rock mass rests on two potential failure surfaces: the shale-middle coal seam contact, and the active block inner shear failure surface. Blocky-type failure is only possible if an outer slip surface develops and an estimate of the overall safety factor of the system is the weighted average of the three safety factors, taking into account the lengths of the respective failure surfaces.

Active block movement is only possible if the reaction force from the passive block fulfils the Mohr-Coulomb failure criterion with the parameters for the internal slip surface – cohesion c, and friction angle ϕ, along the length l. Figure 5.12 shows the detail of the outer shear failure surface together with the passive block reaction force (R) acting on the surface.

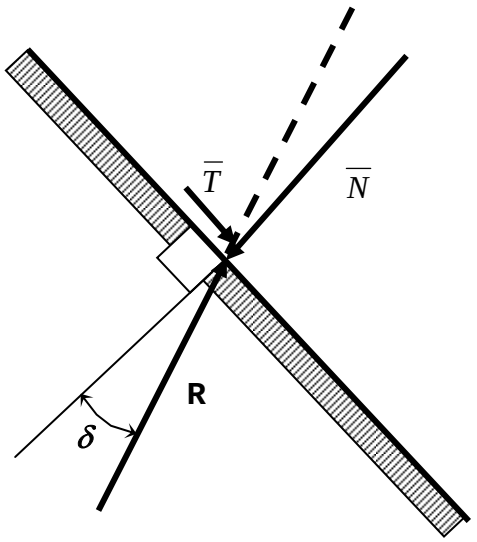

Figure 5.12
Detail of internal shear surface

From Figure 5.12 we can write

$$\overline{T}_{max} = \overline{N}\tan\phi + cl \tag{5.8}$$

If we take into account the definition for safety factor

$$FOS = \left| \frac{\text{maximum shear resistance}}{\text{applied shear stress}} \right| \tag{5.9}$$

Then we can write

$$FOS = \frac{\overline{S}_{max}}{\overline{S}} = \frac{\overline{N}\tan\phi}{\overline{T}} + \frac{cl}{\overline{T}} \tag{5.10}$$

From Figure 5.12 and Equation 5.10 we have

$$\tan\delta = \frac{\overline{T}}{\overline{N}} = \frac{1}{FOS}\left(\tan\phi + \frac{cl}{\overline{N}}\right) \tag{5.11}$$

and

$$\overline{N} = R\cos\delta \tag{5.12}$$

If we combine Equations 5.11 and 5.12 and accept FOS=1, which means that the internal slip surface is at the point of slipping, then we will have

$$\tan\delta = \tan\phi + \frac{cl}{R\cos\delta} \tag{5.13}$$

The angle of internal friction in Equation 5.13 has to satisfy the condition in Equation 5.14 if it is to have a real solution (see Appendix A1.4):

$$\phi \geq \sec^{-1}\left(\frac{cl}{R}\right) \tag{5.14}$$

From Equation 5.14 we can see that under worst-case conditions, $\phi = 0^{\circ}$ if $\frac{cl}{R} = \infty$, which is only possible if $R = 0$, and both $c \neq 0$ and $l \neq 0$. In the case of $l = 0$, we should have a tensile fracture from the surface to the failure surface. Kovari and Fritz (1978) accepted the worst-case scenario in their polygonal model, which gives the angle of reaction forces as equal to the angle of internal friction ($\delta = \phi$).

The following equations can be applied for the active block load distribution along the two shear failure surfaces that form the wedge structure:

$$P_{AO} = \frac{P_A}{2}\left(1 + \sin \varpi_A\right) \tag{5.15}$$

and

$$P_{AI} = \frac{P_A}{2}\left(1 - \sin \varpi_A\right) \tag{5.16}$$

for the outer and inner shear failure surfaces respectively, where P_A is the weight of the active block and ϖ_A is the layer inclination angle at the block wedge.

5.5.3 Calculation of the pore water forces

Figure 5.13 shows the same slope profile as shown in Figure 5.9, with points defining the block boundaries. Let us first calculate the pore-water pressure along the line “CD”. The earlier-calculated induced vertical

tensile fracture depth (z) and a phreatic surface, (z_{WT}), above the tensile fracture depth are indicated.

Therefore, the pore-water pressure at point "D" in Figure 5.14 is equal to:

$$\sigma_w^D = \gamma_w z_{WT} \tag{5.17}$$

where γ_w is the unit weight of water and z_{WT} is the surface tensile fracture depth below the phreatic surface.

The total force acting along the surface vertical tensile fracture at the active block outer side is equal to

$$V_w^{CD} = \frac{\gamma_w z_{WT}^2}{2} \tag{5.18}$$

Let us calculate the pore-water pressure along the line DE. As a first step, let us define pore-water pressure along the line DA. For this purpose we assume zero pore-water pressure at point D. We also have zero pressure at point A at the slope toe position. Hence, we assume that, in the middle of the span between these two points (point I), we will have the highest pore-water pressure value that will be equal to

$$\sigma_w^I = \frac{\gamma_w z_w^{DA}}{2} \tag{5.19}$$

where z_w^{DA} is the difference between depths of points D and A. Now we cam draw a stress diagram (ADJ) between the points A and D.

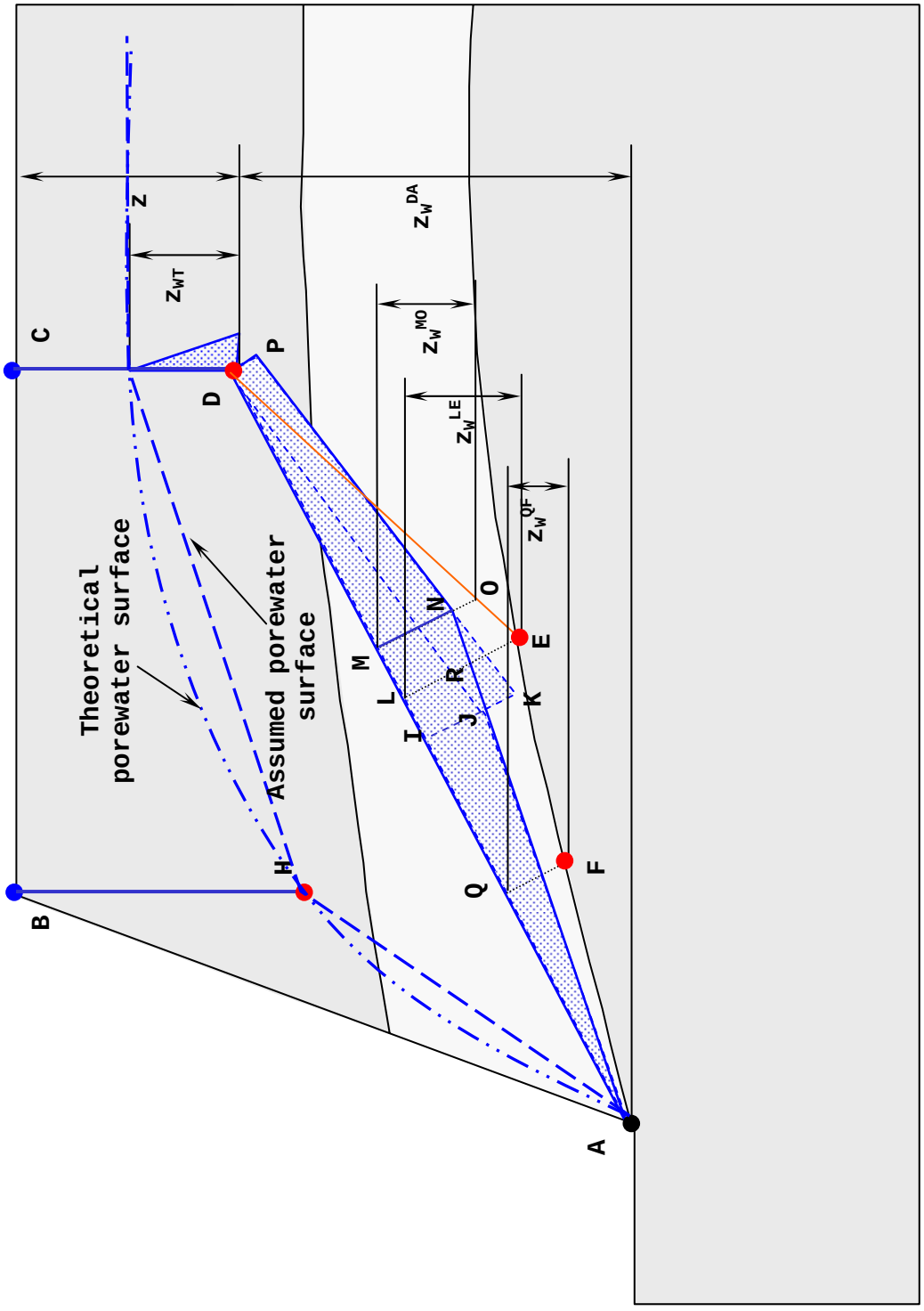

Figure 5.13

Scheme for pore-water pressure calculation on the passive and active block boundaries

From Equation 5.13, we have pore-water pressure at point D. So let us draw the line DP, equal to the pore-water pressure at point D normal to the line AD and add the same stress magnitude at point I as adding stress JK. Now our stress diagram takes a new form (AJKPD), which is unrealistic because of the step AJK. As the point I is in the middle of AD, then half of the stress JK can be added to the portion AI and the other half to the portion ID. Hence, we have a new stress equal to

$$\sigma_w^I = 0.5\gamma_w\left(z_w^{DA} + z_{wt}\right) \tag{5.20}$$

which is equal to the line MN in our stress diagram. Then let us move our stress magnitude MN toward point D until it intersects the stress line KP. This position is shown in Figure 5.13. Now we have a new stress diagram (ANPD), which presents pore-water pressure distribution along the line AD.

Let us now calculate the pore-water pressure at point E. For this reason, let us make its orthogonal projection to the line AD, which is point L, which has pressure with the magnitude LR. Therefore, the pore pressure at point E will have the magnitude

$$\sigma_w^E = \sigma_w^L + \gamma_w z_w^{LE} \tag{5.21}$$

where z_w^{LE} is the depth difference between the points L and E. This pressure is realistic because point E is slightly deeper than point L.

To find the point where we have maximum pore-water pressure along the outer shear failure surface we define point O, whose orthogonal projection to the line

AD is point M. With a high degree of approximation we can say that the pore-water pressure at point O is equal to

$$\sigma_w^O = \sigma_w^M + \gamma_w z_w^{MO}. \quad (5.22)$$

It is now easy to construct a pore-water pressure diagram along the line of the inner shear failure surface (HE) because we have calculated the pore-water pressure at point E (Equation 5.21) and have assumed zero water pressure at point H. This assumption is based on the close point position to the two free surfaces AB and BC.

Pore-water pressure at point F follows the same order as for point E (Equations 5.21 and 5.22):

$$\sigma_w^F = \sigma_w^Q + \gamma_w z_w^{QF} \quad (5.23)$$

where σ_w^Q is the pore-water pressure magnitude at point Q and z_w^{QF} is the depth difference between the points Q and F.

Now we are in position to draw the pore-water pressure diagrams along the active block failure surfaces and the passive block failure surfaces. Figure 5.14 shows pore-water pressure diagrams and resultant forces V_{CD}, U_O, U_I, U_C and U_F acting along the failure surface of the vertical tensile fracture, the active block outer and inner shear failure surfaces, and the cohesive and frictional lengths respectively of the passive block base. The figure also shows the calculated pore-water pressures σ_w^D, σ_w^E, σ_w^0 and σ_w^F at points D, E, O and F

respectively. According to the pore-water pressure diagrams, calculated resultant forces have the following magnitudes:

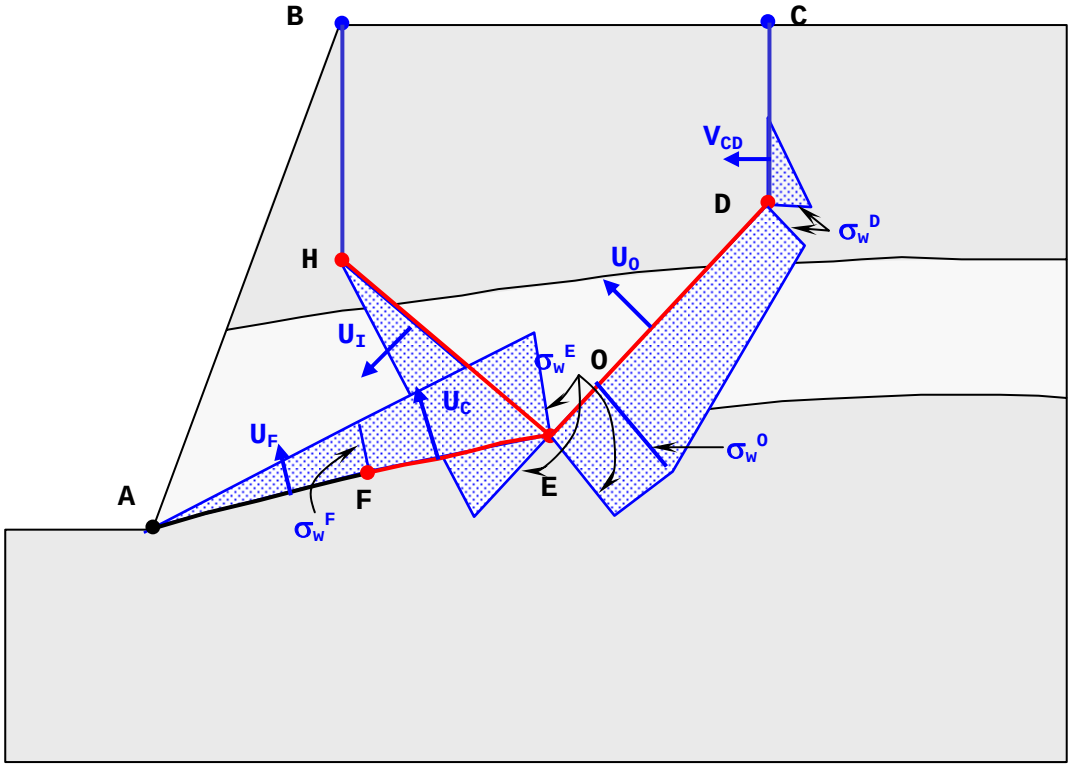

Figure 5.14

Pore-water pressure diagrams

$$U_O = \frac{l_{DO}\left(\sigma_w^D + \sigma_w^O\right)}{2} + \frac{l_{EO}\left(\sigma_w^O + \sigma_w^E\right)}{2} \qquad (5.24)$$

$$U_I = \frac{l_{EH}\,\sigma_w^E}{2} \qquad (5.25)$$

$$U_C = \frac{l_{EF}\left(\sigma_w^E + \sigma_w^F\right)}{2} \qquad (5.26)$$

$$U_F = \frac{l_{AF}\,\sigma_w^F}{2} \qquad (5.27)$$

where l_{DO}, l_{EO}, l_{EH}, l_{EF} and l_{AF} are span lengths between points DO, EO, EH, EF and AF respectively.

Similar pore-water pressure analysis was undertaken by Hoek (1986) in his lecture at the Santiago Technical University (Chapter 7 “A slope stability problems in Hong Kong”).

5.5.4 Criterion for the existence of the inner shear surface

At the inner shear surface we have the combined action of two forces. The first force takes into account the sum of driving and resisting forces (with the signs “-” and “+” respectively) along the potential failure surface of the passive block base, expressed as

$$R_P = P_F^{res} + P_C^{res} - P_F^{dr} - P_C^{dr} \qquad (5.28)$$

and, secondly, the corresponding active block load.

Hence, we could have two directions of the passive block reaction force (Equation 5.28): the first one is when the sum is negative (Figure 5.18a) and the second, when the sum is positive (Figure 5.15b). Acceptance of the reaction force inclination angle ($\delta = \phi$), allows us to use only cohesive strength along the inner shear failure surface. We can transfer the normal to the inner surface component of the passive block reaction force (R_P), to the outer failure surface with the corresponding inclination angle.

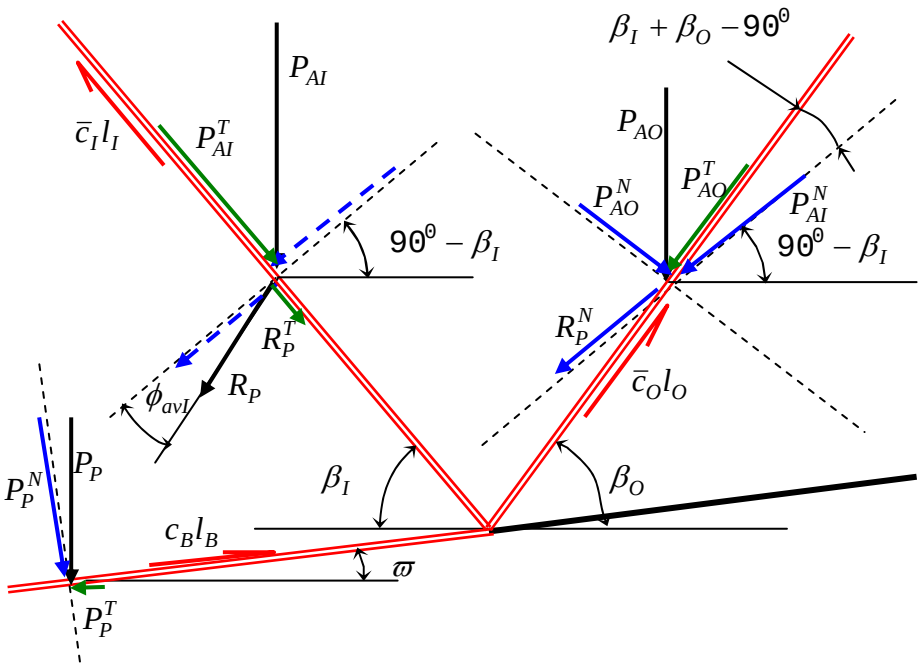

Figure 5.15a

Passive block reaction force R_P acting approximately co-directional to the active block load at the inner shear failure surface

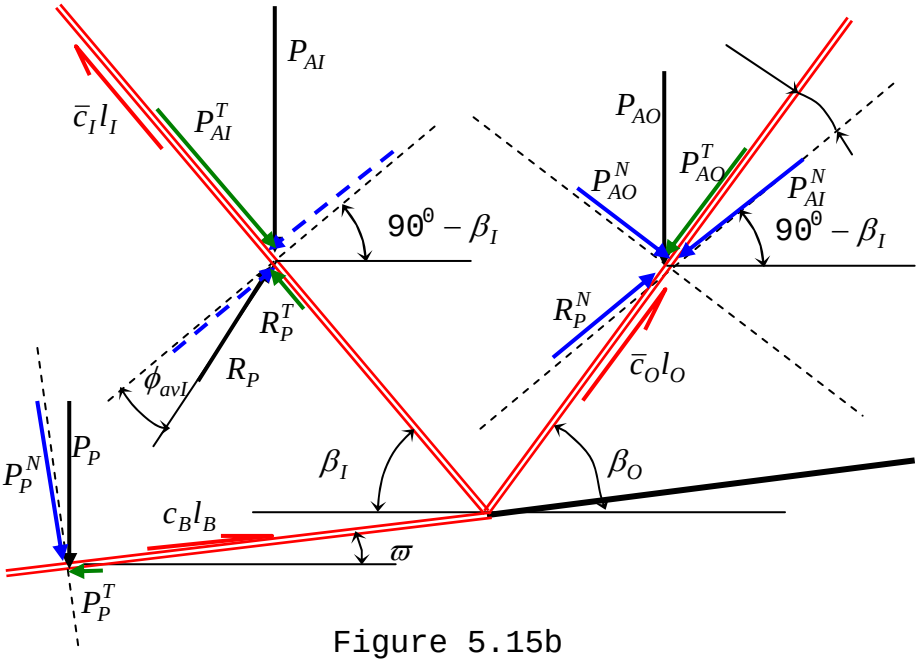

Figure 5.15b

Passive block reaction force R_P acting opposite to the active block load at the inner shear failure surface

In the first case (Figure 5.15a), the normal components on the shear surface under the passive block and the corresponding active block weight (R_P^N and P_{AI}^N) are approximately co-directional, which increases the driving forces of the active block outer shear failure surface and might lead to failure. Hence the active block inner failure surface will have only cohesive strength.

In the second case (Figure 5.15b) we have reaction force, acting opposite to the force of the active block load. Tangential (to the inner shear surface) components of the reaction force and the corresponding active block load are in opposite directions, which will decrease the total driving effect.

Using the above discussion and assumption that $\delta = \phi$ eliminates frictional resistance of the inner failure surface, we can use Equation 5.10 to define the criterion for the existence of the inner shear failure surface, which has the form:

$$\eta = \frac{cl}{P_{AI}^T - R_P^T} \tag{5.29}$$

If we take into account Equations 5.16 and 5.17 and the relationships

$$P_{AI}^T = P_{AI}\, \boldsymbol{sin}\, \beta_I \tag{5.30}$$

$$R_P^T = R_P\, \boldsymbol{sin}\, \phi_I, \tag{5.31}$$

then Equation 5.29 can be rewritten as

$$\eta = FOS_I = \frac{\bar{c}_I l_I - U_I \tan\phi_{avI}}{\frac{P_A(1+\sin\varpi_A)\sin\beta_I}{2} - R_P \sin\phi_{avI}}, \quad (5.32)$$

which is a criterion for the existence of the inner shear failure surface and the surface's factor of safety.

If the shear fracture criterion (η) from Equation 5.32 is higher than 1.3, the inner shear failure surface will not form. Therefore, we will have conditions for other failure types (such as multi planar or polygonal) but not for thrust failure. If the criterion is lower than 1.3, we have to anticipate shear failure at the inner surface and, from there, blocky-type failure.

5.5.5 Calculation of the outer shear failure surface factor of safety

As was discussed earlier, the components normal to the inner failure surface of the corresponding active block load and the passive block reaction force are transferred to the outer shear surface. Then their combined action along the outer surface can be expressed as (Figure 5.18):

$$\bar{R} = \frac{P_A}{2}(1+\sin\varpi_A)\cos\beta_I - R_P \cos\phi_{avI} \quad (5.33)$$

Therefore, the outer shear failure surface will have a factor of safety equal to

$$FOS_O = \frac{\bar{c}_O l_O + \left[\bar{R}\,\sin\left(\beta_I + \beta_O - 90^0\right) + \frac{P_A}{2}\left(1 - \sin\varpi_A\right)\cos\beta_O - U_O - V_{CD}\sin\beta_O \right]\tan\phi_{avO}}{\bar{R}\cos\left(\beta_I + \beta_O - 90^0\right) + \frac{P_A}{2}\left(1 - \sin\varpi_A\right)\sin\beta_O + V_{CD}\cos\beta_O} \quad (5.34)$$

In term of Section 5.3, Equation 5.34 can be further simplified as:

$$FOS_O = \frac{\bar{c}_O l_O + \left[\frac{P_A}{2}\left(1 - \sin\varpi_A\right)\cos\beta_O - U_O - V_{CD}\sin\beta_O \right]\tan\phi_{avO}}{\bar{R} + \frac{P_A}{2}\left(1 - \sin\varpi_A\right)\sin\beta_O + V_{CD}\cos\beta_O} \quad (5.35)$$

5.6.6 Calculation of the basal failure surface factor of safety

The basal surface safety factor presents the balance of already calculated driving and resisting forces along the contact surface in the passive block base (see Figure 5.12), and has the form:

$$FOS_B = \frac{P_F\cos\varpi_F\tan\phi_B + \left(c_B l_C + P_C\cos\varpi_C\tan\phi_B\right) - \left(U_C + U_F\right)\tan\phi_B}{P_F\sin\varpi_F + P_C\sin\varpi_C} \quad (5.36)$$

where ϕ_B is the friction angle along the sedimentary layer and ϖ_F and ϖ_C are the layer inclination angles along the frictional zone and cohesive zone of the passive block base.

5.6.7 Slope stability safety factor

The failure surface lengths (l_I,l_O and l_B - Figure 5.12) vary, and depend on slope angle, layer inclination, layer thickness, and rock properties. To avoid overestimating the influence of the shortest failure surface on the entire slope stability, a weighted function of calculated safety factors should be used. Hence, we have the following weighted average equation for calculation of the entire slope stability factor of safety from the individual failure surface factors of safety and their respective lengths:

$$FOS = \frac{FOS_I l_I + FOS_O l_O + FOS_B l_B}{l_I + l_O + l_B} \qquad (5.37)$$

5.6 CONCLUSION

A simple active-passive block formation mechanism based on the Mohr-Coulomb failure criterion and fracture mechanics has been developed, and will now be applied to the observed failures discussed in Chapter 1.

CHAPTER 6
CALCULATED EXAMPLES AND DISCUSSION

6.1 SUMMARY

In this chapter, with the aid of the proposed thrust failure mechanism, the safety factors of the failures discussed in Chapter 1 are calculated. These safety factors are compared with the safety factors calculated using the widely used program SLOPE/W and based on the limit equilibrium method of slices. The geotechnical parameters used in the calculations appear in Table 6.1 below.

Table 6.1 Rock properties

Rock properties	**Sandy overburden**	**Sandstone**	**Shale (normal to bedding)**	**Shale (parallel to bedding)**
1	2	3	4	5
Density, kg/m^3	1900	2600	2700	-
Shear modulus, GPa	1.6	5.2	2.3	-
Bulk modulus, GPa	2.6	5.9	4.5	-
Tensile strength, MPa	1	5.5	3.5	1
Cohesion, kPa	40	700	400	100
Friction angle, deg.	32	22	14	8
Layer thickness*, m	20	12	8	-

* Average layer thickness

6.2 EXAMPLE 1: PIT A-2 SLOPE FAILURE

Let us begin with the failure that took place in Pit A-2, referred to in Section 1.2.2. The highwall slope profile appears in Figure 1.9. Two FLAC models were prepared for the stress state calculation: the first model corresponds to virgin conditions, and the second to an excavated slope contour (53^0 slope angle). Spoil material is simulated with the aid of applied pressure of 0.30MPa, equal to approximately 20m spoil height and with a unit weight of $15kN/m^3$. The thin sections of the embedded shale layer were taken from the failed area and the critical tensile stress was calculated (as discussed in Chapter 4 and Appendix A1.2).

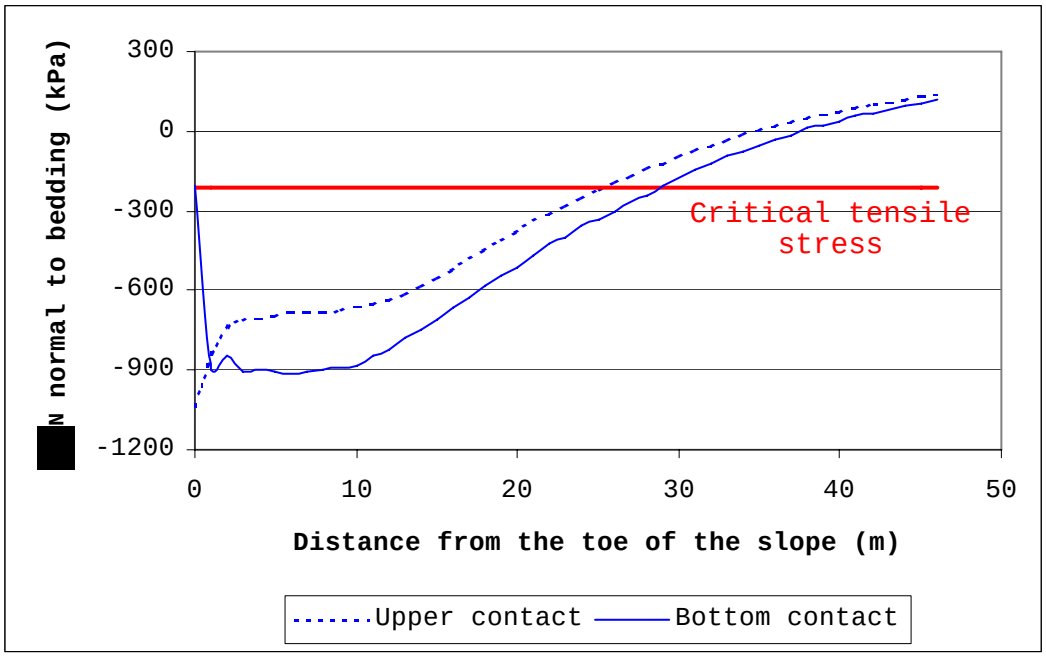

Figure 6.1

Stress component normal to bedding along the upper and bottom contact surfaces of the embedded shale layer with the value of the critical tensile stress, calculated in Chapter 4

Figure 6.1 shows the normal to bedding stress component along the upper and bottom contact surfaces of the embedded shale layer, together with the critical tensile stress $\Delta\sigma_N^P$. From the figure, the frictional zone length along the upper and bottom contact surfaces has values of 25m and 29m respectively.

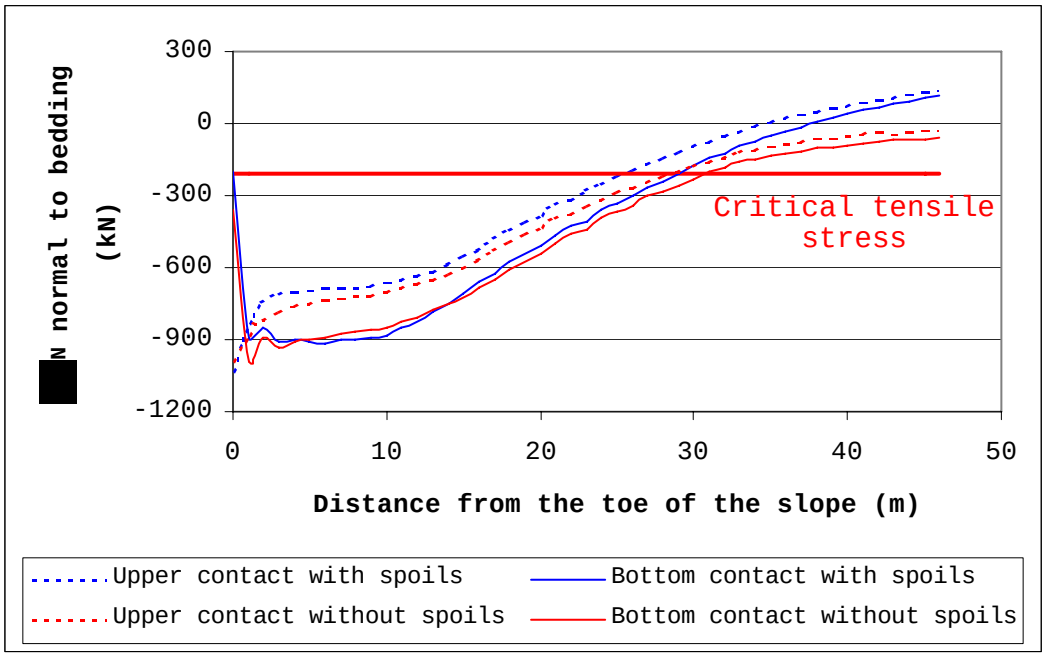

Figure 6.2

Stress component normal to bedding for the slope profile at Pit A-2 with and without spoils, together with the critical tensile stress $\Delta\sigma_N^P$

To determine the effect of the spoil pile, another FLAC model without spoils was run. Figure 6.2 presents the plot of the stresses normal to bedding (cases with and without spoils), together with the critical tensile stress $\Delta\sigma_N^P$. It can be seen that the tensile fracture at the contact increases in length from 25m to 28m and from 29m to 32m at the upper and the bottom contacts respectively, if there were no spoils dumped on the slope. Hence, we can conclude that spoils have an

anchoring effect on slope stability. However, this effect may not be strong enough to prevent failure as, at the same time, the spoil material increases the shear stress component along the active block shear failure surfaces.

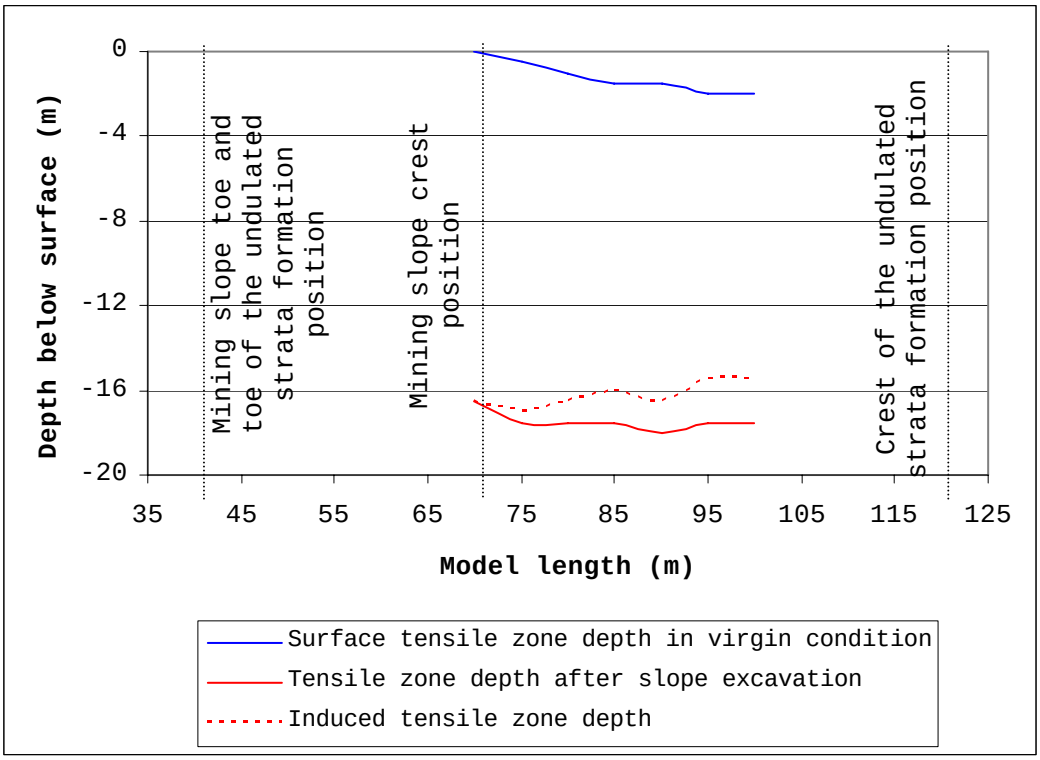

Figure 6.3

Tensile zone depth above the undulated strata formation in virgin conditions and after slope excavation

As was discussed in Section 3.6, there is a pre-existing tensile stress zone at the ground surface above the formation crest, which extension (in both directions: horizontal and vertical) is triggered by the mining activities. Therefore, the induced tensile horizontal stress zone depth we take for the contour of the surface vertical tensile fracture propagation. Figure 6.3 shows the depth of the tensile horizontal stress zone in virgin conditions and after slope

excavation. Their difference indicates the expected surface tensile fracture depth.

It is obvious that we could have two possible failures – along the upper and along the bottom contact surfaces (dash). This means that we have to calculate a safety factor along these two potential failure surfaces. The two possible scenarios with their active and passive blocks are shown in Figures 6.4a and 6.4b for upper and bottom contacts respectively. At the mine, the phreatic surface was measured to be 23m below surface, and this has been taken into account in the subsequent calculations, assuming a dry slope toe.

6.2.1 Example 1a: Safety factor calculations along the upper contact surface

Step 1. Average friction angle along the inner shear failure surface

With the aid of Equation 5.2, Figure 5.9 and Table 6.1 we calculate the average inner friction angle

$$\phi_{avI} = \boldsymbol{arctan}\frac{15.3\boldsymbol{tan}32 + 9.4\boldsymbol{tan}22}{24.7} = 28^0$$

Step 2. Inner shear surface inclination angle

Based on the arguments in Chapter 5, we assume an inner shear zone surface inclination angle of $\beta_I = 45^0$.

Step 3. Inner vertical tensile fracture

A vertical line is drawn from the crest of the slope to the zero horizontal stress contour.

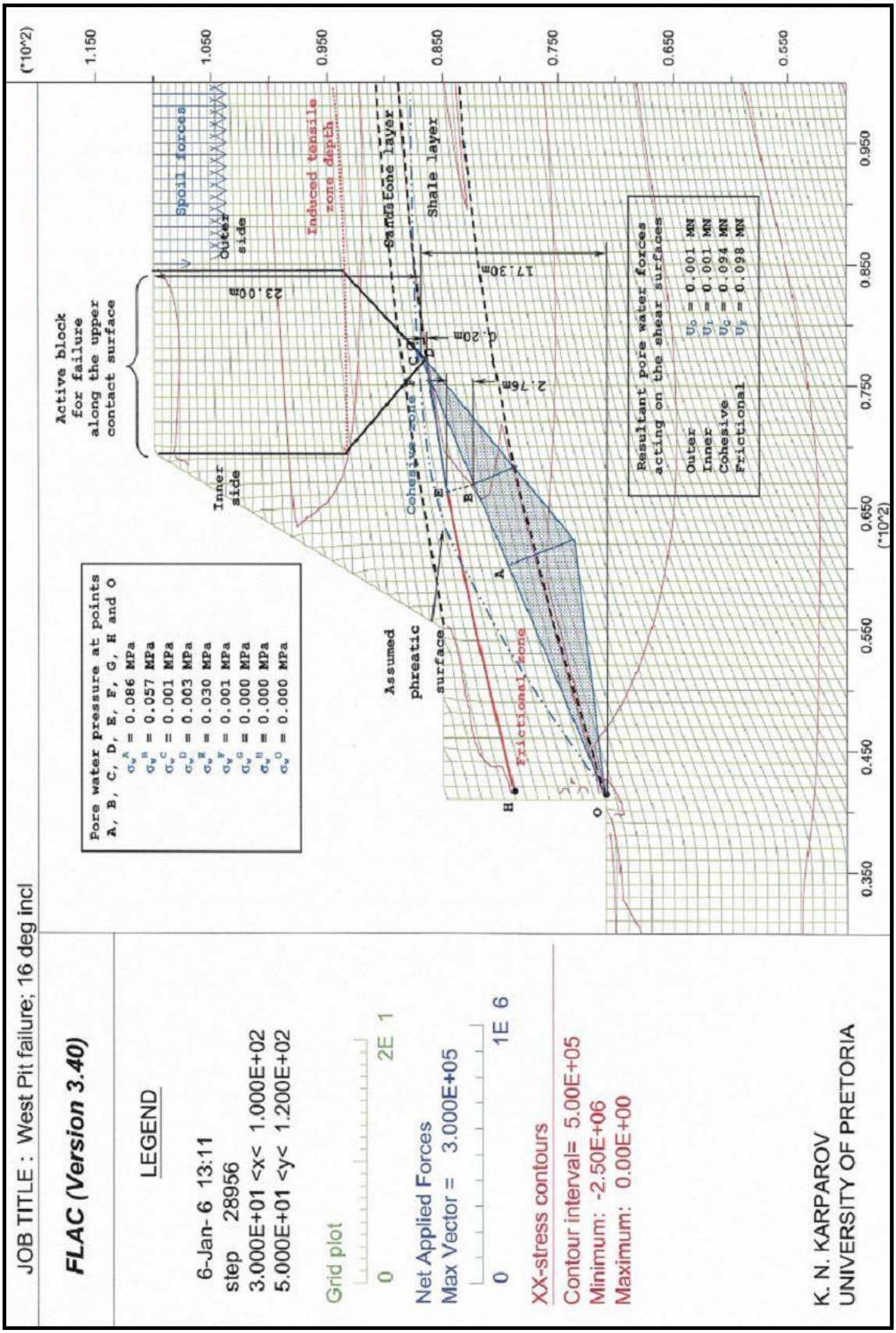

Figure 6.4a
Single slope profile along the upper contact in Colliery A-2 with tensile fractures along the upper contact surface of the embedded shale layer

Step 4. Inner shear failure surface

From the bottom end of the tensile fracture in the overburden to the upper contact surface of the embedded shale layer a line is drawn which dips toward the solid, with angle β_I=45° to the horizontal.

Step 5. Average cohesion of the inner shear failure surface

From Figure 6.4a, after Equation 5.3 and Table 6.1, the average cohesion along the inner shear failure surface:

$$c_{avI} = \frac{6.21*0.04 + 2.76*0.7}{8.97} = 0.243 \text{ MN/m}^2$$

Step 6. Inner shear failure surface length

The length of the shear zone surface is $l_I = \sqrt{2}\Delta h$, where Δh is the elevation difference between the base of the tensile zone and the top shale contact. Hence, l_I = 9.83m.

Step 7. Average friction angle along the outer shear failure surface

After Equation 5.2, Figure 5.9 and Table 6.1 we have:

$$\phi_{avO} = \arctan\frac{14.5\tan 32 + 8.5\tan 22}{23} = 29^0$$

Step 8. Outer shear surface inclination angle

As for the inner shear surface, we assume a 45° inclination, i.e. $\beta_O = 45^0$.

Step 9. Outer shear failure surface

From the intersection of the inner shear failure surface with the upper contact of the embedded shale

layer a line is drawn upwards and towards the solid, with angle β_O=45° to the horizontal, until the intersection with the bottom contour of the induced tensile zone in the overburden.

Step 10. Outer vertical tensile fracture

From the upper end of the outer shear failure surface a line is drawn vertically upwards to surface.

Step 11. Average cohesion of the outer shear failure surface

After Equation 5.3, Figure 6.4a and Table 6.1 for the average cohesion along the outer shear failure surface, we have:

$$c_{avO} = \frac{6.04*0.04 + 2.93*0.7}{8.97} = 0.256\ MPa$$

Step 12. Outer shear failure surface length

The length of the outer shear zone surface is $l_O = \sqrt{2}\Delta h$, where Δh is the elevation difference between the base of the outer tensile zone and the top shale contact. Hence, l_I = 9.24m

Step 13. Frictional zone load

From Equation 5.4, Table 6.1 and Figure 6.4a we calculate the frictional zone load P_f = 4.194 MN/m^2

Step 14. Frictional zone length

From Figure 6.1 we have l_F = 25m frictional zone length, which is plotted in Figure 6.4.

Step 15. Average angle at the frictional zone failure surface

From Figure 6.4a we have an average $\varpi_F = 13^0$ inclination of the frictional zone failure surface.

Step 16. Cohesive zone load

From Equation 5.4, Table 6.1 and Figure 6.4a we calculate the frictional zone load P_c = 2.223 MN/m^2

Step 17. Cohesive zone length

From Figure 6.4a we have l_c = 11m in length after construction of the active block.

Step 18. Average angle at the cohesive zone failure surface

From Figure 6.4a we have an average $\varpi_C = 10^0$ inclination of the frictional zone failure surface.

Step 19. Active block load calculation

After Equation 5.4, Table 6.1 and Figure 6.4a we have P_A = 5.365 *MN*.

Step 20. Angle at the active block wedge

From Figure 6.4a we have $\varpi_A = 9^0$.

Step 21. Passive block reaction force to the inner failure surface

The passive block driving and resisting forces are the sum of respectively driving and resisting forces of the frictional and cohesive zones along the surface of the investigated failure. For the calculation of the driving and resisting forces along the frictional zone we use Equations 5.5b and 5.6 respectively, and for the

calculation of the driving and resisting forces along the cohesive zone we use Equations 5.7b and 5.7a respectively. Hence, after Equation 5.28 we have:

$$P_F^{dr} = P_F \sin \varpi_F = 4.194 \sin 13 = 0.943\ MN$$

$$P_F^{res} = P_F \cos \varpi_F \tan \phi_E = 4.194 \cos 13 \tan 8 = 0.574\ MN$$

$$P_C^{dr} = P_C \sin \varpi_C = 2.223 \sin 10 = 0.386\ MN$$

$$P_C^{res} = c_B l_B + P_C \cos \varpi_C \tan \phi_E = 11 * 0.1 + 2.223 \cos 10 \tan 8 = 1.408\ MN$$

Therefore, the total driving and resisting forces have values $P_P^{dr} = 1.329\ MN$ and $P_P^{res} = 1.982 MN$. Then the net passive block reaction force is $R_P = 0.653 MN$ (Equation 5.28) and this force in an opposite way acts to the active block load reaction (Figure 5.18b).

Step 22. Pore-water pressure calculations

Figure 6.4a shows a pore-water stress diagram and the calculated pore-water pressure at the points along the failure surfaces. From the figure we measure distances between the points GD, FD, DE and EH and their lengths are l_{GD}=1.18m, l_{FD}=1.18m, l_{DE}=2.65m and l_{EH}=11.19m respectively. Then using Equations 5.24 – 5.27 we calculate the resultant forces along the outer, inner, cohesive and frictional failure surface, which have following values:

$$U_O = \frac{l_{GD}\sigma_w^D}{2} = \frac{1.18 x 0.001}{2} \cong 0.001\ MN$$

$$U_I = \frac{l_{FD}\sigma_w^D}{2} = \frac{1.18 x 0.001}{2} \cong 0.001\ MN$$

$$U_C = \frac{l_{DE}\left(\sigma_w^D + \sigma_w^E\right)}{2} = \frac{2.65(0.001 + 0.034)}{2} \cong 0.046\ MN$$

$$U_F = \frac{l_{EH}\sigma_w^D}{2} = \frac{11.19\,x\,0.034}{2} \cong 0.190\ MN$$

In Figure 6.4a the magnitudes of the resultant forces acting on the shear failure planes are also shown. It can be seen that the applied pore-water pressure diagram is different from the diagram in Figure 6.4a, which represents a general scenario and could appear in other geotechnical profiles.

Step 23. Condition for the existence of the inner shear failure surface

At the active block wedge we have a layer inclination angle $\varpi_A = 9^0$. After Equation 5.32 we have:

$$\eta = FOS_I = \frac{0.243 * 9.83 - 0.001\,tan\,28}{\frac{5.365(1 + sin\,9)\,sin\,45}{2} - 0.653\,sin\,28} = 1.266$$

With this value of the criterion η we do not have conditions for the inner shear failure surface formation to be created at the active block. This value is higher than that accepted by the author (1.3 for the minimum safety factor value), which is based on the safety factor coefficients for the open pit mines in other leading mining countries such as USA and Canada, as shown in Appendix 5

Step 24. Calculation of the reaction force acting along the outer shear failure surface

Following Equation 5.33 we have:

$$\overline{R} = \frac{5.365}{2}(1+\sin 9)\cos 45 - 0.653\cos 28 = 1.617\ MN$$

Step 25. Calculation of the outer shear failure surface safety factor

The outer shear failure surface will have a factor of safety equal to (Equation 5.35):

$$FOS_o = \frac{0.256*9.24 + \left[\frac{5.365}{2}(1-\sin 9)\cos 45 - 0.001 - 0*\sin 45\right]\tan 29}{1.617 + \frac{5.365}{2}(1-\sin 9)\sin 45 + 0*\cos 45} = 1.011$$

Step 26. Calculation of the safety factor on the basal shear failure surface

After Equation 5.36 for the base of the passive block we have a safety factor equal to:

$$FOS_B = \frac{4.194\cos 13\tan 8 + 11*0.1 + 2.223\cos 10\tan 8 - (0.094+0.098)\tan 8}{4.194\sin 13 + 2.223\sin 10} = 1.470$$

Step 27. Calculation of the slope stability factor of safety

After Equation 5.37 for the total slope stability factor of safety we have:

$$FOS = \frac{1.266*9.83 + 1.011*9.24 + 1.470*36.00}{9.83 + 9.24 + 36.00} = 1.375.$$

Therefore, the failure along the top contact will not occur.

6.2.2 Example 1b: Safety factor calculations along the bottom contact surface

Figure 6.4b shows the investigated slope profile with failure surface along the bottom contact and the pore-water pressure diagram. In Section 6.2.1 the calculation sequence of the proposed method was demonstrated. For simplicity, in this example, we will discuss only the results, as the calculation sequence itself is tabulated in Table A4.1 (Appendix 4).

As safety factors we have following values:

- FOS of the inner shear failure surface 0.914
- FOS of the outer shear failure surface 0.709
- FOS of the basal shear failure surface 0.750
- FOS of the slope 0.777

In this example we have safety factors 0.914 and 0.709 for the inner and outer shear failure surfaces respectively. Therefore, we have conditions for blocky-type of failure through the thrust failure mechanism.

In the case without spoils, safety factors along the failure surfaces have following values:

- FOS of the inner shear failure surface 1.031
- FOS of the outer shear failure surface 0.875
- FOS of the basal shear failure surface 0.663
- FOS of the slope 0.794

The above results show that we will have failure even in the case without spoils.

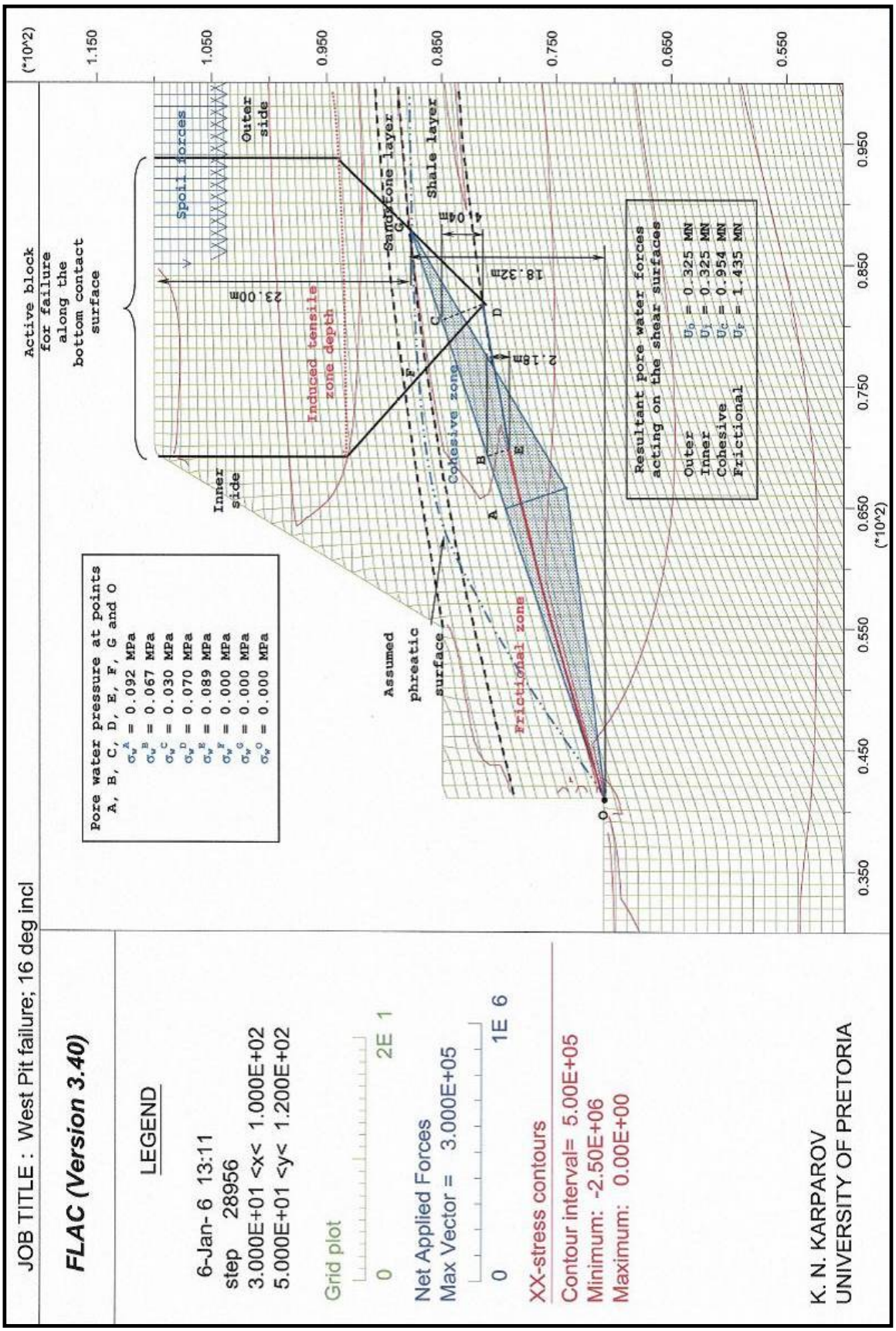

Figure 6.4b
Single slope profile along the upper contact in Colliery A-2 with tensile fractures along the bottom contact surface of the embedded shale layer

6.3 EXAMPLE 2: PIT A-1 SLOPE FAILURE

In Chapter 1 it was mentioned that the slope failure at pit A-1 took place in two stages: first, initial failure (circular type) in the sandy overburden; and a major collapse shortly after the cleaning operations. It is matter of interest what safety factor values for both failures we should have after the application of the proposed method.

The slope profile before failure appears in Figure 1.5. Three FLAC models were prepared for an investigation of the failure sequence. The first model presents the virgin mining conditions. The second model incorporates the slope with a slope angle 55^0 and presents the situation before initial failure (Figure 6.5). The third model (Figure 6.6) has a slope angle of 50^0 and corresponds to the highwall profile after the cleaning operations. From the models, stress differences normal to bedding ($\Delta\sigma_N$) along the top and the bottom contact of the embedded shale layer were calculated (Figure 6.7).

The slope failure took place in the same colliery as the failure discussed as Example 1, but in a mined out area. For this reason, it was impossible to prepare thin sections to study the micromechanical reasons for failure. The author assumes that the shale layer in the failed area had the same matrix and minerals as those for the failure shown in Section 6.2, Example 1. Therefore, we assume the same average carbon flake size and distribution and, consequently, the same calculated critical tensile stress (discussed in Chapter 4).

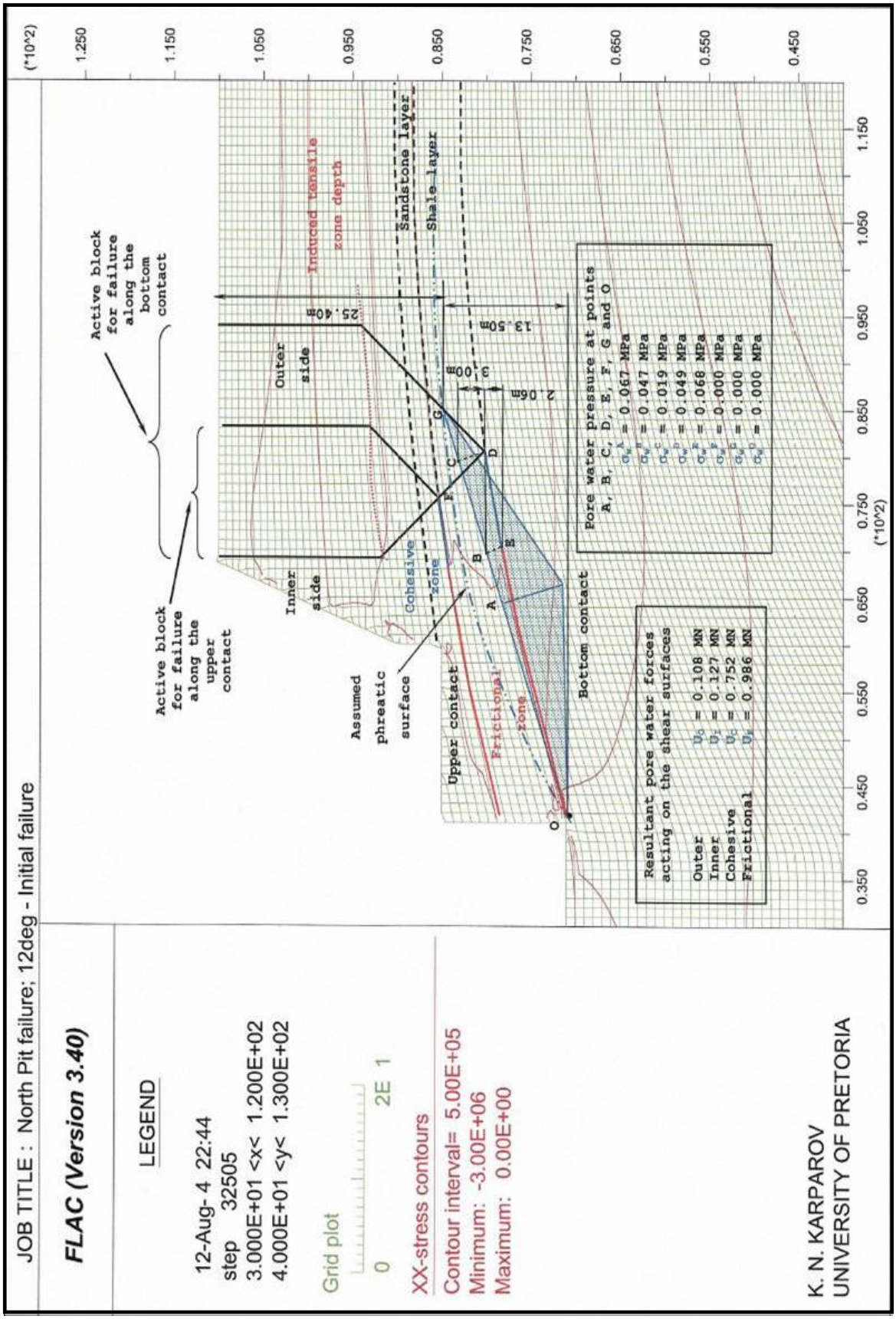

Figure 6.5
Failed slope profile in Colliery A-1 with the tensile fractures along the contact surfaces of the embedded shale layer before initial failure

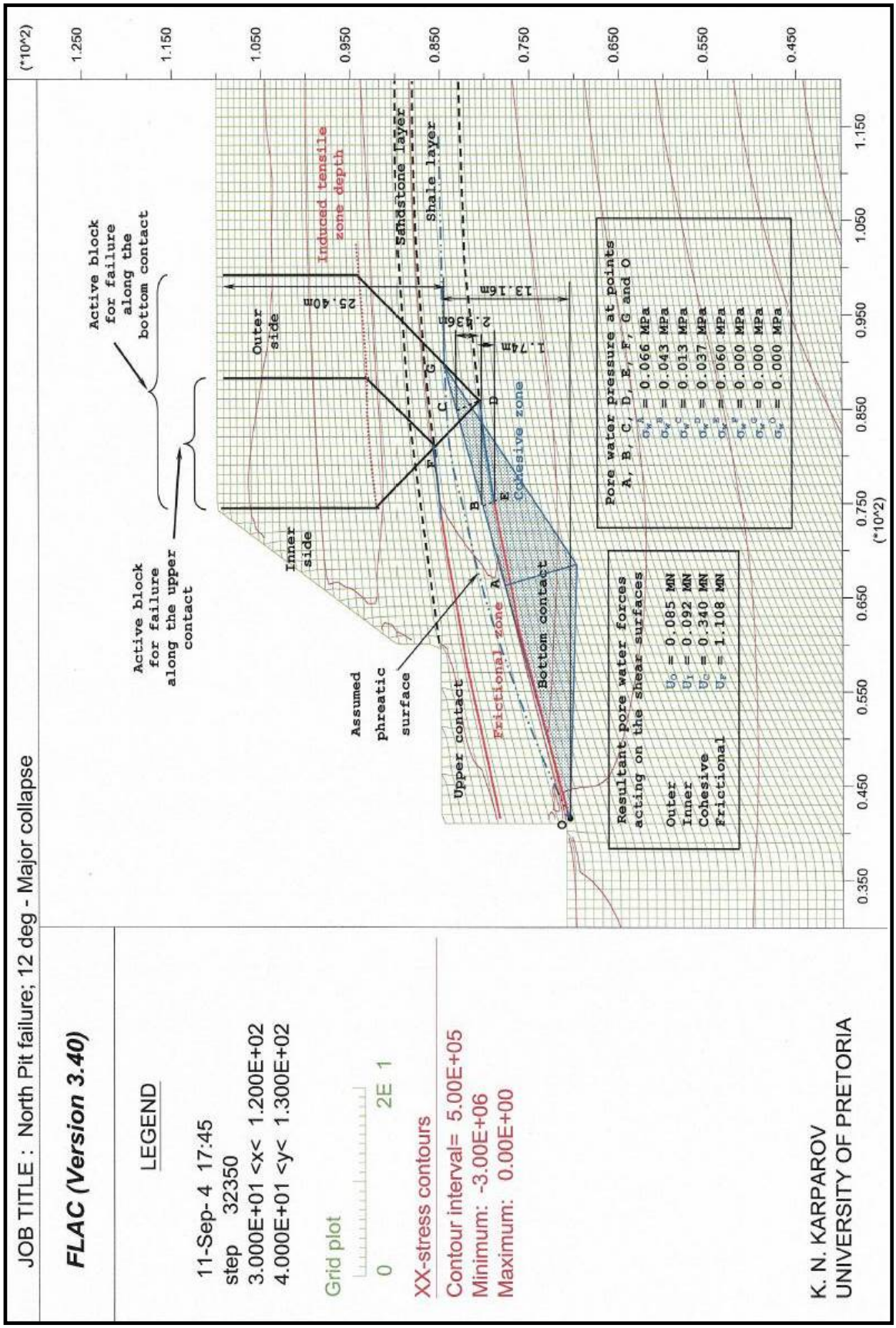

Figure 6.6
Failed slope profile in Colliery A-1 with the tensile fractures along the contact surfaces of the embedded shale layer before major collapse

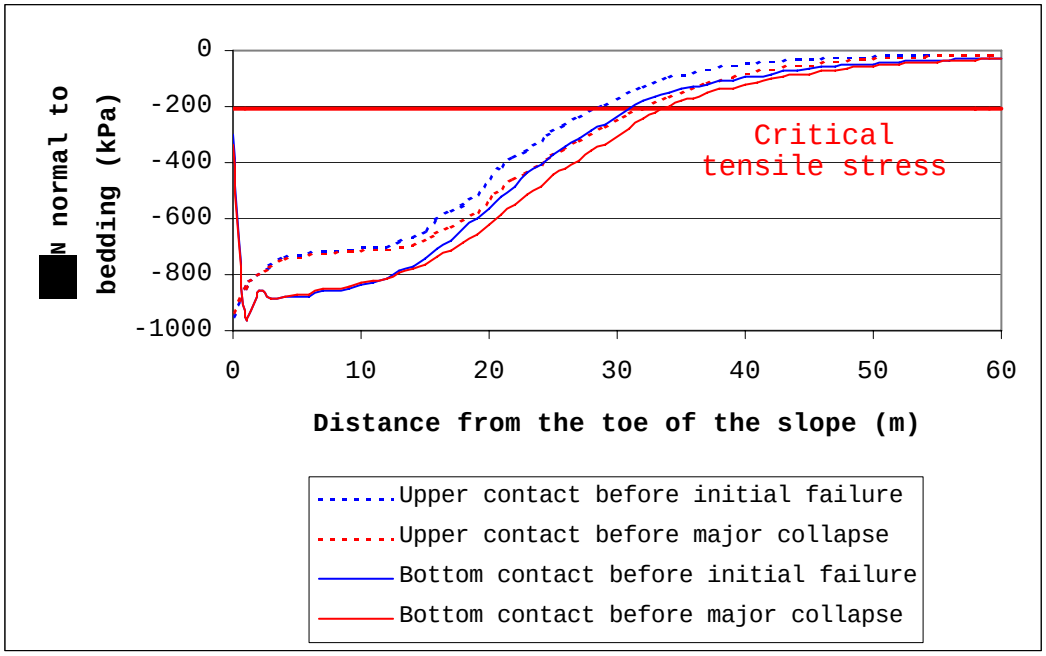

Figure 6.7
Stress component normal to bedding at the upper and bottom contact surfaces of the embedded shale layer with the value of the critical tensile stress, calculated in Chapter 4

Hence, in the figure we can plot the same σ_N^P value as calculated in Chapter 4 (the bold red line in Figure 6.7). It is seen that, because of the relaxation that result from cleaning operations, the tensile fracture increases from 27m to 32m from the toe of the slope along the upper contact and from 29m to 34m along the bottom contact. In this example, with the aid of the proposed method, we will calculate the safety factors of the two consequent failures at pit A-1, as discussed in Chapter 1. The calculated sequence and results are shown in Tables A4.2-A4.5 (Appendix 4). Shown here are only the safety factors of the separate surfaces and the slope safety factor.

According to the data recorded in the mining files, phreatic surface of the underground water was estimated at 25.40m below surface. From Figures 6.5 and 6.6 it can be seen that the upper contact surface of the embedded shale layer is above the estimated phreatic surface. Therefore, the pore-water pressure influence on the slope stability calculations is not taken into account.

Similar to the previous failure, the induced surface tensile zone was calculated and plotted in Figure 6.8. These induced tensile zones can be seen on a bigger scale plotted in Figures 6.5 and 6.6, for the profiles before the initial failure and before the major collapse.

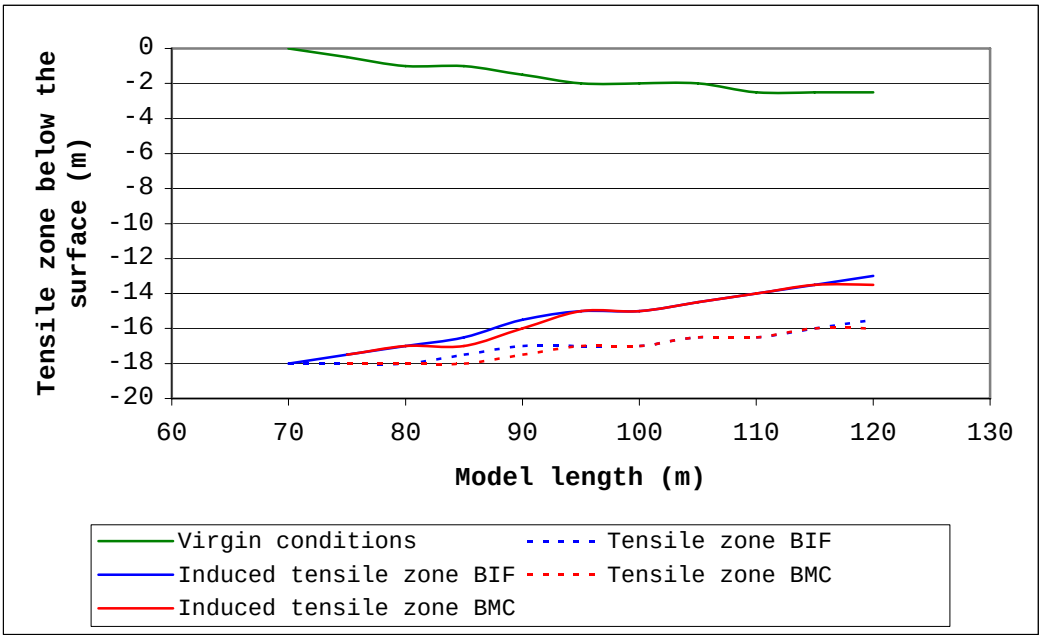

Figure 6.8

Tensile zone depth in virgin conditions, before the initial failure (BIF) and before the major collapse (BMC)

Calculated safety factors of the profile before initial failure:

At the upper contact,

- FOS of the inner shear failure surface 1.010
- FOS of the outer shear failure surface 0.955
- FOS of the basal shear failure surface 1.108
- FOS of the slope 1.062

At the bottom contact,

- FOS of the inner shear failure surface 1.036
- FOS of the outer shear failure surface 0.926
- FOS of the basal shear failure surface 0.833
- FOS of the slope 0.902

Calculated safety factors of the profile before major collapse:

At the upper contact,

- FOS of the inner shear failure surface 1.149
- FOS of the outer shear failure surface 0.935
- FOS of the basal shear failure surface 1.318
- FOS of the slope 1.224

At the bottom contact,

- FOS of the inner shear failure surface 1.161
- FOS of the outer shear failure surface 0.884
- FOS of the basal shear failure surface 0.826
- FOS of the slope 0.908

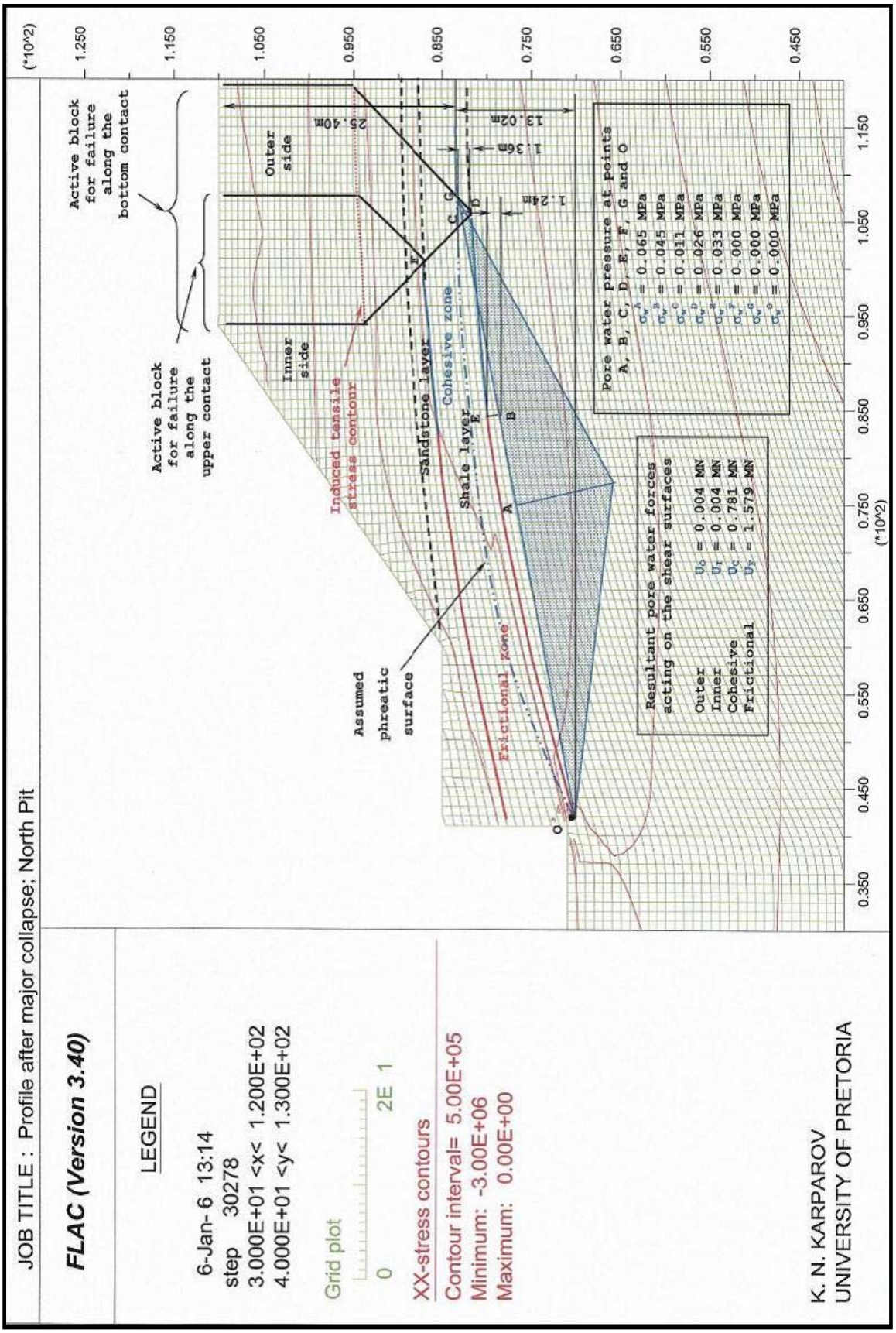

Figure 6.9
Profile after major collapse in Colliery A-1 with the tensile fractures along the contact surfaces of the embedded shale layer

From Figure 6.7 and the relatively lower safety factor along the bottom shale contact with the middle coal seam one might deduce the slope will always fail when the slope angle is reduced. Of course, this is not true and to confirm it let us reduce the slope angle of the profile from Figure 6.6 (slope before major collapse) to 37^0, which is the slope angle of the profile after the major collapse (see also Figure 1.4). This profile is shown in Figure 6.9.

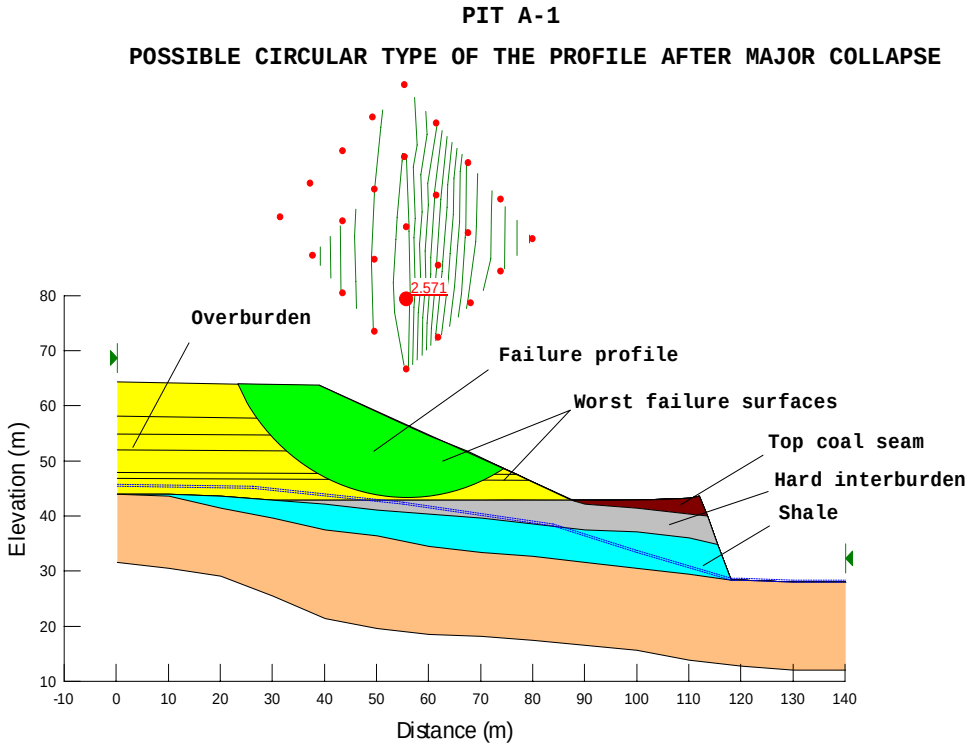

Figure 6.10

Safety factor for circular failure of the profile after major collapse after Morgenstern-Price

Figure 6.10 presents the profile after major collapse with the Morgenstern-Price method for the safety factor calculation. The other slope stability methods show similar values (ordinary – 2.206; Bishop – 2.575; Janbu – 2.164). The same model was run with FLAC and the stress difference normal to the bedding is plotted in

Figure 6.11. For the sake of comparison the stress normal to bedding ($\Delta\sigma_N$) in the contact surfaces from the profile before major collapse (Figure 6.7) and the critical stress ($\Delta\sigma_N^P$) are also plotted. Safety factor calculations are tabulated in Tables A4.6 and A4.7 (Appendix 4).

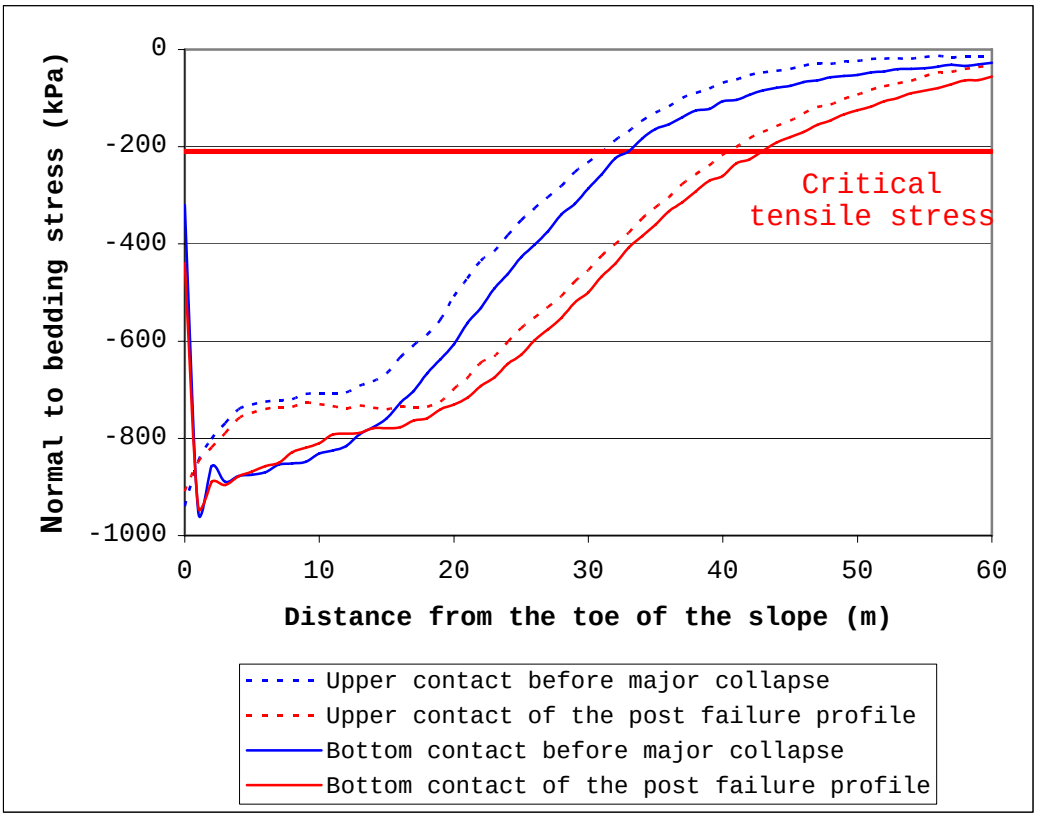

Figure 6.11

Stress component normal to bedding for the slope profile at Pit A-1 for the major collapse and the profile after major collapse

Calculated safety factors of the profile after major collapse:

At the upper contact,

- FOS of the inner shear failure surface 1.710
- FOS of the outer shear failure surface 1.222
- FOS of the basal shear failure surface 2.029
- FOS of the slope 1.860

At the bottom contact,

- FOS of the inner shear failure surface 1.658
- FOS of the outer shear failure surface 1.527
- FOS of the basal shear failure surface 1.291
- FOS of the slope 1.398

From the calculated FOS value it can be seen that the slope stability safety factor increases with further reduction of the slope angle. The reason for this is that flattening the slope angle has the effect of increasing the passive block size while at the same time removing the possible active block formation further away from the slope toe. See Figure 6.9 and compare it with Figure 6.8.

The slope failures in pit A-1 are very challenging to predict in terms of the newly proposed thrust failure mechanism, and at the same time very difficult to analyse with the aid of the well-known limit equilibrium methods. In the first place, both failures appeared in the same area. This means that in two failures we deal with identical rock properties and geotechnical conditions. Secondly, on the basis of the methods of slices the failures are very difficult to explain; why does a major collapse occur (as an event much bigger than the initial failure – see Figure 1.4) after an initial failure, which made the slope angle 5^0 flatter? The verification of the newly proposed thrust failure mechanism lies in the successful analysis of the failures and the mechanism's ability to give reasonable answers to the above question.

6.4 DISCUSSION

In general, the widely used limit equilibrium methods based on slices were created to fulfil the stability needs of earth dam walls, where the structure is relatively homogeneous, which is not the case with slope profiles in the mining industry. Figure 1.2 clearly shows all failure modes in open pit mining and consequently our success to prevent or predict them in practice. As a general weakness of the all known slope stability methods is that they cannot distinguish between natural and artificial slope profiles, where stress redistribution takes place in the strata.

In Chapter 3 we calculated the stress difference between the virgin and resultant stress state in the slope profile, which is actually the difference between the two slope types (natural and artificial). This difference, and particularly the stress component normal to sedimentation ($\Delta\sigma_N$), does not exist in the natural slope profile. For the sake of accuracy, it needs to be said that with time this difference diminishes (dissipates in deformation or fracturing), but this problem is then related more to time-dependent rock behaviour. In the same chapter we calculated the stress difference normal to sedimentation along the basal failure surface, which is tensile. It was interesting to see that the value of $\Delta\sigma_N$ increases with the flattening of the slope angle.

Bieniawski (1967) and Hoek and Bieniawski (1965) suggested that the weakest minerals in the rock matrix could be involved in tensile fracture propagation in low-porosity rock. In Chapter 4 was shown that carbon

flakes in the matrix of the shale layer are most susceptible to the remote tensile stress and could be used as an initial flaw in fracture initiation. This model is based on the Dugdale-Barenblatt analysis (Dugdale, 1960; Barenblatt, 1962) of a cohesive strip model. The Dugdale-Barenblatt model was extended to a periodic row of flaws, corresponding to the observed distribution of carbon flakes in the shale. In the chapter, the critical tensile stress ($\Delta\sigma_N^P$) for the specific embedded shale layer was calculated. We defined the fracture-process zone length as a major element in the $\Delta\sigma_N^P$ calculation. This zone length determines the $\Delta\sigma_N^P$ magnitude and the author's suggestion is that it should be used as a rock property.

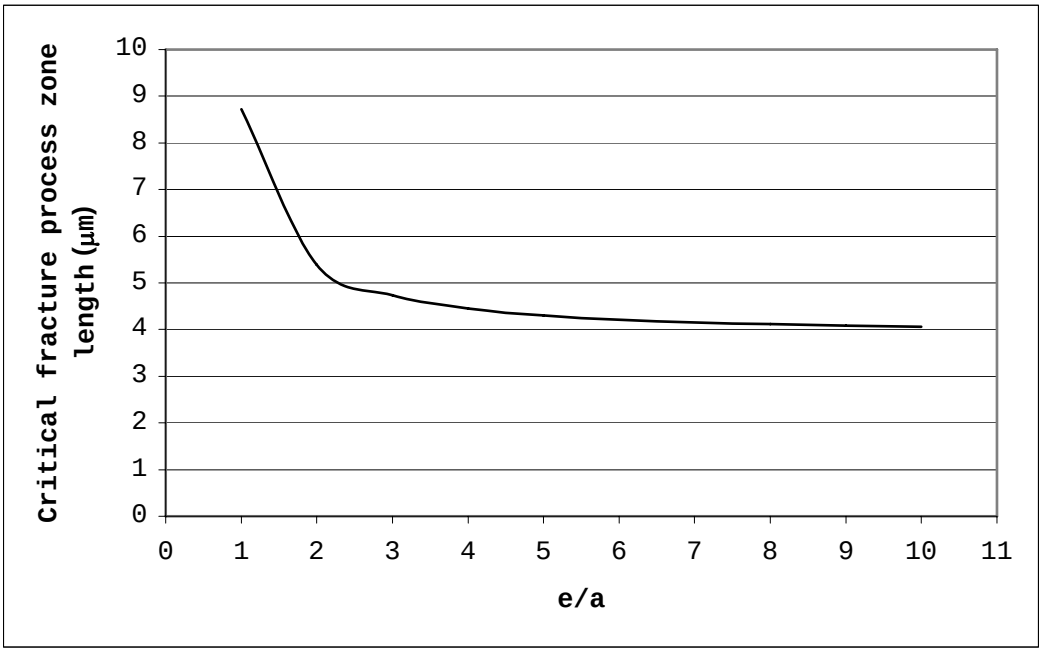

Figure 6.12

Dependence of the critical fracture process zone length (l_c) on a dimensionless coefficient; distance between flakes over half flake length (e/a)

Figure 6.12 shows the relationship (after Equation 4.20) between the critical fracture process zone length (l_c) and a dimensionless coefficient of the distance between flakes (e) and a half flake length (a). In the figure, the critical fracture-process zone length is proportional to the distance between two neighbouring flakes and inversely proportional to the flake length. We can also see that these parameters have a very strong relationship if the distance between neighbouring flakes is shorter than the flake length, and very weak relationship if this distance is longer.

For practical purposes it is more interesting to see the influence of these three parameters on the critical tensile stress value, $\Delta\sigma_N^P$. For this purpose let us use Equation 4.25 (as well as Equation 4.29) where $\Delta\sigma_N^P$ is proportional to the coefficient $\boldsymbol{arccos}\dfrac{\boldsymbol{sin}(\pi a/w)}{\boldsymbol{sin}[\pi(a+l_c)/W]}$. Further calculations show that this coefficient and consequently $\Delta\sigma_N^P$ drop only 0.3% when e/a increases 10 times. This is another confirmation for the constant value of the critical tensile stress ($\Delta\sigma_N^P$) in rocks.

To be sufficiently accurate at this point we should also discuss the influence of the shear stress on the failure process. Owing rock fracture mechanics, if we have shear stress and appropriate stress concentrators (in our case, carbon flakes), we should have conditions for mode II (shear) fracture propagation. Whittaker et al. (1992) discussed the critical fracture toughness coefficient of mode II (K_{IIC}), which is related to the mode I fracture toughness coefficient (K_{IIC} = 0.866K_{IC}). According to the laboratory test results, the shear

strength of most of the embedded weak layers (i.e. shale, siltstone or mudstone) is 25-30% higher than the rocks tensile strength results. Hence, according to the superimposed principle for mixed Mode I-II failure, we have a critical fracture process zone length as a result of the combined action of the remote applied stresses (tensile and shear). Following our Equation 4.20, by analogy we can say that the critical fracture process zone as a result of mode II loading will be shorter than the fracture process zone length as a result of relaxation. Hence for the simplicity of the calculations only the critical fracture process zone length was used in the thesis.

Of course this is not a general rule of analysis. With an increase in the slope depth we have a change in the k-ratio and, consequently a different stress state. The author thinks that with the increase in depth, the role of the relaxation stress will decrease, with the increase of influence of the shear stress on the fracture propagation process. It seems that in shallow-depth cuts (30-40m) the failure is driven by the $\Delta\sigma_N$, not the absolute stress state itself. Then in shallow cuts, the stress across certain flakes must still be compressive after the slope has been cut, even though there is a tensile stress ($\Delta\sigma_N$) that has been superimposed on the virgin stress state as an average value, coming from the continuity of the model. Stress deviation from the average value will occur because of the inhomogeneity of rock.

The new slope stability model is introduced in Chapter 5. We have calculated the safety factors associated with the two slope failures discussed in Chapter 1.

Table 6.2 Minimal safety factors, calculated for the failures presented in Figures 1.5 and 1.8 (including pore-water pressure)

Failure type	Thrust failure mechanism	Ordinary	Bishop	Janbu	Morgenstern - Price	
					Moment	Force
Pit A-2						
Circular failure	-	2.434	2.649	2.354	2.572	2.569
Blocky failure	-	1.198	0.157	0.152	0.113	0.144
Upper contact with spoil	1.375	-	-	-	-	-
Bottom contact with spoil	0.777	-	-	-	-	-
Upper contact - no spoil	1.287	-	-	-	-	-
Bottom contact - no spoil	0.794	-	-	-	-	-
Pit A-1; Initial failure – circular type						
Circular failure	-	0.709	0.729	0.708	0.722	0.716
Blocky failure	-	0.738	0.733	0.715	0.103	0.104
Upper contact	1.062	-	-	-	-	-
Bottom contact	0.902	-	-	-	-	-
Pit A-1; Major collapse – blocky type						
Circular failure	-	1.506	1.516	1.507	1.513	1.509
Blocky failure	-	4.718	4.619	4.329	4.870	4.870
Upper contact	1.224	-	-	-	-	-
Bottom Contact	0.908	-	-	-	-	-

These safety factors, together with the safety factors calculated by some of the well-known equilibrium methods appear in Table 6.2.

The table presents the calculated safety factors of the slope failure that took place in pit A-2, with spoil material behind the slope crest. There is very good agreement between the calculated safety factors in terms of the different methods for circular-type failure, but they indicate stable conditions for a slope that failed (FOS is between 2.354 and 2.649). Calculated results for blocky-type failure are unacceptably low, with values of about 0.12. If we have such low safety factors of the slope profiles, then we definitely will have failure during the construction of the slope. Obviously, the safety factor calculation process for blocky-type failure using slices is interfered with by the external load application.

The safety factors presented in Table 6.2 correspond to the multi-stage failure that took place in pit A-1 where was no external loading behind the crest of the slope (i.e. no spoil pile). Again, we have very good agreement between the safety factors calculated by the different methods for circular failure. Safety factors for blocky-type failure have more realistic values than for the previous case of failure and are close to those for circular failure, with the exception of the Morgenstern-Price calculation. The safety factors suggest both circular and blocky failure, without providing any information on which failure mechanism is more likely. In reality, the initial failure was circular in type and was reported by SRK (1995). The proposed thrust failure mechanism indicates relatively

higher safety factors, (FOS=1.062 and FOS=0.902), along the upper and bottom contact surfaces respectively, compared to the circular safety factor (FOS=0.72), which shows that the initial failure was more likely to be circular.

The major collapse took place shortly after the cleaning operations following the circular-type failure. In Table 6.2 it can be seen that safety factors calculated by the limit equilibrium methods show a stable slope with safety factors of approximately 1.51 and 4.52 respectively for circular and blocky-type failure. Obviously, limit equilibrium methods, used for safety factor calculations, become inapplicable in cases characterized by complex geotechnical conditions such as inclined multi-layered slope profiles.

Figure 6.13 shows a plot of the average safety factors for the circular failure of the slope profiles from pit A-1 before the initial failure, before the major collapse, and of the profile after major collapse. The safety factors calculated by the proposed method along the upper and bottom contact surfaces of the embedded shale layer are also plotted. The figure shows that at the initial failure, the circular-failure type has a lower safety factor than the proposed method safety factor, and as a consequence, circular failure took place, as was observed in the field. The new slope profile after the cleaning operations has a higher safety factor for the circular type of failure in terms of the proposed method and, as a consequence, the major collapse took place as a blocky type of failure.

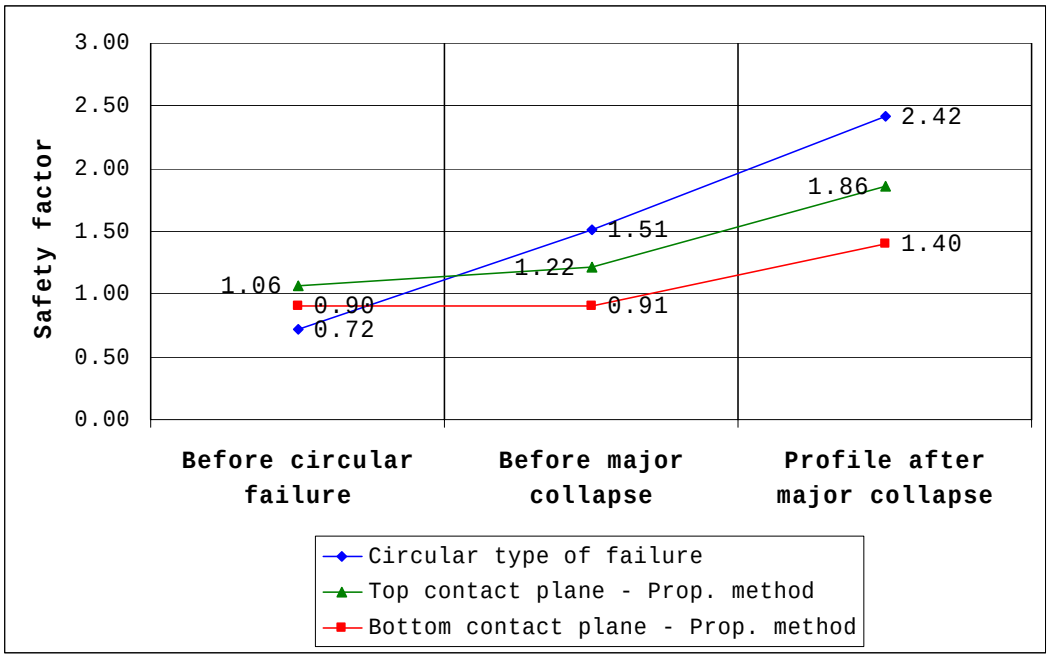

Figure 6.13

Plot of the average safety factors for circular-type failure and proposed method for blocky-type failure for the initial failure, major collapse and the profile after major collapse in pit A-1

The new slope profile (slope profile after major collapse - 10^0 flatter compared to the slope angle of the profile before major collapse) has safety factors indicating a stable slope profile and, in reality, there was no further failure. The other interesting feature, which can be seen on Figure 6.13, is the slope safety factors along the bottom contact surface. Here, despite the steeper slope angle of the profile before the initial collapse (55^0 slope angle), we have a relatively equal slope stability safety factor (0.902) to the slope angle of the profile before the major collapse (50^0 slope angle with FOS=0.909). In such situations there are clearly several conditions that have to be satisfied; e.g. dip angle, slope angle, cut depth and embedded layer thickness, which combination triggers the thrust failure mechanism.

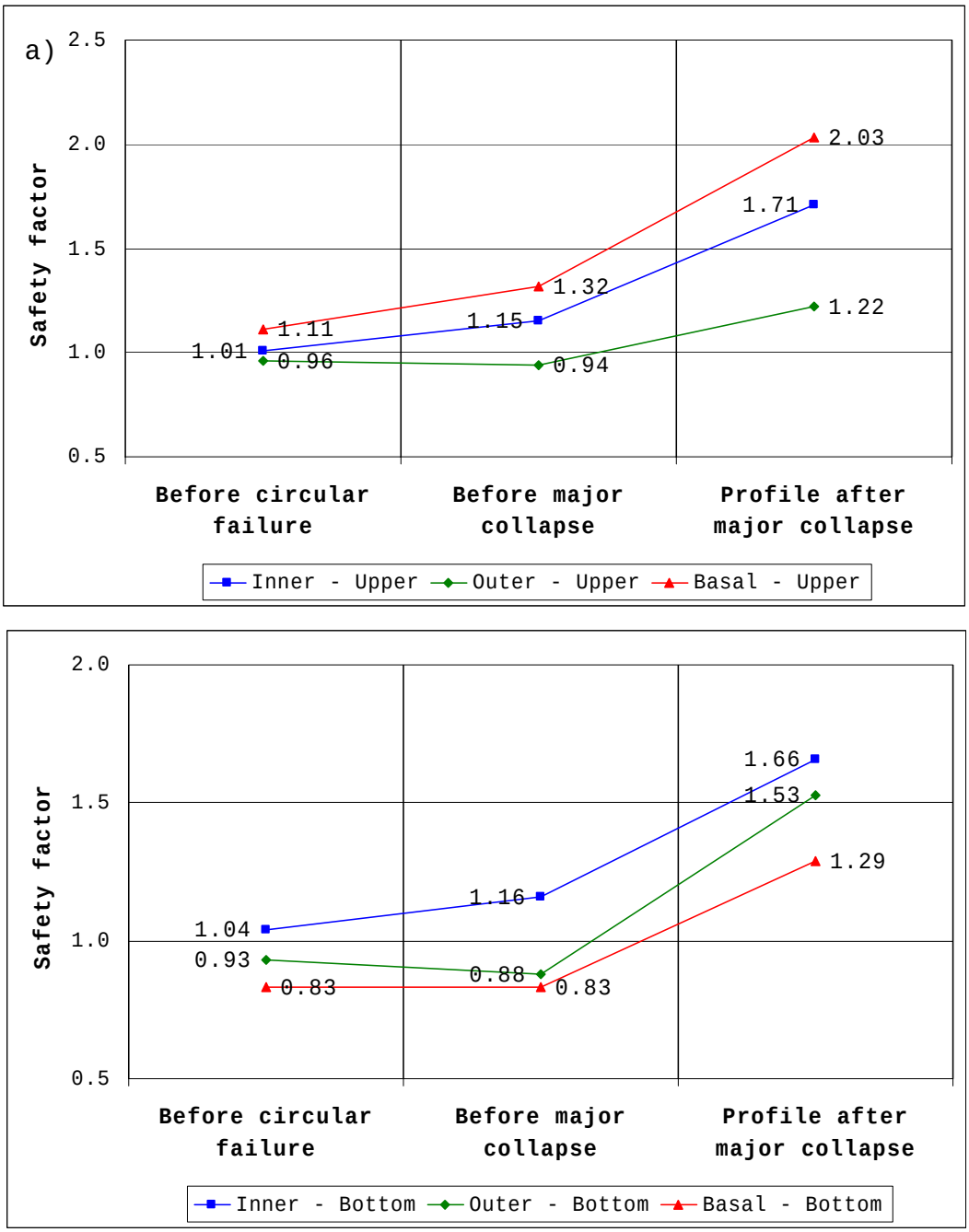

Figure 6.14

Plot of the safety factors on the separate shear failure surfaces of the proposed thrust failure mode for blocky-type failure along the: (a) upper contact surface; and (b) bottom contact surface before initial failure, major collapse and the profile after major collapse in Pit A-1

Figure 6.14 shows safety factors for the separate shear surfaces of failures along the top and bottom contact of the embedded shale layer. It can be seen that in all cases, the inner shear failure surface has a higher safety factor than the outer failure surface and follows the tendency of improvement of safety factors based on limit equilibrium methods in Figure 6.13. It is interesting to mention that the safety factor of the outer failure surface has almost constant value along the upper contact during the failure stages, while along the bottom contact surface the safety factor slightly decreases at the major collapse (FOS=0.88) compared to the initial failure (FOS=0.93). If we compare the calculated safety factors along the bottom contact surface (Figure 6.14b) before the initial failure with the safety factors before the major collapse, we will have confirmation for the specific conditions that triggered the thrust failure mechanism. In Figure 6.14b we have constant safety factor values along the bottom contact for initial failure and the major collapse. This means that initial failure does not improve the profile stability. Therefore, the safety factors along the contact surface has governing role for thrust failure mechanism.

Figure 6.15 shows the plot of the applied forces exerted by the separate blocks (active and passive) along the contact surfaces. Because of the lower depth, the applied load in the upper contact is lower than to the load on the bottom contact. The passive block load increases as a result of the increased length of the basal shear failure surface. Hence, the passive block load is proportional to the slope stability safety factor. This relationship can be used as an indication

that the proposed thrust failure mechanism could occur in deeper slopes with even a flat embedded weaker layer, such as a coal seam at the slope toe.

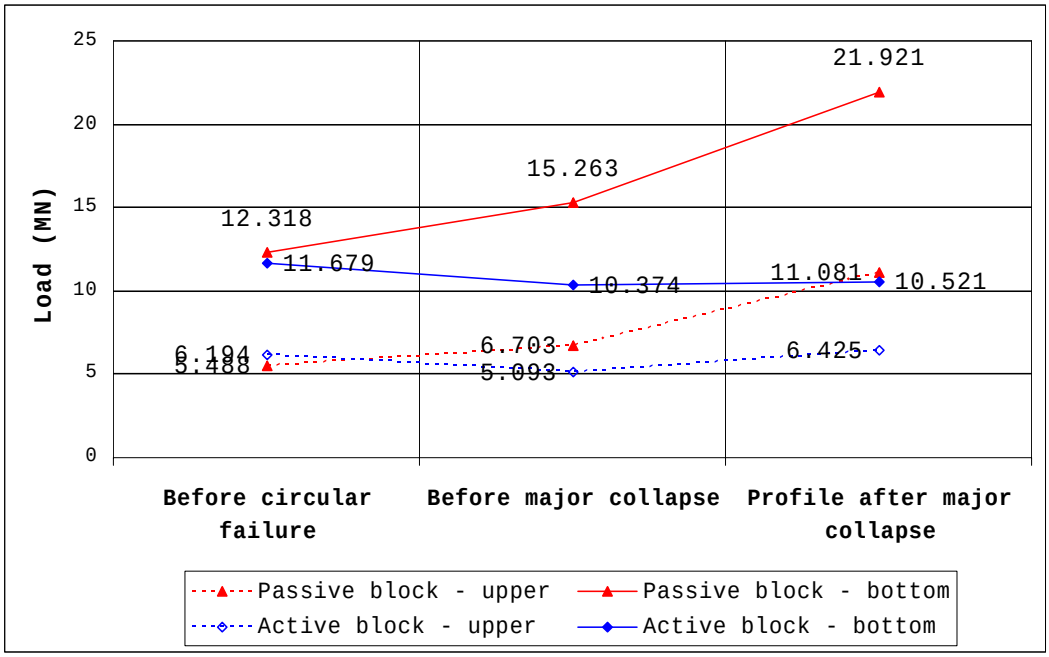

Figure 6.15

Force applied by the passive block (frictional plus cohesive zone) and the active block to the upper and bottom contact surfaces

The relationship of the blocks weight can be seen as a function of the contact surface inclination angle (bottom contact surface is always steeper than the upper). This relationship allows such failures to take place in shallow depths with steep contact surfaces for the embedded weaker layer.

Figure 6.16 presents the percentage of the frictional zone length in relation to the basal failure surface. It can be seen that before the initial failure we have frictional zone lengths of 86.5% and 83.3% from the potential failure surface in the passive block base along the upper and bottom contacts respectively.

Before the major collapse the frictional zone slightly increases to 87.2% and 86.7% along the upper and bottom contact surfaces respectively. In the profile after the major collapse, the frictional zone length along both surfaces drops to about 73%.

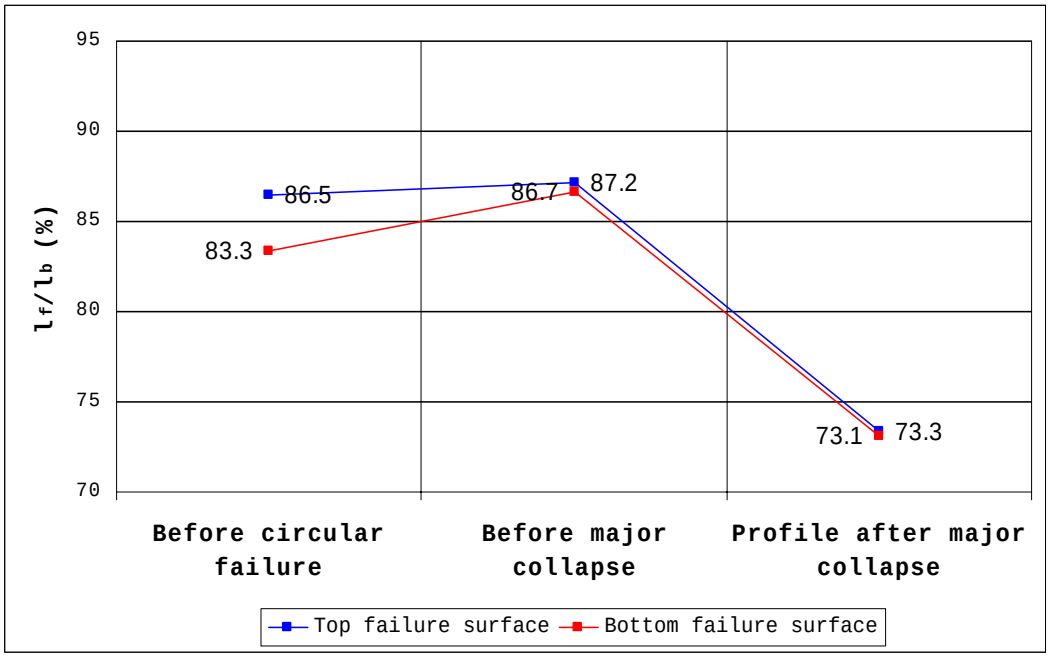

Figure 6.16

Percentage of the frictional zone length to the length of the basal failure surface (from the toe of the slope to the active block wedge)

This relation confirms again that slope failure is not a continuous process as a function of the slope angle flattening, but that there are conditions where the slope profile achieves stability. Surprisingly, in some conditions, the profile with the steeper slope angle is more stable than the profile with the flatter slope angle. Figures 4.10 and 4.11 also confirm where the profiles with a vertical slope angle have shorter frictional zone lengths than the profiles with a flatter slope angle. From Figure 6.16 it can be seen that along the bottom contact we have lower values for

the dimensionless coefficient l_f / l_b than for the upper contact. These findings mean that the upper contact surface of the embedded weak layer is more sensitive to the relaxation process than the layer's bottom contact surface but, because of the lower block weights, and flatter inclination angle we are less likely to have failure there compared to at the bottom contact.

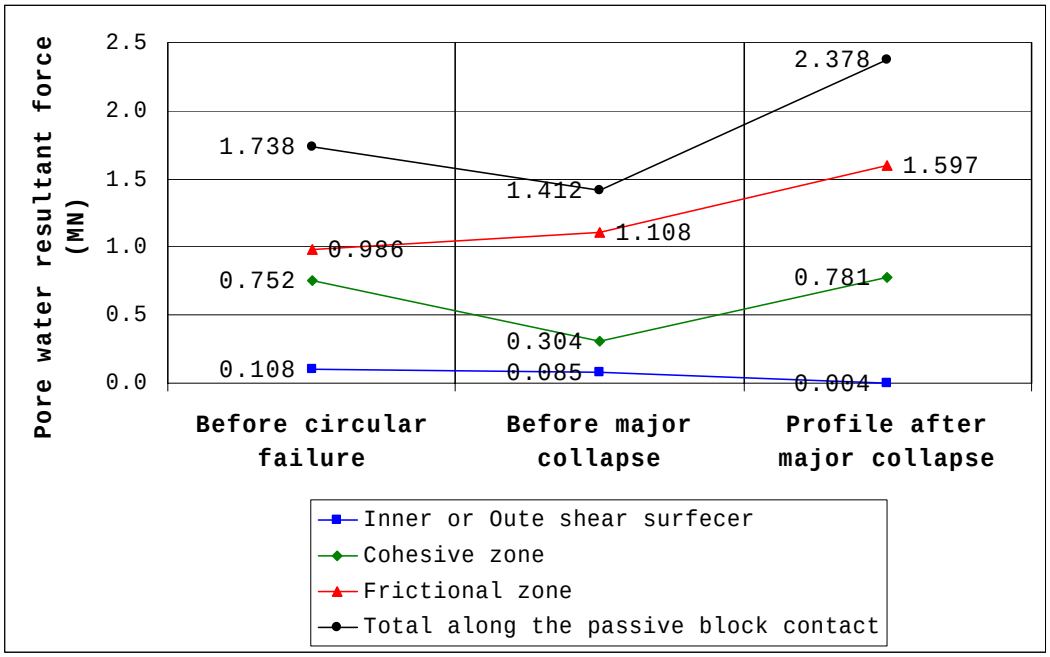

Figure 6.17

Resultant forces, created by the pore-water pressure and acting at the failure surfaces

Resultant forces, created by the pore-water pressure and acting at the failure surfaces, can be seen in Figure 6.17. As can be expected, the inner and outer sides of the active block shear surfaces have the lowest resultant force values, which is a function of their depth compared to the passive block shear surface (total length of the frictional and cohesive zones). In the figure, the lowest value of the pore-water pressure along the passive block contact is in the profile before the major collapse. It can clearly be seen that

before the major collapse we have the lowest value of the resultant pore-water force than for the other profiles. This low value can be explained by the fact that pore-water pressure is a function of depth and of length of the failed rock mass. In other words, the pore-water pressure is not the major factor that triggers the failure, because with the major failure we have the lowest pore-water pressure influence. Hence, we can indicate this as confirmation of the Stead and Scoble (1983) hypothesis that this failure mode is more stress related than the other geotechnical features are.

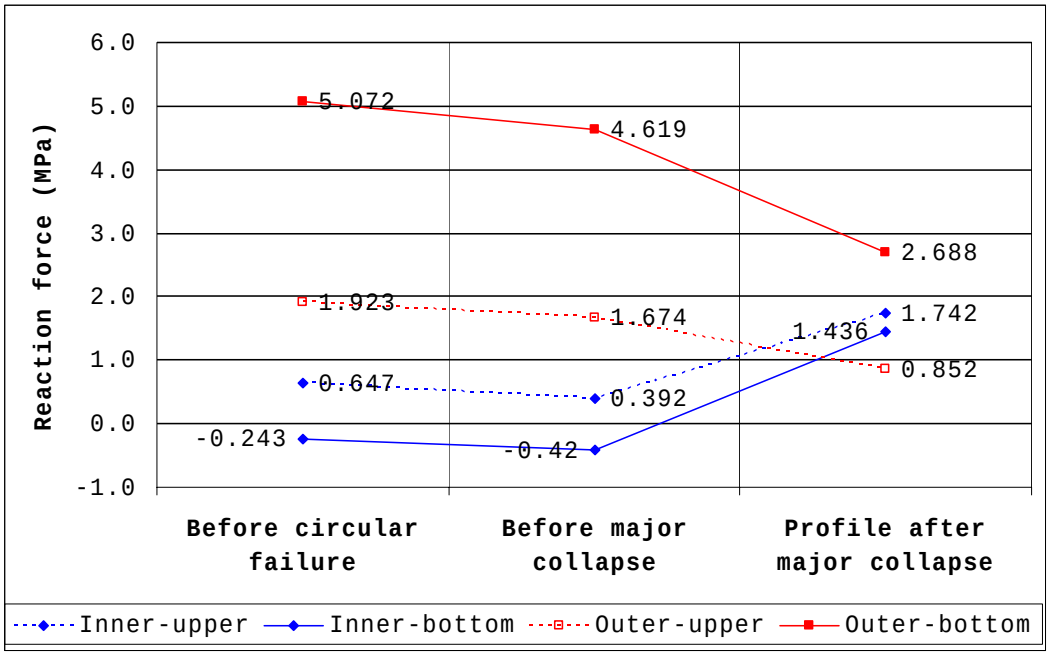

Figure 6.18

Reaction force of the passive block applied to the active block inner and outer shear failure surfaces

Figure 6.18 shows the variations in the passive block reaction force applied to the inner and outer shear failure planes. Their values are inversely proportional; with an increase of the reaction force applied to the inner shear failure surface, the

magnitude of the reaction force applied to the outer decreases. The negative value of the inner reaction force indicates a higher value for the driving forces than for the resisting forces along the basal failure surface. According to Equation 5.34, the negative value of the reaction force acting on the outer shear failure surface means an increase in the resisting forces along the outer shear failure surface. Such a case is apparent in the calculation of the safety factor on the upper contact of the profile after major collapse.

From Figure 6.18 it can be seen that along the upper embedded layer contact, we have an almost uniform reaction force acting on the inner shear failure surface and, respectively, an almost uniform reaction force at the outer shear surface of the profiles before the initial failure and major collapse. This indicates that because of the flatter contact surface, the passive block does not change in volume dramatically. Along the bottom contact surface of the profile before the major collapse we have an increase in the driving forces (see also Figure 6.16), which increase the negative value of the reaction forces along the inner shear surface.

On the other hand, in many slope profiles with developed relaxation cracks parallel to sedimentation, we do not have tensile fractures and stable slope profiles. Therefore, the sequence of fracture development depends on the material anisotropy and the calculated stress state of the profile. If the slopes were homogeneous and isotropic, then we could say that the tensile fractures at the frictional zone in the toe of the slope and the vertical tensile fractures behind

the crest of the slope are developed simultaneously. In the case of an inhomogeneous slope profile with anisotropic rock properties it is very difficult to indicate the right sequence of the tensile fracture appearance. Let us accept the ideal case, which in slope stability terms is the worst case, where the fractures propagate simultaneously. Hence, for the starting point we have two types of tensile fractures, propagated in the slope profile: one - in the bottom contact from the toe of the slope toward the solid; and two – vertical tensile fractures at the slope crest and some distance behind the slope crest (Figure 6.19a). After the formation of these fractures, the author accepts that the slope profile has relaxed and any further failures are the result of dead rock weight. As a result of the surface vertical tensile fracture formation, we do not have horizontal stress between them.

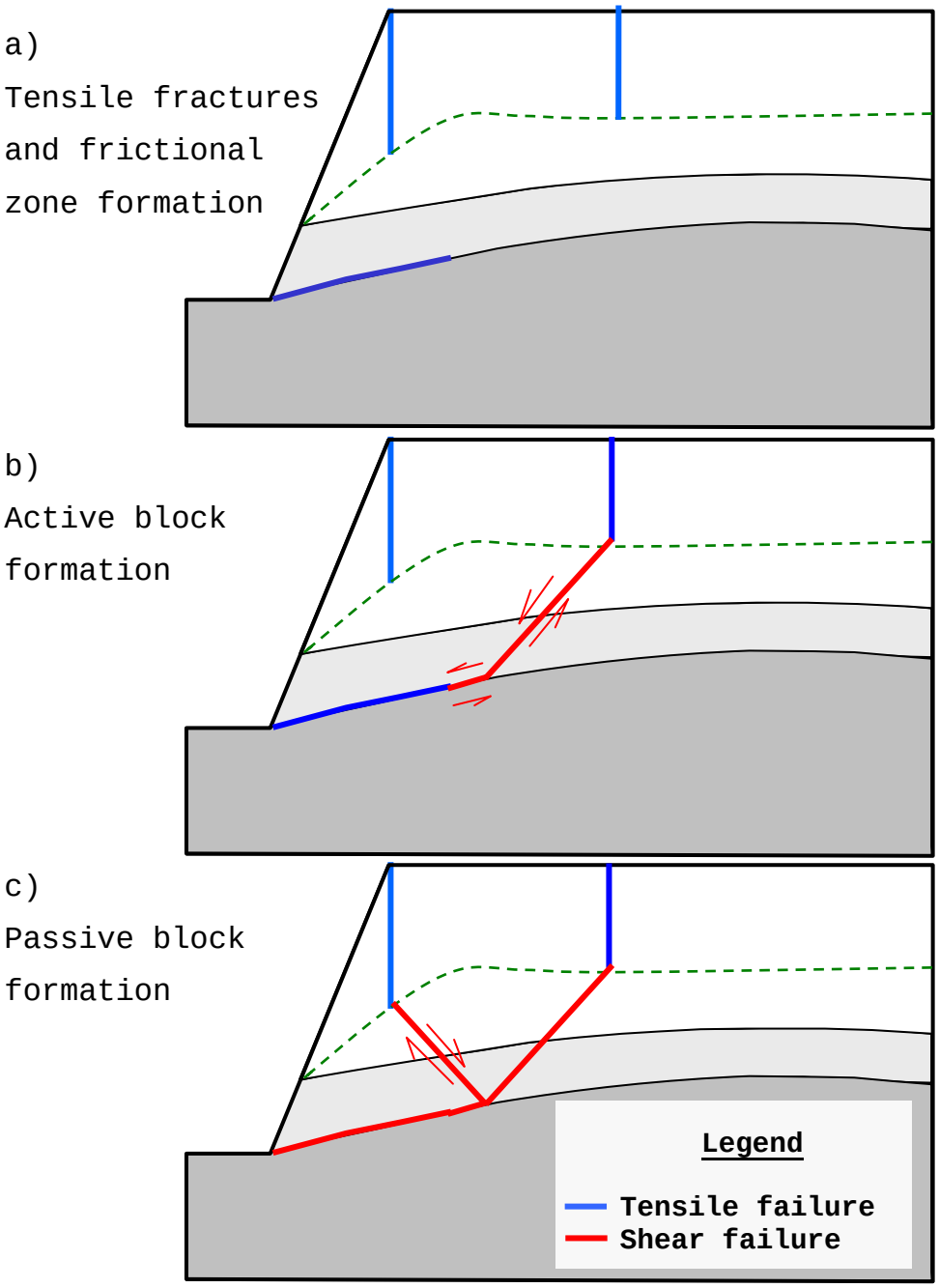

Figure 6.19

Failure sequence of the proposed thrust failure mechanism: a) tensile fracture formation in the slope profile due to stress relaxation; b) shear failure in the contact and inner shear failure surfaces forming the passive block (if we have the necessary conditions as discussed in Chapter 5); c) shear failure in the outer shear failure surface and formation of the active block

The way the shear fracture approaches a joint surface (similar to our frictional zone) in nature is shown in Picture 6.1.

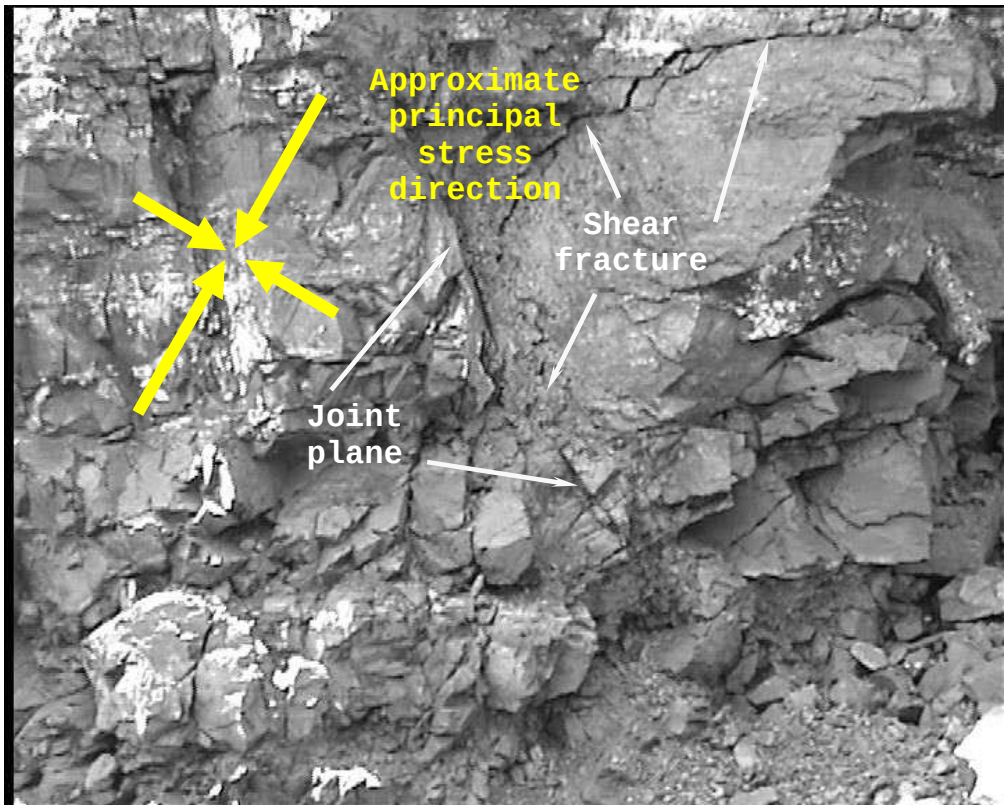

Picture 6.1

Way a shear fracture approaches the pre-existing joint plane

The next step in the slope failure is the shear fracture propagation in the cohesive zone along the bottom contact surface and along the outer shear failure surface (Figure 6.19b).

If we consider the fracture propagation type along the outer shear failure surface, it should strictly be a combination of tensile and shear modes (Atkinson, 1987). This means that the controlling failure parameter will be combined-mode fracture propagation, between Modes I and II, or so-called “Mode I-II”. The

tensile part of the failure Mode I-II is created by the material relaxation and the dip angle of the strata. It can be seen that this failure mode has two boundaries: the first is in the profile with flat layers, where we will have pure shear failure (Mode II), and the second in the profile with almost vertical layers, where we will have pure tension (Mode I). In Mode I-II failure, the outer failure surface should have a straight surface, in the case of the profile with flat layers, and a curved surface in the case of profile with almost vertical layers. Hence, in our discussed failure mechanism it is more likely to have the form of a "stepped ellipse" as can be seen in Picture 6.1, which shows a combination of Mode I and Mode II fracturing. For simplicity of calculation, in the proposed thrust failure mechanism, the author accepts a straight inner shear failure surface based on the relatively low strata dip angle, although this is almost always certainly not the case in actual failures.

The inner shear failure surface will lag behind the inner shear surface if we have the conditions for its creation, as discussed in Chapter 5. This failure surface is less influenced by the rock deadweight, experiences lower tensile stress and, as a consequence, a more planar surface forms compared to that for the outer surface (Figure 6.19c). The other feature that contributes to the inner shear failure surface is the contact undulation. If we have variations in the dip angle of the contact we will have conditions for the creation of more than one inner shear surface. See Figures 1.7 and 1.8.

Once the inner failure surface is formed, the thrust failure mechanism can take place. The active block sags under its own weight, forcing the passive block into the pit. The slightly later formation of the outer shear failure surface, compared to the inner, accelerates the passive block horizontal displacement. This mechanism accounts for all the features observed in the pit failures and those reported by Boyd (1983).

The other key factor in slope stability analysis is related to the pore-water pressure in the strata. The proposed thrust failure mechanism uses an approximation of the pore-water pressure as proportional to the depth. Because of the sandy overburden, the phreatic surface is relatively deep (23-25m) compared to the entire slope height (approximately 40m). For this reason we can say that the pore-water pressure influence on the slope stability calculations is insignificant. This statement is confirmed by the results of the slope stability safety factors, calculated along the shale layer bottom contact surface. After eliminating the pore-water pressure application we have a strengthening of the slope profile before initial failure by 5% (up to FOS=0.95), slope profile before major collapse by 9% (up to FOS=0.98) and the post-major collapse profile by 1% (up to FOS=1.46) compared to the calculated FOS values in Figure 6.13. These calculated differences confirm the low pore-water pressure influence on the slope stability analysis at shallow depths (30-50m).

The applied pore-water pressure approximation used in this thesis requires that all pores in rock are connected, which is not the case in nature and

especially not in the low-porosity rock considered in the failures discussed in this thesis. However, if tensile cracks form relatively early in the slope life, they could fill with rainwater and increase the potential for the formation of the shear stresses and contact shear/tensile surface. This is an extremely complex question because not all pores are hydraulically connected in the rock and their connectivity should be addressed by an independent study.

6.5 PRACTICAL IMPLICATION OF THRUST FAILURE MECHANISM FOR ACTIVE MINING SLOPES

The proposed thrust failure mechanism is a fast and easy method for slope stability assessment in complex geotechnical conditions, including strata inclined toward the pit that contain a weaker embedded layer exposed at the toe of the slope. Geotechnical engineers able to use this failure mechanism as a possible failure mode should first do the following:

1. Define weakest embedded layer at the toe of the slope profile
2. Calculate the critical tensile stress difference for the defined layer.
3. Calculate the cohesive zone length at the base of the passive block for a range of strata inclination angles appropriate for the slope under study.

As soon as this information is obtained, the proposed methodology can be used.

The assessment order for thrust failure mechanism can be seen in Figure 6.20 below.

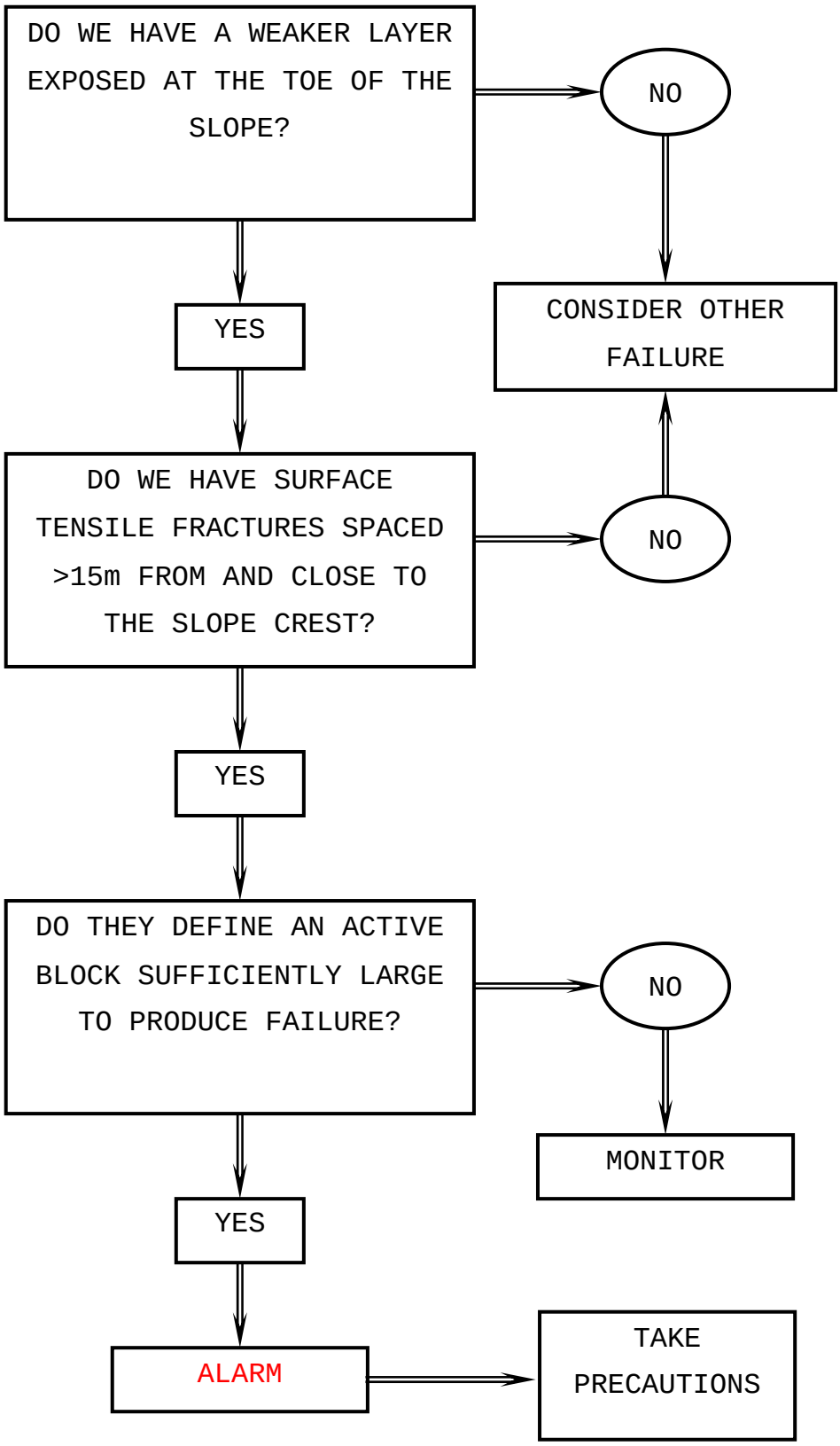

Figure 6.20

Assessment order for thrust failure mechanism

CHAPTER 7
CONCLUSIONS AND RECOMMENDATIONS FOR FUTURE WORK

7.1 CONCLUSIONS

The thrust failure mechanism, identified as a possible mechanism of failure of two slopes in a surface coal mine, shows good potential for use in slope stability analysis. The mechanism is based on a combination of observations at slope failure sites, numerical modelling data from models that account for the geology, micromechanical studies of tensile crack formation, application of the Mohr-Coulomb criterion and Riedel shear structures in the development of shear zones in slopes, and a crude pore water model for the slope. These are combined to create factor of safety computations for the various components of rock material failure that result in a structure that is able to collapse into the pit.

The first phase contributing to eventual slope failure is tension crack formation because of the relaxation of horizontal stresses near the pit edge: tensile cracks are commonly noted features at the crests of all pit slopes. This is followed by tensile crack propagation along the contact surface between (in this case) a shale and an underlying coal seam. Microscope studies revealed carbon flakes aligned with sedimentation in the shale, which would promote the formation of a tensile crack along the shale-coal contact because of the relaxation of vertical stress when the slope was cut. The detailed mechanism of crack formation was not confirmed in this study because the failure surface

becomes a slip surface for the collapsing slope. Once the slip surfaces were exposed at the mine, slickensiding and other slip features masked any evidence of fracture formation mode. The exact detail of fracture formation is not important, it is important that it formed a slip surface, which allowed slope collapse.

The formation of an active thrust block is completed by the development of two shear zones, which propagate from the deepest extent of two vertical surface tension cracks, dipping at 45° towards each other, to form a wedge facing downwards. These shear zones are postulated to meet at the level of the shale-coal contact, although there is no physical reason why they have to meet there. Once the active thrust block has formed, it tends to subside under its own weight, which will force the further growth of the tensile crack already formed along part of the shale-coal contact. This further growth is probably mixed-mode I-II growth. Once the mixed-mode crack has reached the base of the active block wedge, the entire slope stability is dependent on frictional forces alone. If friction is insufficient to maintain stability, the active block will slide downwards under its own dead weight, thrusting the passive block into the excavation.

The thrust failure mechanism of slope failures appears to be a more accurate model compared to the limit equilibrium methods for slope failures in complex geotechnical conditions. The limit equilibrium methods were created to account for failures mainly of earth dam walls and homogeneous soil slopes. The circular failure mode was shown in one slope failure to be a

reliable predictor of failure in such conditions where failure only involves homogeneous sandy overburden.

The following specific conclusions can be drawn:

1. The thrust failure mechanism takes into account the virgin and resultant stress state of the profile along a contact surface involved in frictional zone formation.
2. The proposed mechanism takes into account the rock anisotropy at a micromechanical level, and minerals or pores in the rock, which provide insight into the probable fracturing process.
3. The new failure mechanism takes into account the critical stress for fracture propagation, which is a function of the flaw size and inter-flaw distance.
4. The new failure mechanism defines two zones along the slip surface: frictional and cohesive. In the frictional zone resisting forces are formed only by the normal load and frictional coefficient, while in the cohesive zone, the cohesive rock strength is also included.
5. The critical stress magnitude defines the frictional zone length of the slip surface, which is a vital parameter for frictional-type failure type along the surface.
6. A fracture mechanics approach is not appropriate to determine the potential for the development of a frictional zone in the slope; it does provide some useful guidelines.
7. Since fracture mechanics analyses failure from a stress point of view will not help uncover the actual mechanism of crack development on the shale-

middle coal seam contact, a strain based approach may yield better results.

8. With the aid of this method a more realistic slope stability safety factor and appropriate general slope angle are possible.
9. Pore-water pressure influence in slope stability analysis using the thrust failure mechanism is highly dependent on the strata and could be insignificant in shallow cuts (30-50m deep).
10. Although fracture mechanics were used, this work does not attempt to derive a realistic damage model or fracture-propagation model for either the tensile or shear segments of fractures.
11. The proposed thrust failure mechanism uses the Riedel (1929) shear structure model for shear zone orientation in the slope.
12. This study is merely a practical study of evaluating the potential for the block thrust failure mechanism to take place, and the safety factor derived for two observed failures in the field appear to be reasonably accurate.
13. The further application on the proposed thrust failure mechanism in slope failures could indicate some possible weak points and increase the accuracy of the method.

The objectives of this study are to explain the mechanism of slope failure in complex geotechnical conditions, and to find a simple and practical way to evaluate the potential for slope failure in a practical mining situation. The block thrust mechanism proposed here meets both objectives above, but will require wider application before its value as a slope stability indicator can be established.

7.2 FUTURE WORK

Future work should include the influence of pore-water pressure in the proposed method for blocky-type failure using the linear porosity theory. Encouragement for the success of the work is based on the work done by Wong et al. (2001a and 2001b) and Mandal et al. (2001). The linear porosity theory was not applied in the thesis because the embedded shale layer is rock with very low porosity and, as was mentioned earlier, the fracture initiates from the carbon flakes. In other rock types, sandstone for example, fractures initiate from the pores in the rock matrix (El Bied et al., 2002). For this purpose, the linear porosity has to be used for the pore size measurements. The work done by Olson (1993 and 1997) and Olson and Pollard (1989) regarding natural fracture propagation and the influence of the pore-water pressure promises to be successful. The author's opinion is that including the pore water pressure, using linear porosity theory, will further decrease the values of the pore-water forces applied along the failure surfaces. As a result, the defined shear failure surface safety factors are expected to be slightly higher.

The critical length of the fracture-process zone between carbon flakes needs further confirmation. The length of the fracture-process zone is one of the most important parameters, which could be used even as a rock property, because this value is used directly in the critical tensile stress calculation. Alternatively, a future research should follow strain-

based approach, as this is more likely to yield acceptable results.

The distance between surface tensile cracks is a third important area of study. The fracture mechanics analysis made by Parker (1999), Bai and Pollard (2000a and 2000b) show that the minimal distance between two tensile fractures should be equal to their length. On the basis of this development, the horizontal distance between the surface tensile fractures involved in active block formation must be at least equal to their depth. Hence, the failure along the upper contact plane at shallow cuts (with depth less than 30m) will not develop because the active block width is too small, resulting in its weight being too low to allow the thrust failure mechanism to work.

The Riedel (1929) shear failure model is virtually unknown in rock mechanics, yet it is widely used in structural geology. Combining Riedel's (1929) findings in shear failure structure with the modern fracture mechanics using a strain-based approach could shed more light on the complexities of shear zone formation and failure. Final confirmation of the block thrust failure mechanism will only come with the confirmation of fracture processes within slopes.

APPENDIX 1. FLAC MODELS AND DERIVATIONS

A1.1 Applied models for FLAC code

A1.1.1 Model for the vertical stress comparison between the FLAC *ubiquitous joints* model and the theoretical development in Jaeger and Cook (1979)

```
title
Compressive strength of a shale specimen with a plane of
weakness
g 5 10
set mess off
def hsol
  loop k (0,18)
    beta=90.0*(18.0-k)/18.0
    alfa=90-beta
    command
      mo null
      mo ubi
      pro den 2700 bulk 4.5e9 she 2.3e9 fric 19 co 1.4e5 ten
3.5e5
      pro jco 1e5 jfric 8 jang alfa jten 1e6
      fix y j 1
      fix y j 11
      ini yvel -1e-7 j 11
      ini yvel 1e-7 j 1
      set st_damp comb
      step 4000
      print beta
      print sigmav
      print anal
    end_command
  end_loop
end
;
def sigmav
  sum=0.0
  loop i (1,igp)
    sum=sum+yforce(i,jgp)
  end_loop
  sigmav=sum/(x(igp,jgp)-x(1,jgp))
end

def ve
  ve=(ydisp(3,1)-ydisp(3,11))/(y(3,11)-y(3,1))
end
```

```
;
def anal
  mc=cohesion(1,1)
  mfi=friction(1,1)*degrad
  jc=jcohesion(1,1)
  jfi=jfriction(1,1)*degrad
  sm=2.0*mc*cos(mfi)/(1.0-sin(mfi))
  if beta=90*int(beta/90) then
    sj=-1
  else
    divsj=((1.0-
tan(jfi)*tan(beta*degrad))*sin(2.0*beta*degrad))
    if divsj=0.0 then
      sj=-1
    else
      sj=2.0*jc/divsj
    end_if
  end_if
  if sj<0 then
    anal=sm
  else
    anal=min(sj,sm)
  end_if
end

hist nstep 100
hist unbal
hist sigmav
hist anal
hist beta
hist ve
hist yv i 1 j 1
hsol
save UCT.sav
plot hold grid
plot hold his 2 3 cross vs 4 begin 4000 skip 40
return
```

A1.1.2 Model for homogeneous sandstone profile with undulated ground surface – 15^0 inclination at the limb's surface

```
g 250,100
m m
prop s=5.2e9 b=5.9e9 d=2600 fri=21 coh=1e10 ten=1e10
def mon
        rj=1.0/jzones
        sum=0.0
        loop i (130,235)
                y_change=-1.1*sin(igp*degrad)
                y(i,1)=y(i-1,1)+0.9*y_change
```

```
                sum=sum+(y(i-1,1)-y(1,1))
                y(i,1)=y(i,1)-0.2*sum/i
                loop j (2,jgp-1)
                        y(i,j)=y(i,1) + (y(i,jgp)-
y(i,1))*(j-1)*rj
                end_loop
         end_loop
end
mon
fix x i=1
fix x i=251
fix x y j=1
hist unbal
set large
solve
;
;
title
k=2.0; 15 deg incl.
prop s=5.2e9 b=5.9e9 ten=5.5e6 coh=7e5 fri=21 d=2600
def k0_set
        loop i (1,izones)
                loop j (1,jzones)
                        sxx(i,j)=2.0*syy(i,j)
                end_loop
        end_loop
end
k0_set
;
set grav=9.81
ini xdis=0 ydis=0
solve
save k15-sst.sav
```

A1.1.3 FLAC model for 2m thick embedded shale layer at 30m depth and 5^0 inclination at the limb's surface

```
g 250,100
m m j 1 70
m u j 71 72
m m j 73 100
prop s=5.2e9 b=5.9e9 d=2600 fri=21 coh=1e10 ten=1e10 j=1,70
prop s=2.3e9 b=4.5e9 d=2700 fri=14 coh=1e10 ten=1e10 j=71,72
prop ja=0 jc=1e10 jf=8 jt=1e10 j=71,72
prop s=5.2e9 b=5.9e9 d=2600 fri=21 coh=1e10 ten=1e10
j=73,100
def mon
        rj=1.0/jzones
        sum=0.0
        loop i (130,235)
```

```
                y_change=-1.1*sin(igp*degrad)
                y(i,1)=y(i-1,1)+0.3*y_change
                sum=sum+(y(i-1,1)-y(1,1))
                y(i,1)=y(i,1)-0.2*sum/i
                loop j (2,jgp-1)
                        y(i,j)=y(i,1) + (y(i,jgp)-
y(i,1))*(j-1)*rj
                end_loop
        end_loop
end
mon
set grav=9.81
fix x i=1
fix x i=251
fix x y j=1
hist ydis i=76 j=100
solve
;
;
title
k=2.0; 2m shale; 05 deg
prop s=5.2e9 b=5.9e9 ten=5.5e6 coh=7e5 fri=21 d=2600   j=1
70  ;SST
prop s=2.3e9 b=4.5e9 ten=3.5e6 coh=4.4e5 fri=14 d=2700
j=71,72 ;Shale
prop ja=0 jc=1e5 jf=8 jt=1e6 i=36 120 j=71,72
prop s=5.2e9 b=5.9e9 ten=5.5e6 coh=7e5 fri=21 d=2600
j=73,100;SST
def k0_set
        loop i (1,izones)
                loop j (1,jzones)
                        sxx(i,j)=2.0*syy(i,j)
                end_loop
        end_loop
end
k0_set
ini xdis=0 ydis=0
set large
solve
```

A1.2 Stress analysis

Many authors, such as Singh (1979) and Feda (1992), discuss shear stress as the only stress that triggers slope failure. Kulhawy et al. (1973) seem to be the first to mention the difference between the Mohr-Coulomb shear failure criterion and the stress failure criterion developed authors. Using finite element

analysis, these calculated the safety factor based on stress level after the assumption that the rock is brought to failure by increasing the value of one of the principal stresses σ_1, while holding the other, σ_3, constant.

Figure A1.1a shows a flaw or a micro fracture in a two-dimensional Cartesian coordinate system. Let us assume that a pair of stresses acts on the flaw (presented by horizontal and vertical stress components). Their result is the stress normal to the flaw's plane. Since the flaw is not collinear with one of the principal stress directions, there is some shear stress at the flaw's plane as well. These stresses in the virgin stress conditions are in equilibrium at the flaw, so there is no flaw extension, propagation or coalescence with the neighbouring ones. These stress conditions are known as a virgin stress state and could be denoted as virgin horizontal (σ_{XX}^{V}), virgin vertical (σ_{YY}^{V}) and virgin shear (σ_{XY}^{V}) stress components. In this case we can denote the stress normal to the flaw's plane as σ_{N}^{V}.

mining activities (Figure A1.1b) bring about a change in the stress state, known as "resultant stress state". These stresses could be denoted as resultant horizontal stress (σ_{XX}^{R}), resultant vertical stress (σ_{YY}^{R}), and resultant shear stress (σ_{XY}^{R}). The first two resultant stress components (horizontal and vertical) will form a new resultant state, normal to stress of the flaw's plane (σ_{N}^{R}).

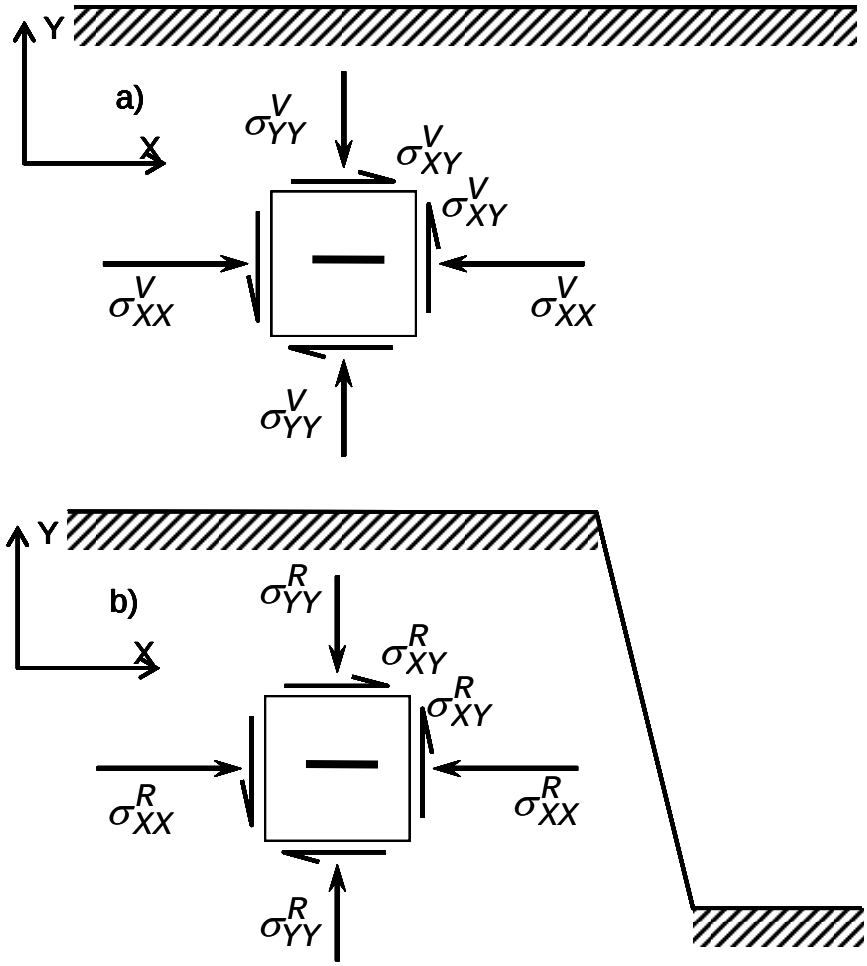

Figure A1.1
Stress state in the infinitesimal flaw, in virgin conditions, and b) after excavation

Therefore, we can say that any possible changes in the flaw pattern (extension, new flaw propagation, coalescence between microcracks in the rock or even failure) will result from the difference between those two loading conditions. Hence, it follows that:

$$\Delta\sigma_{XX} = \sigma^R_{XX} - \sigma^V_{XX} \tag{A1.1}$$

$$\Delta\sigma_{YY} = \sigma^R_{YY} - \sigma^V_{YY} \tag{A1.2}$$

$$\Delta\sigma_{XY} = \sigma_{XY}^{R} - \sigma_{XY}^{V} \tag{A1.3}$$

where $\Delta\sigma_{XX}$, $\Delta\sigma_{YY}$ and $\Delta\sigma_{XY}$ are the stress differences for the horizontal, vertical, and shear stress components. Olson (1993) uses this principle to calculate stress changes caused by tectonic irregularities.

One can easily see that the stress difference in Equations A1.1 – A1.3 has a negative sign in the case when the material relaxes from the virgin stress state or a positive sign in the case of increased loading when using rock mechanics sign conversion.

Normal force to the failure plane is in use as a basal element for the limit equilibrium methods in slope stability analyses. As mentioned in Chapter 1, observed failure planes with embedded anisotropic weaker layers are mainly parallel to the sedimentation.

According to the type of horizontal and vertical stresses (virgin and resultant), the normal to the failure plane induced stress (after Equations A1.1-A1.3) can be a combination of two compressive stresses, a combination of two tensile stresses or a combination of tensile and compressive stress. Figure A1.2 shows the case of biaxial tension applied to the material plane of weakness.

In matrix notation, stress transforms as follows

$$[\sigma]' = [\lambda][\sigma][\lambda]^{T} \tag{A1.4}$$

where $[\lambda]$ is directional *cosine* matrix. For the angle α shown in Figure A1.2

$$[\lambda]=\begin{bmatrix} \cos\alpha & \sin\alpha \\ -\sin\alpha & \cos\alpha \end{bmatrix} \tag{A1.5}$$

Applying Equation A1.4, we could write

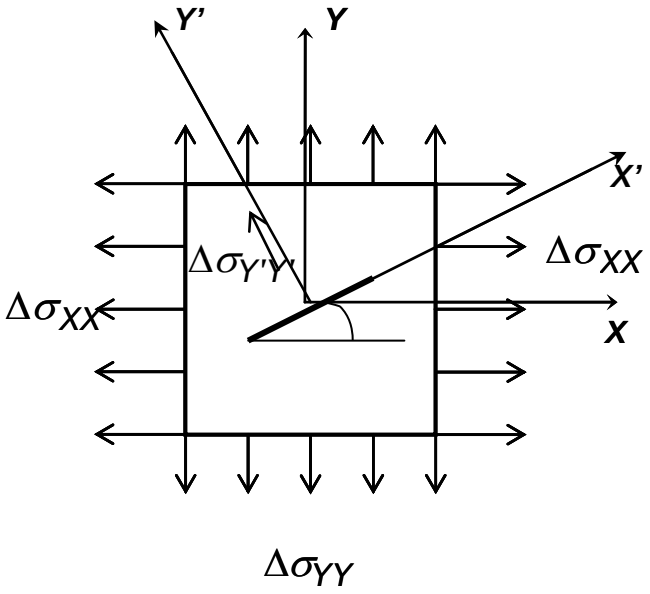

Figure A1.2
Stress state applied to the plane of weakness and remote biaxial loading

$$\begin{aligned}\sigma'_{11} &= \lambda_{11}\lambda_{11}\sigma_{11} + \lambda_{11}\lambda_{12}\sigma_{12} + \lambda_{12}\lambda_{11}\sigma_{21} + \lambda_{12}\lambda_{12}\sigma_{22} \\ &= \sigma_{11}\cos^2\alpha + \sigma_{12}\sin\alpha\cos\alpha + \sigma_{21}\sin\alpha\cos\alpha + \sigma_{22}\sin^2\alpha\end{aligned} \tag{A1.6}$$

$$\begin{aligned}\sigma'_{12} &= \lambda_{11}\lambda_{21}\sigma_{11} + \lambda_{11}\lambda_{22}\sigma_{12} + \lambda_{12}\lambda_{21}\sigma_{21} + \lambda_{12}\lambda_{22}\sigma_{22} \\ &= -\sigma_{11}\sin\alpha\cos\alpha + \sigma_{12}\cos^2\alpha - \sigma_{21}\sin^2\alpha + \sigma_{22}\sin\alpha\cos\alpha \\ &= \sigma'_{21}\end{aligned} \tag{A1.7}$$

$$\begin{aligned}\sigma'_{22} &= \lambda_{21}\lambda_{21}\sigma_{11} + \lambda_{21}\lambda_{22}\sigma_{12} + \lambda_{22}\lambda_{21}\sigma_{21} + \lambda_{22}\lambda_{22}\sigma_{22} \\ &= \sigma_{11}\sin^2\alpha - \sigma_{12}\sin\alpha\cos\alpha - \sigma_{21}\sin\alpha\cos\alpha + \sigma_{22}\cos^2\alpha\end{aligned} \tag{A1.8}$$

Hence, for the new set of the co-ordinate system (*X'Y'*), the normal stress difference $\Delta\sigma_{Y'Y'} = \Delta\sigma_N$ will have the form of

$$\Delta\sigma_{Y'Y'} = \Delta\sigma_N = \Delta\sigma_{XX}\,\sin^2\alpha - 2\Delta\sigma_{XY}\,\sin\alpha\cos\alpha + \Delta\sigma_{YY}\cos^2\alpha \qquad \text{(A1.9)}$$

where $\Delta\sigma_{XX}$, $\Delta\sigma_{YY}$ and $\Delta\sigma_{XY}$ are the stress differences between the stress state after slope excavation and the virgin stress state for the horizontal, vertical and shear stress components respectively. See Equations A1.1 to A1.3.

A1.3 Equations in Chapter 4

A1.3.1 Equation 4.16

$$K_I^D = -2\sigma_t\sqrt{\frac{1}{W}\tan\frac{\pi c}{W}}\int_a^c \cos\frac{\pi\xi}{W}\left[\left(\sin\frac{\pi c}{W}\right)^2 - \left(\sin\frac{\pi\xi}{W}\right)^2\right]^{-\frac{1}{2}} d\xi \qquad \text{(A1.10)}$$

Replace $\sin\frac{\pi\xi}{W} = u$. Then $du = \frac{\pi}{W}\cos\frac{\pi\xi}{W}d\xi$ and Equation A1.10 has the form:

$$K_I^D = -\frac{2\sigma_t W\sqrt{\frac{1}{W}\tan\frac{\pi c}{W}}}{\pi}\int_{\sin\frac{\pi}{W}a}^{\sin\frac{\pi}{W}c}\frac{du}{\sqrt{\left(\sin\frac{\pi c}{W}\right)^2 - u^2}} = \qquad \text{(A1.11)}$$

$$= -\frac{2\sigma_t W}{\pi}\sqrt{\frac{1}{W}\tan\frac{\pi c}{W}}\arcsin\frac{u}{\sin\frac{\pi c}{W}}\Bigg|_{\sin\frac{\pi a}{W}}^{\sin\frac{\pi c}{W}} = \tag{A1.12}$$

$$= -\frac{2\sigma_t W}{\pi}\sqrt{\frac{1}{W}\tan\frac{\pi c}{W}}\left[\arcsin 1 - \arcsin\frac{\sin\left(\frac{\pi a}{W}\right)}{\sin\left(\frac{\pi c}{W}\right)}\right] = \tag{A1.13}$$

$$= -\frac{2\sigma_t W}{\pi}\sqrt{\frac{1}{W}\tan\frac{\pi c}{W}}\left[\frac{\pi}{2} - \arcsin\frac{\sin\left(\frac{\pi a}{W}\right)}{\sin\left(\frac{\pi c}{W}\right)}\right] = \tag{A1.14}$$

$$= -\sigma_t\sqrt{W\tan\frac{\pi c}{W}}\left[1 - \frac{2}{\pi}\arcsin\frac{\sin\left(\frac{\pi a}{W}\right)}{\sin\left(\frac{\pi c}{W}\right)}\right] \tag{A1.15}$$

A1.3.2 Equation 4.19

$$\Delta\sigma_N\sqrt{W\tan\frac{\pi c}{W}} - \sigma_t\sqrt{W\tan\frac{\pi c}{W}}\left[1 - \frac{2}{\pi}\arcsin\frac{\sin\left(\frac{\pi a}{W}\right)}{\sin\left(\frac{\pi c}{W}\right)}\right] = 0 \tag{A1.16}$$

Dividing both sides on Equation A1.16 by $\sqrt{W\tan\frac{\pi c}{W}}$:

$$\Delta\sigma_N - \sigma_t\left[1 - \frac{2}{\pi}\arcsin\frac{\sin\left(\frac{\pi a}{W}\right)}{\sin\left(\frac{\pi c}{W}\right)}\right] = 0 \tag{A1.17}$$

$$\frac{2\sigma_t}{\pi}\,\mathbf{arcsin}\frac{\mathbf{sin}\left(\frac{\pi a}{W}\right)}{\mathbf{sin}\left(\frac{\pi c}{W}\right)} = \sigma_t - \Delta\sigma_N \qquad \text{(A1.18)}$$

$$\mathbf{arcsin}\frac{\mathbf{sin}\left(\frac{\pi a}{W}\right)}{\mathbf{sin}\left(\frac{\pi c}{W}\right)} = \frac{\pi\left(\sigma_t - \Delta\sigma_N\right)}{2\sigma_t} \qquad \text{(A1.19)}$$

$$\frac{\mathbf{sin}\left(\frac{\pi a}{W}\right)}{\mathbf{sin}\left(\frac{\pi c}{W}\right)} = \mathbf{sin}\frac{\pi\left(\sigma_t - \Delta\sigma_N\right)}{2\sigma_t} \qquad \text{(A1.20)}$$

$$\mathbf{sin}\left(\frac{\pi c}{W}\right) = \frac{\mathbf{sin}\left(\frac{\pi a}{W}\right)}{\mathbf{sin}\left(0.5\pi - \frac{0.5\pi\Delta\sigma_N}{\sigma_t}\right)} \qquad \text{(A1.21)}$$

$$\frac{\pi c}{W} = \mathbf{arcsin}\frac{\mathbf{sin}\left(\frac{\pi a}{W}\right)}{\mathbf{cos}\left(\frac{0.5\pi\Delta\sigma_N}{\sigma_t}\right)} \qquad \text{(A1.22)}$$

$$c = \frac{W}{\pi}\,\mathbf{arcsin}\frac{\mathbf{sin}\left(\frac{\pi a}{W}\right)}{\mathbf{cos}\left(\frac{0.5\pi\Delta\sigma_N}{\sigma_t}\right)} \qquad \text{(A1.23)}$$

Replacing c with $c = a + l$

$$l = \frac{W}{\pi}\,\mathbf{arcsin}\,\frac{\mathbf{sin}\left(\frac{\pi\, a}{W}\right)}{\mathbf{cos}\left(\frac{0.5\pi\Delta\sigma_N}{\sigma_t}\right)} - a \qquad \text{(A1.24)}$$

A1.3.3 Equation 4.21

$$l_c = \frac{W}{\pi}\,\mathbf{arcsin}\,\frac{\mathbf{sin}(\pi\, a/W)}{\mathbf{cos}(0.5\pi\ \Delta\sigma_N/\sigma_t)} - a \qquad \text{(A1.25)}$$

$$\frac{\pi(l_c + a)}{W} = \mathbf{arcsin}\,\frac{\mathbf{sin}(\pi\, a/W)}{\mathbf{cos}(0.5\pi\ \Delta\sigma_N/\sigma_t)} \qquad \text{(A1.26)}$$

$$\mathbf{sin}\left[\pi(l_c + a)/W\right] = \frac{\mathbf{sin}(\pi\, a/W)}{\mathbf{cos}(0.5\pi\ \Delta\sigma_N/\sigma_t)} \qquad \text{(A1.27)}$$

$$\mathbf{cos}(0.5\pi\ \Delta\sigma_N/\sigma_t) = \frac{\mathbf{sin}(\pi\, a/W)}{\mathbf{sin}\left[\pi(l_c + a)/W\right]} \qquad \text{(A1.28)}$$

$$0.5\pi\ \Delta\sigma_N/\sigma_t = \mathbf{arccos}\,\frac{\mathbf{sin}(\pi\, a/W)}{\mathbf{sin}\left[\pi(l_c + a)/W\right]} \qquad \text{(A1.29)}$$

$$\Delta\sigma_N^P = \frac{2\sigma_t}{\pi}\,\mathbf{arccos}\,\frac{\mathbf{sin}(\pi\, a/W)}{\mathbf{sin}\left[\pi(l_c + a)/W\right]} \qquad \text{(A1.30)}$$

A1.3.4 Equation 4.24

Substituting Equation 4.19 into Equation 4.23:

$$2a + \frac{2W}{\pi}\,\mathbf{arcsin}\,\frac{\mathbf{sin}(\pi a / W)}{\mathbf{cos}(0.5\pi\Delta\sigma_N / \sigma_t)} - 2a = W \qquad \text{(A1.31)}$$

and

$$\frac{2}{\pi}\,\mathbf{arcsin}\,\frac{\mathbf{sin}(\pi a / W)}{\mathbf{cos}(0.5\pi\Delta\sigma_N / \sigma_t)} = 1 \qquad \text{(A1.32)}$$

$$\frac{\mathbf{sin}(\pi a / W)}{\mathbf{cos}(0.5\pi\Delta\sigma_N / \sigma_t)} = \mathbf{sin}\left(\frac{\pi}{2}\right) = 1 \qquad \text{(A1.33)}$$

$$\mathbf{sin}(\pi a / W) = \mathbf{cos}\left(\frac{\pi}{2}\frac{\Delta\sigma_N}{\sigma_t}\right) \qquad \text{(A1.34)}$$

We can replace $\mathbf{sin}\left(\frac{\pi a}{W}\right)$ at the left hand side of the Equation A1.34 with a $\mathbf{cos}(f)$, which is shown in Equations A1.35a and A1.35b below.

$$\mathbf{sin}\left(\frac{\pi a}{W}\right) = \begin{cases} -\mathbf{cos}\left(\frac{\pi}{2} + \frac{\pi a}{W}\right) & \text{(A1.35a)} \\ \text{or} & \\ \mathbf{cos}\left(\frac{\pi}{2} - \frac{\pi a}{W}\right) & \text{(A1.35b)} \end{cases}$$

Let us first combine Equations A1.34 and A1.35a. Then we have:

$$-\mathbf{cos}\left(\frac{\pi}{2} + \frac{\pi a}{W}\right) = \mathbf{cos}\left(\frac{\pi\,\Delta\sigma_N}{2\sigma_t}\right) \qquad \text{(A1.36)}$$

As the $\cos\upsilon = \cos(-\upsilon)$, then the Equation A1.36 has four possible solutions. If the both arguments are with the same sign ("+" or "-"), then after applying the inverse cosine function the Equation A1.36 can be written as:

$$-\left(\frac{\pi}{2}+\frac{\pi a}{W}\right)=\frac{\pi}{2}\frac{\Delta\sigma_N}{\sigma_t} \qquad \text{(A1.37)}$$

Dividing both sides of Equation A1.37 by $\pi/2$ we obtain with further manipulation:

$$-\frac{W+2a}{W}=\frac{\Delta\sigma_N}{\sigma_t} \qquad \text{(A1.38)}$$

It is seen that Equation A1.38 is an impossible solution because the left-hand side of the equation always will have negative value (W and a are real positive numbers), while the right-hand side always will be positive.

If we assume that both arguments of cosine functions in Equation A1.36 are with opposite signs, then we will have:

$$\frac{\pi}{2}+\frac{\pi a}{W}=\frac{\pi}{2}\frac{\Delta\sigma_N}{\sigma_t}. \qquad \text{(A1.39)}$$

and similar to Equation A1.38 we can write:

$$\frac{W+2a}{W}=\frac{\Delta\sigma_N}{\sigma_t} \qquad \text{(A1.40)}$$

It is also seen that Equation A1.40 is impossible solution because left-hand side of the equation always will have value bigger than one, while the right-hand side always will have value lower than one.

Let us now combine Equations A1.34 and A1.35b. Then we have again two options: both cosine arguments are either the same or opposite sign. Let us first consider the case with the same sign arguments. Hence, we will have equation in the form of:

$$\cos\left(\frac{\pi}{2}-\frac{\pi a}{W}\right)=\cos\left(\frac{\pi\Delta\sigma_N}{2\sigma_t}\right) \qquad \text{(A1.41)}$$

Therefore,

$$\frac{\pi}{2}-\frac{\pi a}{W}=\frac{\pi}{2}\frac{\Delta\sigma_N}{\sigma_t} \qquad \text{(A1.42)}$$

Dividing both sides of Equation A1.40 by π/2, we obtain after further manipulation:

$$\frac{W-2a}{W}=\frac{\Delta\sigma_N}{\sigma_t}. \qquad \text{(A1.43)}$$

Equation A1.43 has only meaning if $W-2a>0$ (particularly, when $W>2a$.) and can be used in the further because its both sides are with the same sign. After assuming that $2a$ is smaller than W, both sides of Equation A1.43 are positive and smaller than one.

If we assume that the cosine arguments in Equation A1.41 have different signs, then we can write:

$$\frac{\pi a}{W}-\frac{\pi}{2}=\frac{\pi}{2}\frac{\Delta\sigma_N}{\sigma_t} \qquad \text{(A1.44)}$$

and

$$\frac{2a-W}{W}=\frac{\Delta\sigma_N}{\sigma_t}. \qquad \text{(A1.45)}$$

It can be seen that Equation A1.45 is also possible solution because both sides of the equation are the

same sign and smaller than one in cases where $2a > W$. On the other hand the condition $2a > W$ does not comply with Equation 4.23 and Figure 4.9, Chapter 4. Therefore, the only possible solution is the equation A1.43. If 2a = W, then we will have pre-existing tensile fracture propagation and consequently, $\Delta\sigma_N = 0$.

Hence we can write

$$\sigma_N^P = \sigma_t \frac{W - 2a}{W} \tag{A1.46}$$

A1.4 Equations in Chapter 5

Equation 5.16

$$\tan\delta = \tan\phi + \frac{cl}{R\cos\delta} \tag{A1.47}$$

Multiply both sides of Equation A1.47 by $\cos\delta$, we will have

$$\sin\delta = \tan\phi\cos\delta + \frac{cl}{R} \tag{A1.48}$$

Substituting $\cos\delta = \sqrt{1 - \sin^2\delta}$ in Equation A1.48:

$$\sin\delta = \tan\phi\sqrt{1 - \sin^2\delta} + \frac{c\,l}{R} \tag{A1.49}$$

If we transfer the coefficient $\frac{c\,l}{R}$ from right-hand side of Equation A1.48 to the left-hand side and square both sides:

$$\sin^2\delta - 2\frac{c\,l}{R}\sin\delta + \left(\frac{c\,l}{R}\right)^2 = \tan^2\phi - \sin^2\delta\tan^2\phi \tag{A1.50}$$

Equation A1.50 becomes after simplification:

$$\sin^2\delta\left(1+\tan^2\phi\right)-2\frac{c\,l}{R}\sin\delta+\left(\frac{c\,l}{R}\right)^2-\tan^2\phi=0 \qquad \text{(A1.51)}$$

This is a quadratic equation in $\sin\delta$ in which there is a real solution only if:

$$4\left(\frac{cl}{R}\right)^2-4\left(1+\tan^2\phi\right)\left(\frac{c^2l^2}{R^2}-\tan^2\phi\right)\geq 0\,. \qquad \text{A1.52)}$$

Equation A1.51 simplifies to

$$\sec^2\phi-\left(\frac{c\,l}{R}\right)^2\geq 0 \qquad \text{(A1.53)}$$

where

$$\sec\phi\geq\frac{cl}{R} \qquad \text{(A1.54)}$$

and

$$\phi\geq\sec^{-1}\left(\frac{cl}{R}\right) \qquad \text{(A1.55)}$$

APPENDIX 2. FIGURES

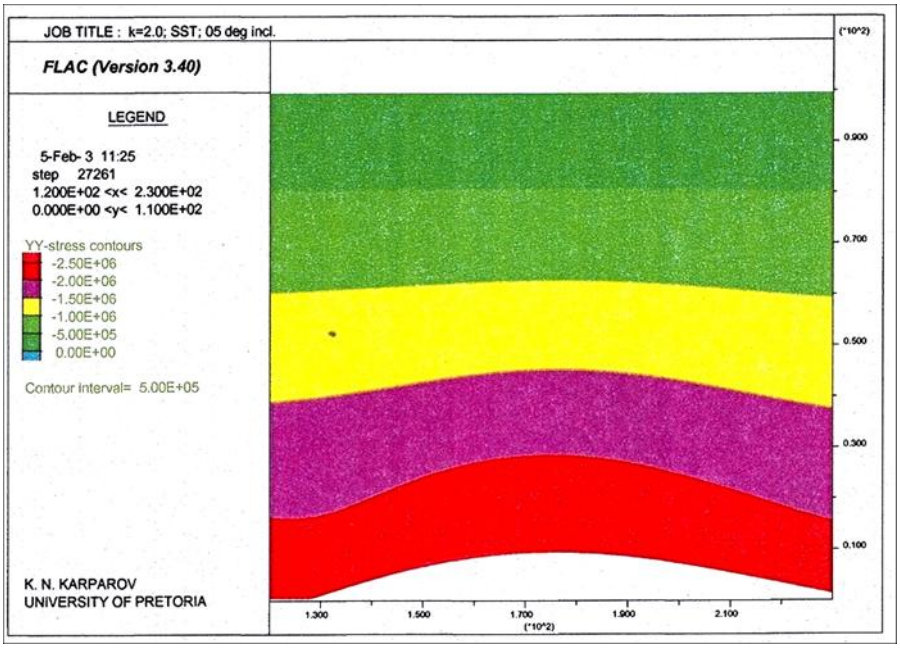

Figure A2.1

Vertical stress component of the FLAC model with homogeneous sandstone and 5^0-layer inclination of the undulated strata formation

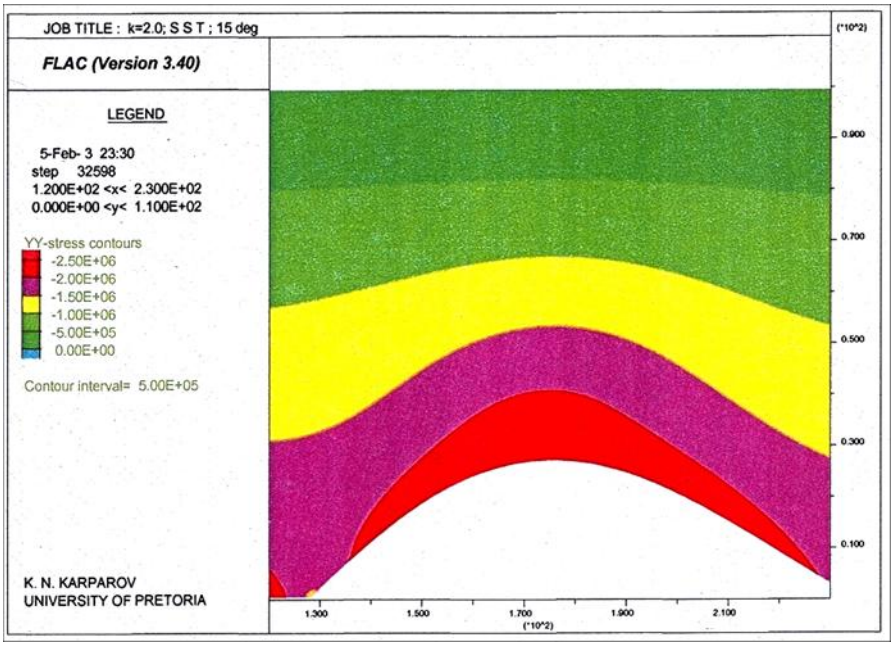

Figure A2.2

Vertical stress component of the FLAC model with homogeneous sandstone and 15^0-layer inclination of the undulated strata formation

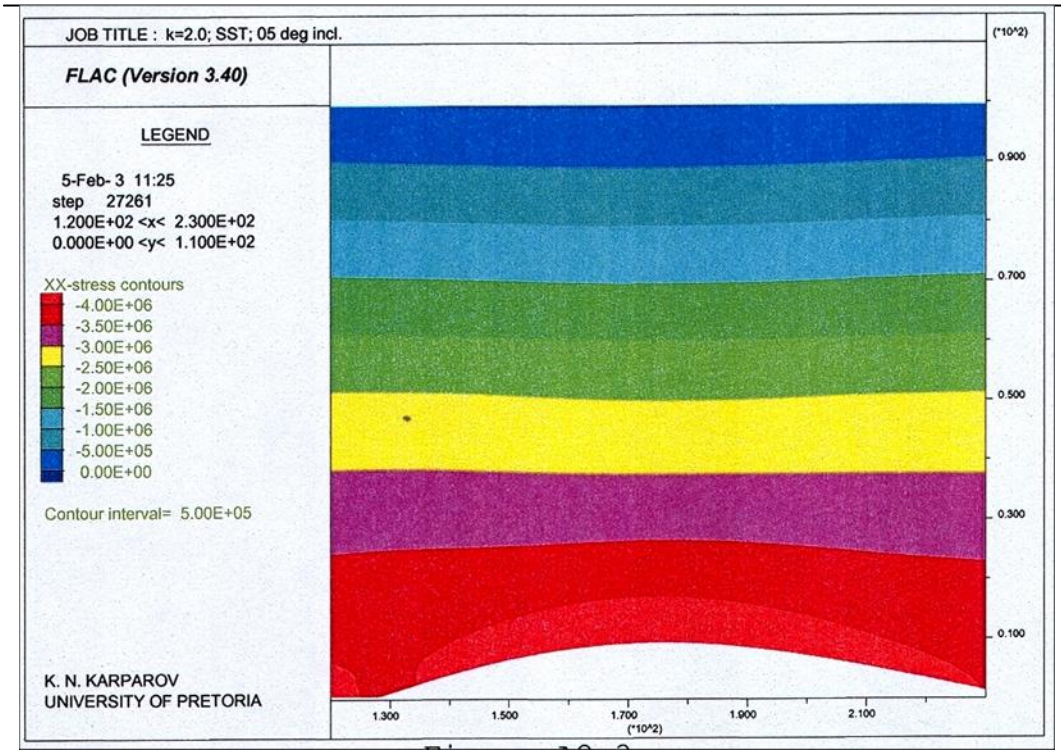

Figure A2.3

Horizontal stress component of the FLAC model with 5^0-layer inclination of the undulated strata formation in massive sandstone

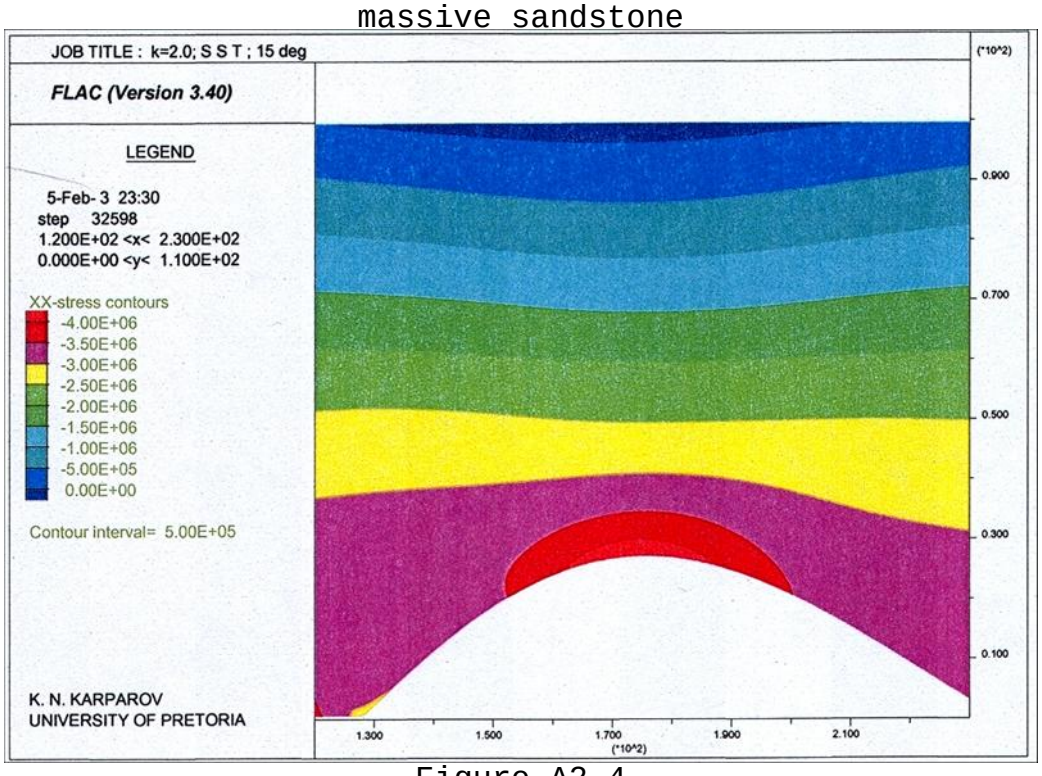

Figure A2.4

Horizontal stress component of the FLAC model with 15^0-layer inclination of the undulated strata formation in massive sandstone

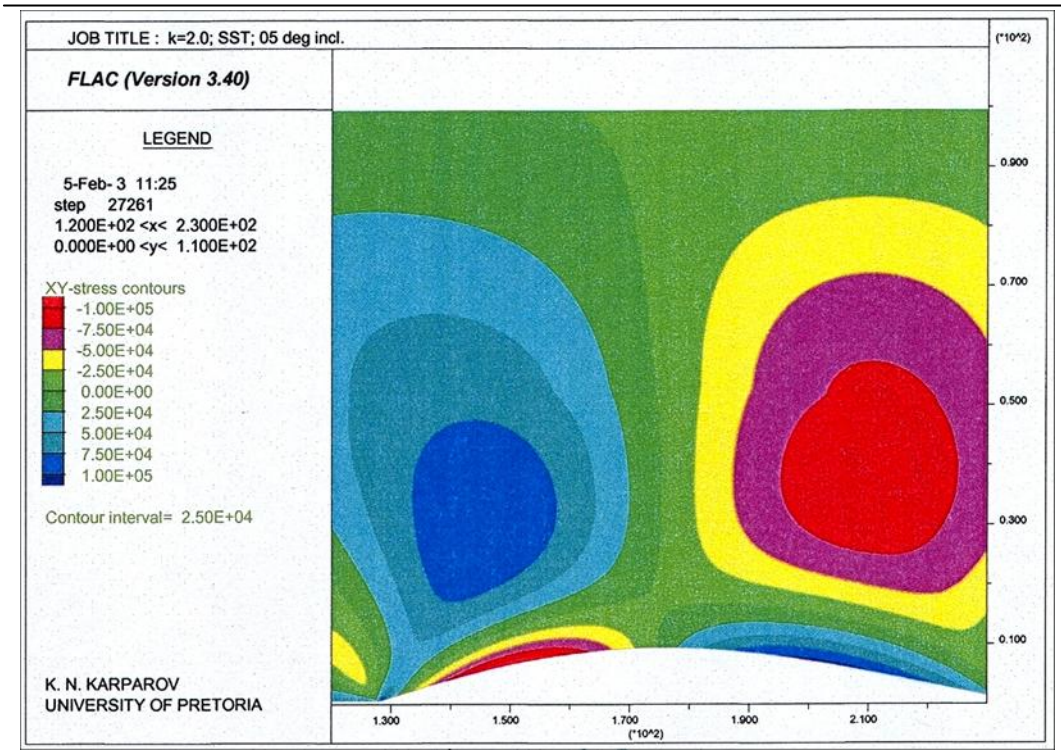

Figure A2.5

Sear stress component of the FLAC model with 5^0-layer inclination of the undulated strata formation in massive sandstone

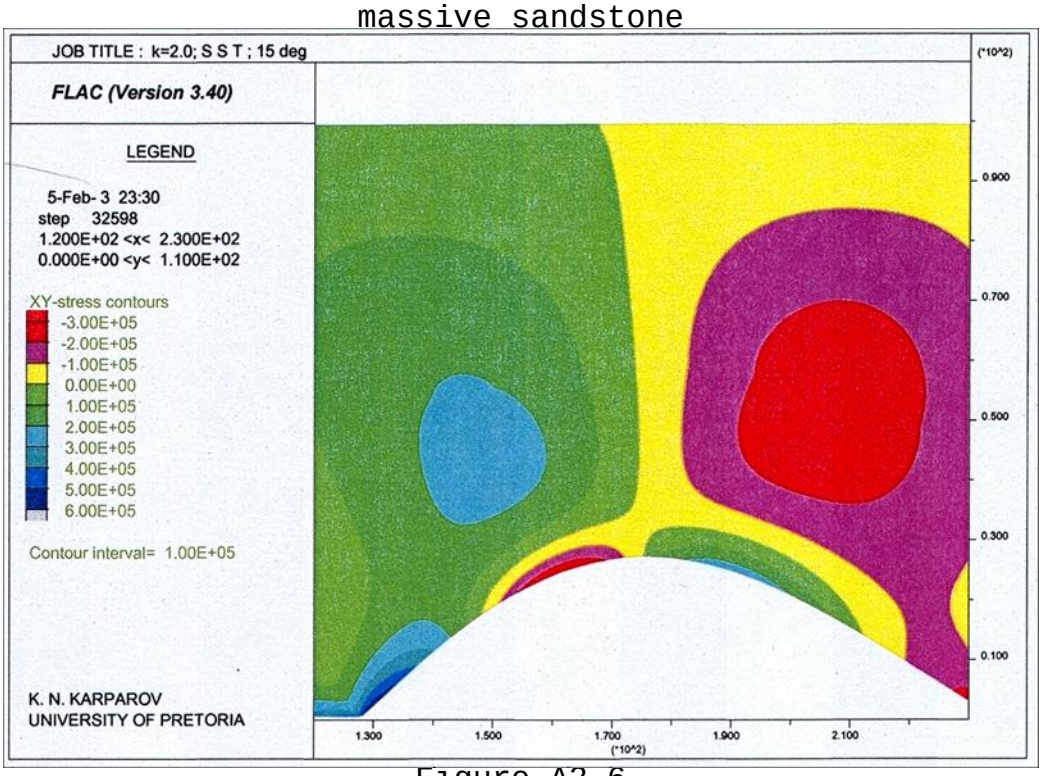

Figure A2.6

Shear stress component of the FLAC model with 15^0-layer inclination of the undulated strata formation in massive sandstone

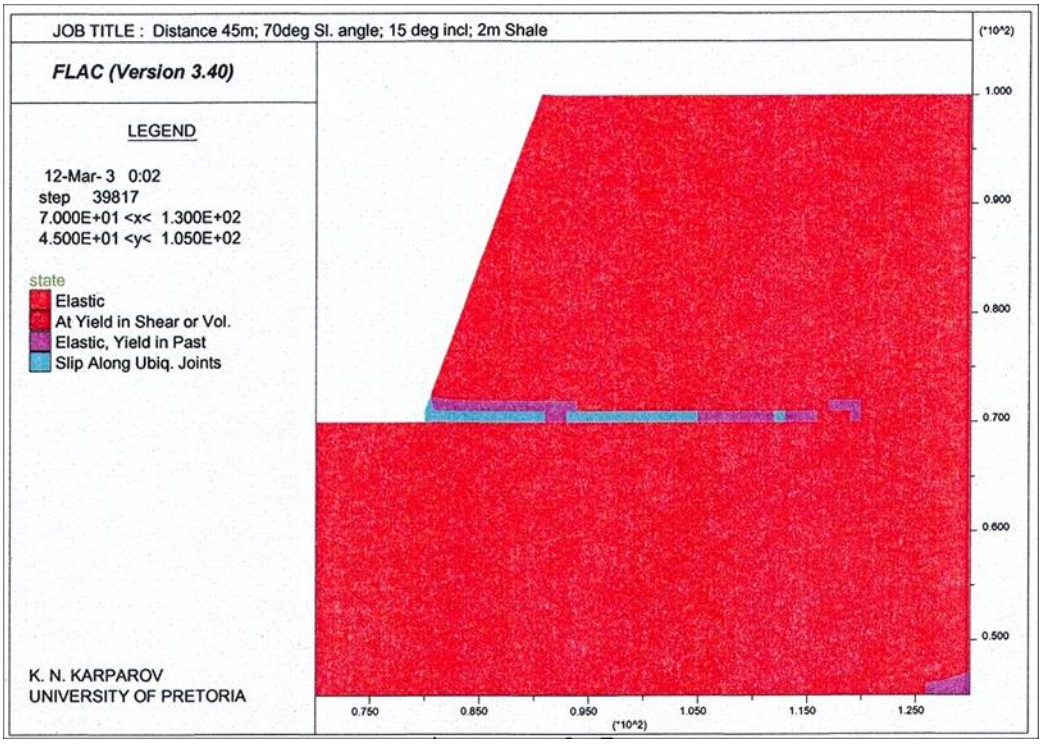

Figure A2.7

State condition of the 70^0-slope profile with 2m embedded shale layer, adjacent to anticline formation with 15^0-layer inclination

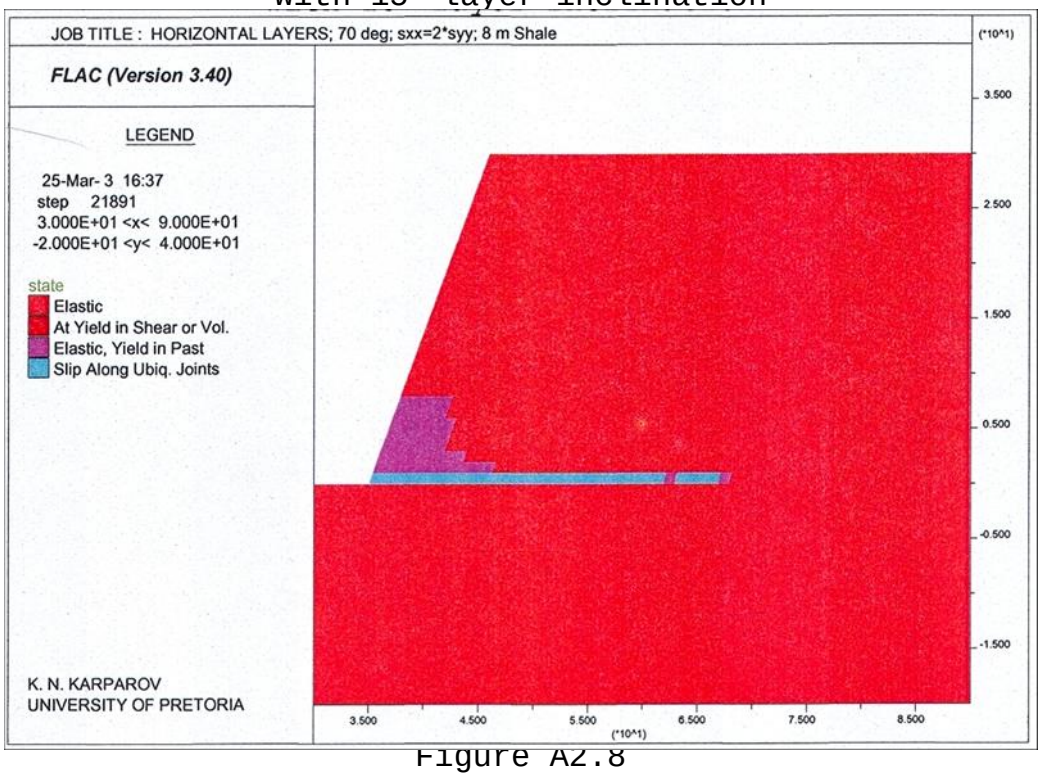

Figure A2.8

State condition of the 70^0-slope profile with 8m thick embedded flat shale layer

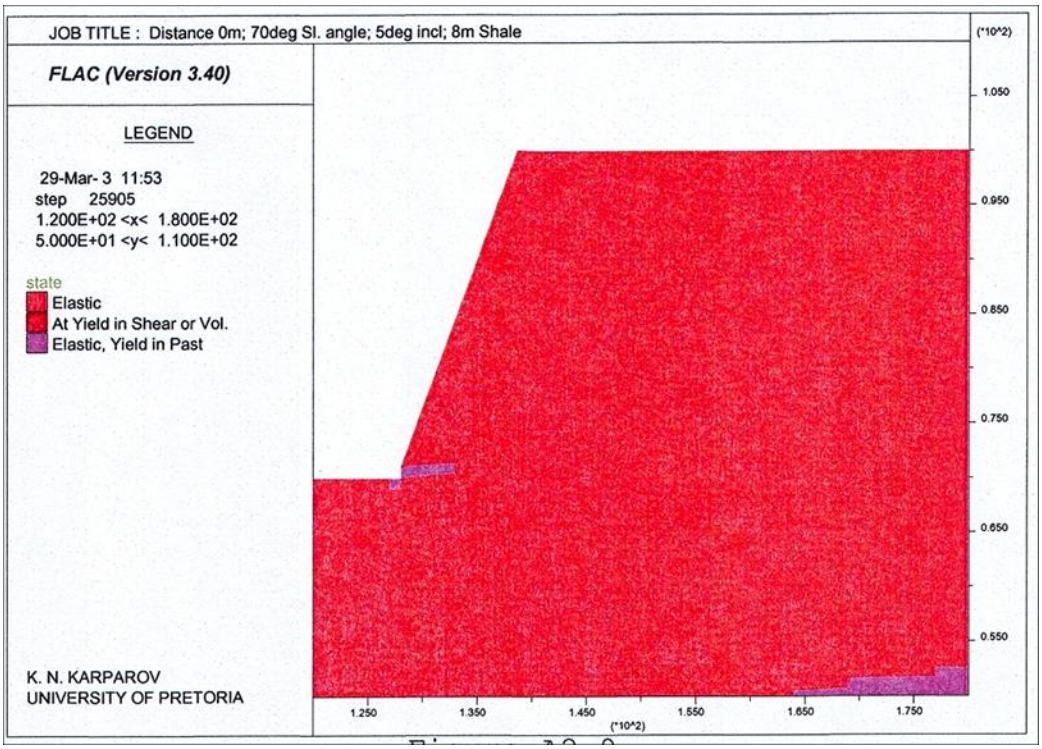

Figure A2.9

State condition of the 70^0-slope profile with 8m thick embedded shale layer at the anticline formation with 5^0-layer inclination

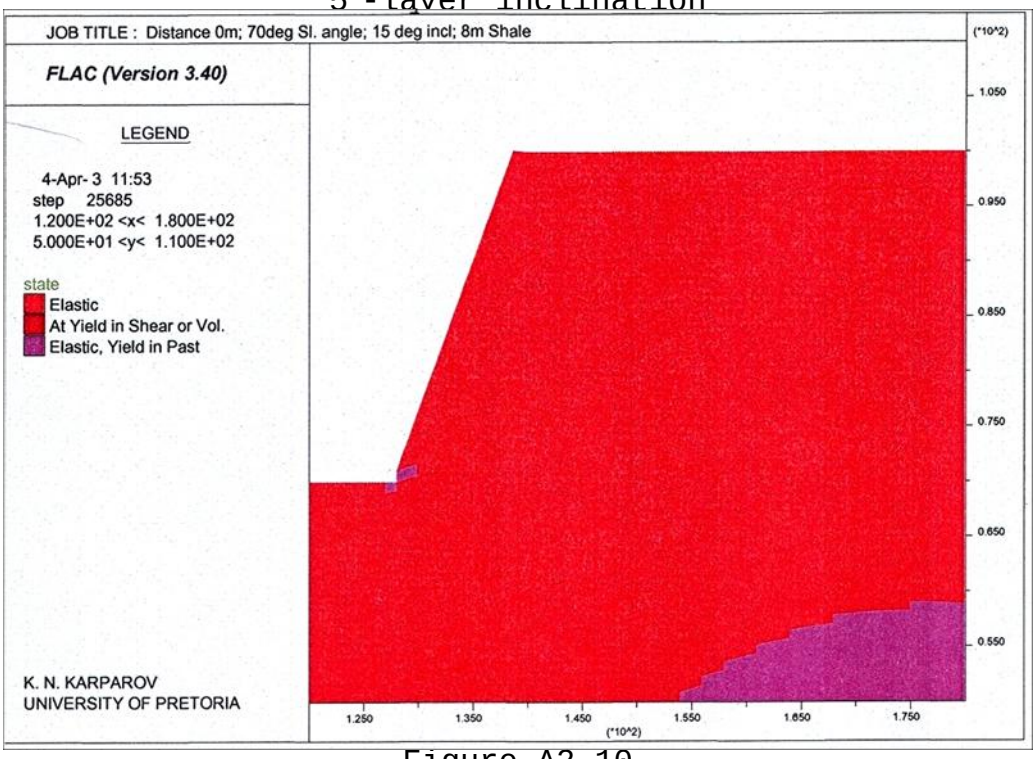

Figure A2.10

State condition of the 70^0-slope profile with 8m thick embedded shale layer at the anticline formation with 15^0-layer inclination

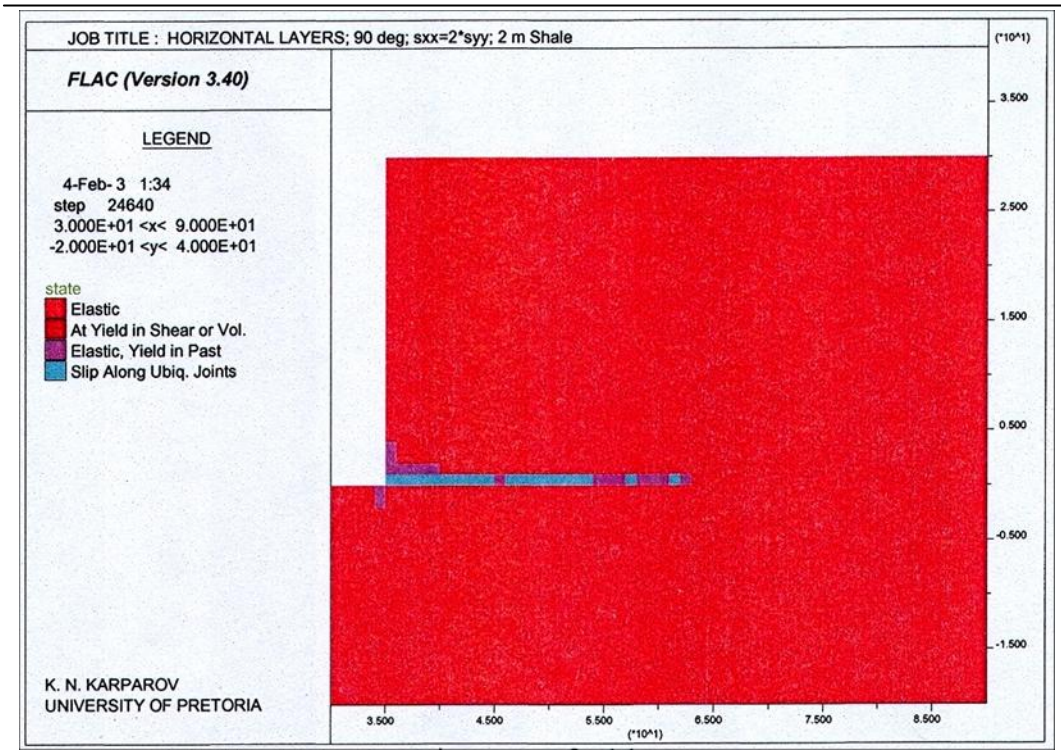

Figure A2.11

State condition of the 90^0-slope profile with 2m thick embedded flat shale layer

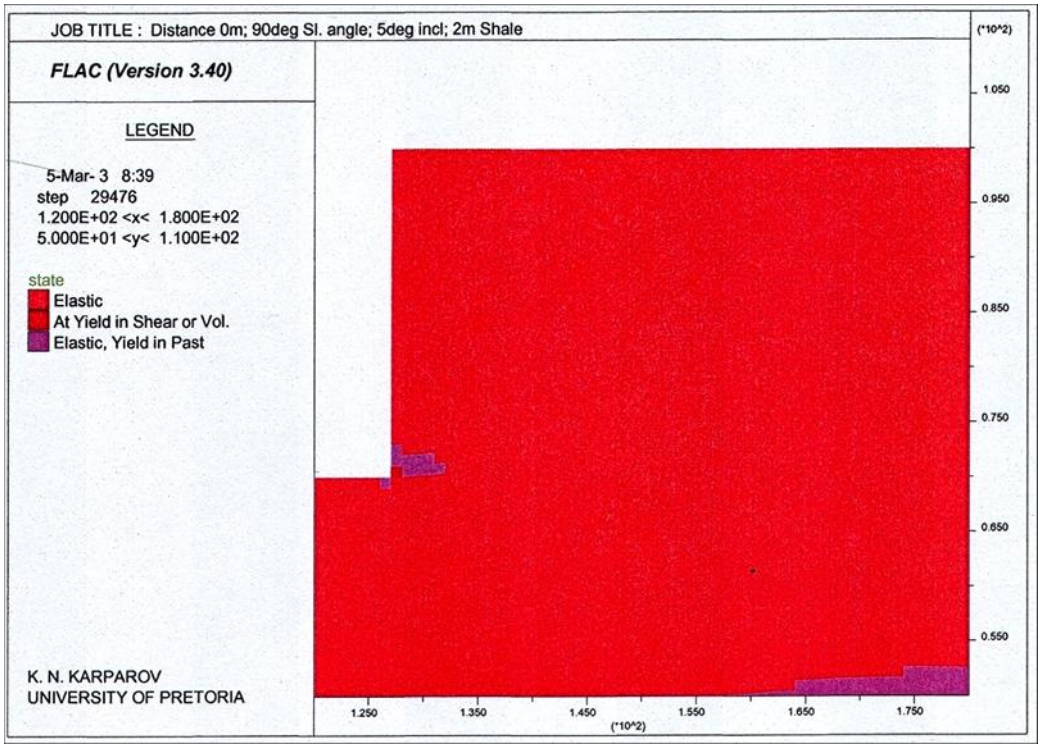

Figure A2.12

State condition of the 90^0-slope profile with 2m thick embedded shale layer at the anticline formation with 5^0-layer inclination

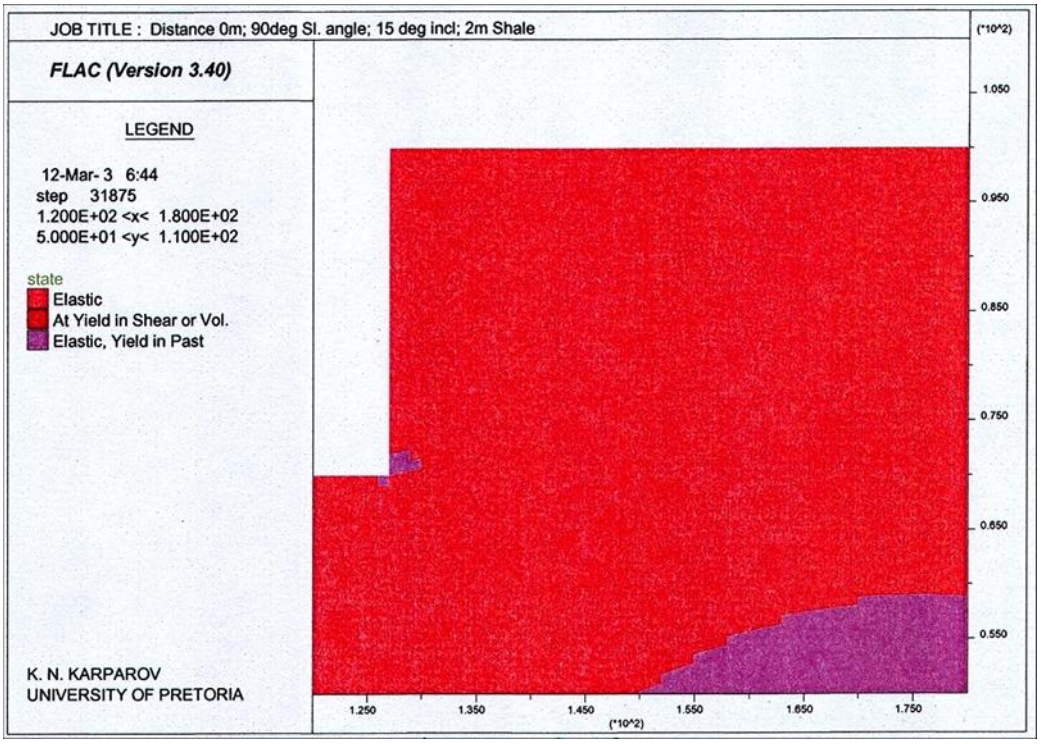

Figure A2.13

State condition of the 90^0-slope profile with 2m embedded shale layer at the anticline formation with 15^0-layer inclination

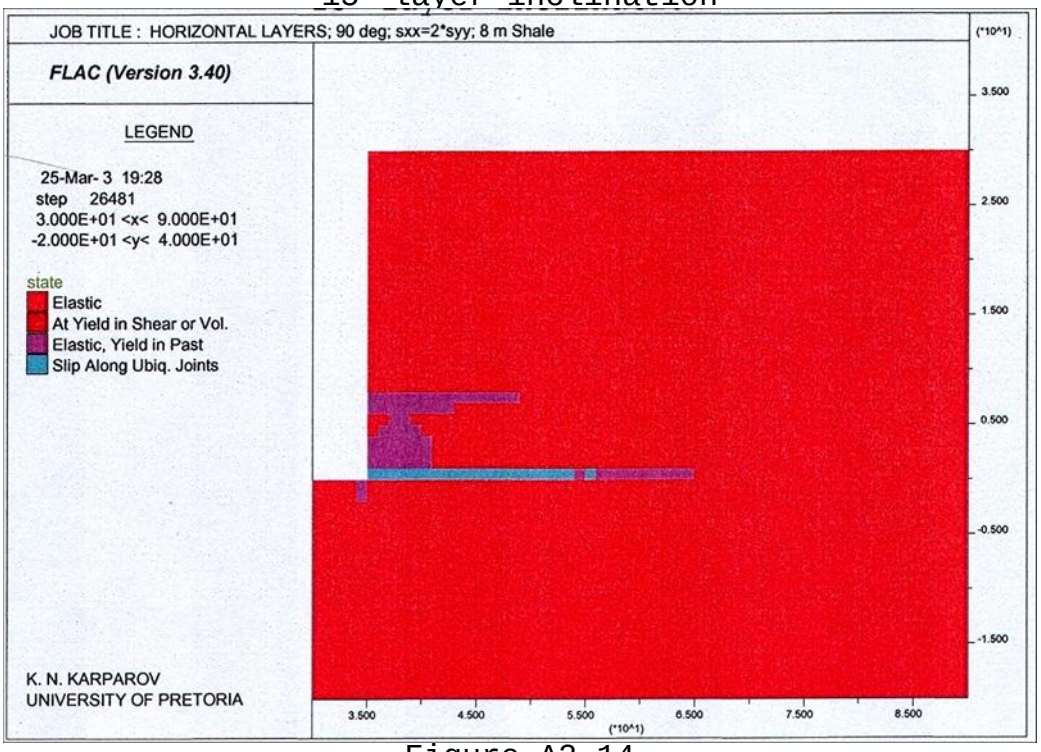

Figure A2.14

State condition of the 90^0-slope profile with 8m thick embedded flat shale layer

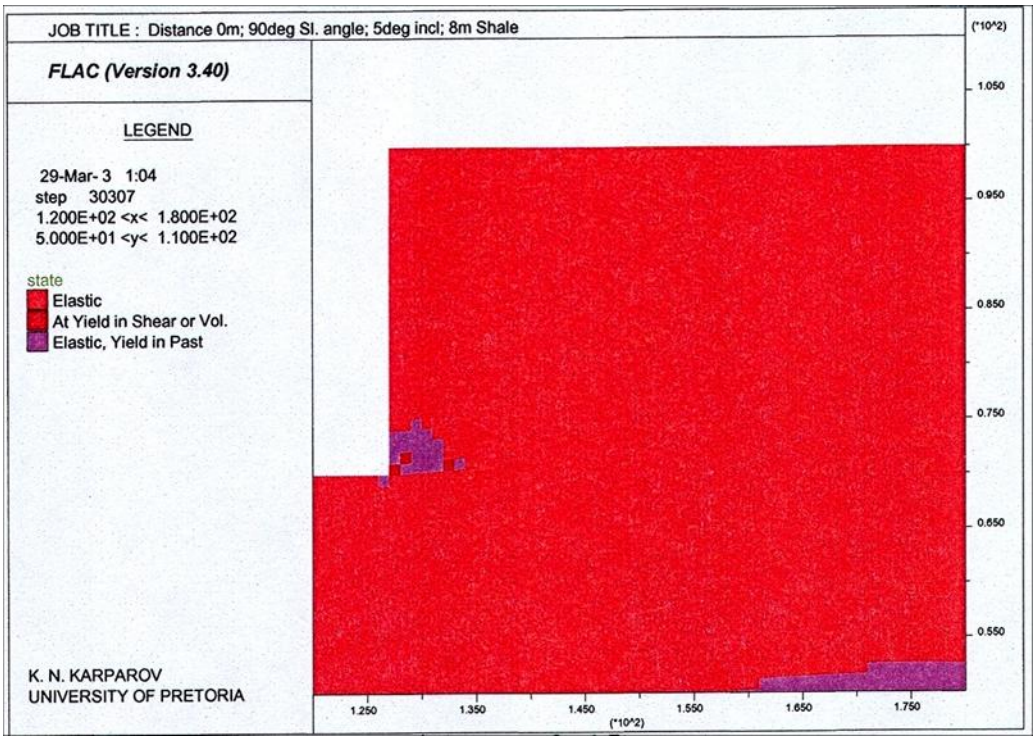

Figure A2.15

State condition of the 90^0-slope profile with 8m thick embedded shale layer at the anticline formation with 5^0-layer inclination

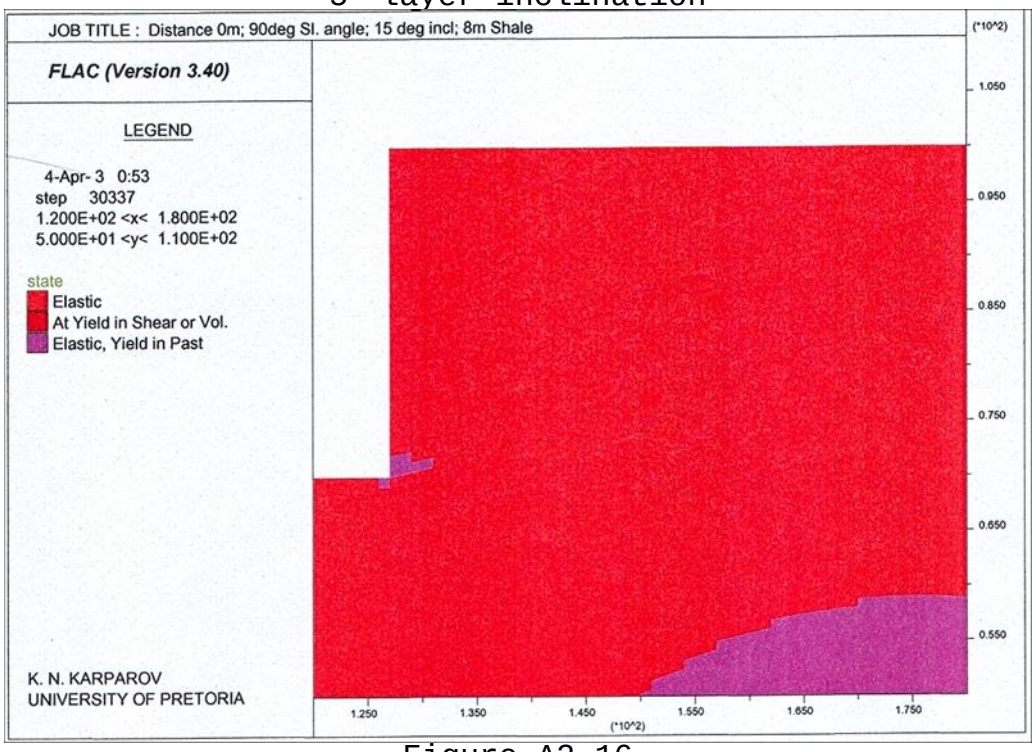

Figure A2.16

State condition of the 90^0-slope profile with 8m thick embedded shale layer at the anticline formation with 15^0-layer inclination

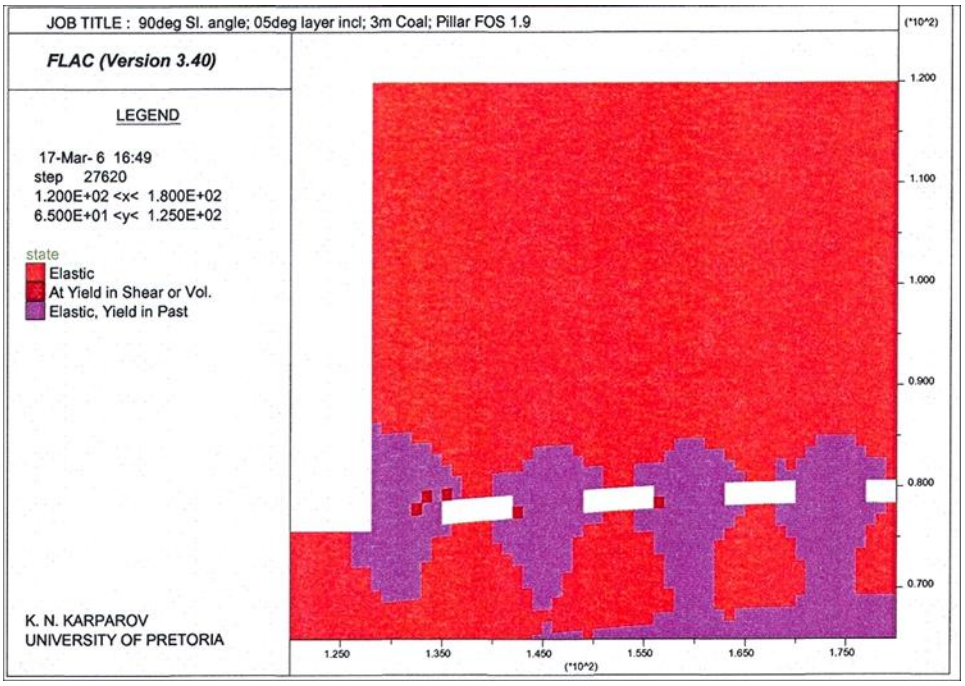

Figure A2.17

State in the profile with 90^0-slope angle, pillar safety factor 1.9 at the anticline formation with 5^0-limb inclination

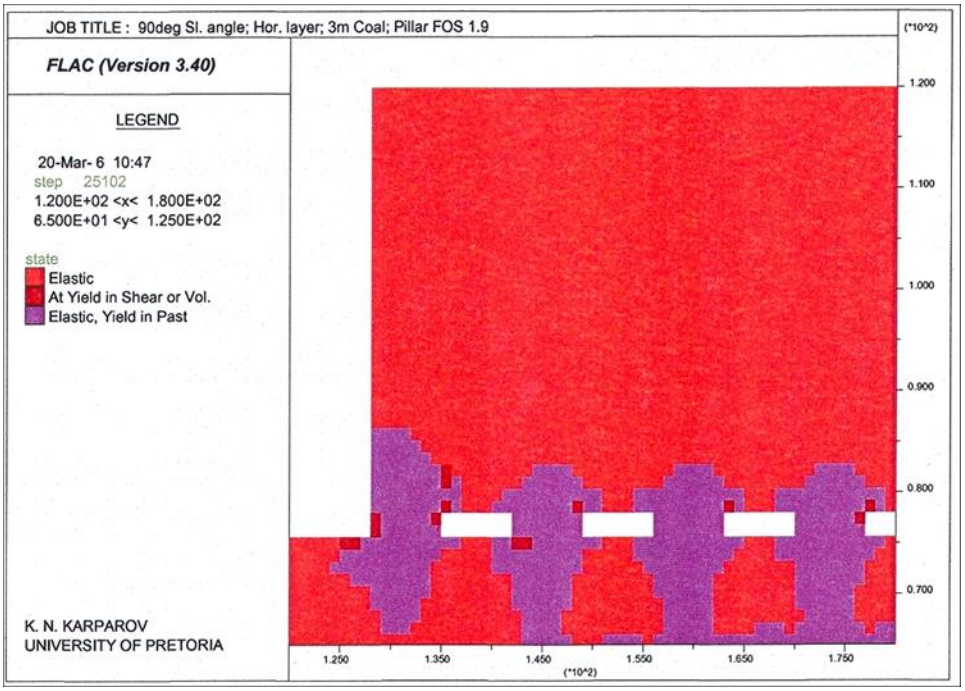

Figure A2.18

State in the profile with 90^0-slope angle, pillar safety factor 2.2 and flat coal seam

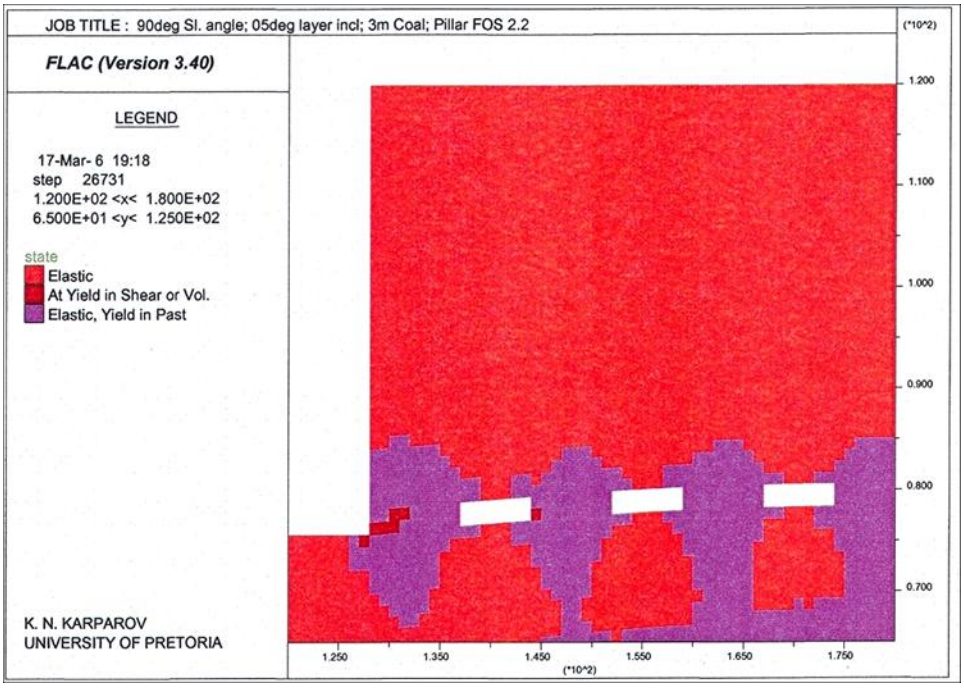

Figure A2.19

State in the profile with 90^0-slope angle, pillar safety factor 2.2 at the anticline formation with 5^0-limb inclination

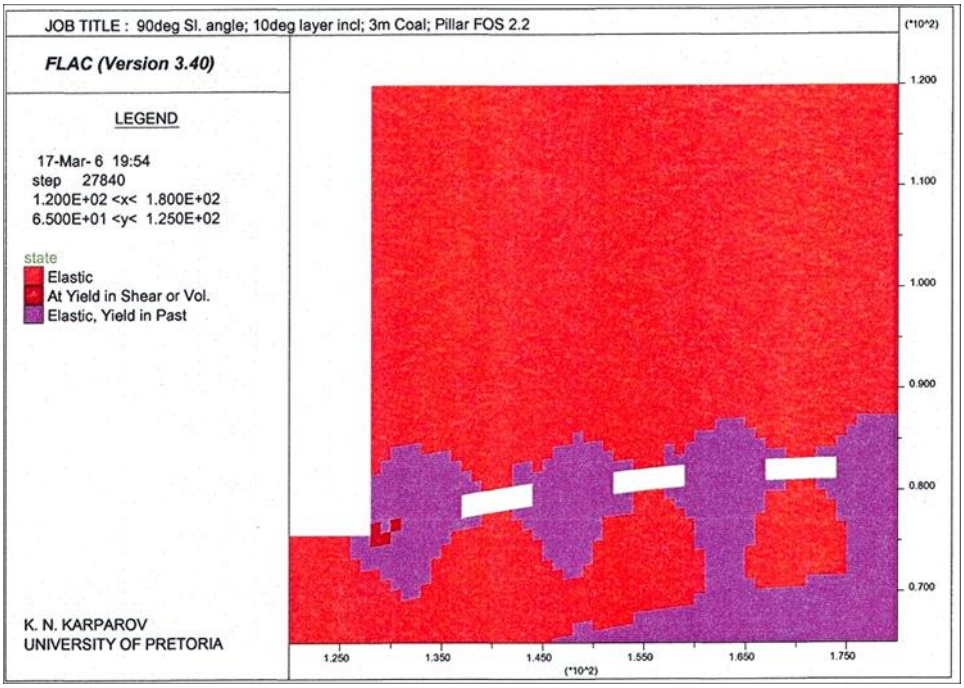

Figure A2.20

State in the profile with 90^0-slope angle, pillar safety factor 2.2 at the anticline formation with 10^0-limb inclination

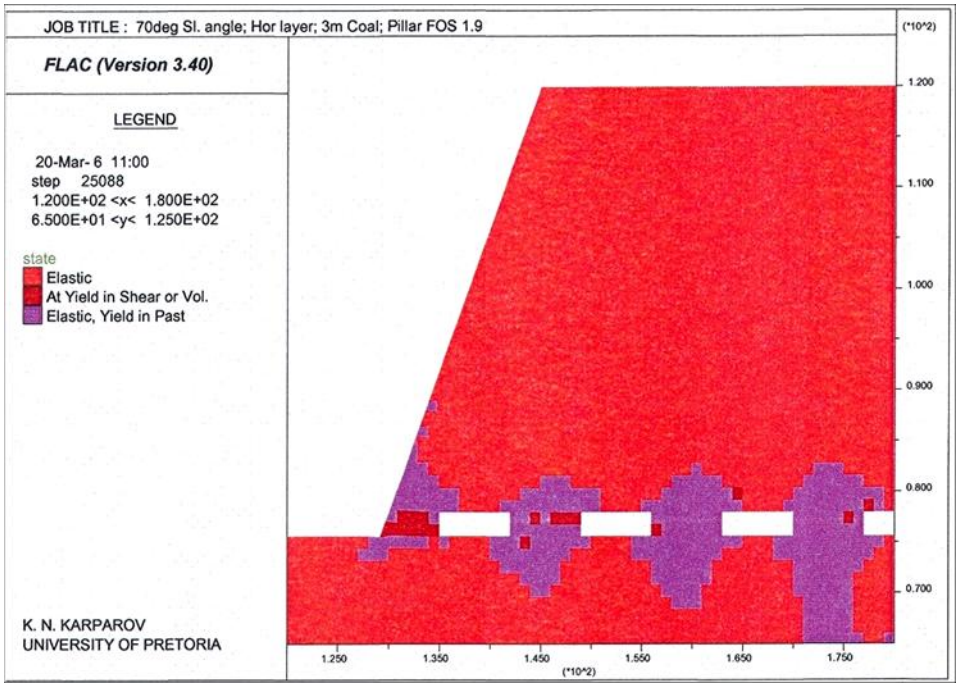

Figure A2.21

State in the profile with 70^0-slope angle, pillar safety factor 1.9 and flat coal seam

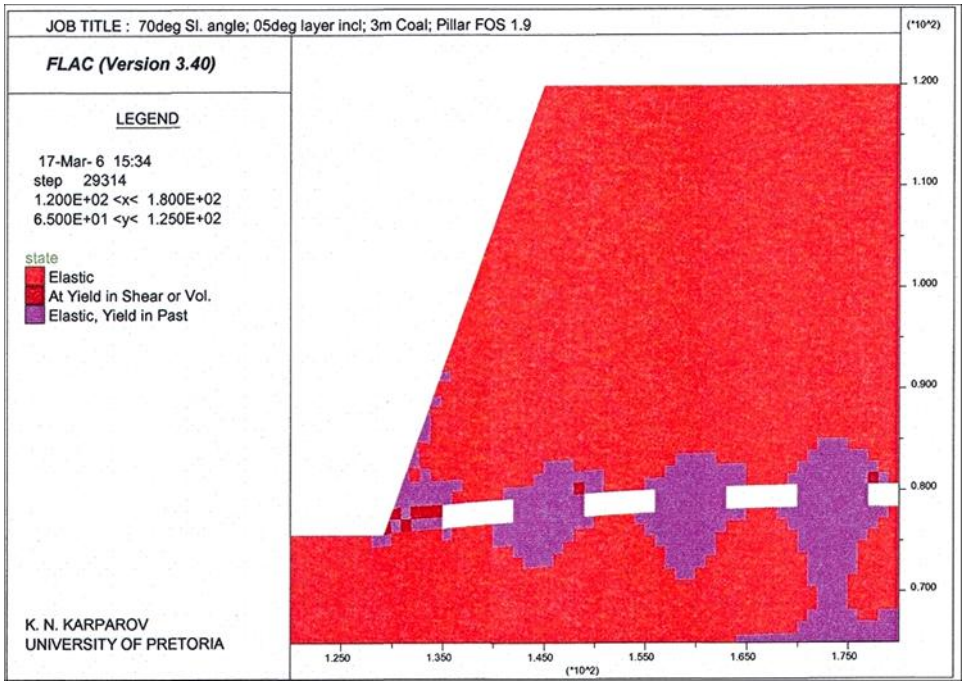

Figure A2.22

State in the profile with 70^0-slope angle, pillar safety factor 1.9 at the anticline formation with 5^0-limb inclination

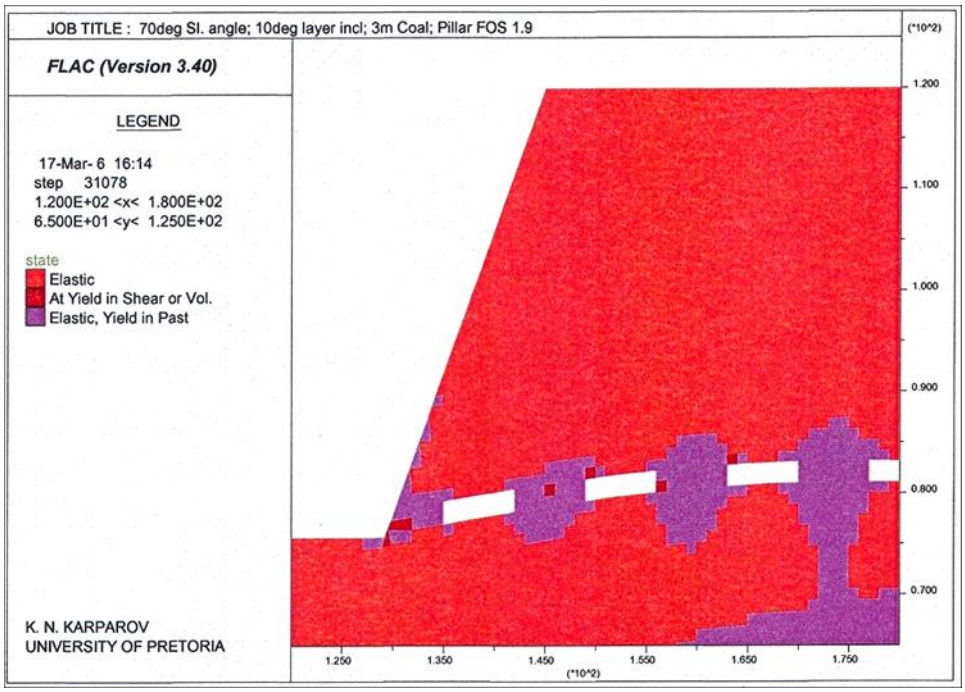

Figure A2.23

State in the profile with 70^0-slope angle, pillar safety factor 1.9 at the anticline formation with 10^0-limb inclination

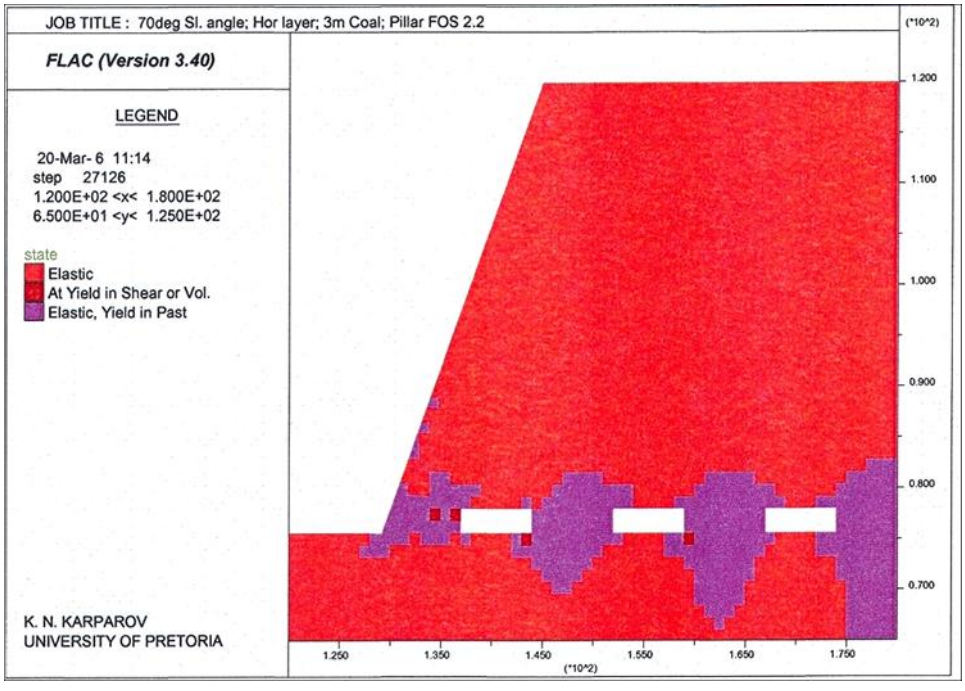

Figure A2.24

State in the profile with 70^0-slope angle, pillar safety factor 2.2 and flat coal seam

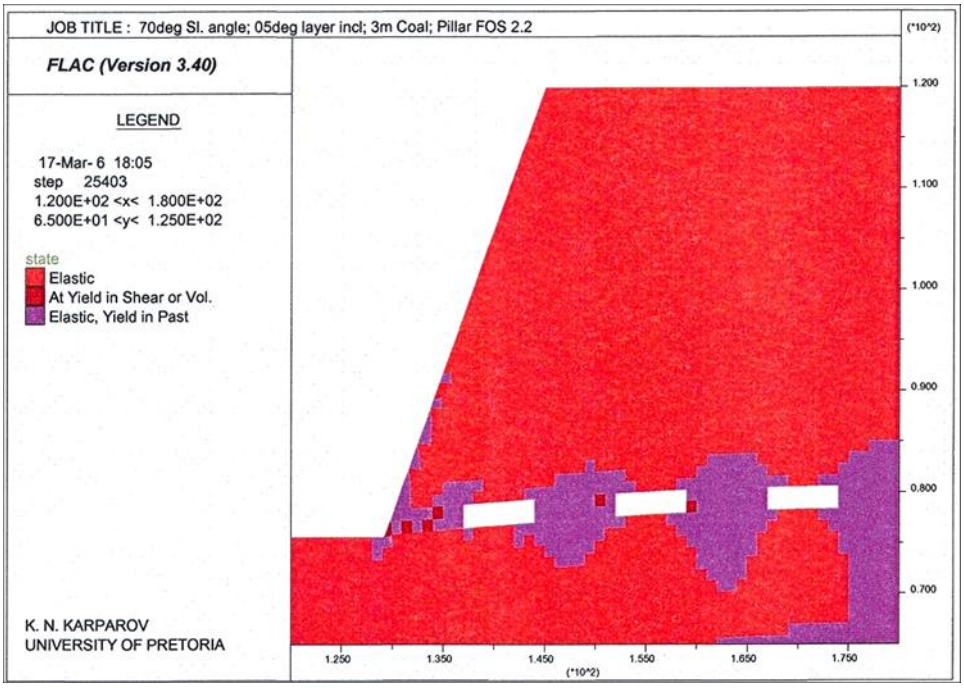

Figure A2.25

State in the profile with 70^0-slope angle, pillar safety factor 2.2 at the anticline formation with 5^0-limb inclination

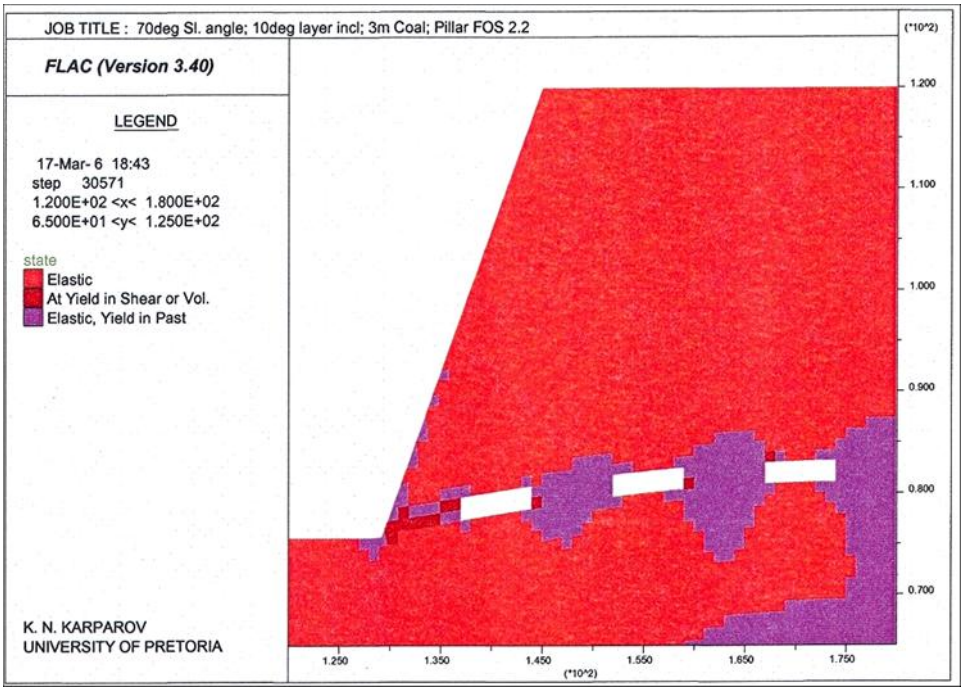

Figure A2.26

State in the profile with 70^0-slope angle, pillar safety factor 2.2 at the anticline formation with 10^0-limb inclination

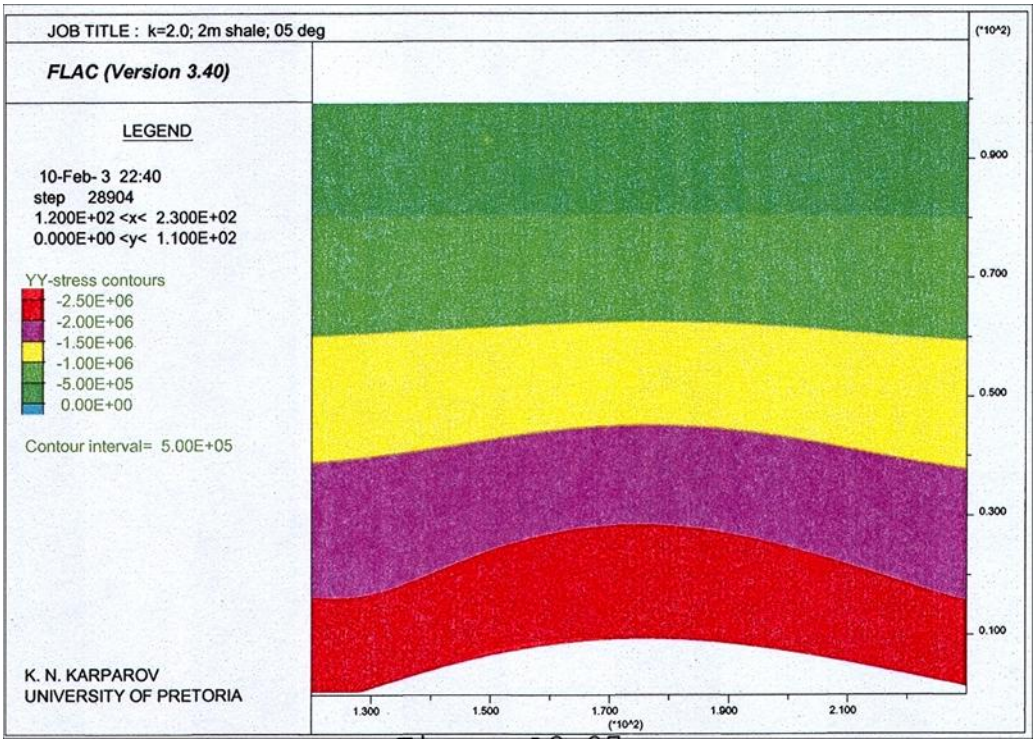

Figure A2.27

Vertical stress component of the FLAC model with 2m thick shale layer and 5^0-layer inclination of the anticline formation

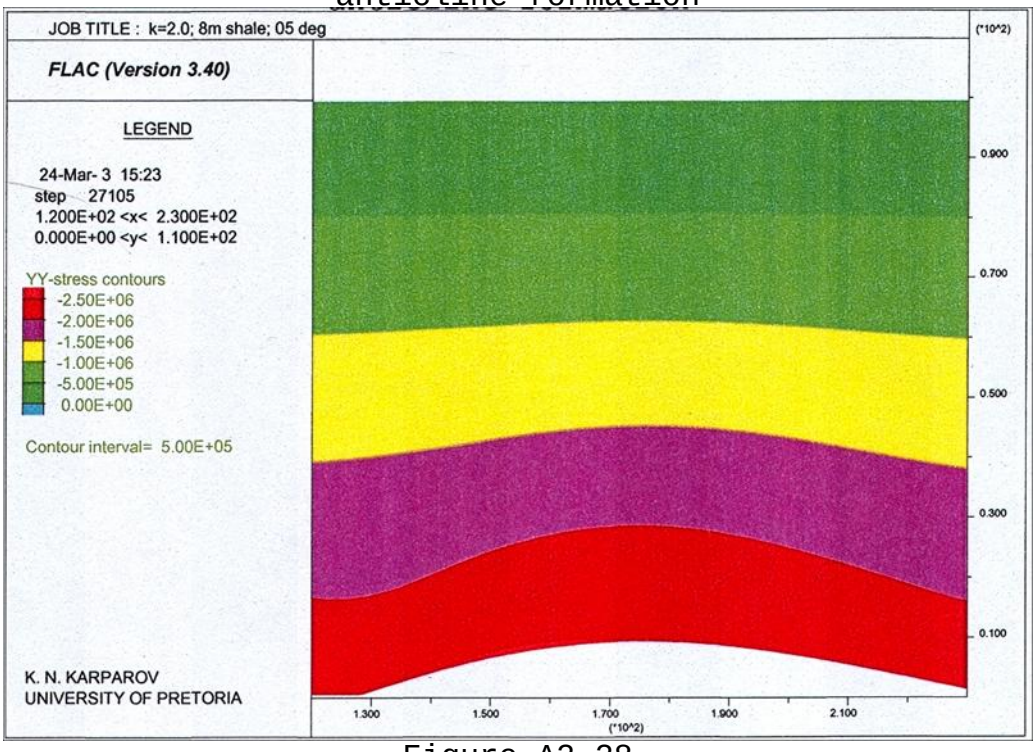

Figure A2.28

Vertical stress component of the FLAC model with 8m thick shale layer and 5^0-layer inclination of the anticline formation

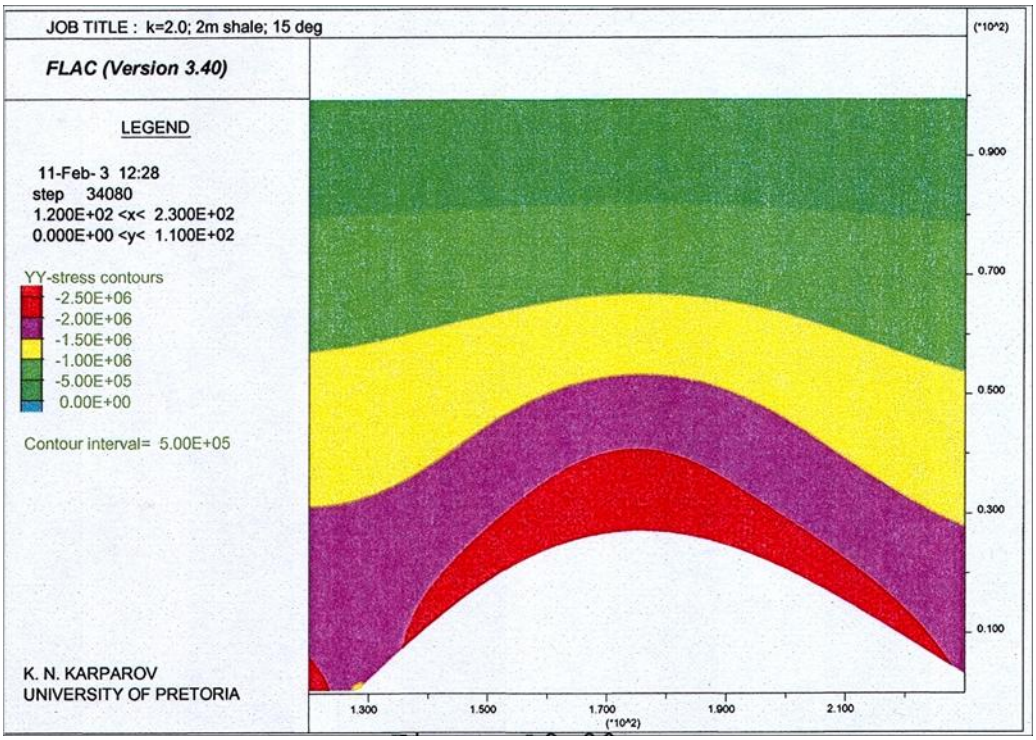

Figure A2.29

Vertical stress component of the FLAC model with 2m thick shale layer and 15^0-layer inclination of the anticline formation

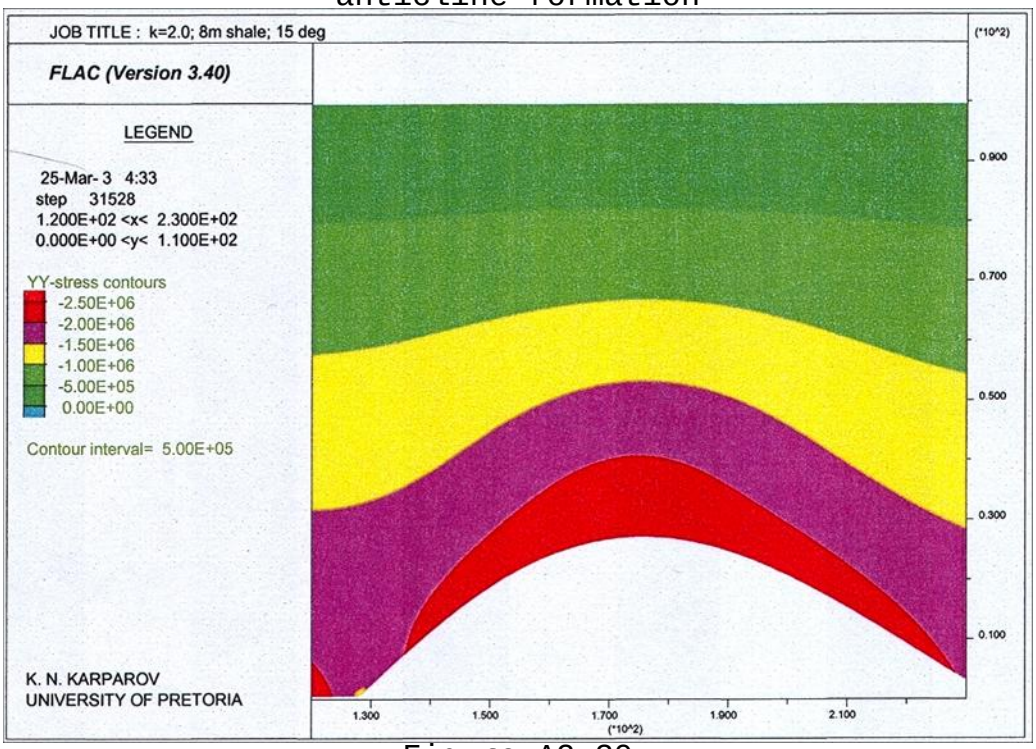

Figure A2.30

Vertical stress component of the FLAC model with 8m thick shale layer and 15^0-layer inclination of the anticline formation

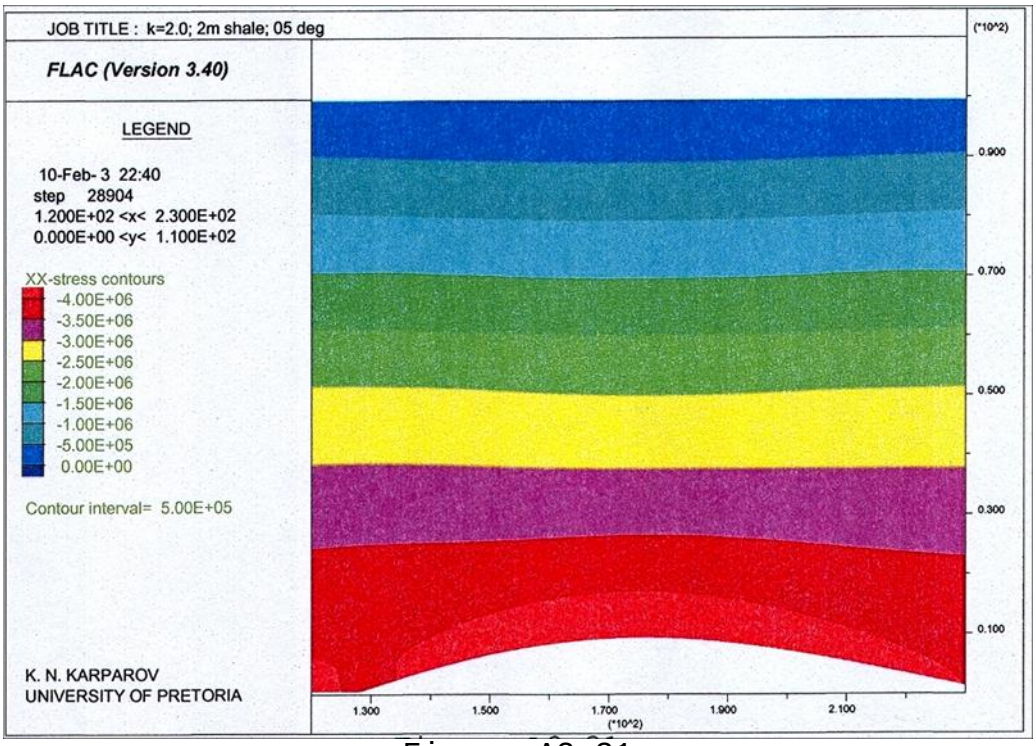

Figure A2.31

Horizontal stress component of the FLAC model with 2m thick shale layer and 5^0-layer inclination of the anticline formation

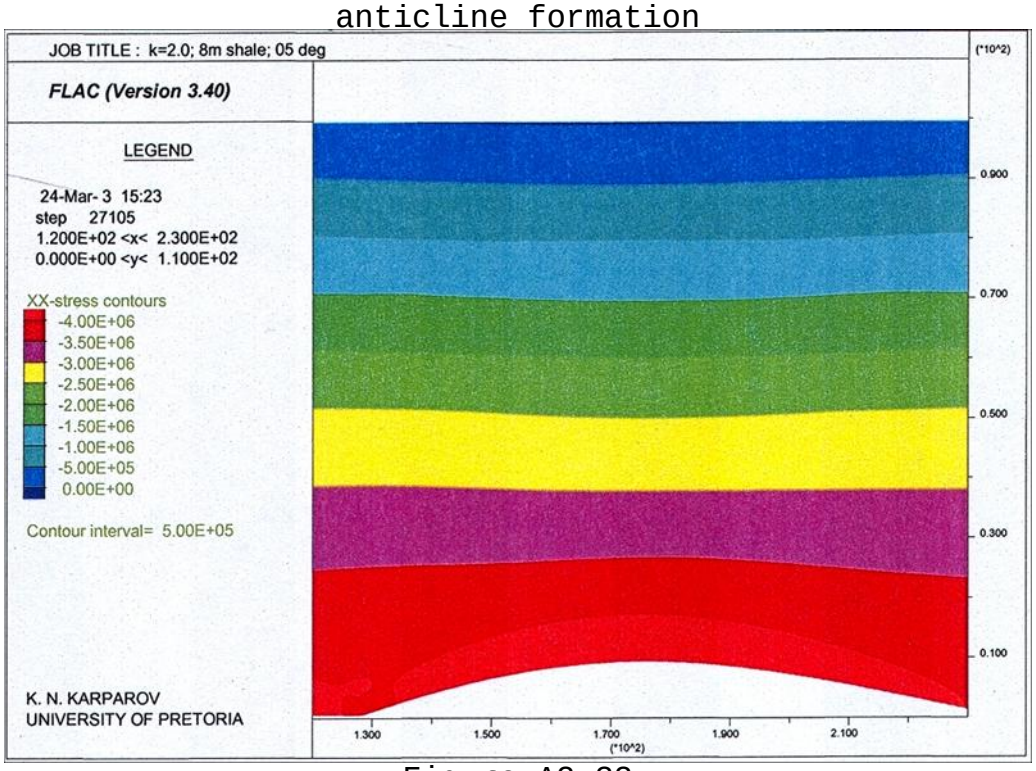

Figure A2.32

Horizontal stress component of the FLAC model with 8m thick shale layer and 5^0-layer inclination of the anticline formation

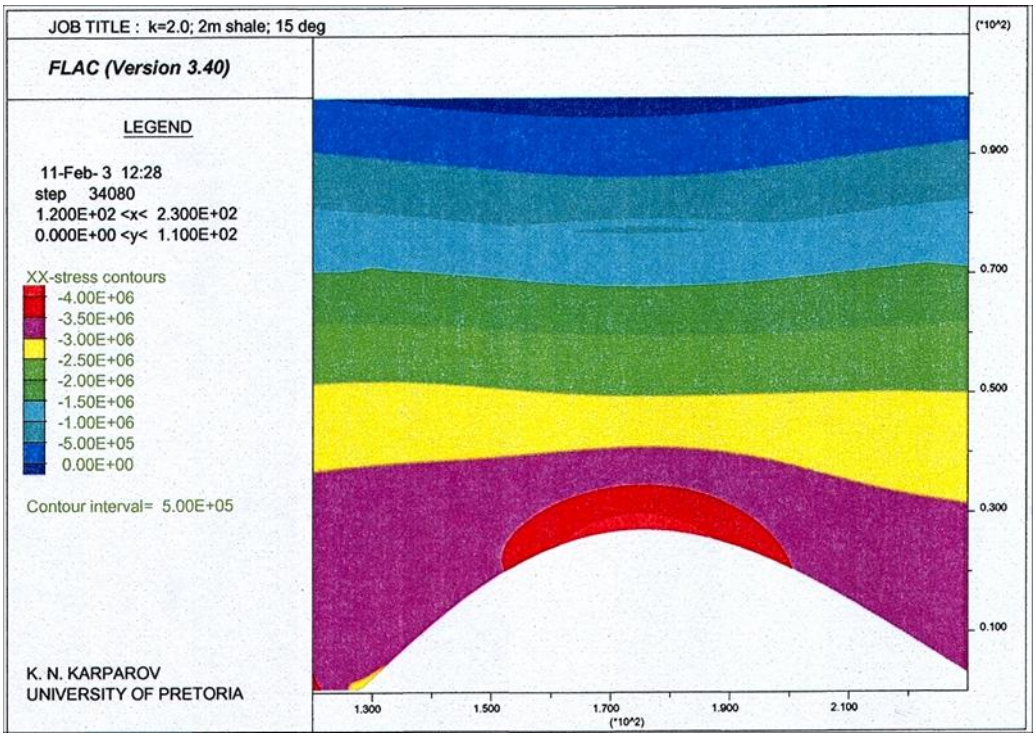

Figure A2.33

Horizontal stress component of the FLAC model with 2m thick shale layer and 15^0-layer inclination of the anticline formation

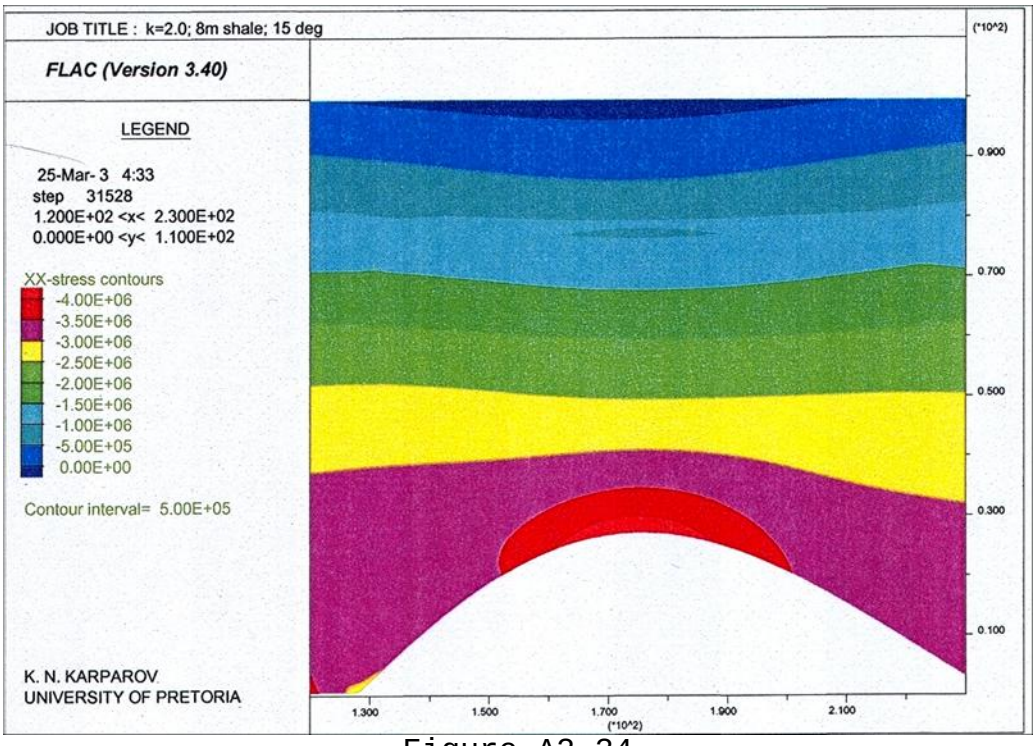

Figure A2.34

Horizontal stress component of the FLAC model with 8m thick shale layer and 15^0-layer inclination of the anticline formation

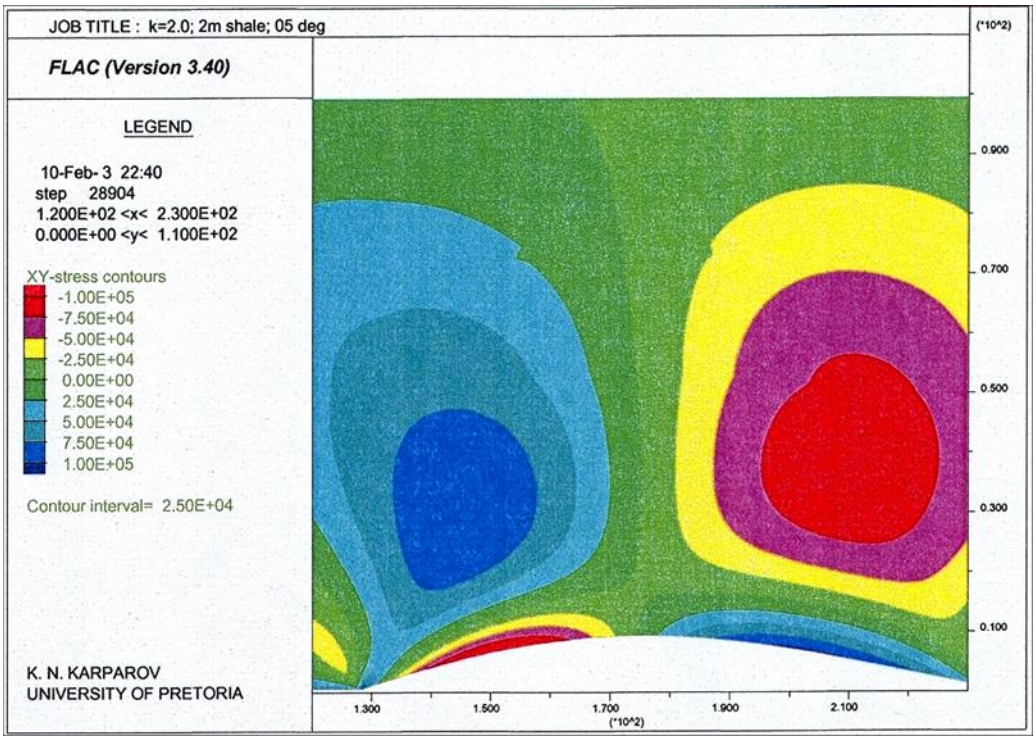

Figure A2.35

Shear stress component of the FLAC model with 2m thick shale layer and 5^0-layer inclination of the anticline formation

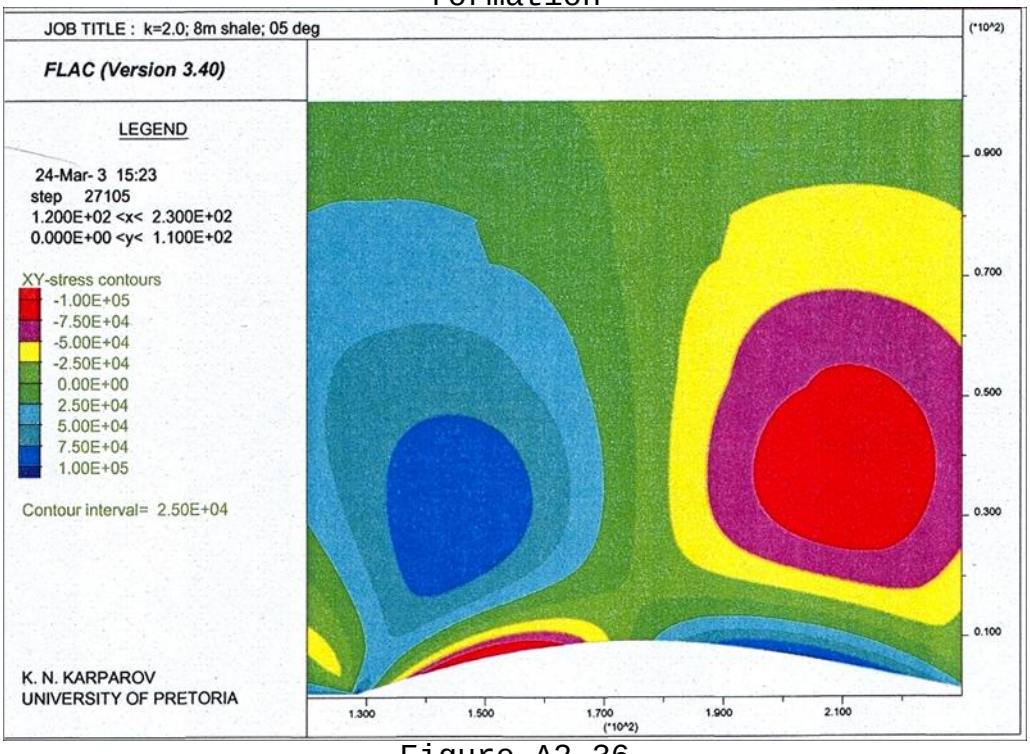

Figure A2.36

Shear stress component of the FLAC model with 8m thick shale layer and 5^0-layer inclination of the anticline formation

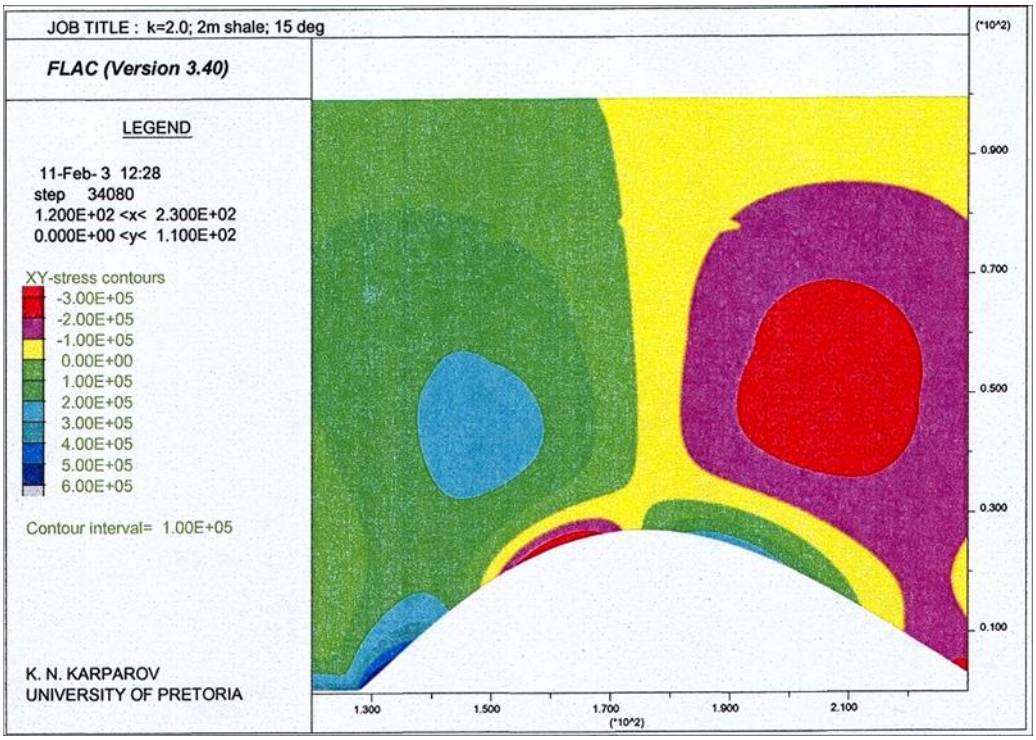

Figure A2.37

Shear stress component of the FLAC model with 2m thick shale layer and 15^0-layer inclination of the anticline formation

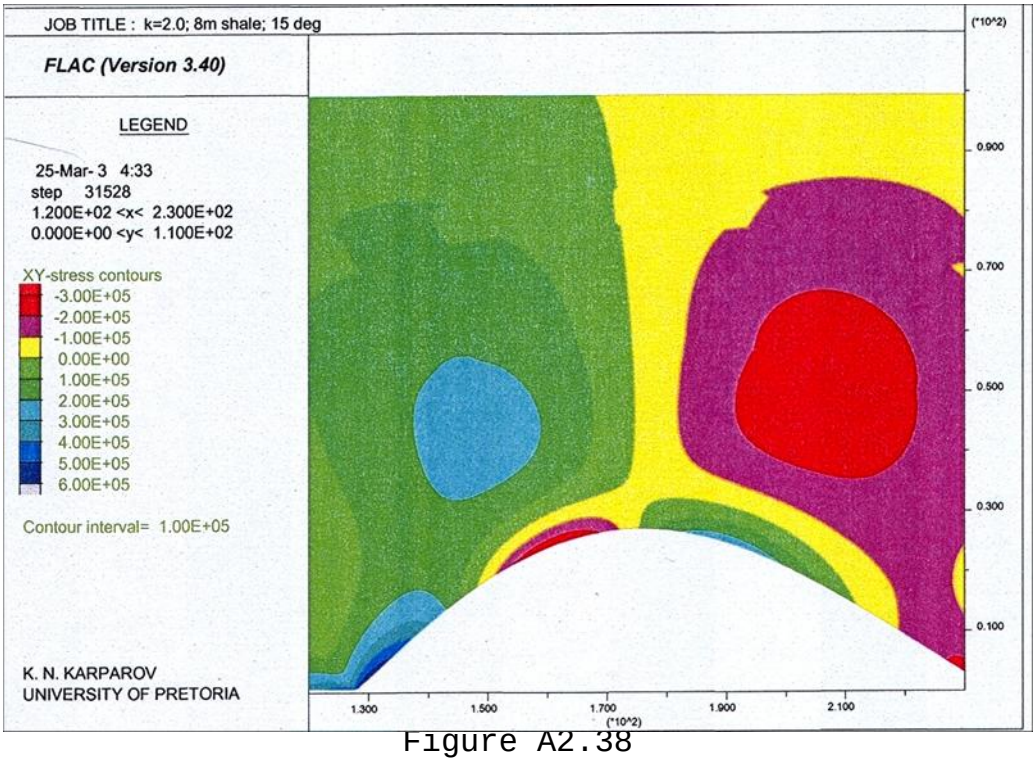

Figure A2.38

Shear stress component of the FLAC model with 8m thick shale layer and 15^0-layer inclination of the anticline formation

APPENDIX 3. GRAPHS

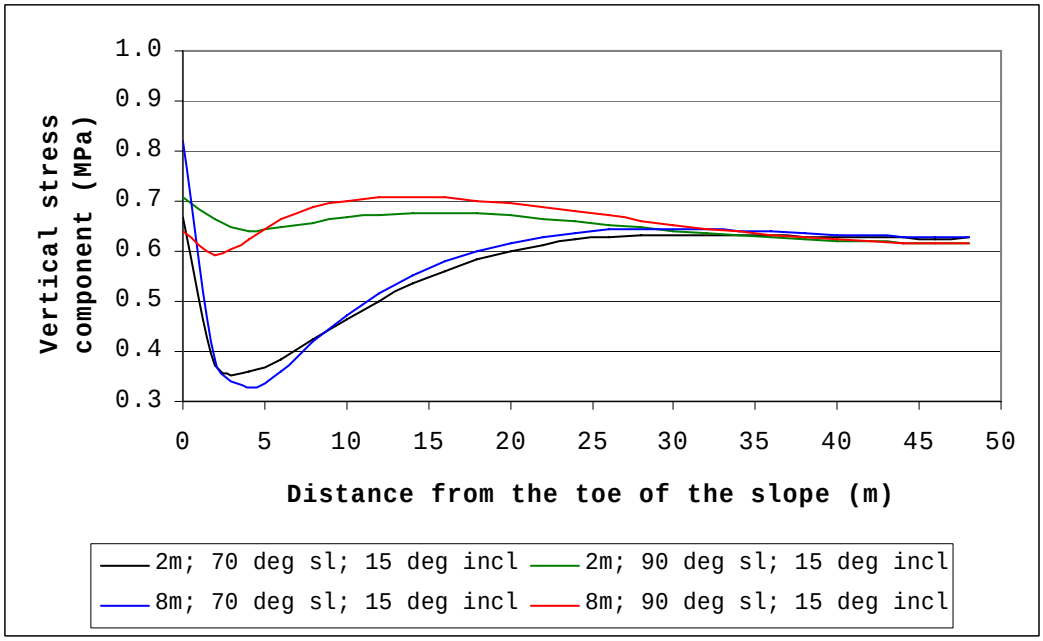

Figure A3.1

Vertical stress component along profile line with 2m- and 8m-thick shale layer and 70^0 and 90^0 slope angle, in the undulated strata formation with 15^0 inclination

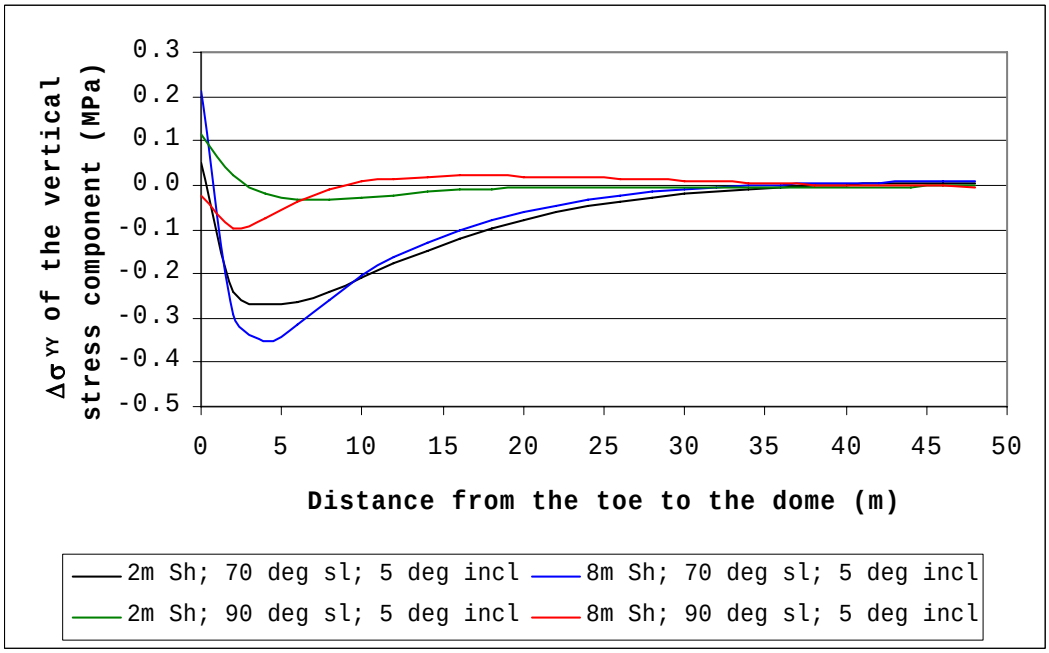

Figure A3.2

Vertical stress difference along profile line with 2m- and 8m-thick shale layer and 70^0 and 90^0 slope angle, in the undulated strata formation with 5^0 inclination

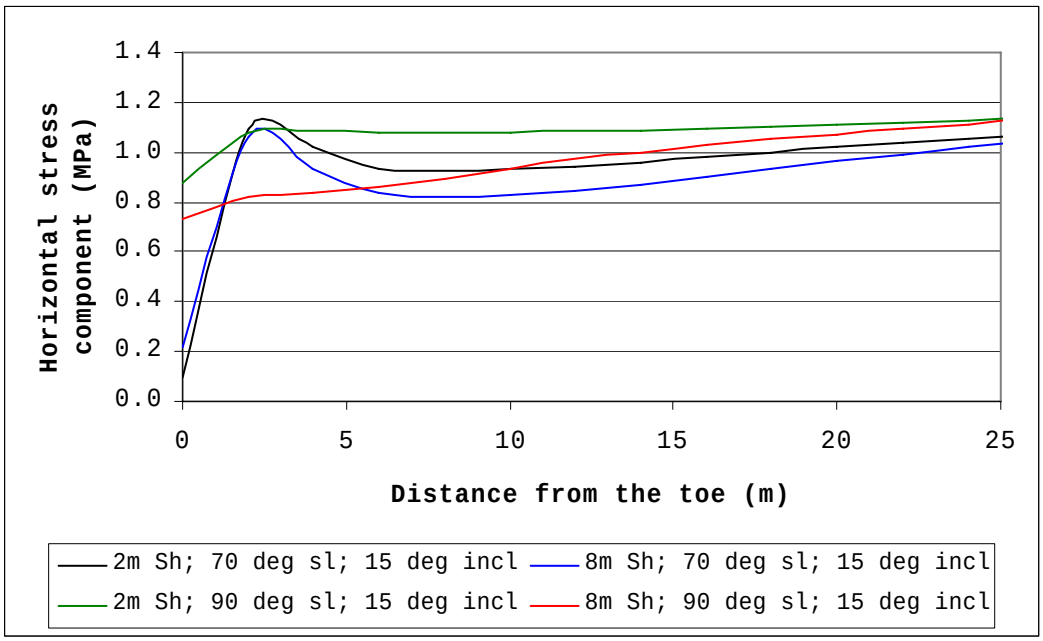

Figure A3.3

Resultant horizontal stress component of the slope with 2m- and 8m-thick embedded shale layer and 70^0 and 90^0-slope in the undulated strata formation with 15^0 layer inclinations

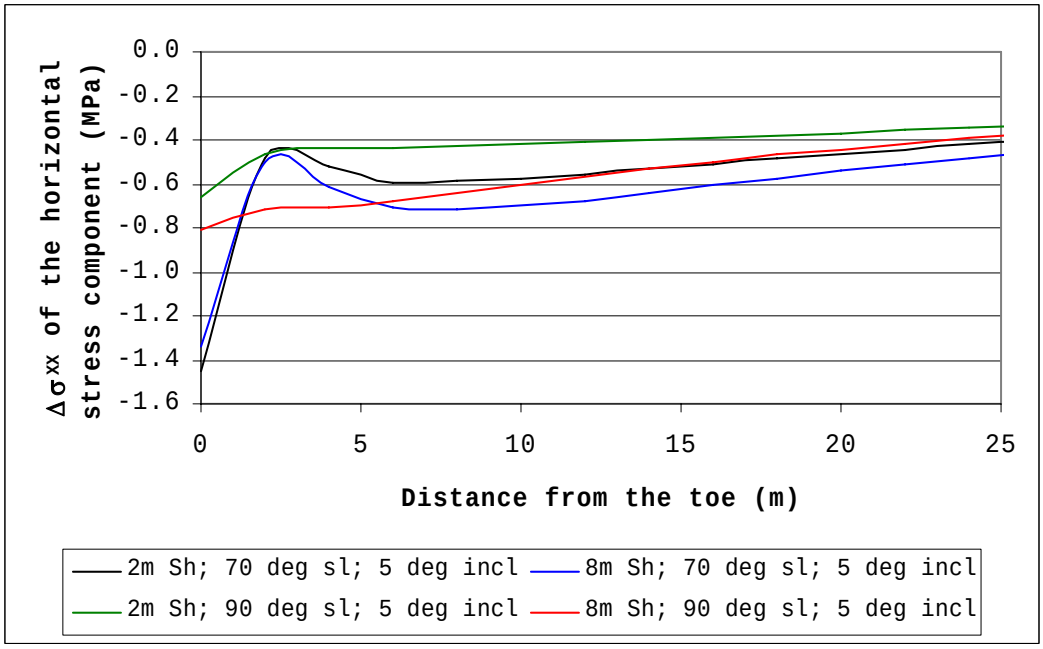

Figure A3.4

Horizontal stress component difference ($\Delta\sigma_{XX}$) of the slope with 2m- and 8m-thick embedded shale layer and 70^0 and 90^0 slope in the undulated strata formation with 5^0 layer inclinations

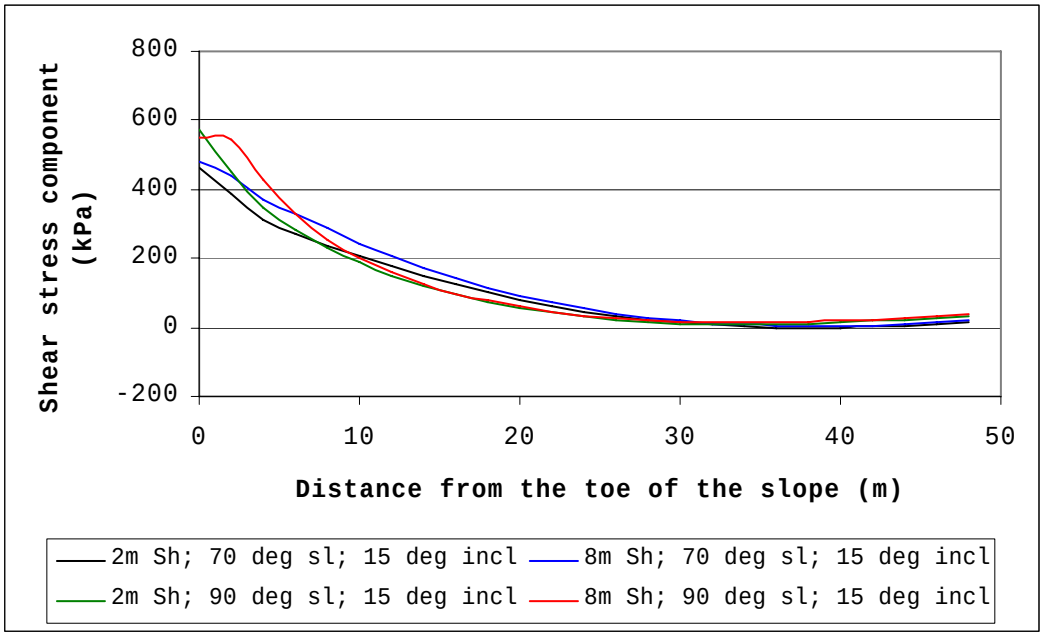

Figure A3.5

Shear stress component of the profile with 2m- and 8m-thick embedded shale layer, 70^0 and 90^0-slope angle in the undulated strata formation (15^0 inclination) in the model

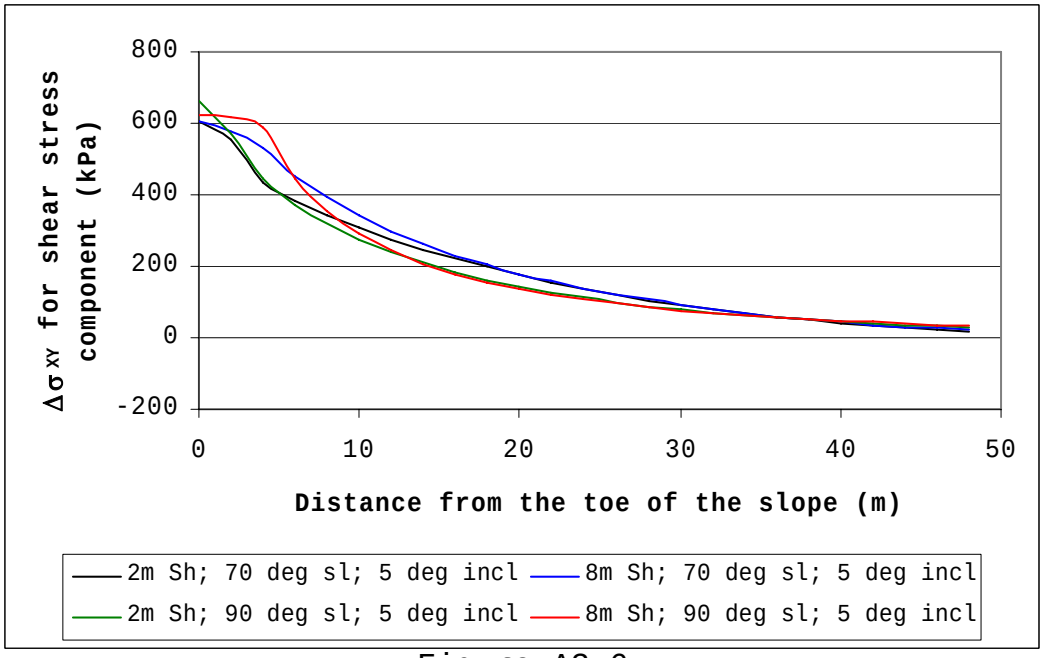

Figure A3.6

Shear stress difference ($\Delta\sigma_{XY}$) of the profile with 2m- and 8m-thick embedded shale layer, 70^0 and 90^0 slope angle in the anticline formation (5^0 layer inclinations) in the model

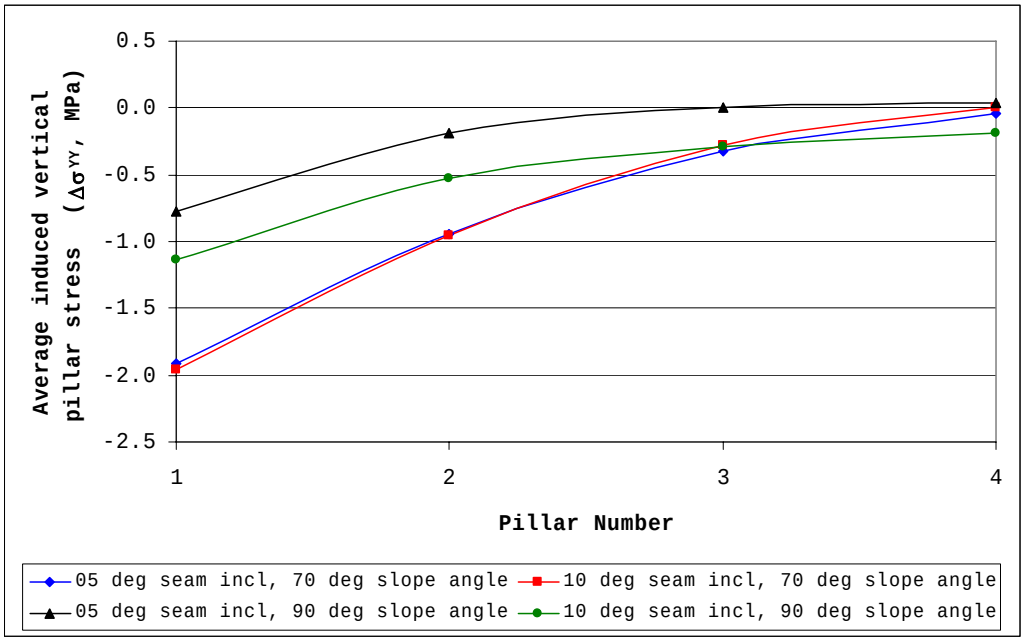

Figure A3.7

Vertical stress component difference ($\Delta\sigma_{YY}$) of the pillars with safety factor of 2.2 for the profiles with slope angles 70^0 and 90^0 and the undulated strata formation (layer inclinations 5^0 and 15^0) in the model

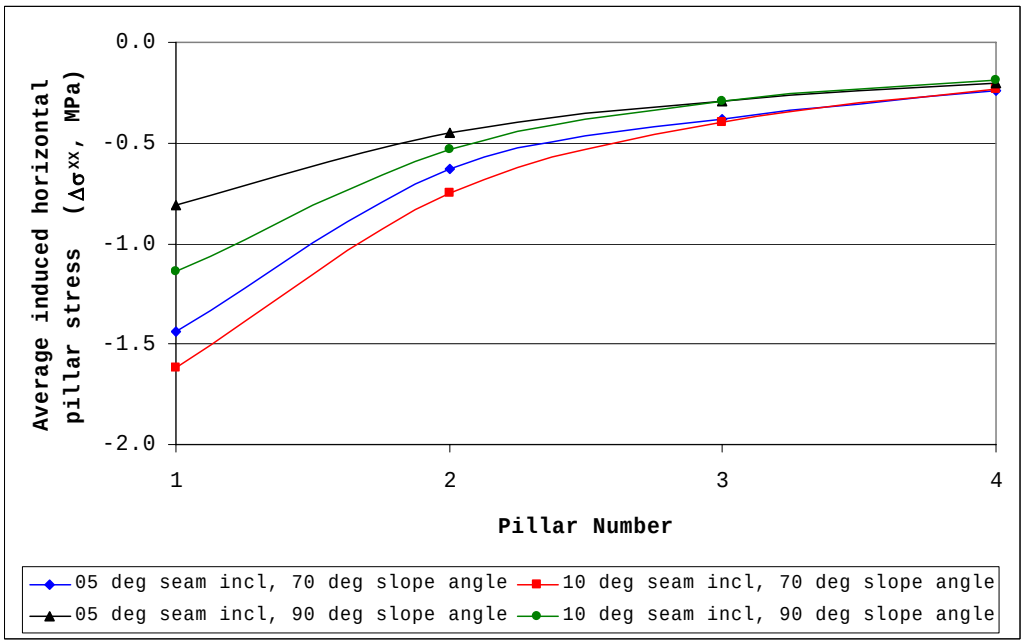

Figure A3.8

$\Delta\sigma_{XX}$ of the pillars with a pillar safety factor of 2.2 of profiles with 70^0 and 90^0 slope angle and undulated strata formation (5^0 and 15^0 layer inclination) in the model

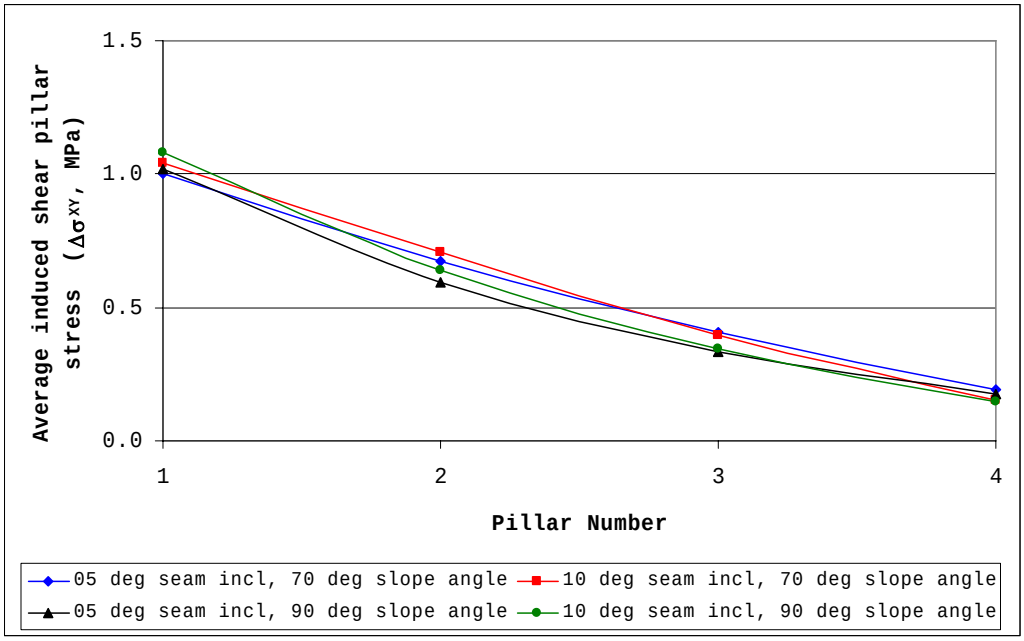

Figure A3.9

Shear stress component difference ($\Delta\sigma_{XY}$)of the pillars with a pillar safety factor of 2.2 in the profiles with 70^0 and 90^0 slope angle and undulated strata formation (5^0 and 15^0 layer inclination) in the model

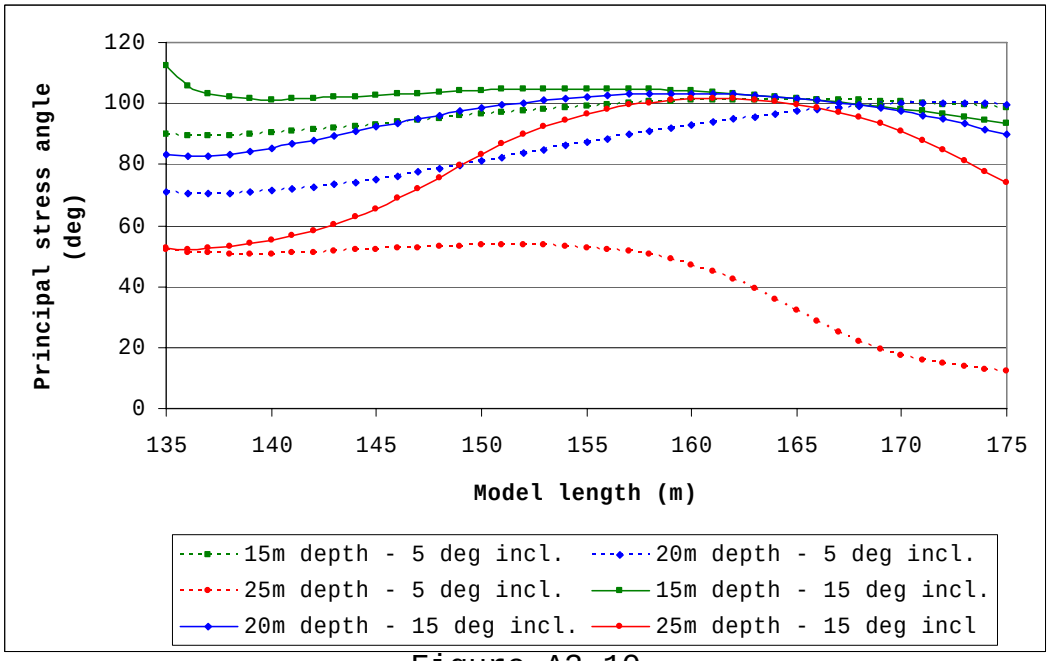

Figure A3.10

Inclination of the principal stress direction angles along the profile lines at 15m, 20m and 25m depth (Figure 5.3) in the homogeneous sandstone slope profile with 70^0 slope angle and different layer inclination

a)

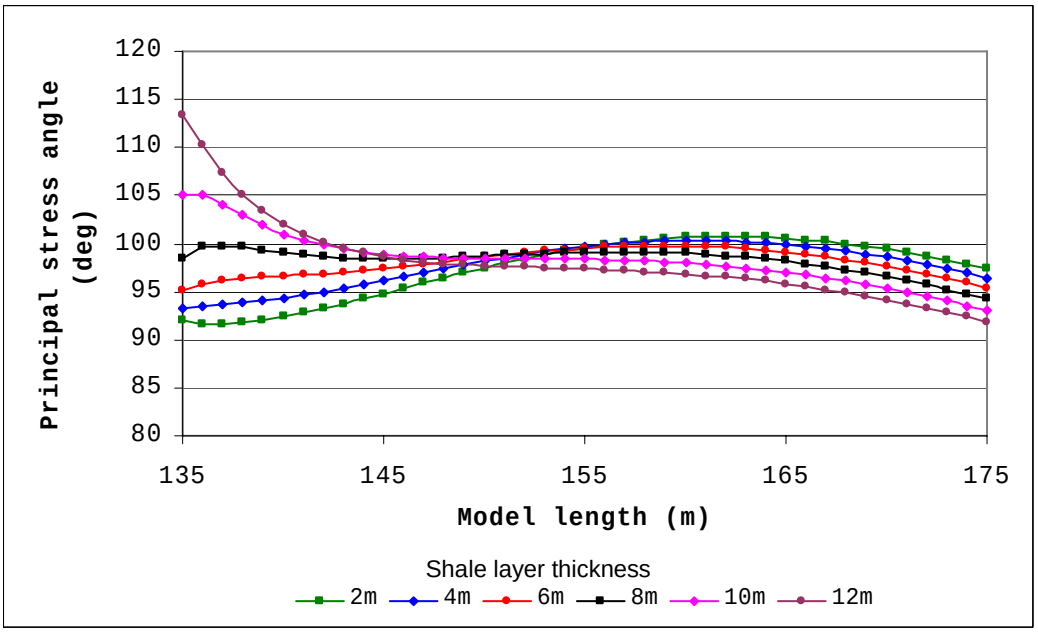

b)

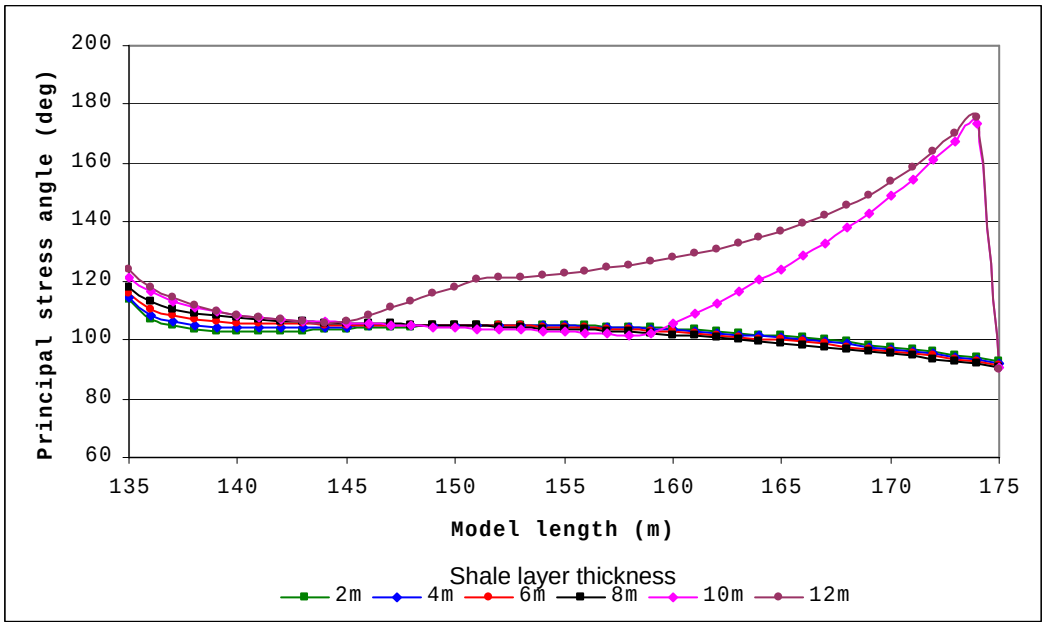

Figure A3.11

Inclination of the principal stress direction inclination angles along the profile line at 15m depth (Figure 5.3) in the profile with different embedded shale layer thickness at the undulated strata formation with: a) 5^0 layer inclination and b) 15^0 layer inclination

a)

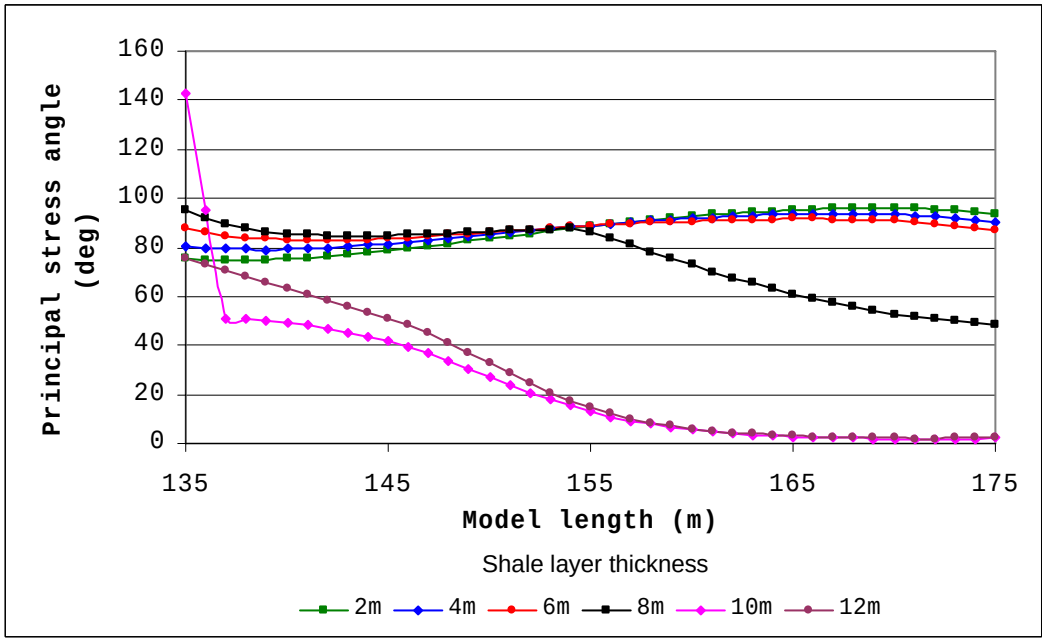

b)

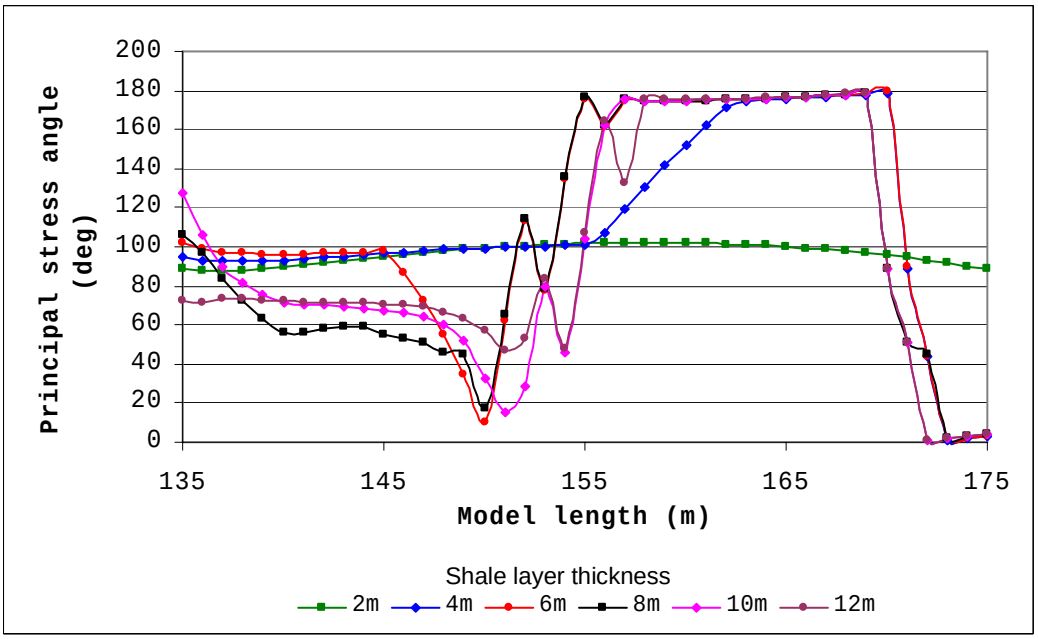

Figure A3.12

Inclination of the principal stress direction inclination angles along the part of profile line at 20m depth (Figure 5.3) in the profile with different embedded shale layer thickness at the undulated strata formation with: a) 5^0 layer inclination and b) 15^0 layer inclination

a)

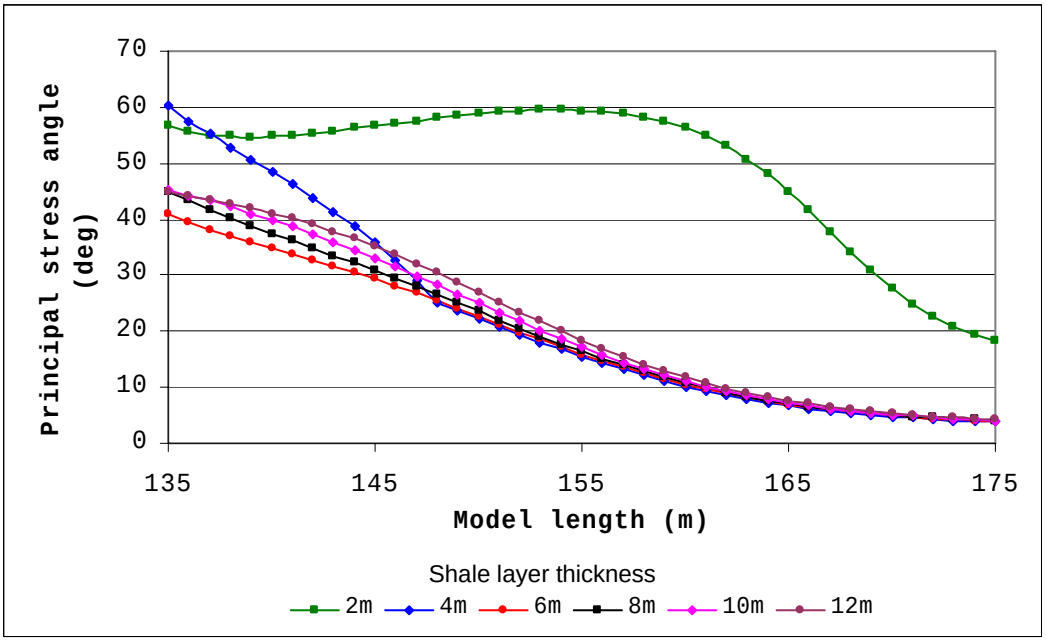

b)

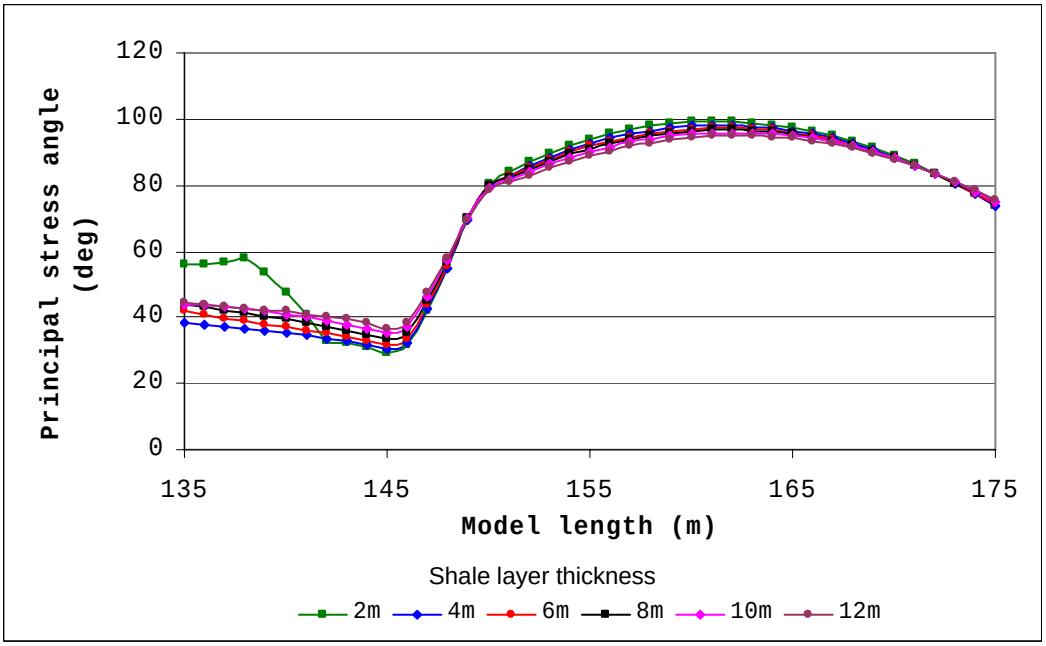

Figure A3.13

Inclination of the principal stress direction angles along the profile line at 25m depth in the profile with different embedded shale layer thickness at the undulated strata formation with: a) 5^0 layer inclination and b) 15^0 layer inclination

APPENDIX 4. SLOPE STABILITY CALCULATIONS

Table A4.1 *Example 1b*: Safety factor calculations along the bottom contact

Step No	Parameter	Value	Equation No
Inner shear failure surface (ISFS)			
Step 1	Average friction angle, deg	26	5.2
Step 2	Inclination angle of the ISFS, deg	45	-
Step 3	Average cohesion of the ISFS, MN/m^2	0.307	5.3
Step 4	Length of the ISFS, m	16.69	-
Step 5	Inner side of the active block construction	-	-
Outer shear failure surface (OSFS)			
Step 6	Average friction angle, deg	28	5.2
Step 7	Inclination angle of the OSFS, deg	45	-
Step 8	Average cohesion of the OSFS, MN/m^2	0.344	5.3
Step 9	Length of the ISFS, m	17.28	-
Step 10	Outer side of the active block construction	-	-
General parameters			
Step 11	Frictional zone load, MN/m^2	11.527	5.4
Step 12	Frictional zone length, m	29.0	-
Step 13	Frictional zone inclination angle, deg	16	-
Step 14	Cohesive zone load, MN/m^2	2.084	5.4
Step 15	Cohesive zone length, m	12.0	-
Step 16	Cohesive zone inclination angle, deg	12	-
Step 17	Active block load, MN	12.486	5.4
Step 18	Active block wedge angle, deg	10	-
Step 19	Passive block reaction forces to the inner failure surface, MN	-0.567	5.28

Step 20	Pore water pressure calculations		5.24-5.27
Step 21	Safety factor of the inner shear failure surface (condition of existence)	0.914	5.32
Step 22	Reaction force along the outer shear failure surface, MN	5.619	5.33
Step 23	Outer shear failure surface safety factor	0.709	5.35
Step 24	Basal shear surface safety factor	0.750	5.36
Step 25	Slope stability safety factor	0.777	5.37

Table A4.2 *Example 2a*: Safety factor calculations along the upper contact surface before initial failure

Step No	**Parameter**	**Value**	**Equation No**
Inner shear failure surface (ISFS)			
Step 1	Average friction angle, deg	28	5.2
Step 2	Inclination angle of the ISFS, deg	45	-
Step 3	Average cohesion of the ISFS, MN/m^2	0.238	5.3
Step 4	Length of the ISFS, m	9.24	-
Step 5	Inner side of the active block construction	-	-
Outer shear failure surface (OSFS)			
Step 6	Average friction angle, deg	28	5.2
Step 7	Inclination angle of the OSFS, deg	45	-
Step 8	Average cohesion of the OSFS, MN/m^2	0.228	5.3
Step 9	Length of the ISFS, m	11.55	-
Step 10	Outer side of the active block construction	-	-
General parameters			
Step 11	Frictional zone load, MN/m^2	4.524	5.4
Step 12	Frictional zone length, m	27	-

Step 13	Frictional zone inclination angle, deg	12	-
Step 14	Cohesive zone load, MN/m^2	0.964	5.4
Step 15	Cohesive zone length, m	10.0	-
Step 16	Cohesive zone inclination angle, deg	10	-
Step 17	Active block load, MN	9.194	5.4
Step 18	Active block wedge angle, deg	8	-
Step 19	Passive block reaction forces to the inner failure surface, MN	0.674	5.28
Step 20	Pore water pressure calculations	Above the phreatic level	
Step 21	Safety factor of the inner shear failure surface (condition of existence)	1.010	5.32
Step 22	Reaction force along the outer shear failure surface, MN	1.923	5.33
Step 23	Outer shear failure surface safety factor	0.955	5.35
Step 24	Basal shear surface safety factor	1.108	5.36
Step 25	Slope stability safety factor	1.062	5.37

Table A4.3 *Example 2b*: Safety factor calculations along the bottom contact surface before initial failure

Step No	**Parameter**	**Value**	**Equation No**
Inner shear failure surface (ISFS)			
Step 1	Average friction angle, deg	26	5.2
Step 2	Inclination angle of the ISFS, deg	45	-
Step 3	Average cohesion of the ISFS, MN/m^2	0.323	5.3
Step 4	Length of the ISFS, m	16.17	-
Step 5	Inner side of the active block construction	-	-

Outer shear failure surface (OSFS)			
Step 6	Average friction angle, deg	26	5.2
Step 7	Inclination angle of the OSFS, deg	45	-
Step 8	Average cohesion of the OSFS, MN/m^2	0.326	5.3
Step 9	Length of the ISFS, m	19.25	-
Step 10	Outer side of the active block construction	-	-
General parameters			
Step 11	Frictional zone load, MN/m^2	10.704	5.4
Step 12	Frictional zone length, m	29	-
Step 13	Frictional zone inclination angle, deg	14	-
Step 14	Cohesive zone load, MN/m^2	1.614	5.4
Step 15	Cohesive zone length, m	10.0	-
Step 16	Cohesive zone inclination angle, deg	12	-
Step 17	Active block load, MN	11.679	5.4
Step 18	Active block wedge angle, deg	10	-
Step 19	Passive block reaction forces to the inner failure surface, MN	-0.243	5.28
Step 20	Pore water pressure calculations		5.24-5.27
Step 21	Safety factor of the inner shear failure surface (condition of existence)	1.036	5.32
Step 22	Reaction force along the outer shear failure surface, MN	5.064	5.33
Step 23	Outer shear failure surface safety factor	0.927	5.35
Step 24	Basal shear surface safety factor	0.917	5.36
Step 25	Slope stability safety factor	0.945	5.37

Table A4.4 *Example 2c*: Safety factor calculations along the upper contact surface before major collapse

Step No	**Parameter**	**Value**	**Equation No**
Inner shear failure surface (ISFS)			
Step 1	Average friction angle, deg	28	5.2
Step 2	Inclination angle of the ISFS, deg	45	-
Step 3	Average cohesion of the ISFS, MN/m^2	0.249	5.3
Step 4	Length of the ISFS, m	8.47	-
Step 5	Inner side of the active block construction	-	-
Outer shear failure surface (OSFS)			
Step 6	Average friction angle, deg	28	5.2
Step 7	Inclination angle of the OSFS, deg	45	-
Step 8	Average cohesion of the OSFS, MN/m^2	0.269	5.3
Step 9	Length of the OSFS, m	10.40	-
Step 10	Outer side of the active block construction	-	-
General parameters			
Step 11	Frictional zone load, MN/m^2	5.821	5.4
Step 12	Frictional zone length, m	32	-
Step 13	Frictional zone inclination angle, deg	11	-
Step 14	Cohesive zone load, MN/m^2	0.882	5.4
Step 15	Cohesive zone length, m	7	-
Step 16	Cohesive zone inclination angle, deg	8	-
Step 17	Active block load, MN	5.093	5.4
Step 18	Active block wedge angle, deg	7	-
Step 19	Passive block reaction forces to the inner failure surface, MN	0.392	5.28
Step 20	Pore water pressure calculations	Above the phreatic level	

Step 21	Safety factor of the inner shear failure surface (condition of existence)	1.149	5.32
Step 22	Reaction force along the outer shear failure surface, MN	1.674	5.33
Step 23	Outer shear failure surface safety factor	0.935	5.35
Step 24	Basal shear surface safety factor	1.318	5.36
Step 25	Slope stability safety factor	1.224	5.37

Table A4.5 *Example 2d*: Safety factor calculations along the bottom contact surface before major collapse

Step No	**Parameter**	**Value**	**Equation No**
Inner shear failure surface (ISFS)			
Step 1	Average friction angle, deg	26	5.2
Step 2	Inclination angle of the ISFS, deg	45	-
Step 3	Average cohesion of the ISFS, MN/m^2	0.315	5.3
Step 4	Length of the ISFS, m	1615	-
Step 5	Inner side of the active block construction	-	-
Outer shear failure surface (OSFS)			
Step 6	Average friction angle, deg	26	5.2
Step 7	Inclination angle of the OSFS, deg	45	-
Step 8	Average cohesion of the OSFS, MN/m^2	0.322	5.3
Step 9	Length of the ISFS, m	19.23	-
Step 10	Outer side of the active block construction	-	-
General parameters			
Step 11	Frictional zone load, MN/m^2	13.589	5.4
Step 12	Frictional zone length, m	34	-
Step 13	Frictional zone inclination angle, deg	14	-

Step 14	Cohesive zone load, MN/m^2	1.674	5.4
Step 15	Cohesive zone length, m	11	-
Step 16	Cohesive zone inclination angle, deg	11	-
Step 17	Active block load, MN	10.374	5.4
Step 18	Active block wedge angle, deg	9	-
Step 19	Passive block reaction forces to the inner failure surface, MN	-0.420	5.28
Step 20	Pore water pressure calculations		5.24-5.27
Step 21	Safety factor of the inner shear failure surface (condition of existence)	1.161	5.32
Step 22	Reaction force along the outer shear failure surface, MN	4.619	5.33
Step 23	Outer shear failure surface safety factor	0.884	5.35
Step 24	Basal shear surface safety factor	0.883	5.36
Step 25	Slope stability safety factor	0.939	5.37

Table A4.6 *Example T-1*: Safety factor calculations along the upper contact plane of the test profile (5^0 flatter slope angle compared to the slope angle of the profile before major collapse)

Step No	**Parameter**	**Value**	**Equation No**
Inner shear failure surface (ISFS)			
Step 1	Average friction angle, deg	28	5.2
Step 2	Inclination angle of the ISFS, deg	45	-
Step 3	Average cohesion of the ISFS, MN/m^2	0.260	5.3
Step 4	Length of the ISFS, m	10.40	-
Step 5	Inner side of the active block construction	-	-

Outer shear failure surface (OSFS)			
Step 6	Average friction angle, deg	28	5.2
Step 7	Inclination angle of the OSFS, deg	45	-
Step 8	Average cohesion of the OSFS, MN/m^2	0.250	5.3
Step 9	Length of the ISFS, m	13.48	-
Step 10	Outer side of the active block construction	-	-
General parameters			
Step 11	Frictional zone load, MN/m^2	6.195	5.4
Step 12	Frictional zone length, m	41	-
Step 13	Frictional zone inclination angle, deg	11	-
Step 14	Cohesive zone load, MN/m^2	4.886	5.4
Step 15	Cohesive zone length, m	19	-
Step 16	Cohesive zone inclination angle, deg	6	-
Step 17	Active block load, MN	6.425	5.4
Step 18	Active block wedge angle, deg	3	-
Step 19	Passive block reaction forces to the inner failure surface, MN	1.742	5.28
Step 20	Pore water pressure calculations	Above the phreatic level	
Step 21	Safety factor of the inner shear failure surface (condition of existence)	1.710	5.32
Step 22	Reaction force along the outer shear failure surface, MN	0.852	5.33
Step 23	Outer shear failure surface safety factor	1.222	5.35
Step 24	Basal shear surface safety factor	2.029	5.36
Step 25	Slope stability safety factor	1.860	5.37

Table A4.7 *Example T-2*: Safety factor calculations along the bottom contact plane of the test profile (5^0 flatter slope angle compared to the slope angle of the profile before major collapse)

Step No	**Parameter**	**Value**	**Equation No**
Inner shear failure surface (ISFS)			
Step 1	Average friction angle, deg	26	5.2
Step 2	Inclination angle of the ISFS, deg	45	-
Step 3	Average cohesion of the ISFS, MN/m^2	0.321	5.3
Step 4	Length of the ISFS, m	17.31	-
Step 5	Inner side of the active block construction	-	-
Outer shear failure surface (OSFS)			
Step 6	Average friction angle, deg	26	5.2
Step 7	Inclination angle of the OSFS, deg	45	-
Step 8	Average cohesion of the OSFS, MN/m^2	0.302	5.3
Step 9	Length of the ISFS, m	18.86	-
Step 10	Outer side of the active block construction	-	-
General parameters			
Step 11	Frictional zone load, MN/m^2	14.547	5.4
Step 12	Frictional zone length, m	43	-
Step 13	Frictional zone inclination angle, deg	12	-
Step 14	Cohesive zone load, MN/m^2	7.374	5.4
Step 15	Cohesive zone length, m	22.0	-
Step 16	Cohesive zone inclination angle, deg	6	-
Step 17	Active block load, MN	10.521	5.4
Step 18	Active block wedge angle, deg	4	-
Step 19	Passive block reaction forces to the inner failure surface, MN	1.463	5.28

Step 20	Pore water pressure calculations		5.24-5.27
Step 21	Safety factor of the inner shear failure surface (condition of existence)	1.658	5.32
Step 22	Reaction force along the outer shear failure surface, MN	2.688	5.33
Step 23	Outer shear failure surface safety factor	1.527	5.35
Step 24	Basal shear surface safety factor	1.378	5.36
Step 25	Slope stability safety factor	1.454	5.37

APPENDIX 5. SAFETY FACTORS FOR OPENCAST MINING

UNITED STATES

1. FEDERAL REGISTER – 1977

		Minimum FOS
I.	End of construction	1.3
II.	Partial pool with steady seepage saturation	1.5
III.	Steady seepage from spillway or decent crest	1.5
IV.	Earthquake (cases II and III with seismic loading)	1.0

2. D'APPOLONIA CONSULTING ENGINEERS, Inc. – 1975

Suggested minimum FOS with hazard potential

	High	Moderate	Low
Designs based on shear strength parameters measured in laboratory	1.5	1.4	1.3
Designs that consider maximum seismic acceleration expected at the site	1.2	1.1	1.0

CANADA

MINES BRANCH – 1972

Suggested minimum FOS with hazard potential

		High	Low
1.	Design is based on peak shear strength parameters	1.5	1.3
2.	Design is based on residual shear strength parameters	1.3	1.2
3.	For horizontal sliding on the base of dyke in seismic areas assuming shear strength of fine refuse in impoundment reduced to zero	1.3	1.3

REFERENCES

1. Al-Ostaz A. and Jasiuk I. (1997), “Crack initiation and propagation in materials with randomly distributed holes”, *Eng. Fracture Mechanics,* Vol. 58, pp. 395-420.
2. Anderson M.G. and Richards K.S. (1992), “Slope stability – geotechnical engineering and geomorphology”, *Reprinted, John Wiley & Sons*, pp.22-23.
3. Andersson H. (1977), “Analysis of a model for void growth and coalescence ahead of a moving crack tip”, *J Mech Phys Solids*, pp.25.
4. Andrade C., Bard E.O., Garrido H. and Campana J. (2000), "Slope Stability in Surface Mining", Ch. 48, pp. 427-434. W. A. Hustrulid, M. K. McCarter and D.J.A. Van Zyl, Eds. Littleton, Colorado: SME
5. Ashby M.F. and Hallam S.D. (1986), “The failure of brittle solids containing small cracks under compressive stress states”, *Acta Metall*, 34(3), pp.497–510.
6. Atkinson B.K. (1987), “Fracture mechanics of rock”, *London: Academic Press*.
7. Atkinson B.K. and Meredith P.G. (1987), "The theory of subcritical crack growth with applications to minerals and rocks", *Atkinson, B. K., ed., Fracture Mechanics of Rock, Academic Press,* San Diego, USA.
8. Baer, G. (1991), “Mechanisms of dike propagation in layered rocks and in massive porous sedimentary rocks”, *Journal of Geophysical Research* 96, 11,911-11,929.
9. Bai T. and Pollard D.D. (2000-a), “Closely spaced fractures in the layered rocks: initiation

mechanism and propagation kinematics", *Journal of Structural Geology*, 22, pp. 1,409-1,425.

10. Bai T. and Pollard D.D. (2000-b), "Fracture spacing in layered rocks: a new explanation based on the stress transition", *Journal of Structural Geology*, 22, pp. 43-57.
11. Barenblatt G.I. (1962), "The mathematical theory of equilibrium cracks in brittle fracture", *Advances in Applied Mechanics*, 7.
12. Barker L.M. (1979), "Theory for determining K_{IC} from small non-LEFM specimens, supported by experiments on aluminum", *Int J Fracture*, 15, pp.515-36.
13. Barla G. and Chiriotti E. (1995), "Insights into the Behaviour of the Large Deep Seated Gravitational Slope Deformation of Rosone, in the Piemont Region (Italy)", Felsbau, 13(6), pp. 425-432.
14. Bartlett W.M., Friedman M. and Logan J.M. (1981), "Experimental folding and faulting in rocks under confining pressure", Part IX, *Wrench faults in limestone layers*, Technophysics 79, pp. 255-277.
15. Barton N.R. (1971), "A model study of the behavior of excavated slopes", *Ph.D. Thesis*, University of London, Imperial College of Science and Technology.
16. Bassett R.H. (1970), Discussion. Proc. I.C.E. Conf. "Behaviour of piles", London, pp. 208-210
17. Batzle M.L., Simmons G. and Siegfried R.W. (1980), "Microcrack closure in rocks under stress: direct observation", *J Geophys Res*, 85, pp.7072–90.
18. Bazant Z.P. and Xiang Y. (1997), "Size effect in compression fracture: splitting crack band

propagation", *J Engineering Mechanics*, 123(2), pp.162-73.

19. Becker A. and Gross M. (1988), "About the Dugdale crack under mixed mode loading", *Int J Fracture*, 37.
20. Becker A. and Gross M. (1996). "Mechanism for joint saturation in mechanically layered rocks: an example from southern Israel". Tectonophysics 257, 223-237.
21. Bhagat RB (1985), "Mode I fracture toughness of coal", Int J Min Eng, 3, pp. 229–36.
22. Bieniawski Z.T. (1967), "Mechanism of brittle fracture of rock", Part II- experimental study, *Int. J. Rock Mech. Min. Sci. and Geotech.* Abstr., 4, pp. 407-423.
23. Bishop A.W. (1955), "The use of the clip circle in the stability analysis of earth slopes", *Geotechnique, 5,* pp. 7-17
24. Bishop A.W., Webb D.L. and Lewin P.I. (1965), "Undisturbed samples of London clay from the Ashford common shaft; strength-effective stress relationships", Geotechnique 15, 1, pp. 1-31.
25. Boyd G.L. (1983), "Geomechanics research applied to open strip coal mining in Australia", Surface mining and quarrying, Second international Surface mining and quarrying symposium, Bristol, UK, pp. 193-204.
26. Brace W.F. (1978), "Volume changes during fracture and frictional sliding: a review". *PAGEOGH 116*, pp.603–614.
27. Brady B.H.G. and Brown E.T. (1993), "Rock Mechanics for Underground Mining", *2nd edn. Chapman & Hall, London*, 571 pp.59– 108.

28. Broek D. (1996), “Elementary engineering fracture mechanics”, *4th ed. Dordrecht: Kluwer Academic Publishers.*
29. Bromhead E.N. (1992), “The stability of slopes”, Surrey University Press, Chapman and Hall, New York, pp. 109-165
30. Broms, B.B. (1971), "Lateral earth pressure due to compaction of cohesionless soils", Proc. 4th COSMFF, Budapest, 1, pp. 373-384.
31. Brooker E.W. and Ireland H.O. (1965), "Earth pressure at rest related to the stress history", Can. Geot. J., 2, 1, p. 1-15.
32. Bui H.D. and Ehrlacher A. (1981), “Propagation of damage in elastic and plastic solids”, *In: Francois D, Bathias C, Bilby BA, editors. Proceedings of the 5th International Conference of Fracture, Cannes, France*, pp.533-551.
33. Bui H.D., Ehrlacher A. and Renard C. (1984), “The steady state propagation of a damaged zone of an elastic brittle solid”, In: Valluri S.V., Taplin D.M.R and Rao P.R. (Eds). *Proceedings of the 6th International Conference of Fracture, New Delhi, India*, pp.1061-1067.
34. Cairncross B. (1989), “Paleodepositional environments and tectono-sedimentary controls of the postglacial Permian coals, Karoo Basin, South Africa”, *International Journal of Coal Geology*, v. 12, pp. 365-380.
35. CANMET, Mining research Laboratories (1997), *“Pit Slope Manual”*, CANMET.
36. Carpinteri A., Tomasso A.D. and Fanelli M. (1986), “Influence of material parameters and geometry on cohesive crack propagation”, In “Fracture toughness and fracture energy of concrete”,

Wittmann F.H. (Ed*), Elsevier Science Publishers, Amsterdam*, pp.117-135.

37. Carranza-Torres C., Fairhurst C. and Lorig L. (1997), "Insights on the Stability of Large Excavations from Analytical and Numerical Models," *Felsbau*, 15(1), pp. 45-63.
38. Cherepanov G.P. (Ed) (1998), "Fracture, a topical encyclopedia of current knowledge*". Malabar, FL. Krieger Publishing Company*.
39. Collieries Research Laboratory (1972), "Design tables for bord and pillar workings in coal mines", *Chamber of Mines of South Africa.*
40. Cox H.L. (1952), "The elasticity and strength of paper and other fibrous materials", British Journal of Applied Physics, 3, pp. 72-79.
41. Dey T.N. and Wang C.Y. (1981), "Some mechanisms of microcrack growth and interaction in compressive rock failure*". Int J Rock Mech Min Sci Geomech Abstr,* 18, pp.199–209.
42. DIGS, (1996), CSIR – Miningtek, Boundary element code.
43. Dugdale D.S. (1960), "Yielding of steel sheets containing slits", *J Mech Phys Solids*, 8.
44. Dyskin A.V. and Germanovich L.N. (1993), "Model of rock burst caused by cracks growing near free surface", In: Young P (ed.), "Rockbursts and seismicity in mines 93", Rotterdam, Balkema, pp. 169-175.
45. El Bied A., Sulema J. and Martineaub F. (2002), "Microstructure of shear zones in Fontainebleau sandstone", *International Journal of Rock Mechanics and Mining Sciences*, 39, pp. 917–932.
46. Eberhardt E., Stead D. and Stimpson B. (1999), "Quantifying progressive pre-peak brittle fracture

damage in rock during uniaxial compression", *Int. J. Rock Mech. Min. Sci. Geomech. Abstr., 36*, pp. 361–380.

47. Ewy R.T. and Cook N.G.W. (1990), "Deformation and fracture around cylindrical openings in rock", *Part II, Int J Rock Mech Min Sci and Geomech Abstr*, 27, pp.409-427.
48. Fairhurst C. and Cook N.G.W. (1966), "The phenomenon of rock splitting parallel to the direction of maximum compression in the neighborhood of a surface", Proceedings of the 1st Congress International Society for Rock Mechanics, Lisbon, p. 687-692.
49. Feda J. (1992), "Creep of soils and related phenomena", *Elsevier*.
50. Feda, J (1978), "Stress in subsoil and methods of final settlement calculation", Development in Geotechnical Engineering 18, Elsevier, p. 20-33.
51. Fellenius W. (1936), "Calculation of the stability of earth dams", *Trans. 2nd Congr. On Large Dams, Washington, 4,* pp. 445-459
52. Feng X.Q. and Yu S.W. (1995), "Micromechanical modeling of tensile response of elastic-brittle materials", *Int J Solids Struct*, 32.
53. FLAC2D, Itasca Consulting Group (1999), "Fast Lagrangian Analysis of Continua".
54. Fredrich J.T., Evans B. and Wong T.F. (1990), "Effects of grain size on brittle and semi brittle strength: implications for micromechanical modeling of failure in compression", *J. Geophys. Res.*, 95, pp.10907-10920.
55. Fueten F. and Goodchild J.S., (2001), "Quartz c-axis orientation using the rotating polarizer microscope", J. of Str. Geol., 23, pp. 895-902.

56. Gammond J.F. (1983), “Displacement features associated with fault zones: a comparison between observed examples and experimental models”, *Journal of Structural Geology* 5, pp. 33-45.
57. Germanovich L.N. (1984), “Stress state in the vicinity of a drill-hole cut by flame”, *Soviet mining sciences, vol. 20. New York: Consultants Bureau and Plenum Publishing Corp*, pp.245-53.
58. Germanovich L.N. (1997), “Thermal spalling of rock”. In*: Advances in fracture research, vol. 6. Amsterdam, Oxford: Pergamon*, pp.2771-82.
59. Germanovich L.N. and Dyskin A.V. (2000), "Fracture mechanisms and instability of openings in compression", *Int. J. Rock Mech. Min. Sci.*, 37, pp.263-284.
60. Germanovich L.N., Salganik R.L., Dyskin A.V. and Lee K.K. (1994), “Mechanisms of brittle fracture of rock with multiple pre-existing cracks in compression”, Pure and Applied Geophysics (PAGEOPH), 143 (13), pp. 117-149.
61. Griffith A.A. (1921), “The phenomena of rupture and flow in solids”, *Phil Trans Royal Soc London, Ser*, A221, pp.163–98.
62. Griffith A.A. (1924), “The theory of rupture”, *Proceeding of First International Congress Applied Mechanics*, 1st Delft, pp.55–63.
63. Griffiths D.V. and Lane P.A. (1999), “Slope stability analysis by finite elements”, Geotechnique 49, No: 3, pp. 387-403.
64. Gross M., Fischer M., Engelder T. and Greenfield R. (1995). “Factors controlling joint spacing in interbedded sedimentary rocks; integrating numerical models with field observations from the Monterey Formation, USA”. In: Ameen, M.S. (Ed.).

Fractography. Geological Society Special Publication, Geological Society, London, pp. 215-233.

65. Haimson B.C. and Herrick C.G. (1986), “Borehole breakouts - a new tool for estimating in-situ stress”, *Proceedings of the International Symposium on Rock Stress Measurements”, Stockholm, 1-3 September*, pp.271-80.
66. Haimson B.C. and Song I. (1993), “Laboratory study of borehole breakouts in Cordova Cream: a case of shear failure mechanism*”, Int J Rock Mech Min Sci and Geomech Abstr.*, 30, pp.1047-56.
67. Haimson B.C. and Song I (1998), “Borehole breakouts in Berea sandstone: two porocity-dependent distinct shapes and mechanisms of formation”, SPE/ISRM Eurock '98, Trondheim, Norway, vol. 1, p. 229-238.
68. Hallbauer D.K., Wagner H. and Cook N.G.W. (1973), “Some observations concerning the microscopic and mechanical behavior of quartzite specimens in stiff triaxial compression tests*”, Int J Rock Mech Min Sci Geomech Abstr,* 10, pp.713–26.
69. Hao T.H., Zhang X.T. and Hwang K.C. (1991), “The anti-plane shear field in an infinite slab of an elasto-damaged material with a semi-infinite crack”, *Acta Mechanica Sinica*, 7.
70. Hardy, M.P. (1973), "Fracture mechanics applied to rock", PhD thesis, University of Minessota.
71. Hatzor Y.H. and Palchic V. (1997), “The influence of grain size and porosity on crack initiation stress and critical flaw length in dolomites”, *Int. J. Rock Mech. Min. Sci.*, 34(5), pp.805-816.
72. Helgeson D.E. and Aydin A. (1991), “Characteristics of joint propagation across layer

interfaces in sedimentary rocks". *Journal of Structural Geology* 13, 897-991.

73. Helsing J. (1999), "Stress intensity factors for a crack in front of an inclusion". *Eng Fract Mech*, 64: pp.245–53.
74. Hilleborg A. (1985), "The theoretical basis of a method to determine the fracture energy G_F of concrete", *Materials and structures*, 18, No 106, pp.291-296.
75. Hobbs D.W. (1967), "The formation of tension joints in sedimentary rock: an explanation", *Geological Magazine,* 104, pp. 550-556.
76. Hoek E. (1986), "Slope stability analysis", *Lecture at Santiago Technical University*, Chapter 7 - A slope stability problems in Hong Kong, pp.92-104.
77. Hoek E. and Bieniawski Z.T. (1965), "Brittle fracture propagation in rock under compression." *Int J Fract Mech*, 1, pp.137–55.
78. Hoek E. and Bray J.W. (1981), "Rock slope engineering", IMM, London.
79. Hoek E. and Bray J.W. (1991), "Rock slope engineering", *Elsevier, Preprinted*, pp.161.
80. Horii H. and Nemat-Nasser S. (1985), "Compression-induced microcrack growth in brittle solids: axial splitting and shear failure", *J Geophys Res* 90, pp.3105-25.
81. Horii H. and Nemat-Nasser S. (1986), "Brittle failure in compression: splitting, faulting and brittle-ductile transition". *Phil Trans Roy Soc London*, A319, pp.163–98.
82. Horii H., Hasegawa A. and Nishino F. (1987), "Process zone model and influencing factors in fracture of concrete", *SEM/RILEM, Int. Conf. On*

fracture of concrete and rock, Houston, Texas, Shah and Swarts (Eds), pp.299-307.

83. Hoyaux, B. and Ladanyi, B. (1972), "Basic and applied rock mech.", Port City Press, Baltimore, pp. 621-631.
84. Huang Q. and Angelier J. (1989), "Fracture spacing and its relation to bed thickness", *Geological Magazine*, 126, pp. 355-362.
85. Hugman R.H.H. and Friedman M. (1979), "Effects of texture and composition on mechanical behavior of experimentally deformed carbonate rocks", *Am. Assoc. Petr. Geol. Bull.*, 63, pp.1478-1489.
86. Ingraffea R.A. and Gerstle W.H. (1984), "Non-linear fracture models for discrete fracture propagation", *Application of fracture mechanics to cementitious composites, Shah S.P. (Ed), Martinus Nijhoff, The Hague*, pp.247-285.
87. Itasca Consulting Group, 1999: "FISH in FLAC", Complete guide FISH.
88. Jaeger J.C. and Cook N.G.W. (1979), "Fundamentals of Rock Mechanics", 3rd Ed. New York, Chapman and Hall.
89. Janbu N. (1954), "Application of composite slip surfaces for stability analysis", *Proc. Europ. Conf. Stability of Earth Slopes,* V.3.
90. Janbu N. (1957), "Stability analysis of slopes with dimensionless parameters", *Harvard University Soil Mech. Series,* No 46
91. Janson J. (1977), "Dugdale crack in a material with continuous damage formation", *Eng. Fracture Mech*, 9.
92. Ji S. and Saruwatari K. (1998). "A revised model for the relationship between joint spacing and

layer thickness", *Journal of Structural Geology,* 20, 1495-1508.

93. Jiang J. and Xie Q. (1988), "Finite element analysis of the stresses in slopes", *Numerical methods in Geomechanics,* Innsbruck, Swoboda (ed.), Balkema, Rotterdam, pp. 1375-1383.
94. Kachanov L.M. (1988), "Delamination buckling of composite materials", *Dordrecht, Boston, London, Kluwer*.
95. Kanninen M.F. and Popelar C.P. (1985), "Advanced fracture mechanics", *London: Oxford University Press*.
96. Karparov K.N. (1998), "Fracture toughness estimation on some rocks encountered in South African mining environment", *Unpublished MSc Thesis, University of the Witwatersrand, Johannesburg, RSA*.
97. Kemeny J.M. and Cook N.G.W. (1987), "Crack models for the failure of rock under compression", *Proc. of the Second International Conference on Constitutive Laws for Engineering Materials*, vol.2, pp.879–87.
98. Kitahara,Y. Tokue,T. Motojima,M. (1986), "The observed results of displacements during the excavation of slope and the numerical analysis of its stability" pp. 691-697.
99. Kovari K. and Fritz P. (1978), "Special contribution: Slope stability with plane, wedge and polygonal sliding surfaces", Symp. on rock mechanics related to dam foundations, Rio de Janeiro.
100. Krajcinovic D. (1997), "Damage Mechanics", *Elsevier, Amsterdam*.

101. Kranz R.L. (1979), “Crack–crack and crack–pore interactions in stressed granite”, *Int J Rock Mech Min Sci Geomech Abstr*, 16, pp.37–47.
102. Kulatilake P.H.S.W., Wathugala D.N., and Stephansson O. (1993), “Joint network modeling with a validation exercise in Strip mine”, Sweden, *Int. J. Rock Mech. Min. Sci. and Geomech. Abstr.*, 30(5), 503-526.
103. Kulhawy F.H., Duncan J.M. and Bolton Seed H. (1973), Finite element analyses of stresses and movements in embankments during construction”, *Report No: TE-69-4,* U.S. Army Corp. Engineers, Waterways Experiment Station.
104. Labuz J.F., Shah S.P. and Dowding C.H. (1987), “The fracture process zone in granite: evidence and effect”, *Int. J. Rock Mech. and Min. Sci. and Geotech. Abstr.*, 24, No: 4, pp.235-246.
105. Ladd, C.C. (1964), "Stress-strain modulus of clay in undrained shear", J. SM Div. ASCE 90, 5, p. 103-132
106. Lambe, T.W. and Whitman, R.V. (1979), "Soil mechanics, SI version", John Wiley & Sons, p. 99-100.
107. Leung C.K.Y. and Li V.C. (1987), “Determination on fracture toughness parameters of quasi-brittle materials with laboratory-size specimens”, *SEM/RILEM, Int. Conf. On fracture of concrete and rock, Houston, Texas, Shah and Swarts (Eds)* pp.695-709.
108. Lipetzky P. and Knesl Z. (1995), “Crack–particle interaction in two-phase composites”, *Part II Crack defection. Int J Fract*, pp.81–92.
109. Lipetzky P. and Schmauder S. (1994), “Crack–particle interaction in two-phase composites”,

Part I: Particle shape effects. Int J Fract, pp.345–58.

110. Lockner D.A. (1993). "The role of acoustic emissions in the study of rock fracture", *Int. J. Rock Mech. Min. Sci. and Geomech. Abs.*, 7, pp.883-889.
111. Lowe J. and Karafiath L. (1960), "Stability of earth dams upon draw down", *Proc. 1st Pan-Am. Conf. Soil Mech. Found. Eng., Mexico, 2,* pp. 537-560.
112. Malgot J., Baliak F. and Mahr T., (1986), "Prediction of the influence of underground coal mining on slope stability in the Vtacnik mountains", Bulletin of the international association of engineering geology, 33, pp. 57-65
113. Mandal N., Chakraborty C. and Samanta S.K. (2001), "Flattening in shear zones under constant volume: a theoretical evaluation", *J. of Structural Geology*, 23, pp. 1771-1780.
114. Markgraaff J. (1986), "Elastic behavior of quartz during stress induced Dauphine twinning", *Phys. Chem. Minerals*, Vol. 13, pp.102-112.
115. Martin C.D. and Chandler N.A. (1994), "The progressive fracture of Lae du Bonnet granite", *Int. J. Rock Mech. Min. Sci. and Geotech. Abstr.*, 31, pp.643-659.
116. Mattushek M. (2005), Personal Communication, Divisional Geologist, New Vaal Colliery.
117. McKinnon S.D. and de la Barra I.G. (1998), "Fracture initiation, growth and effect on stress field: a numerical investigation", *Journal of Structural Geology*, Vol. 20, No. 12, pp. 1673-1689.

118. Mitchell J.K. (1976), “Fundamentals of soil behavior”, *J. Wiley and Sons*.
119. Morgenstern N.R. and Price V.A. (1967), “The analysis of the stability of general slip surfaces”, *Geotechnique,* 15, pp. 79-93.
120. Mou Y. and Han R.P.S. (1994), “Damage zones based on Dugdale model for materials”. *Int J Fracture*, 68.
121. Muller W.H. and Schmauder S. (1993), “Stress-intensity factor of r-cracks in fiber-reinforced composites under thermal and mechanical loading”. *Int J Fract*, 59, pp.307–43.
122. Myer L.R., Kemeny J.M., Zheng Z., Suarez R., Ewy R.T. and Cook N.G.W. (1992), “Extensile cracking in porous rock under differential compressive stress”, Applied Mechanics Review; 45(8), pp. 263-280.
123. Narr W. and Suppe J. (1991), “Joint spacing in sedimentary rocks”, *Journal of Structural Geology,* 13, 1037-1048.
124. Nemat-Nasser S. and Horii H. (1982), “Compression-induced nonlinear crack extension with application to splitting, exfoliation, and rockburst”. *J Geophys Res*, 87(B8), pp.6805–21.
125. Nemat-Nasser S. and Hori M. (1993), “Micromechanics: overall properties of heterogeneous materials”, *Amsterdam, North-Holland*.
126. Okland D. and Cook J.M. (1998), “Bedding-related instability in high-angle wells”, *In: SPE/ISRM Eurock '98*, pp.413-22.
127. Olson J.E. (1993), “Effects of subcritical crack growth and mechanical crack interaction”, *J. of Geoph. Res.*, 98(B7), pp.12251-12265.

128. Olson J.E. (1997), “Natural fracture pattern characterization using mechanical based model constrained by geologic data – moving closer to a predictive tool”. *Int. J. Rock Mech. & Min. Sci.*, 34(3/4), 391, Paper No. 237.
129. Olson J.E. and Pollard D.D. (1989), “Inferring paleostresses from natural fracture patterns: A new method”, *Geology*, 17, 345-348.
130. Olsson W.A. (1974), “Grain size dependence of yield stress in marble”, *J. Geophys. Res.*, 79, pp.4859-4862.
131. Olsson W.A. and Peng S.S. (1976), “Microcrack nucleation in marble”, *Int J Rock Mech Min Sci Geomech Abstr*, 13, pp.53–9.
132. Ortlepp W.D. and Stacey T.R. (1994), “Rockburst mechanisms in tunnels and shafts”, *In: Tunnelling and Underground Space Technology,* 9(1), pp.59-65.
133. Ortlepp W.D. (1997): *Rock Fracture and Rockbursts: an illustrative study.* Monograph Series M9, South African Institute of Mining and Metallurgy, Johannesburg.
134. Ouchterlony F.D. (coordinator) (1988), “Suggested methods for determining the fracture toughness of rock”, ISRM, *Int J Rock Mech Sci & Geomech Abstr*, 25, pp.71-96.
135. Palchik V. and Hatzor Y.H. (2002), “Crack damage stress as a composite function of porosity and elastic matrix stiffness in dolomites and limestones”, *Eng. Geol.*, 63, pp.233-245.
136. Papaioannou S.G. and Hilton P.D. (1974), “A finite element method for calculation stress intensity factors and its application to composites”, *Eng Fract. Mech.*, 6, pp.807–23.

137. Papamichos E. and Vardoulakis I.G. (1989), “The coupling effect of surface instabilities and surface parallel Griffith cracks in rock”, In: Maury V. and Fourmaintraux D. (ed.), *“Rock at great depth”, Rotterdam: Balkema*, pp. 481-487.
138. Parker A.P. (1999), “Stability of arrays of multiple edge cracks”, *Engineering Fracture mechanics*, 62, pp. 577-591.
139. Paterson M.S. (1978), “Experimental Rock Deformation — The Brittle Field”, *Springer-Verlag, New York*, 254 pp.
140. Peng S. and Johnson A.M. (1972), “Crack growth and faulting in cylindrical specimens of Chelmsford granite”, *Int J Rock Mech Min Sci Geomech Abstr*, 9, pp.37–86.
141. Petch N.J. (1953), “The cleavage strength of polycrystals”, *J. Iron Steel Inst.*, pp.25-28.
142. Poisel R. and Eppensteiner W. (1988),"A contribution to the systematics of rock mass movements", *LANDSLIDES* - Proc. Of the 5th Int. Symp. On landslides, Lausanne, 10-15 July, pp. 1353-1359.
143. Pollard D.D. and Aydin A. (1988), “Progress in understanding jointing over the past century”, *Geological Society of America*, Bulletin, 100, pp. 1181-1204.
144. Pollard D.D. and Segall P. (1987), “Theoretical displacements and stresses near fractures in rocks: with applications to faults, joints, veins, dikes and solution surfaces”. In: Atkinson, B.K. ed., *Fracture Mechanics of Rock*. Academic Press, London, 277-349.

145. Price N.J. (1966), “Fault and Joint Development in Brittle and Semi-Brittle Rocks”, *Pergamon Press*, *Oxford.*
146. Renshaw C.E. (1994), “Are large differential stresses required for straight fracture propagation paths?”, *Journal of Structural Geology*, 16 (6), 817-822.
147. Riedel W. (1929), “Zur mechanik geologisher brucherscheinungen”, Zentralblatt fur Mineralogie, Geologie und Paleontologie B, p. 354-368 (Abhandlung).
148. Rives T., Razack M., Petit, J.P. and Rawnsley K.D. (1992), “Joint spacing: analogue and numerical simulations”, *Journal of Structural Geology*, 14(8/9), 925-937.
149. Sammis C.G. and Ashby M.F. (1986), “The failure of brittle porous solids under compressive stress states”, *Acta Metall*, 34(3), pp.511–26.
150. Santarelli F.J. and Brown E.T. (1989), “Failure of three sedimentary rocks in triaxial and hollow cylinder compression tests”, *Int J Rock Mech Min Sci and Geomech Abstr*, 26, pp.401-13.
151. Scavia C. (1999), “The displacement discontinuity method for the analysis of rock structures: a fracture mechanic”, In: *Aliabadi M.H. (Ed.) “Fracture of Rock”. Boston: WIT press, Computational Mechanics Publications*, pp.39–82.
152. Scavia C. and Castelli M. (1996), In: Barla G., editor. “Analysis of the propagation of natural discontinuities in rock bridges”, *EUROCK’98. Rotterdam: Balkema*, pp.445–51.
153. Schmidt R.A. (1980), “A microcrack model and its significance to hydraulic fracturing and fracture

toughness testing", *Proc. 21st US Symp. On Rock Mech.*, pp.581-590.

154. Schock R.N., Heard H.C. and Stevens D.R. (1973), "Stress–strain behavior of a granodiorite and two graywackes on compression to 20 kilobars.", *J. Geophys. Res.*, pp.5922– 5941.
155. Shen B. and Duncan Fama M.E., 1999, "Review of highwall mining experience in Australia and case studies", CSIRO, *Exploration and mining report 616F*.
156. Shen B. and Stephanson O. (1993), "Numerical analysis of mixed mode I and mixed mode II fracture propagation", *Int J Rock Mech Min Sci and Geomech Abstr*, 30, pp.861-7.
157. Shen B. and Stephanson O. (1994), "Modification of the G-criterion for crack propagation subjected to compression", *Eng Fract Mech*, 47(2), pp.177-89.
158. Shen B., Tan X., Li C. and Stephanson O. (1997), "Simulation of borehole breakouts using fracture mechanics model", In*: Sugawara K, Obara Y (Eds.) "Rock Stress", Proc. of the International Symposium on Rock Stress, Kumamoto, Japan, 7-10 October, Balkema, Rotterdam*, pp.289-98.
159. Sih G.C., Hilton P.D. and Wei R.P. (1970), "Exploratory development fracture mechanics of composite systems", *Air Force Technical Report*, AFML-TR-70-112.
160. Singh D.P. (1979), "A study of frictional properties of rock", *4th congress Int. Soc. Rock Mech., Montreux,* pp. 301-305
161. Singh T.N. and Singh D.P. (1992), "Assessing stability of voids in multi seam opencast mining", Colliery guardian, July, pp. 159-164

162. Skempton, A.W. (1961), “Horizontal stress in overconsolidated Eocene clay”, Proc. 5th ICOSMFE, Paris, 1, p. 351-357.
163. Snyman C.P. and Barclay J. (1989), “The coalification of South African Coal”, Int. J. of Coal Geology, v.13, pp. 375-390.
164. Spencer E.E. (1967), “A method of the analysis of the stability of embankments assuming parallel inter-slice forces”, *Geotechnique,* 17, pp. 11-26.
165. SRK (1995), “Failure analysis of the North Pit Failure, Colliery A-1”, *unpublished.*
166. Stacey T.R. (1981): A simple extension strain criterion for fracture of brittle rock. *Int. J. Rock. Mech. Min. Sci. & Geomech. Abstr.* Vol. 18, pp. 469-474.
167. Stacey, T.R. (1970), “Planning Open-pit mines”, J.G. Ince & Son, Johannesburg, pp. 199-207;
168. Stacey, T.R. (1973), “A three-dimensional consideration of stresses surrounding open-pit mine slopes”, I. J. Rock Mech. & Min. Sci., 10.
169. Stead D. and Scoble M.J. (1983), "Rock slope stability assessment in British surface coal mines", *Second international Surface mining and quarrying symposium*, 4–6 October, Bristol, UK, pp. 205-216
170. Stead D., Eberhardt E., Coggan J. and Benko B. (2001), “Advanced numerical techniques in rock slope stability analysis – Applications and limitations”, *Landslides – Causes, Impacts and Countermeasures*, Davos, Switzerland, pp. 615-624.
171. Steif P.S. (1984), “Crack extension under compressive loading”, *Eng. Fract. Mech.*, 20(3), pp.463–73.

172. Sturman J.M. (1984), "Influence of slope stability on economics of opencast coal mining in the east and north midlands of England", Surface mining and quarrying, 2nd Int. Surface mining and quarrying symposium, Bristol, UK, pp. 217-224
173. Sultan H.A. and Seed B.H. (1967), “Stability of sloping core earth dams”, *J. Soil Mech. Found. Div., Proc. ASCE.*
174. Sylvester A.G. (1988), “Strike-slip faults”, *Geological Society of America*, Bulletin 100, pp. 1666-1703.
175. Tada H., Paris P.C. and Irwin G.R. (1985), “The stress analysis of cracks handbook”, *2nd ed. St. Louis, Paris Production Incorporated*.
176. Tamate O. (1968), “The effect of a circular inclusion on the stresses around a line crack in a sheet under tension”, *Int J Fract*, 4, pp.257–66.
177. Tapponnier P. and Brace W.F. (1976), “Development of stress-induced microcracks in Westerly granite”, *Int J Rock Mech Min Sci Geomech Abstr*, 13, pp.103–12.
178. Tchalenko, J.S. and Ambraseys, N.N. (1970), “Structural analysis of the Dasht-e Bayaz (Iran) earthquake fractures”, *Geological Society of America*, Bulletin 81, pp. 41-60.
179. Terzaghi, K. (1961), “Discussion of Prof. A. W. Skempton’s paper - Horizontal stress in overconsolidated Eocene clay”, Proc. 5th ICOSMFE, Paris, 3, p. 144-145.
180. Timoshenko, S. (1934), “Theory of elasticity”, McGraw-Hill book company, New York, pp. 333-339.
181. Tsang Y.W. (1984), “The effect of tortuosity on fluid flow through a single fracture”. *Water Resources Research* 20, 1209-1215.

182. Ugular, A.C. (1999), "Stresses in plates and shells", 2nd Edition, McGraw-Hill, p. 39.
183. Van den Hoek P.J., Smit D.J., Kooijman A.P., de Bree P.H. and Kenter C.J. (1994), "Size dependency of hollow-cylinder stability", *Rock Mechanics in Petroleum Engineering, Proceedings of EUROCK '94, Delft, Netherlands, SPE/ISRM International Conference, 29-31 August. Balkema, Rotterdam and Brookfield*, pp.191-8.
184. Van der Merwe N. (1998), "Practical coal mining strata control", *ITASCA Africa*.
185. Van der Merwe, J.N. (2002-a), Personal conversation.
186. Van der Merwe, J.N. (2002-b), "Horizontal stress: The root of all evil?", Proc. 19th Conf. On Ground Control in Mining, Teheran.
187. Vardoulakis I.G. and Papamichos E. (1991), "Surface instabilities in elastic anisotropic media with surface-parallel Griffth cracks", *Int J Rock Mech Min Sci and Geomech Abstr*, 28(2/3), pp.163-73.
188. Vasarhelyi B. and Bobet A (2000), "Modeling of crack initiation, propagation and coalescence in uniaxial compression", *Rock Mech Rock Eng*, 33(2), pp.119–39.
189. Vermeer P.A. and de Borst R. (1984), "Non-associated plasticity for soil, concrete and rock", *Heron* Vol. 29, No. 3, Delft University of Technology, Delft, The Netherlands.
190. Vermeer P.A. (1990), "The orientation of shear bands in biaxial tests", *Geotechnique* 40, pp. 223-236.
191. Wang C., Libardi N. and Baldo J.B. (1998), "Analysis of crack extension paths and toughening

in two-phase brittle particulate composites by the boundary element method". *Int J Fract*, 94, pp.177-88.

192. Whittaker B.N., Singh R.N. and Sun G. (1992), "Rock fracture mechanics – principles, design and applications", *Elsevier, Amsterdam*.
193. Wong H.C., Chau K.T. and Wang P. (1995), "Microcracking in coarse and fine grain marble", *Proc. 35th US Symp. On Rock Mech., Lake Tahoe, Balkema, Rotterdam*, pp.477-482.
194. Wong R.H.C., Chau K.T., C.A. Tang C.A. and Lin P. (2001-a), "Analysis of crack coalescence in rock-like materials containing three flaws-Part I: experimental approach", *Int. Journal of Rock Mechanics and Mining Sciences,* 38, pp. 909–924
195. Wong R.H.C., Chau K.T., C.A. Tang C.A. and Lin P. (2001-b), "Analysis of crack coalescence in rock-like materials containing three flaws-Part II: numerical approach", *Int. Journal of Rock Mechanics and Mining Sciences,* 38, pp. 925–939
196. Wong R.H.C., Tang C.A., Chau K.T. and Lin P. (2002), "Splitting failure in brittle rocks containing pre-existing flaws under uniaxial compression", *Eng. Fracture Mech.*, 69 (2002), pp.1853-1871.
197. Wong T.F. (1982), "Micromechanics of faulting in westerly granite". *Int J Rock Mech Min Sci, Geomech Abstr*, 19, pp.49–64.
198. Wright S.K., Kulhawy F.H. and Duncan J.M., (1973), "Accuracy of equilibrium slope stability analysis", J. of the Soil Mech. and Found. Div., ASCE, Vol. 99, No SM10, pp. 783-791
199. Wu H. and Pollard D.D. (1995), "An experimental study of the relationship between joint spacing

and layer thickness", *Journal of Structural Geology*, 17, pp. 887-905.

200. Xia L., Shih C.F. and Hutchinson J.W. (1995), "A computational approach to ductile crack growth under large scale yielding conditions", *J Mech Phys Solids*, 43.
201. Yu S.W. and Fan X.J. (1992), "Temperature fields at crack tip in a damaging medium", *ZAMM*, 72.
202. Zhang Ch. and Gross D. (1994), "Ductile crack analysis by a cohesive damage zone model", *Engineering Fracture Mech.*, 47.
203. Zheng Z. (1998), "Integrated borehole stability analysis - Against tradition", *ISPE/ISRM Eurock '98, Trondheim, Norway*, vol. 1, pp. 395-402.
204. Zheng Z., Kemeny J. and Cook N.G.W. (1989), "Analysis of borehole break-outs", *J. Geophys. Res., B94*, pp. 7171-7182.